THE CHARACTERISATION AND MODELLING OF POROSITY FORMATION IN ELECTRON BEAM WELDED TITANIUM ALLOYS

By

JIANGLIN HUANG

A dissertation submitted to
The University of Birmingham
for the degree of
DOCTOR OF PHILOSOPHY

School Metallurgy and Materials
The University of Birmingham
September 2011

Abstract

This thesis is concerned with the porosity formation mechanism during electron beam welding of titanium-based alloys. During the welding of titanium alloys for structural applications, porosity is occasionally found in the solidified welds. Hence the key factors responsible for porosity formation need to be identified, and guidance to minimise porosity occurrence needs to be provided.

The aim of this project is twofold. First, porosity formed in electron beam welded titanium samples is characterised to rationalise the porosity formation mechanism. Second, models based on sound physical principles are built to aid understanding of porosity formation, and to provide predictive capability. Chapter 1 contains the introduction and background of the project. A literature review is reported in chapter 2 which covers the metallurgy of titanium and its alloys, the electron beam welding process, and porosity formation in titanium welds.

In chapter 3, electron beam welds of commercially pure titanium (CP-Ti), Ti-6Al-4V, Ti-6246, IMI 834 are characterised to rationalise the porosity formation mechanism by using metallographic sectioning, high resolution X-ray tomography, residual gas analysis, scanning electron microscopy (SEM) and energy and wavelength dispersive spectroscopy (EDS/WDS) analysis. The results confirm porosity formed in electron beam welded titanium-based alloys is associated with gas dynamics; hydrogen is very likely to be responsible for porosity formation.

In chapter 4, numerical models are developed to improve the understanding of the electron beam welding process, including heat cycling, weld pool and keyhole formation, which are prerequisites for further investigation of the physical phenomena occurring, such as hydrogen behaviour and bubble formation and entrapment.

In chapter 5, based on the numerical models for electron beam welding process, a coupled thermodynamic/kinetic model is proposed to study the hydrogen migration behaviour. The modelling results confirm hydrogen migrates from the cold region towards the hot region and thus causes hydrogen accumulation inside the weld pool. This model enables the prediction of hydrogen content inside the weld pool. The

comparison between the predicted hydrogen distribution and previous experimental data is shown to be reasonable.

In chapter 6, a hydrogen driven bubble growth model is proposed to study the hydrogen effect on porosity formation, in which bubble is assumed to be initiated due to the effect of asperities at the joint surfaces. This model is used to estimate the hydrogen effect on stationary bubble growth in the melt, and thus to make predictions of the hydrogen concentration barrier needed for pore formation. The effects of surface tension of liquid metal and the radius of pre-existing micro-bubble size on the barrier are also investigated.

In chapter 7, to study the effect of hydrogen on porosity formation and to confirm whether hydrogen is the root cause for porosity formation, Ti-6Al-4V samples were electrochemically charged to achieve different hydrogen levels before welding. The results confirm that bubbles are nucleated at the melting front during the welding process. With optimised electron beam parameters and perfect joint alignment, porosity can be suppressed even at a very high hydrogen levels; on the other hand, porosity is exacerbated when a small beam offset (BOF) is employed. This is because any BOF alters the size of the liquid zone at the melting front, where joint edges are melted. Thus the thickness of the liquid film at the melting front is crucial for bubble nucleation and their survival in the weld pool. It would appear that the nucleation rate in the liquid zone at the melting front determines the likelihood of porosity occurrence. This suggests that BOF is likely to be one factor influencing porosity formation in these circumstances.

Finally, in chapter 8, conclusions are drawn and suggestions for further work made.

To my family

Acknowledgements

I am grateful to the Engineering and Physical Sciences Research Council (EPSRC) of the United Kingdom and to Rolls-Royce plc for sponsorship of this work, via a Dorothy Hodgkin Postgraduate Award (DHPA).

I would like to thank my supervisor Professor R. C. Reed, for all the help and direction he gave me throughout the course of this work. I benefitted a great deal from his insight and encouragement during the discussions about this work. His enthusiasm and hard-working really impressed me, which will be an inspiration throughout my future life. I also want to thank my co-supervisor Dr Martin Strangwood; I am really impressed by his profound professional knowledge and scientific rigour and enthusiasm. Without his guidance and great patience, this work could not have been accomplished.

A special thank you must go to Dr Jean-Christophe Gebelin and Dr Nils Warnken, members of Partnership for Research in the Simulation and Manufacturing and Materials Group (PRISM2), for the considerable help and guidance I received from them.

I would like to thank all members of PRISM2 group, my colleagues and friends in the department, who make my life more enjoyable during this work. The assistance from the workshop, the technicians and staff of Metallurgy and Materials is appreciated.

Support from Dr Steve Beech and Alistair Smith at Rolls-Royce plc are appreciated for sharing their knowledge and experience of electron beam welding. Special thanks to Alistair Smith for his help on all the electron beam welding work performed during this study. I also thank Professor Ian Sinclair and Dr Mark Mavrogordato for providing X-ray Computed Tomography (CT) support at the University of Southampton.

I would like to dedicate this work to Yangzi Hu, withour her, it would have been impossible for me to make my decision to study abroad. I greatly appreciate the encouragement from her, which has changed my life forever.

At last and not least, I thank my family for their continuous love and support.

Preface

This dissertation is submitted for the degree of the Doctor of Philosophy at the University of Birmingham. It describes research carried out in School of Metallurgy and Material Science between October 2007 and September 2011, under the supervision of Prof. R. C. Reed and Dr. M. Strangwood. Except where appropriately referenced, this work is original and has not been submitted for any other degree, diploma and other qualification. It does not exceed 50,000 words in length.

Parts of this dissertation have been published or submitted for publication in:

- Jianglin Huang, A. Smith, N. Warnken, J-C, Gebelin, M. Strangwood and R. C. Reed. On The Mechanism of Porosity formation During Welding of Titanium Alloys. ***Acta Materialia*** (Accepted)

- Jianglin Huang, N. Warnken, J-C, Geblin, M. Strangwood and R. C. Reed. Hydrogen Transport and Rationalisation of Porosity Formation during Welding of Titanium Alloys. ***Metallurgy and Materials Transaction A***. (Accepted)

- Jianglin Huang, N. Warnken, J-C, Geblin, M. Strangwood and R. C. Reed. A Coupled Thermodynamic/Kinetic Model for Hydrogen Transport during Electron Beam Welding of a Titanium Alloy. ***Material Science and Technology***. (Accepted)

- Jianglin Huang, N. Warnken, J-C Geblin, M. Strangwood and R. C. Reed(2010). Modeling of Hydrogen Effect on Porosity Formation in Electron Beam Welded Titanium-based Alloys. paper presented at ***4th International Conference on Thermal Process Modelling and Computer Simulation***, Shanghai, China, 1-3 June, 2010. paper No. G01

- Jianglin Huang, A.Smith, N. Warnken, J-C, Geblin, M. Strangwood and R. C. Reed. On Porosity Formation in Electron Beam Welding of Titanium Alloys. ***The 12th World Conference on Titanium***, Beijing, China, 19-24 June, 2011.

- Jianglin Huang, J-C, Gebelin, N. Warnken, M. Strangwood, R. C. Reed. Theoretical and Experimental Investigation of Hydrogen Effect on Porosity Formation during Electron Beam Welding of Titanium Alloys. ***The 9th International Conference on Trends in Welding Research, June 4-8, 2012, Chicago, Illinois USA***. (Submitted)

Jianglin Huang

September 2011

Contents

List of Figures xi

List of Tables xvii

1 Introduction 1

1.1 Research Background . . . 1

1.1.1 Titanium Alloys in The Jet Engine . . . 2

1.1.2 Compressors in The Jet Engine . . . 4

1.1.3 Compressor Discs Assembly Using Electron Beam Welding . . . 5

1.1.4 The Problem of Porosity Formation in Electron Beam Welds . . . 6

1.2 Aims and Scope of This Work . . . 9

1.3 Thesis layout . . . 9

2 Literature Review 11

2.1 Titanium and Its Alloys . . . 11

2.1.1 Metallurgy and Classification of Titanium Alloys . . . 11

2.1.2 Processing and Microstructures . . . 14

2.1.2.1 Fully Lamellar Structure . . . 14

2.1.2.2 Bimodal Microstructures . . . 16

2.1.2.3 Fully Equiaxed Structure . . . 17

2.1.2.4 Alpha Case . . . 18

2.1.2.5 Martensite Formation . . . 19

2.1.3 Ti-6Al-4V . . . 20

2.1.4 Ti-6246 . . . 21

2.1.5 IMI 834 . . . 22

2.2 Electron Beam Welding . . . 23

2.2.1 Principles of Electron Beam Welding Process . . . 23

2.2.2 Deep Penetration Welding Effect . . . 25

2.2.3 Influence of Welding Parameters . . . 27
2.2.4 Modelling of Electron Beam Welding Process . . . 29
2.3 General Reasons for Porosity Formation in Welds . . . 35
2.4 Porosity Formation in Electron Beam Welded Titanium . . . 36
2.5 Hydrogen in Titanium Alloys . . . 39

3 Characterisation of Electron Beam Welds of Titanium Alloys and Porosity Formation 45
3.1 Background . . . 45
3.2 Experiment Details . . . 47
3.2.1 EB welds for Porosity Characterisation . . . 47
3.2.2 X-Ray Detection of Porosity . . . 49
3.2.3 Metallographic Investigation . . . 50
3.2.4 Energy and Wavelength Dispersive Spectroscopy Analysis (EDS/WDS) . . . 50
3.2.5 Residual Gas Analysis . . . 51
3.3 Results . . . 52
3.3.1 Characteristics of Titanium EB Welds . . . 52
3.3.2 Pore Morphology and Distribution . . . 68
3.3.3 Chemical Composition Analysis around Porosity Edges . . . 73
3.3.4 Gas Composition inside Porosity . . . 74
3.4 Discussion . . . 75
3.4.1 Hydrogen Effect on Porosity Formation . . . 75
3.4.2 Bubble Initiation and Growth . . . 76
3.4.3 Fusion Zone Shapes and Bubble Escape . . . 77
3.5 Summary and Conclusions . . . 77

4 Numerical Process Models for Electron Beam Welding 79
4.1 Introduction . . . 79
4.2 Modelling the Heat Source . . . 81
4.2.1 Three-Dimensional Conical (TDC) Heat Source Model . . . 81
4.2.2 Modified Three Dimensional Conical (MTDC) Heat Source Model . . . 83
4.2.3 Determination Parameters in Heat Source Model . . . 84
4.3 Keyhole Profile Calculation . . . 85
4.3.1 Assumptions for Keyhole Modelling . . . 85
4.3.2 Electron Beam Focus Properties . . . 86
4.3.3 Energy Balance at Keyhole Wall . . . 87

4.4 Material Properties . . . 91
4.5 Mesh Generation . . . 91
4.6 Beam Focus Point Measurement . . . 93
4.7 Beam Probing Measurement . . . 95
4.8 Metallographic Sectioning . . . 96
4.9 Results and Discussion . . . 97
4.9.1 Focusing Position and Weld Zone Profiles . . . 97
4.9.2 Beam Current Probing Results . . . 99
4.9.3 Comparison of Calculated and Measured Weld Zone . . . 100
4.9.4 Keyhole Profile and Melting Front . . . 106
4.10 Summary and Conclusions . . . 111

5 Modelling of Hydrogen Transport during Electron Beam Welding Process 112
5.1 Introduction . . . 112
5.2 Process Model . . . 114
5.2.1 Governing equations . . . 115
5.2.1.1 Thermal model for EBW process . . . 115
5.2.1.2 Hydrogen diffusion equation . . . 116
5.2.1.3 Treatment of two phase region . . . 119
5.2.1.4 Hydrogen escape during welding . . . 119
5.3 The Numerical Implementation of the Model . . . 120
5.4 Results and Discussion . . . 121
5.5 Conclusions . . . 132

6 Modelling and Rationalisation of Hydrogen Effect on Porosity Formation 133
6.1 Background . . . 133
6.2 Model Description . . . 135
6.2.1 Governing Equation . . . 135
6.2.2 Boundary and Initial Conditions . . . 137
6.2.3 Implementation of the Model . . . 138
6.3 Results . . . 138
6.3.1 Dynamic growth of bubble inside weld pool . . . 138
6.3.2 Critical hydrogen level analysis . . . 140
6.4 Discussion . . . 141
6.5 Summary and Conclusions . . . 143

7 Experimental Investigation of Proposed Porosity Formation Mechanism 145
7.1 Background . . . 146
7.2 Experiment Details . . . 146
7.2.1 Sample . . . 146
7.2.2 Welding Trials Design . . . 147
7.2.3 Electrochemical Hydrogen Charge . . . 148
7.2.4 Electron Beam Welding . . . 150
7.2.5 Quantitative Hydrogen Measurement . . . 151
7.2.6 X-Ray examination of defects in welds . . . 152
7.3 Results and Discussion . . . 153
7.3.1 Characterisation of Hydrogen Charged Samples . . . 153
7.3.2 Electron Beam Welding of the Hydrogen Charged Sample . . . 155
7.4 Summary and Conclusions . . . 161

8 Conclusions and Future Work 162

References 166

List of Figures

1.1 Section of a typical single-spool axial flow turbo-jet engine showing the air flow through the 3 main stages: (a) compressor, (b) combustor and (c) turbine 3
1.2 Rotors of disc and drum construction in compressor assembly. 4
1.3 Discs assembly: (a) Electron beam welding of compressor drum, (b) compressor disc and spacer, (c) surface of close-up of welded joint 5
1.4 Typical cross section of compressor disc and the joint position. 7
1.5 A 4-mm thick welded region in electron beam welded Ti-6Al-4V (the solid lines separate different regions of the welded region). 7
1.6 Porosity found at the cross section of the electron beam welded Ti-6Al-4V. . . . 8
1.7 Conventional film X-ray radiography results showing large pores formed in electron beam welded Ti-6Al-4V. 8

2.1 Effects of alloy elements on structure and some selected properties. 12
2.2 Thermomechanical treatment of titanium alloys. 13
2.3 Effect of cooling rate from beta phase field on lamellar microstructures, Ti-6242, LM: (a) 1°C/min, (b) 100°C/min, (c) 8000°C/min. 14
2.4 Schematic illustration of the development of a Widmanstatten structure in Ti-6Al-4V alloy at slow cooling rate. 15
2.5 Bimodal microstructure 25 IMI 834 alloy. 17
2.6 (a) Fully equiaxed α with intergranular β, and (b) bimodal microstructures (primary α and transformed β) in Ti-6Al-4V alloy. 18
2.7 Ti-O phase diagram. 19
2.8 Arrhenius plot of the oxygendiffusivity in titanium. 20
2.9 Different phases and structures developed in Ti-6Al-4V under different cooling rate. 21
2.10 Ti-6246 Continuous cooling transformation diagram. 22
2.11 Principle of electron beam welding. 24

2.12 Schematic illustration of vapour keyhole and weld pool formation during electron beam welding. . . . 26
2.13 Photographs of the metallographic sections welded at different beam defocus current (upper) and relevant simulation results of fusion zone boundary isotherms. . 30
2.14 Influence of weld pool motion influence on porosity (a) inward surface flow; (b) outward surface flow. . . . 31
2.15 Common driving force inside weld pool (a) thermocapillary (Marangoni) forces M(+) or M(-); (b) electromagnetic (Lorentz) forces E, resulting from interaction of current; (c) buoyancy forces B, resulting from density differences caused by temperature gradients; (d) aerodynamic drag forces A, caused by passage of plasma over surface. . . . 32
2.16 Marangoni effect on fluid flow in weld pool with negative temperature coefficient (left) and positive temperature coefficient (right). . . . 33
2.17 ERDA measurement result shows hydrogen concentration profile in the surface of Ti-6Al-4V plate. . . . 37
2.18 Evaluated concentration profile from SIMS measurement and calibrations. . . . 38
2.19 Solubility curve for hydrogen in titanium as a function of temperature, at 1 atmosphere external pressure. . . . 40
2.20 Hydrogen solubility in titanium. . . . 41
2.21 Hydrogen solubility in Ti-60 alloys as a function of reciprocal absolute temperature. 42
2.22 Hydrogen solubility as function of hydrogen partial pressure in temperature range of 800°C to 950°C. . . . 43
2.23 Solubility limits of hydrogen in β-titanium. . . . 44

3.1 Schematic diagram of the residual gas analysis system. . . . 51
3.2 Optical micrograph illustrating the microstructure of as-received CP-Ti. . . . 53
3.3 Typical cross section of EB welds of CP-Ti with a large pore located in the weld FZ centre. . . . 53
3.4 Optical micrograph illustrating microstructure transition from HAZ to BM in electron beam welded CP-Ti. . . . 54
3.5 Optical micrograph illustrating the typical microstructure of the FZ, locating at the centre line of electron beam welded CP-Ti. . . . 54
3.6 Microhardness across the weld in electron beam welded CP-Ti. . . . 55
3.7 Optical micrograph illustrating the microstructure of BM in as-received Ti-6Al-4V sample. . . . 56
3.8 Typical cross section of electron beam welded Ti-6Al-4V alloy. . . . 57

3.9 Optical micrograph illustrating transition of microstructures between BM and HAZ in electron beam welded Ti-6Al-4V. 57
3.10 (a) optical micrograph illustrating transition of microstructures between BM and HAZ in electron beam welded Ti-6Al-4V; (b) SEM micrograph with higher magnification illustrating the microstructure in BM; (c) SEM micrograph with higher magnification illustrating the microstructure in HAZ. 58
3.11 Acicular martensite in fusion zone of electron beam welded Ti-6Al-4V alloy. . . . 58
3.12 Microhardness across the weld in electron beam welded Ti-6Al-4V. 59
3.13 Optical micrograph illustrating the microstructure of BM in as-received Ti-6246 sample. 60
3.14 Typical cross section of electron beam welded of Ti-6246. Note the pores in the toe of the weld. 60
3.15 (a) optical micrograph illustrating transition of microstructures between BM and HAZ in electron beam welded Ti-6246; (b) SEM micrograph with higher magnification illustrating the microstructure in BM; (c) SEM micrograph with higher magnification illustrating the microstructure in HAZ. 61
3.16 Optical micrograph illustrating transition of microstructures between HAZ and FZ in electron beam welded Ti-6246. 61
3.17 Microstructure in fusion zone of electron beam welded Ti-6246 alloy. 62
3.18 Microhardness profile across the weld cross section in electron beam welded Ti-6246. 62
3.19 Optical micrograph illustrating the microstructure in base material of as-received IMI 834. 64
3.20 Typical cross section of EB weld of IMI-834. 65
3.21 Optical micrograph illustrating transition of microstructures between BM and HAZ in electron beam welded IMI 834. 66
3.22 Optical micrograph illustrating transition of microstructures between HAZ and FZ in electron beam welded IMI 834. 66
3.23 Acicular martensite in fusion zone of electron beam welded IMI 834 alloy. 67
3.24 Hardness profile across the electron beam welded IMI 834 alloy. 67
3.25 Porosities formed in EB weld of CP-Ti. 68
3.26 Reconstructed image from X-ray tomography (CT) results illustrating pore distribution inside electron beam welded CP-Ti. 69
3.27 SEM micrograph illustrating the inner surface of a small pore formed in electron beam welded CP-Ti. 70
3.28 Pores formed in electron beam welded Ti-6Al-4V alloy. 71

3.29 Series of tomography sections across a detected porosity in IMI-834 EB welds. . . 71
3.30 SEM micrograph illustrating the morphology of pore formed in electron beam welded IMI-834 alloy. 72
3.31 Merged pores found in electron beam welded IMI-834 alloy. 72
3.32 Line scanning along pore edge formed in electron beam welded Ti-6246 alloy to identify the chemical composition distribution. 74
3.33 Gas analysis result by using MID (Multiple Ion Detection) mode. 75

4.1 Schematic illustration of (a) standard three dimensional conical (TDC) heat source and (b) modified three dimensional conical (MTDC) heat source model. . 82
4.2 Waisting of the electron beam at focus showing the definition of aperture angle towards the workpiece. 86
4.3 Schematic illustration of heat balance at keyhole wall in the longitudinal section through the weld centreline. 88
4.4 Flow diagram for the keyhole profile calculation. 90
4.5 Temperature dependent material properties of Ti6Al4V: (a) density, (b) heat capacity and (c) heat conductivity. 92
4.6 Graded mesh used in this study. 93
4.7 Measurement of focus position. 94
4.8 Electron beam probing by using slit sensor. 95
4.9 Cross sections located at different distance from the start of the welds designed for beam focus measurement: (a) upper plate, welded at working distance at 244 mm; (b) lower plate, welded at working distance of 277 mm. 98
4.10 The relationship between the focus distance and the given specific range of focus current. 99
4.11 Beam probing profiles from two directions by using slit sensors. 100
4.12 Heat source parameter fitting: (a) measure the fusion zone width at different thickness position; (b) fitting the curve to get Gaussian parameter distrubtion fuction f(z). 102
4.13 (a) measured and predicted cross section for plane near the electron beam centre; (b) measured microhardness profile and predicted temperature profile across the weld region in the middle of thickness direction. 103
4.14 Predicted weld pool dimensions. 104
4.15 Measured weld pool dimensions at the top and bottom surfaces. 105
4.16 Calculated keyhole profile. 107
4.17 Calculated beam intensity and heat flow at keyhole wall. 107

4.18 Calculated local keyhole angles. 108
4.19 Reconstructed CT image illustrating the captured melt front. 108
4.20 Optical micrograph showing the captured melting front at the longitudinal section through the weld bead centre. 109
4.21 Optical micrograph illustrating the melting front at the upper part of the longitudinal section through the weld bead centre. 109
4.22 Optical micrograph illustrating the melting front at the middle part of the longitudinal section through the weld bead centre. 110
4.23 Optical micrograph illustrating the melting front at the lower part of the longitudinal section through the weld bead centre. 110

5.1 Schematic diagram of electron beam full penetration welding (Cartesian coordinate system and conical heat source). 115
5.2 Arrhenius plots of the hydrogen diffusivity in HCP and BCC phases in Ti-6Al-4V. 118
5.3 Flow chart illustrating the numerical implementation of the model. 122
5.4 Locations of the two planes in the 3D calculation domain. 123
5.5 (a) Weld pool shape and (b) hydrogen distribution at middle plane of z direction with welding speed of 14 mm/s, t = 1.7s. 124
5.6 (a) Fusion zone and (b) hydrogen distribution and fusion zone profile at cross section at 1.48 s. 125
5.7 Predicted temperature, hydrogen chemical potential and hydrogen distribution profile of along the probing line at time, (a) $t = 1.42$ s, (b) $t = 1.45$ s and (c) = 2.0 s. 126
5.8 Associated (a) phase fraction and (b) hydrogen concentration in each phase along probing line at time $t = 1.45$ s. 128
5.9 (a) Predicted hydrogen distribution at cross section and (b) Calculation results compared to the reported experimental measurement results 131

6.1 Schematic illustration of the hydrogen diffusion-controlled bubble growth model. 136
6.2 Calculated bubble radius evolution with differnt hydrogen content in the melt. . 139
6.3 Pressure evolution during bubble growth with hydrogen content of 300 ppm in the melt. 140
6.4 The evolution hydrogen concentration at gas-liquid interface during the bubble growth with hydrogen content of 300 ppm in the melt. 141
6.5 Effect of pre-existing bubble size, surface tension and ambient pressure on critical hydrogen level for bubble growth. 142

7.1 Scanning electron microscopy illustrating the microstructure of the as-received Ti-6Al-4V sample. 147
7.2 Measure surface roughness profile of as-received Ti-6Al-4V samples. 148
7.3 Reported hydrogen uptake in Ti6Al4V alloy after electrochemical hydrogen charge with different charging time. 149
7.4 SEM micrograph of uncharged (a) and 12-hours charged (b) sample surfaces. . . 154
7.5 Crack at sample edge after 12 hours hydrogen charge. 155
7.6 Measured pressure rise in the working chamber. 156
7.7 Detected pressure rise during welding of sample charged with different time. . . . 157
7.8 Top surfaces of weld beads for samples charged for different times. 158
7.9 Undercut found in 6-hours charged sample with small pores at fusion boundary. . 159
7.10 Liquid zone size around joint edges at melting front, and changes due to beam offset (BOF). 159
7.11 Porosity found in beam offset welding samples. 160

List of Tables

2.1 The maximum power density of the various heat sources used for welding. 23

3.1 Chemical composition of the alloys in this study (weight percentage). 48

4.1 Material properties of Ti-6Al-4V used in the keyhole calculations. 91

5.1 EB parameters used in calculation. 120

6.1 Material properties and physical constants used in calculation. 138

7.1 Sample preparation of the 1st set of welding trials. 150

7.2 Sample preparation in the 2nd set of welding trials. 151

Nomenclature*

Item	***Description***
BCC	Body-centred-cubic
BM	Base material
BOF	Beam offset
C_H	Hydrogen concentration (mol/m^3)
C_p	Heat capacity (J.kg^{-1}K^{-1})
CP-Ti	Commercially pure titanium
CT	Computed tomography
df_0	Beam wait size (m)
D_H	Hydrogen diffusivity (m^2/s)
EBW	Electron beam welding
EDS	Energy and dispersive spectroscopy
FZ	Fusion zone
HAZ	Heat-affected zone
HCP	Hexagonal-close-packed
HP	High pressure
I	Current (mA)
IP	Intermediate pressure
J_H	Hydrogen flux (mol/m^2)
LB	Laser beam
LP	Low pressure
MS	Mass spectrometry
MTDC	Modified three-dimensional conical
P	Power (W)
ppm	Parts per million

Item	***Description***
Q_0	Maximum heat intensity (W/m^3)
r_0	Gaussian distribution radius (m)
r_e	Gaussian distribution radius at top surface (m)
RGA	Residual gas analysis
r_i	Gaussian distribution radius at bottom surface (m)
SEM	Scanning electron microscopy
t	Time (s)
T	Absolute temperature (K)
TDC	Three-dimensional conical
TGA	Thermogravimetric analysis
U	Voltage (kV)
WDS	Wavelength dispersive spectroscopy
x, y, z	Space coordinates (m)
z_e	z coordinates at the top plane (m)
z_i	$z$coordinates at the bottom plane (m)
z_R	Rayleigh range (m)
θ_w	Local wall angle
η	Power efficiency
μ_H	Hydrogen chemical potential (J/mol)

* For symbols and abbreviations used more than three times

1

Introduction

Summary

This chapter covers the research background, which concerns the electron beam welding of titanium-based alloys for aeroengine applications. First, a brief description of the application of titanium alloys in jet engine design, compressors and compressor discs assemblies is given, following an overview of porosity formation in electron beam welded titanium-based alloys. The second part defines the aims and scope of this research and describes the dissertation layout.

1.1 Research Background

Titanium-based alloys offer remarkable mechanical properties, which are especially impressive when judged on a density-corrected basis. For this reason, they are used widely for high performance structural applications, particularly in the aerospace sector [1, 2]. In the example of the modern aero-engine, a number of critical components in the fan and compressor regions (particularly blades and discs) are fabricated from them, on account of their excellent specific properties. Indeed, it is likely that the levels of performance that have been achieved (*e.g.* thrust/weight ratio and fuel economy) would not have been possible without their widespread insertion into aero-engine designs [3, 4].

Electron beam welding is used widely for the manufacturing of aerospace engine components due to its several special characteristics, such as extremely high power density, high welding

speed, narrow welds and heat affected zone, low distortion, high reproducibility and consistency and good protection of weld pool under vacuum [5]. All these unique advantages enable very high quality welds to be made during the manufacturing of complex components. For example, welding of rotors requires both a high degree of dimensional accuracy as well as excellent weld quality and high reliability [6].

Like all other fusion welding methods, defect formation cannot be absolutely avoided in the electron beam welds. One of the current practical problems during electron beam welding of titanium-based alloy is that porosity is found occasionally in the solidified welds. The pores detected by using non-destructive testing (NDT) methods, such as radiographic and ultrasonic testing, are found to have diameter around 0.1∼0.3 mm; very occasionally, porosity is found to have a size larger than 1 mm, large enough to cause component rework. With the high costs associated with the materials used, the cost due to rejection of the component is significant. As a result, porosity formation must be minimised. At this stage, the porosity formation mechanism is not sufficiently understood. Guidance for electron beam welding optimisation to minimise the porosity is needed.

1.1.1 Titanium Alloys in The Jet Engine

A jet engine employs Newton's third law of motion to generate thrust by ejecting high velocity gases due to the combustion of mixed air and fuels inside the engine. The generated thrust is normally used in aircraft application. Although the broad definition of a jet engine includes ramjets, pulse jets, rockets, turbojets, and turbofans, today the jet engine is more commonly associated with the gas turbine engine, which consists of rotary air compressors powered by turbines. The fundamental operating principle of the gas turbine engine can be illustrated by using a typical axial flow turbojet engine as shown in Figure 1.1, in which three main sections are included: the compressor, the combustor and the turbines. At the first section, the air is mechanically compressed by going through multi-stage axial flow compressors, which is made up of the fan and alternating stages of rotating blades and static vanes. The blades accelerate

the air increasing its dynamic pressure, and then the vanes decelerate the air transferring kinetic energy into static pressure rises. The compressed air is delivered into the combustion system. At the second section, highly compressed air is diffused around the outside of the combustion chamber. The mixed air and fuel is burned inside the annular combustion chamber and the temperature increases beyond 2000 °C. The hot combustion gases enter the turbines systems. Turbine blades convert the energy stored within the gas into kinetic energy. Like the compressor, the turbine comprises of a rotating disc with blades and static vanes, called nozzle guide vanes [7]. The hot air flow that passes through the turbines produces a thrust to propel the engine.

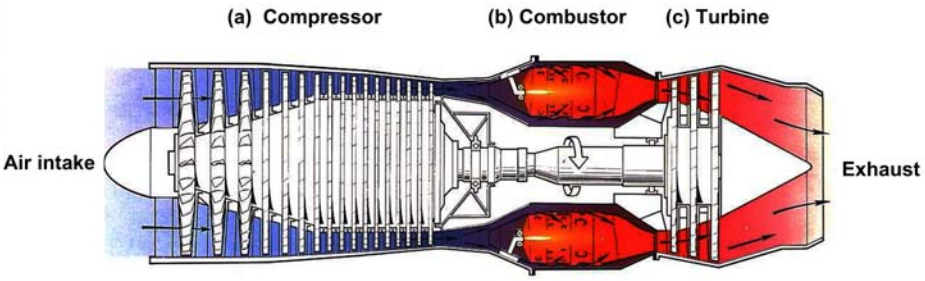

Figure 1.1: Section of a typical single-spool axial flow turbo-jet engine showing the air flow through the 3 main stages: (a) compressor, (b) combustor and (c) turbine [7]

Since the jet engine is heat engine which converts the chemical energy of fuel into mechanical energy used to generate thrust, the efficiency of these engines depends on the combustion temperature and compression ratio of air. Thermodynamic efficiency increases as combustion temperature and compression ratio of the air increase, which requires higher temperature strength for materials. In the combustor and turbine sections, the nickel-based superalloys are used almost exclusively due to their excellent high temperature properties, while in the compressor section, the most common materials for the compressors in modern jet engines are now titanium alloys due to their high specific strength compared to steels and aluminium alloys. Superalloys are used also in the final stage (high pressure) stage of the compressor [8]. The following parts give a brief introduction to compressor design and compressor discs assembly.

1.1.2 Compressors in The Jet Engine

Compressors in the jet engine are designed to increase the pressure of the air through the gas turbine core. Figure 1.2 shows a typical axial flow compressor, which consists of rotors and static vanes. The rotors contain a number of blades fixed on a drum formed from a series of compressor discs. The discs are fitted onto rotor shaft, which is coupled to turbine shaft, providing driving

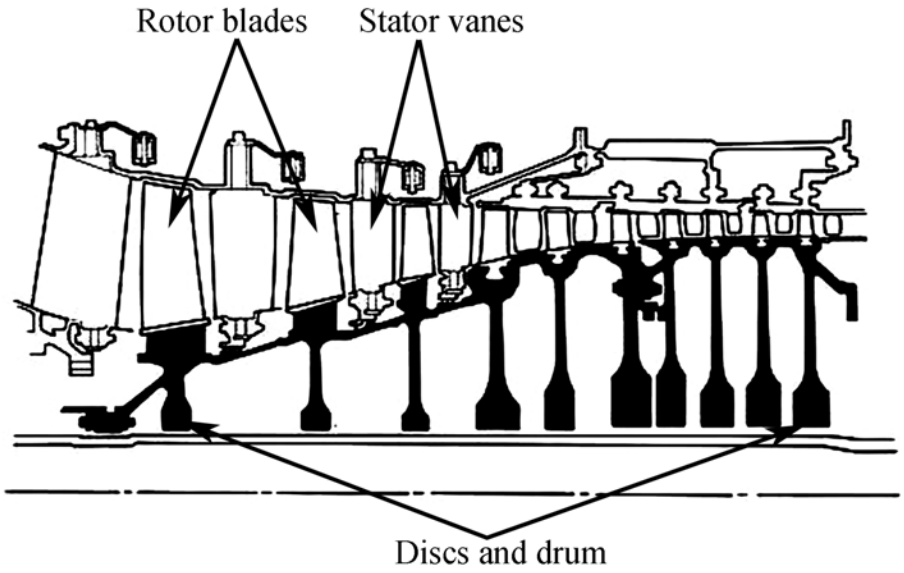

Figure 1.2: Rotors of disc and drum construction in compressor assembly.[7]

force for the rotors. Air flow is accelerated and driven into the engine via the rotating blades. Each row of blades is followed with a row of static vanes, which are designed to direct the airflow onto the succeeding row of blades with appropriate angle and to cause a pressure rise at the same time. To achieve high compression ratio, a multistage compressor is used in modern jet engine, due to the different airflow characteristics (speed, temperature, pressure) in each stage. Generally, multistage compressors are divided into low pressure (LP), intermediate pressure (IP), and high pressure (HP) compressors according to the different working conditions. Depending on the working temperature, the usage of titanium alloys in different stages of the compressors

varies. For instance, Ti-6Al-4V is commonly used in the low LP section, where the typical working temperature is below 300°C, while in the IP section, as the temperature rises to above 500°C, titanium alloys with better oxidation resistance are applied, such as Ti-6246. The hottest part in the compressor is the HP section, where the temperature reaches the limit of titanium-base alloys application due to the poor oxidation resistance at high temperature. For this reason, the disk and blades at the HP section have to be manufactured from nickel-base alloys.

1.1.3 Compressor Discs Assembly Using Electron Beam Welding

During the manufacture of compressors, rotor blades need to be mounted on a drum, which is formed by welding a number of stages of discs and spacers together. Figure 1.3 (a) shows a series of discs and spacers, which are mechanically clamped and ready to be loaded into an electron beam welding chamber. Typical shapes of discs and spacers are shown in Figure 1.3 (b). Since the disc and spacers are radially symmetrical, autogenously circumferential electron

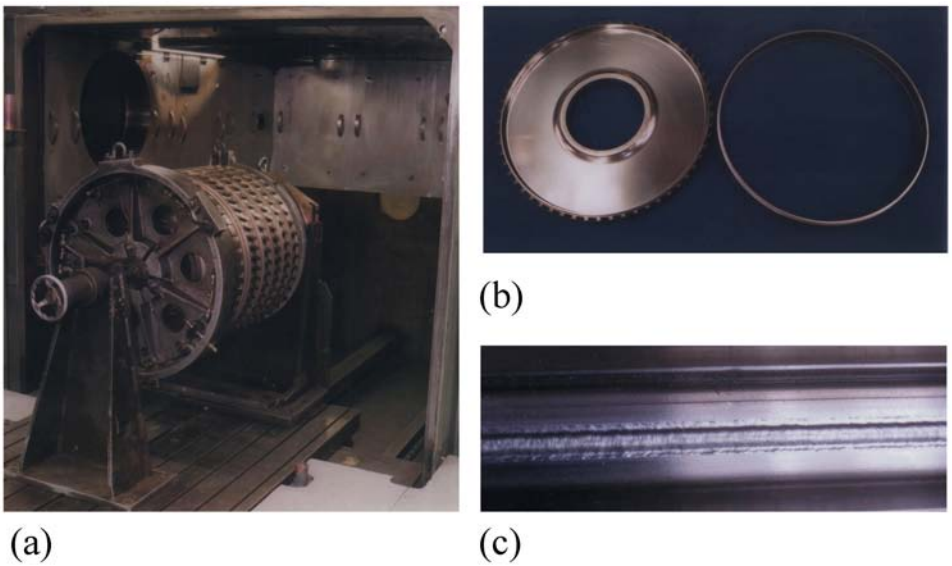

Figure 1.3: Discs assembly (a) Electron beam welding of compressor drum, (b) compressor disc and spacer, (c) surface of close-up of welded joint (Photographs courtesy of Rolls Royce plc)

beam welding under axial loading is applied. The welding process can be briefly described as follows: first, after loading the work-piece, the working chamber is pumped down to a high vacuum condition (around 10^{-4} mbar) in order to avoid electron beam dispersion and protect the

work-piece. After the working chamber reaches the required vacuum condition, the workpiece is positioned to ensure the required working distance and good beam to seam alignment. To make sure the electron beam is always in the right position during welding, the work-piece is rotated 360° with 4 beam position check evenly distributed around the whole circumference by using reduced beam intensity. Then the following welding process is conducted in two welding passes. In the first, the component rotates 360° with a low power beam applied, to achieve a partial penetration, the so-called seal pass. A second, single pass full penetration with high power beam at slight over-focus is performed to finish the welding. The influence of electron beam parameters, including accelerating voltage, beam current, welding velocity and focus position etc. will be discussed in Chapter 2 in this dissertation. A typical finished electron beam welded seam surface is given in Figure 1.3 (c), in which the typical width of seam surface is found to be around 3mm. The weld seams are examined using X-ray radiography to evaluate the defects level before the components enter service. Potential defects include porosity, undercut, spiking and cracks. In this thesis, the problem of porosity formation is targeted.

1.1.4 The Problem of Porosity Formation in Electron Beam Welds

In practice, it is not possible to eliminate porosity formation in welding, but the number and size of pores need to be limited. Although electron beam welding has a potential to minimise porosity formation due to a good weld pool protection in high vacuum condition, pores are still occasionally found in electron beam welded titanium-base alloys. This section gives an overview of the problem of porosity formation during electron beam welding of titanium-based alloys during compressor discs assembly.Figure 1.4 shows a typical cross section of the compressor disc. Typically the thickness of the welding region may vary from 4 mm to 7 mm due to the different locations and stages of compressor discs. Figure 1.5 shows a typical 4-mm thick welded region, in which the heat affected zone is found with width around 800 μm, and the fusion zone width varies from 1.3 mm$\sim$3.2 mm due to the curved fusion profile along the welding thickness direction. Within this 4 mm thick and very narrow fusion zone region, the occasional

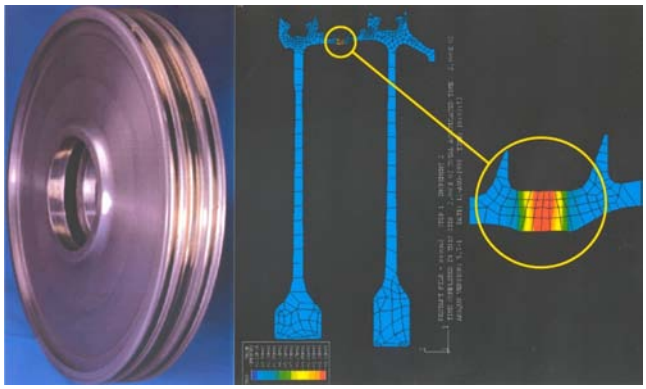

Figure 1.4: Typical cross section of compressor disc and the joint position.

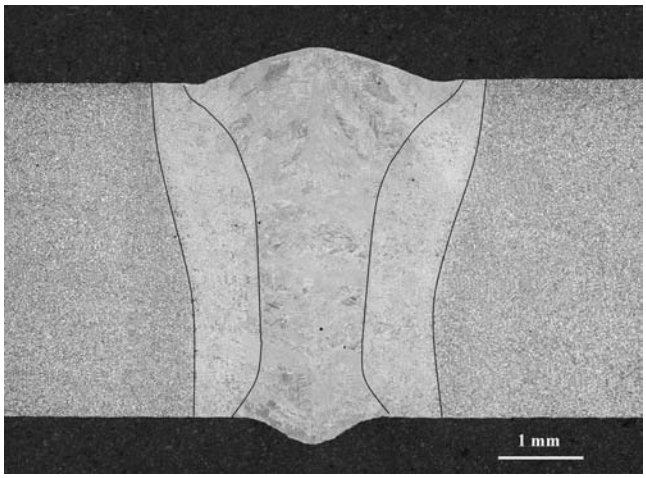

Figure 1.5: A 4-mm thick welded region in electron beam welded Ti-6Al-4V (the solid lines separate different regions of the welded region).

pores identified have a diameter from tens of μm up to hundreds of μm as shown in Figure 1.6; very occasionally the size can reach 1 mm. Figure 1.7 shows the detected large pores formed in electron beam welds by using conventional X-ray film radiography. It can be seen that the porosity with diameter of $\sim$ 0.6 mm has a perfectly round shape, while the larger one appears to have an oval shape with the larger dimension along the welding direction exceeds 1 mm. Since X-ray radiography can only produce projected images, three-dimensional tomography and location of the porosity inside the weld beads is ideally required. Various reasons for porosity formation during the electron beam welding process have been proposed, such as collapse of the keyhole, surface contaminants and gas evolution inside the weld pool [5, 9, 10, 11]. A number of

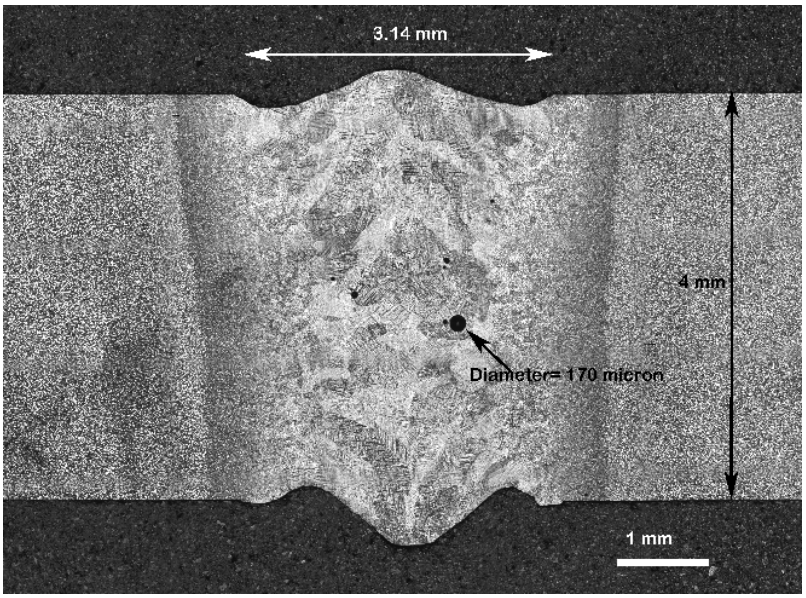

Figure 1.6: Porosity found at the cross section of the electron beam welded Ti-6Al-4V.

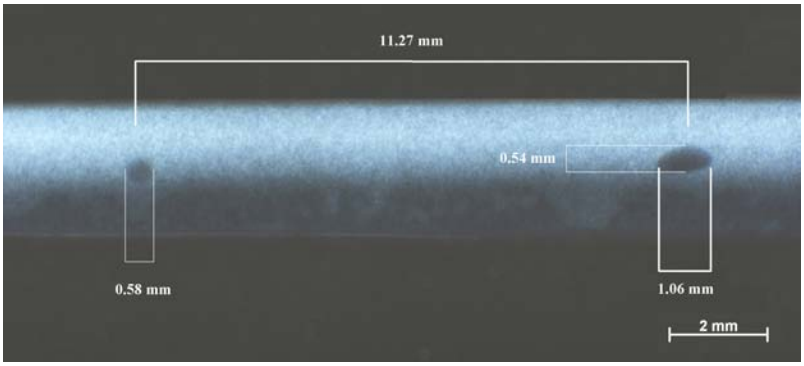

Figure 1.7: Conventional film X-ray radiography results showing large pores formed in electron beam welded Ti-6Al-4V.

methods have been used to suppress porosity formation, such as beam parameter optimisation, joint edge cleaning, and control of the dissolved gas level inside the base material. One can try to improve all the above aspects to minimise the porosity formation, but this may lead to unacceptable preparation time and high cost. Therefore, it is critical to identify the dominant factor controlling porosity formation during electron beam welding of titanium-based alloys, to provide practical and effective ways to suppress porosity formation.

1.2 Aims and Scope of This Work

To address the above concerns, the aims of this work are:

- To characterise porosity formation in electron beam welded titanium alloys and rationalise the porosity formation mechanism.
- To build models based on sound physical principles for understanding electron beam welding and porosity formation, to provide predictive capability for porosity formation.
- To investigate the effect of beam alignment and hydrogen content on porosity formation during electron beam welding.

To achieve these goals, both experimental work and numerical modelling approaches have been carried out. It is hoped that increased understanding of energy and mass transfer during welding process will shed some light on the problem of porosity formation during electron beam welding of titanium-based alloys.

1.3 Thesis layout

The thesis is organised in the following way. A literature review is given in Chapter 2 including: metallurgy of titanium and its alloys, electron beam welding process, and porosity formation in titanium welds. In chapter 3, electron beam welds of commercially pure titanium (CP-Ti), Ti-6Al-4V, Ti-6246, IMI 834 are characterised by metallographic sectioning. Pores formed in these samples are examined using high resolution X-ray tomography, residual gas analysis, scanning electron microscopy and energy and wavelength dispersive spectroscopy (EDS/WDS) analysis, aiming to rationalise the porosity formation mechanism. Since the porosity characterisation results show that it is very likely hydrogen involved with the porosity formation, hydrogen behaviour during electron beam welding process is investigated, mainly based on numerical modelling due to the difficulty of experimental hydrogen measurement. One of the prerequisite for hydrogen behaviour modelling during electron beam welding is to quantify the energy

transfer during the electron beam welding process, which is done in chapter 4. Numerical models are developed to improve the understanding of electron beam welding process, including heat cycling, weld pool formation, fluid flow, and the keyhole phenomena etc. In chapter 5, a newly proposed hydrogen transport model is coupled with the energy transport during the electron beam welding, aiming to predict the hydrogen transport during electron beam welding of titanium-based alloys. The coupled thermodynamic/kinetic model enables the prediction of hydrogen migration and estimation of hydrogen content inside the weld pool. A comparison between the predicted hydrogen distribution and previous experimental data shows reasonable agreement. After estimating the hydrogen content inside the weld pool, a hydrogen diffusion driven bubble growth model is proposed in chapter 6, aiming to investigate the bubble behaviour inside the weld pool, and effects of hydrogen content level, surface tension and initial bubble size on bubble growth dynamics. By investigation of bubble behaviour inside the weld pool, a porosity formation mechanism is proposed and the possibility of porosity occurrence is also discussed. To investigate the proposed porosity formation mechanism, a series of experiments have been designed, such as electrochemical hydrogen charging, surface degrading, beam offset welding etc. Experimental results are reported in chapter 7. Finally, summary of this work and principal conclusions are given in chapter 8.

2

Literature Review

Summary

This chapter provides a literature review concerning previous work related to this study. First, a brief description of the metallurgy of titanium alloys is presented, including three alloys, namely Ti-6Al-4V, Ti-6246, and IMI 834, which are widely used in the compressor discs of aeroengines are . The second part describes some fundamental aspects of electron beam welding process, such as electron beam welding parameters and modelling aspect. In the third part, previous work related to porosity formation in electron beam welded titanium based alloys are discussed.

2.1 Titanium and Its Alloys

2.1.1 Metallurgy and Classification of Titanium Alloys

Pure titanium crystallises at low temperature in a hexagonal close packed (HCP) structure, called α titanium. At the temperature of 882.5 °C, titanium undergoes allotropic transformation to form the body-centred cubic (BCC) structure, referred to as β titanium, which is stable to the melting point [3]. These two phases form the basis of all titanium-based alloys.

By adding different alloying elements, the β-transus can be changed to shift α phase and β phase fields to different temperature ranges. Depending on influence of alloying element on the $\beta-$transus, the alloying elements of titanium are classified as neutral, $\alpha-$stabilisers, or $\beta-$stabilisers. The $\alpha-$stabilising elements, such as Al, C, O, N can increase the α-β trans-

formation temperature and stabilise the α phase at higher temperatures. On the other hand, $\beta-$stabilising elements, such as Mo, V, Ta, Fe, Mn, Cr, Co, Ni, Cu, Si and H, shift the field to lower temperatures by reducing the $\beta - \alpha$ transformation temperature. Neutral elements, such as Sn, Zr have only very small influence on the $\beta-$ transus temperature [1, 3]. Due to the different usage of alloy elements and the fabrication process, titanium alloys can form as a combination of various amounts and arrangement of α and β phases. According to the amount of the two phases, titanium alloy can be classified as α, near α, $\alpha + \beta$, β and metastable β alloys. Figure 2.1 summarises the effects of alloy elements on structure, properties and classes of titanium alloys [12].

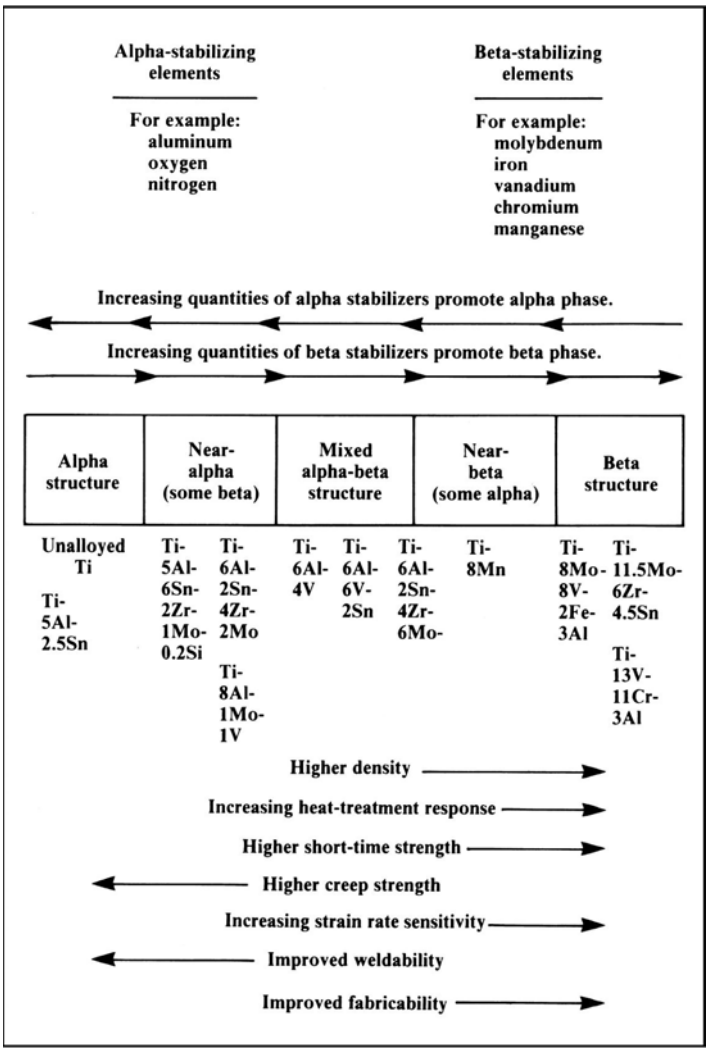

Figure 2.1: Effects of alloy elements on structure and some selected properties [12].

As for the combination of the two phase titanium alloys, microstructure is normally characterised by morphology and arrangement of the two phases. Two specific cases of phase arrangement namely lamellar microstructure and equiaxed microstructure exist. Normally, the lamellar microstructure is generated upon cooling from the β phase field, while the equiaxed microstructure is a result of the recrystallisation process. Both types of microstructure can have fine as well as a coarse arrangement of the two phases [3]. In what follows the common thermomechanical process of titanium-based alloys and microstructures evolution is detailed. Afterwards, microstructure evolution in three important titanium-based alloys, Ti6-Al-4V, Ti-6246 and Ti 834, which have been widely used for compressor manufacturing in aerospace engines, are discussed. Microstructures in titanium-based alloys are highly dependent on the thermomechanical treatment including deformation, solution heat treatment, recrystallisation aging and annealing. Commonly used thermomechanical treatment is outlined in Figure 2.2, in which β-transus temperature is a central concern [3]. By combining the complex sequence of processes, various microstructure morphologies can be formed in titanium-based alloys.

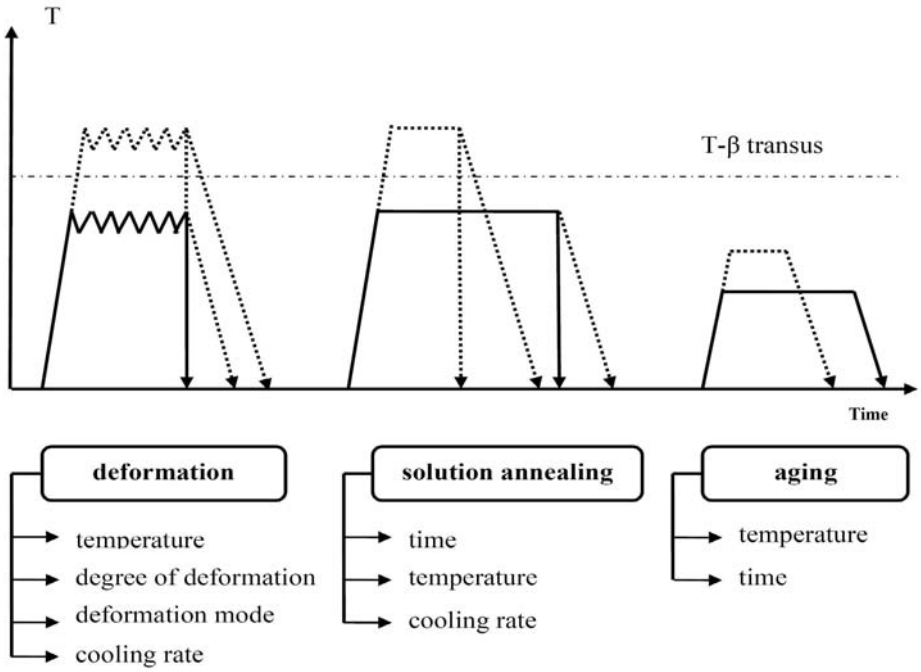

Figure 2.2: Thermomechanical treatment of titanium alloys [3].

2.1.2 Processing and Microstructures

2.1.2.1 Fully Lamellar Structure

Since lamellar microstructures can be obtained by annealing treatment in the β phase field (β recrystallisation), lamellar microstructure are also called "β-annealed" structures. The annealing temperature is usually kept with 30∼50°C above the β transus to control the β grain size. Lamellar microstructures can be characterised by the width of α lamellae (α plates), the size of α colony and thickness of α layers at β grain boundaries, which can be various depending on the cooling rate from the β phase field. Figure 2.3 shows an example of the variation of lamellar structure as a function of cooling rate from the β phase field for the Ti-6242 [1]. When the cooling rate increases from 1°C/min (typical furnace cooling) to fast cooling at 8000°C/min (fast quenching), the lamellar structures changes from a colony type to a acicular martensite structure. The formation of a colony or Widmanstatten type microstructure is often found in cast ingots of titanium alloys, and the formation mechanism is illustrated in Figure 2.4, by taking the example of slow cooling rate in the Ti-6Al-4V alloy [12]. When this alloys cools below

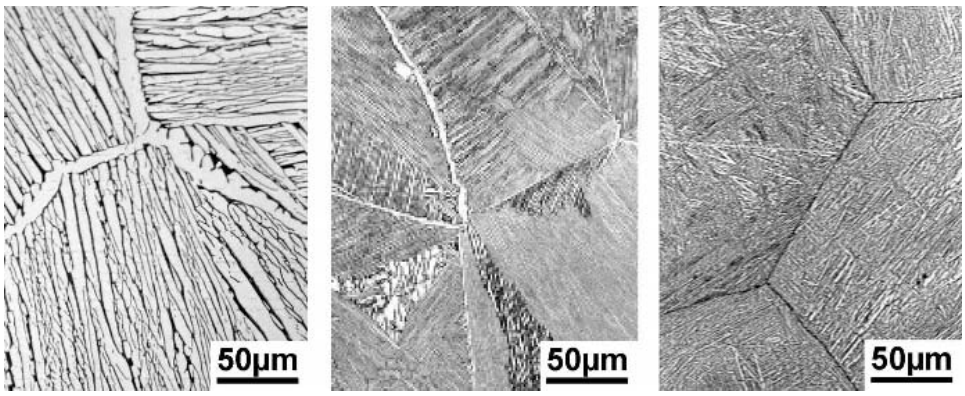

Figure 2.3: Effect of cooling rate from beta phase field on lamellar microstructures, Ti-6242, LM: (a) 1°C/min, (b) 100 °C/min, (c) 8000°C/min [1].

the β transus at about 980°C, α phase nucleates at the β grain boundary, the alpha plates form with their basal (close-packed) plane parallel to a special plane in the beta phase. Upon slow cooling, a nucleus of alpha forms and because of the close atomic matching along this common plane, the alpha phase thickens relatively slowly perpendicular to this plane but grows faster

along the plane. Thus, plates are developed. The microstructure in Figure 2.3 (b) obtained by a medium cooling rate with 100°C/min is typical for majority of commercial cooling rates employing water quenching or forced gas cooling. An acicular martensite structure is often found very thin sections with fast quenching and it also produced during high energy beam welding, in which the fusion zone undergoes very fast cooling during the solidification process [13].

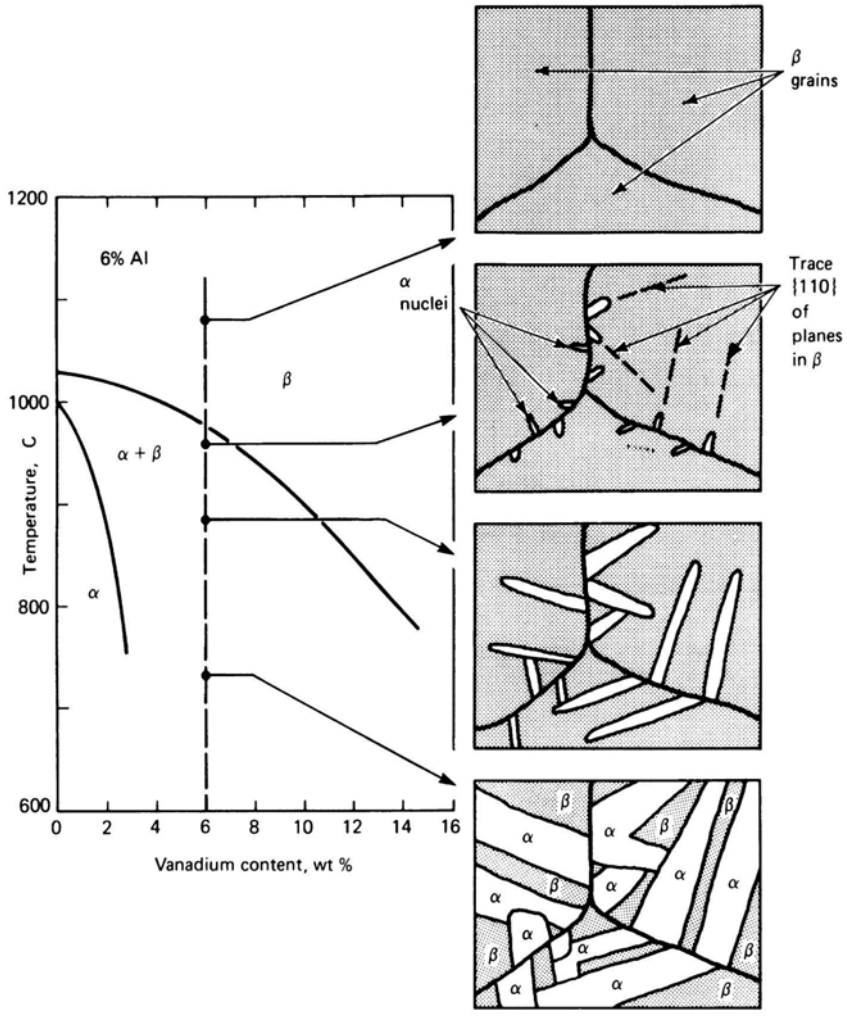

Figure 2.4: Schematic illustration of the development of a Widmanstatten structure in Ti-6Al-4V alloy at slow cooling rate [12].

Depending on the cooling rate, the grain size and α colony size vary and have a strong effect on the mechanical properties of titanium alloys with lamellar microstructure, such as yield stress, tensile ductility, fatigue and creep etc. Yield stress, tensile ductility, and fatigue properties of

fine-grained materials are superior to that of coarse-grained ones, mainly owing to a much shorter length of α lamellae. This is because the shorter individual α colonies decrease the effective slip length and crack nucleation sites [14, 15]. For high temperature application, creep resistance is the main concern in addition to fatigue resistance. Wider α lamellae lead to large distance between obstacles for dislocation motion and to lower strain hardening, thus decrease the creep resistance. But with high cooling rates, the creep resistance decrease dramatically. The possible explanation is due to the high dislocation and boundary density generated with the fast cooling rate [1]. To balance the mechanical properties, the cooling rates need to be carefully controlled to optimise α colony size.

2.1.2.2 Bimodal Microstructures

A typical bimodal microstructure is shown in Figure 2.5. It consists of primary globular alpha (α_p) phase (while area) and transformed beta regions [16]. The formation of bimodal structure is created via several thermomechanical processes. After primary stages such as cogging, ingot breakdown or β homogenisation, the lamellar structure is deformed plastically in the $\alpha+\beta$ phase field. Significant plastic deformation is needed to provide enough stored energy (dislocations) to complete the recrystallisation. During recrystallisation, the recrystallised β phase penetrates into the recrystallised α lamellae along α/β grain boundaries causing separation into the individual α_p grains. The final microstructure is dependent on the various structural features inherited from the primary stages, the last forming and heat treatment operations [17].

The microstructure parameters which influence the mechanical properties most strongly are the β grain size and the volume fraction of α_p phase. Excluding high volume fraction of α_p phase bimodal microstructure, in which α_p grains start to interconnect, the β grain size is about equal to the distance between α_p grains [12]. Similar to the above mentioned effect of slip length on the mechanical properties, smaller grain sizes confer higher yield stress, higher ductility and slower fatigue crack propagation rate of microcracks.

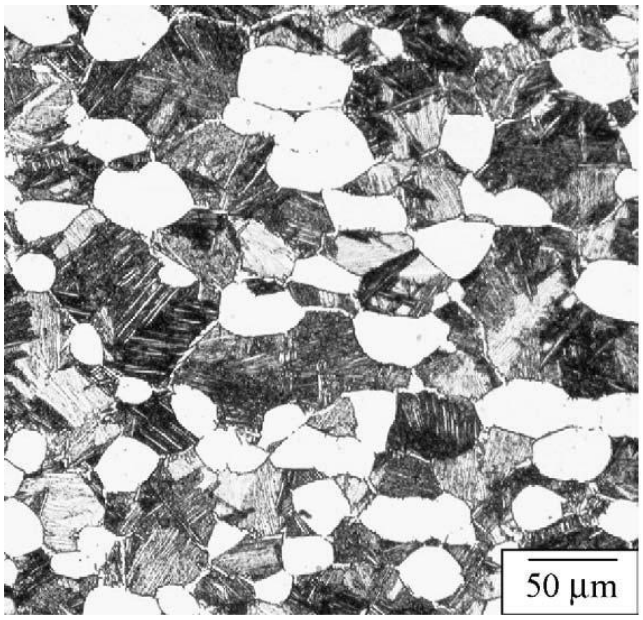

Figure 2.5: Bimodal microstructure of IMI 834 alloy [16].

2.1.2.3 Fully Equiaxed Structure

The routes to obtain a fully equiaxed structure are almost the same as those used to produce the bimodal microstructure, except that a lower cooling rate from the $\alpha + \beta$ recrystallisation temperature is required. This allows α_p to form without α lamella formation within the β grains, resulting in a fully equiaxed microstructure. Figure 2.6 illustrates the morphologies of fully equiaxed and bimodal microstructures in Ti-6Al-4V [18]. For example, to obtain the bimodal structure from the fully equiaxed microstructure, the material needs to be heated to the $\alpha + \beta$ phase field to achieve the desired α_p and subsequently cooling with sufficient high rate to form the α lamellae inside the β grains. In a similar way, by heating up a material with bimodal microstructure into the $\alpha + \beta$ phase field and holding the material until the α lamellae completely dissolve inside the β grains and then cooling it with sufficiently low cooling rate. In each heat treatment performed to change the microstructure, the α and β grain sizes will be changed [12], thus influencing the mechanical properties.

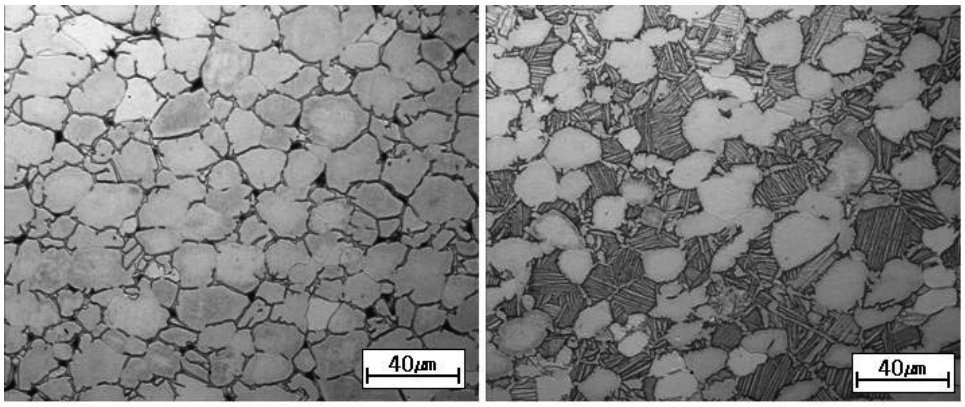

Figure 2.6: (a) Fully equiaxed α with intergranular β, and (b) bimodal microstructures (primary α and transformed β) in Ti-6Al-4V alloy [18].

2.1.2.4 Alpha Case

α case is an oxygen-rich metallic phase which is formed when hot titanium is exposed to oxygen. At elevated temperature, titanium has a high affinity for oxygen. Oxygen can dissolves readily in titanium up to a weight percentage of 14% when the temperature is around 600-1000°C [19]. When liquid titanium solidifies the oxygen solubility increases dramatically as it can be seen from the titanium-oxygen phase diagram (see Figure 2.7) [20]. The formation of an α case can occur through several methods all of which are linked to the presence oxygen or nitrogen in the atmosphere, and of temperatures high enough to allow diffusion into the alloy due to the relatively low oxygen diffusivity in titanium as it can be seen in Figure 2.8. Oxygen and nitrogen are regarded as α stabilisers as they promote the formation of the α phase. By providing sufficient quantities of these stabilising elements and a sufficient temperature for diffusion to occur, a case of α phase is produced. It has been reported that the alpha-case is formed by not only interstitial oxygen atoms but also substitutional metal atoms dissolved from mould materials during the casting of titanium [21]. The formation of an 'α case' on titanium is generally regarded as undesirable due to the significant differences in the mechanical properties of the α and β phases. As the α phase is harder and more brittle than an α/β matrix its formation reduces component performance, especially fatigue performance [22].

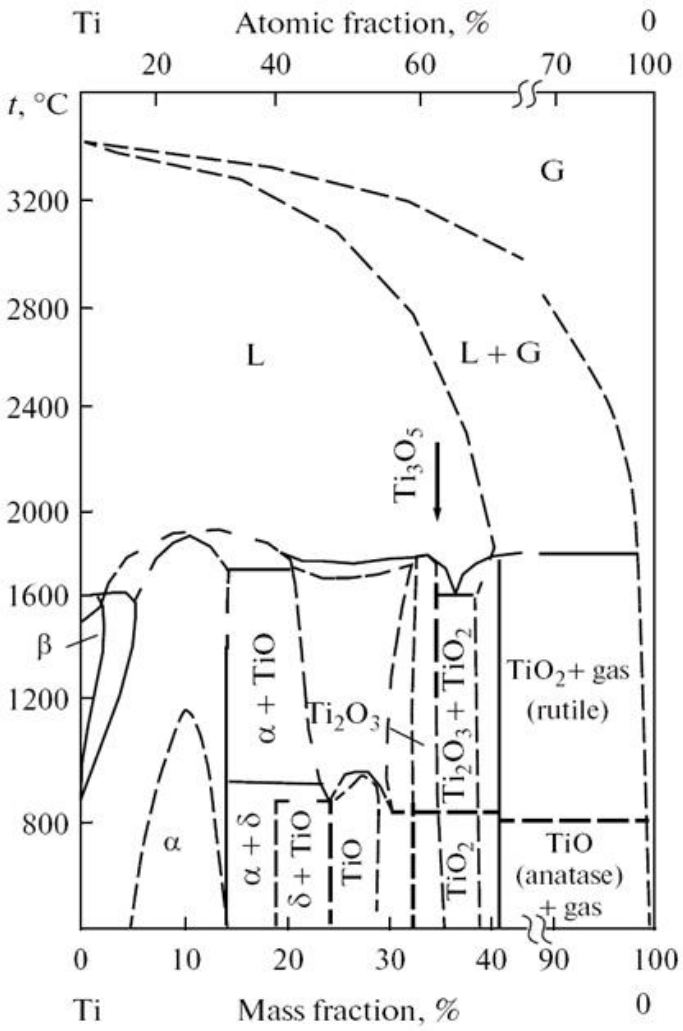

Figure 2.7: Ti-O phase diagram [20].

2.1.2.5 Martensite Formation

Martensitic transformation occurs when titanium and titanium-based alloys cool rapidly from the β phase field. The beta phase decomposes to form martensite, which consists of large irregular zones subdivided into parallel arrays of fine plates less than 1 micron across [24]. Depending on the alloy compostion, the hexagonal martensite designated as α' is observed in two morphologies: massive martensite (also known as lath or packet martensite) and acicular martensite [12]. Massive martensite consisting of large irregular regions occurs only in pure

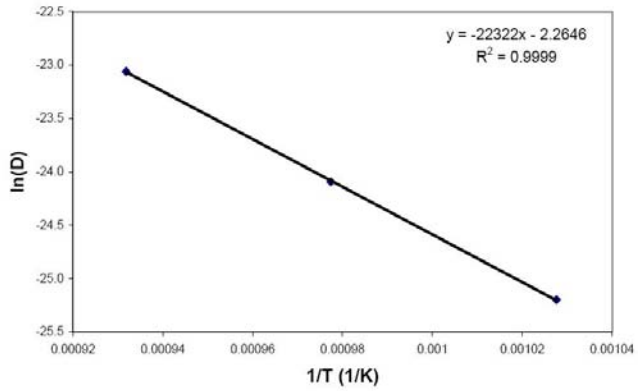

Figure 2.8: Arrhenius plot of the oxygendiffusivity in titanium [23].

titanium or very dilute alloys, while acicular martensite is formed in alloys of higher solute content. With increasing solute content the hexagonal structure of the martensite becomes distorted, and is known as orthorhombic α". The formation of α" is less common and strongly composition dependent.

As mentioned above, titanium-based alloys can present different microstructure morphologies due to different chemical composition and processing route. Depending on the design criteria, the desired microstructures need to be developed to meet the required material properties. In the following section three titanium alloys which have been widely employed in compressor design are considered.

2.1.3 Ti-6Al-4V

Ti-6Al-4V is a typical $\alpha + \beta$ alloy, containing 6 wt% aluminium an α-stabiliser and 4 wt% vanadium, a β-stabiliser (weight percentage), which enables a dual phase microstructure to be developed. The β transus is 995 $\pm$ 15°C and liquidus 1650°C [25]. Different phases and microstructures can be developed under different cooling rate as it can be seem in Figure 2.9. This alloy has been widely used in aerospace application, *e.g.* front fan and low pressure sections in gas turbines [2, 4], in both annealed or in solution-treated and aged (STA) conditions. After a typical process route, the lamellar structures contains a β grain size of 600 μm, while the

bimodal contains primary α grains of 20 μm and volume fraction of $\sim$60%, and small β grains of 20$\sim$40 μm [26, 27].

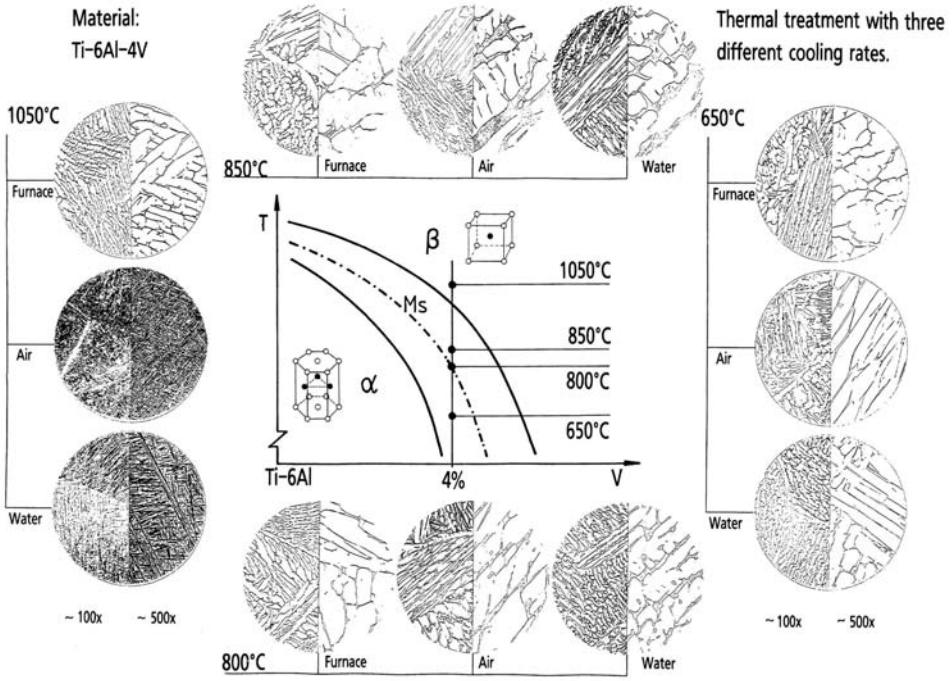

Figure 2.9: Different phases and structures developed in Ti-6Al-4V under different cooling rate [28].

2.1.4 Ti-6246

Ti-6246 is a high-strength alloy with a composition of 6% Al, 2% Sn, 4% Zr and 6% Mo (weight percent), which is used for elevated temperature applications, such as intermediate pressure stage in gas turbine compressors [12]. Ti-6246 displays a strong microstructure to mechanical properties relationship, with α and β grain size and morphology playing important roles [29], especially fatigue [30].A microstructure with an optimum combination of strength, ductility, and toughness contains about 10% equiaxed α (primary α) plus a transformed β matrix with relatively coarse secondary α and aged β [28]. Figure 2.10 shows the Ti-6246 continuous cooling transformation diagram.

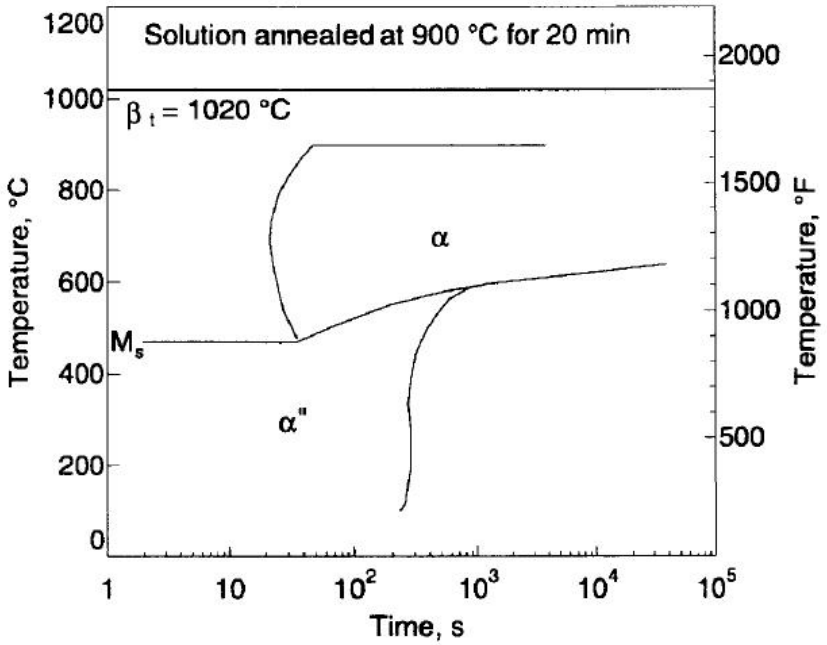

Figure 2.10: Ti-6246 Continuous cooling transformation diagram[28].

2.1.5 IMI 834

IMI 834 is a near-α alloy, which was developed for high temperature application. This alloy provides improved creep strength, fatigue performance and fine defect tolerant microstructure, which thus extends the application temperature capability to around 590°C, which make it possible to be used in the high pressure stages of aerospace engine compressors. It has been reported that this alloy has replaced nickel-based superalloys in some parts of the aeroengine compressor [31]. IMI 834 is normally processed as an $\alpha + \beta$ alloy by adding carbon to the conventional near-α alloy (*e.g.* IMI 829), which lowers the rate of change from $\alpha + \beta$ to β microstructure during the heat treatment near to the β-transus in the $\alpha + \beta$ field to produce a low level of equiaxed primary α. About 15% of equiaxed primary α in a fine-grained matrix of lamellar transformed β microstructure provides the optimised balance of properties, especially fatigue and creep resistances [22, 32].

2.2 Electron Beam Welding

Electron beam welding (EBW) has become established as a high quality precision welding process, which has been widely used in high-integrity manufacturing in the aerospace and automobile industries [5, 9]. This welding process is classified as a high-energy beam fusion welding, which has the following main characteristics compared to other welding methods:

1. High power density of about 10^7 W/cm^2 when the beam is focussed. A comparison of power density in different welding methods is listed in Table 2.1.

2. High welding speed which results in narrow welds, small heat affected zones and little distortion.

3. The welding process is commonly carried out under vacuum, thus providing better protection of the weld pool against contamination by oxidation.

4. Very flexible welding parameters which be easily controlled and monitored, thus providing high reproducibility and consistent welds.

Table 2.1: The maximum power density of the various heat sources used for welding [5].

Heat source	Maximum power density (W/m^{-2})
Gas flame	5×10^7
Electric arc	10^8
Plasma	10^9
Laser beam (continuous)	10^{11}
Electron beam	10^{11}

2.2.1 Principles of Electron Beam Welding Process

The principle of electron beam welding process is illustrated schematically in Figure 2.11 [9]. In the EBW system, electrons are generated by passing a low current (*e.g.* 50-200 mA) through a tungsten filament, which can emit a large number of electrons for long time while consuming only little thermal energy. The free electrons emitted by the tungsten filament need to be

accelerated to achieve high kinetic energy for welding. To do this, the filament is attached to the negative side of a high-voltage power supply (30-150 kV); thus the electrons are accelerated away from the cathode towards the anode. At high vacuum condition, electrons accelerated with a voltage of 150 kV can reach a speed of 2×10^8 m/s, which is two thirds the speed of light, carrying significant kinetic energy [10]. The divergent high speed electrons needs to be focussed to a small spot to achieve the power density of about 10^{11} W/m^2 required to weld metals. The beam is focussed by magnetic and electrostatic lenses. In most cases the welding process is performed with a stationary electron beam and the workpiece moves beneath it. Sometimes it is also necessary to move the electron beam itself to meet the requirement of the welding process. This is accomplished using a beam deflecting system which can deflect the beam by application of a magnetic field. By applying an alternating current in the deflection system, the beam can be made to oscillate.

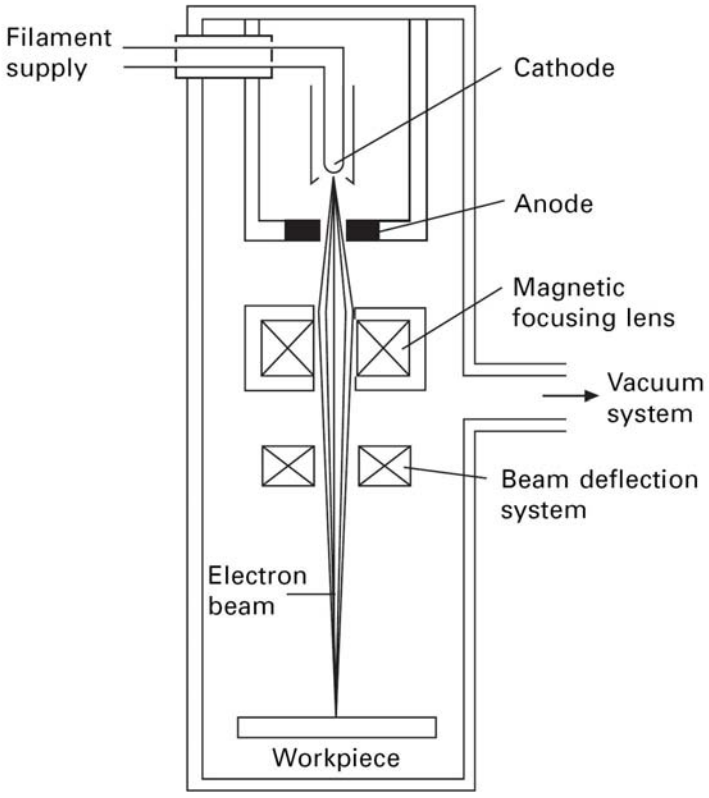

Figure 2.11: Principle of electron beam welding [9].

When the focussed electron beam impacts on the metal surface, the kinetic energy of electrons is transferred into the metal, causing a rapid increase in temperature. Due to the rapid energy transfer, the metal is locally melted or even evaporated when the temperature is above the boiling point. By using appropriate beam current, accelerating voltage, focus current and welding speed, a weld can be made with a single pass with full penetration.

2.2.2 Deep Penetration Welding Effect

One of the prime advantages of electron beam welding is the ability to make deeper and narrower welds compared to other conventional welding methods such as arc welding. This makes it possible to create a thick weld with a single pass, thus eliminating the need for multi-pass welding, which is needed for conventional arc welding. This characteristic is associated with the complex physics of the interaction between the high energy density electron beam and the weld material, which is discussed bellow. When the high energy beam is focussed down to a spot size of 0.25 to 1.3 mm diameter, a maximum power density 10^{11} W/m^2 is achieved. The temperature in the small impact area can rise up to 14,000°C, which exceeds the boiling point of all known materials [11]. The extremely high temperature causes a very high vapour density in the vicinity of the heating zone (Knudsen layer), causing explosive evaporation [34]. This produces a high recoil pressure, which blows away the liquid metal at the impact area and exposes fresh material to the electron beam. This digging effect can generate a vapour hole inside the metal, the so-called "keyhole". When the beam moves forward, metal at the leading edge of keyhole melts and the molten metal flows sideways and around the keyhole mainly driven mainly by the recoil pressure. The continuous molten metal flows backwards around the keyhole to fill the trailing edge of the keyhole as the beam move forwards, thus producing a continuous weld. The dynamic of the keyhole effect is very complicated and often found to be non-stationary [35, 36]. A schematic illustration of keyhole formation and possible force balance is given in Figure 2.12 [33]. Among these forces surface tension and gravitational forces counteract the deep keyhole formation, but these are normally weak compared to the force associated with the

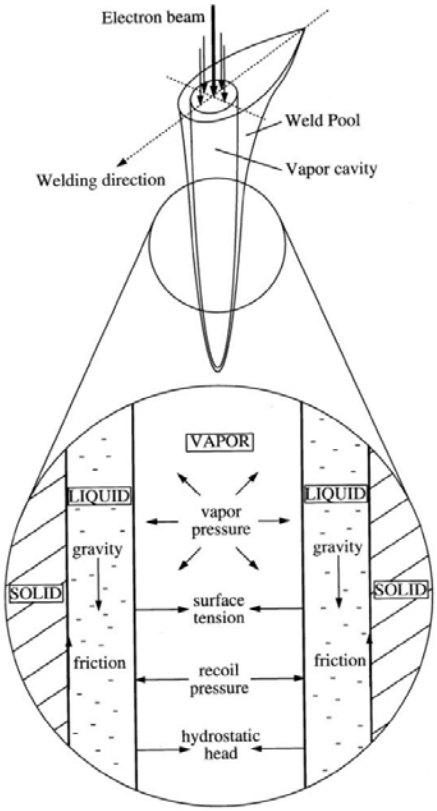

Figure 2.12: Schematic illustration of vapour keyhole and weld pool formation during electron beam welding [33].

recoil vapour pressure. For example, the surface tension of liquid Ti-6Al-4V is around 1.65 N/m at [37], while in liquid aluminium the surface tension is around 0.91 N/m [38]. Considering a keyhole size with diameter of 0.5 mm, and taking the above estimates for the surface tensions of liquid metals, this gives a surface tension force around $2\times10^3 \sim 3\times10^3$ N/m^2 according to Young-Laplace equation [39]. The recoil pressure has been estimated to be up to 10^6 N/m^2 based on Clausius-Clapeyron equation [40], which is much higher than the surface tension. This sheds some light on the deep penetration effect during the electron beam welding process.

Attempts have been made to predict the electron beam penetration depth, by correlating electron beam welding parameters and material properties with the penetration depth by using

empirical or semi-analytical modelling approach [41, 42]. In practice, due to the nature of the process, estimates depend on the calibration of input data so that the predictions are not always reliable. To improve the understanding of deep penetration effect, influence of welding parameters on the welding need to be further investigated.

2.2.3 Influence of Welding Parameters

In electron beam welding, different penetration depths and different shapes of weld joints can be achieved. For a desired penetration depth and fusion zone shape, the combination of electron beam parameters may not be unique. To optimise the power efficiency and control the weld quality, the influence of electron beam welding parameters needs to be sufficiently understood. In practice, the following parameters are considered to be key parameters to define the electron beam welding process: accelerating voltage, beam current, welding speed, focus current, and beam deflection. A review of the effects of these parameters is now given.

(1) Accelerating voltage: This determines the kinetic energy of the accelerated electrons. Its main influence arises from its effect on the power density. The power density can be compensated by increasing the beam current when the accelerating voltage is low. Compared to the ways to control the accelerating voltage and the beam current, it is easier and more flexible to control the beam current. For this reason, for most welding operations, the welding voltage is kept constant at 60 kV or 150 kV [5]. To achieve the required power, beam current is selected appropriately selected. It should be pointed out that high accelerating voltage and low beam current favour a small focus diameter. For this reason, when a wider seam is needed, it is appropriate to use low accelerating voltage and large beam current, while for narrow welds with high depth-to-width ratio, high accelerating voltage is preferred. With increasing accelerating voltage, the penetration depth will increase and narrow, parallel-sided welds bead can be obtained [43].

(2) Beam current: For any given accelerating voltage, increasing the beam current increase the penetration depth. In addition to the beam current, the current distribution also has a great

effect on penetration depth, fusion zone shape and weld quality. By changing the electron beam activated zone (EBAZ), which is defined as the region, where the power density is higher than the critical value required to initiate and sustain deep penetration [44].

(3) Travel speed: Travel speed is also referred to as welding speed. For a given beam energy, the travel speed determines the line energy input into the workpiece, which is defined as the energy delivered per unit length of weld line. By controlling the welding speed, the heating and cooling rate can be changed, as well as the fusion zone and penetration depth. Increasing the welding speed makes the weld bead narrower and decreases the penetration depth [36, 41, 42].

(4) Focus current: The accelerated electrons are focussed by magnetic fields, which are generated by applying current through annular coils. The current is referred to as focus current and it determines the focus distance when other welding parameters are fixed. The focus distance is inversely proportional to the square of the focus current, and is also directly proportional to the accelerating voltage [5]. By changing the focus current the focus point can be above the workpiece surface (overfocusing), inside the workpiece (sharp focus) and below the workpiece (underfocusing). Sharp focus (focus point inside the workpiece) of the beam will produce a narrow, parallel-sided weld geometry. Defocusing the beam either by overfocusing or by underfocusing will increase the beam diameter and reduce the power density [43].

(5) Beam deflection: The focused electron beam can be deflected by applying current through the coils of deflection system. With periodically varying current, the electron beam can be deflected dynamically with required shape and frequency, which is also called beam oscillation. It has been reported that beam oscillation can be useful to improve the weld quality. For example, beam oscillation can be used to increase the keyhole size, preventing the molten liquid metal from collapsing, which results in porosity formation. Beam oscillation also affects the dynamics of the molten zone, thus favouring the formation of sound weld bead surfaces [5].

2.2.4 Modelling of Electron Beam Welding Process

Process modelling allows a greater understanding of the complex physical phenomena that occur within the material, such as residual stress, distortion, microstructure evolution and defect formation [45]. In early studies, due to the complexity of the process physics, welding process modelling was typically restricted to investigations of the heat transfer, typically using closed form analytical or semi-analytical solutions [46]. However, all these studies were limited to very simple geometries and temperature-independent material properties, and were necessarily simplified. With the rapid development of modern computers and numerical methods, computation-intensive numerical approaches have been increasingly used to improve the capability for all aspects of the welding process. The following sections contain a brief review of models for weld process modelling.

The first issue to be addressed is the description of the energy input. In early work, simple instantaneous concentration heat sources were used to obtain the temperature solution analytically. A number of simplified assumptions were applied, including: (a) infinite or semi-infinite geometry; (b) temperature-independent material properties; (c) no phase changes in the material; (d) restricted line, point or simple Gaussian instantaneous concentration heat sources, which yields unrealistic temperature estimates at the heat source position; and (e) only steady-state solutions available in a constant velocity moving reference frame [46].

Numerical models also have been developed to modelling the heat conduction during the electron beam welding process with volumetric heat source models. To describe heat input in electron beam welding, it is desirable that the heat source model must account for the keyhole effect and have the correct volumetric distribution of energy along the thickness direction of the material. Consider the presently available heat source models: (i) Gaussian heat source model assumes a heat flux deposited on the surface of work piece which is suitable for surface treatment and shallow penetration arc welding [47]; (ii) Double ellipsoidal model simulates deep penetration welds, such as gas metal arc welding (GMAW), but it is still not applicable

to high depth to width ratio of weld penetration in high-density energy welding process; (iii) Three-dimensional conical heat source (TDC) is a volumetric heat source which are applicable to model the high-density energy welding [48]. Three-dimensional conical (TDC) heat source model considers the heat intensity distribution though the workpiece thickness. The maximum heat intensity deposited region is at the top surface of workpiece, and the minimum region is at the bottom surface of workpiece. The radius is assumed to be decreasing linearly along the thickness of weld. Heat density is kept constant along the central axis (z axis). On any plane perpendicular to (the plane normal), the heat intensity is distributed in a Gaussian form. In a previous studies [6, 49], a heat source model which combined a uniform circular surface heat flux and conical volumetric source was used to perform thermal calculations. The results in Figure 2.13 show a reasonable degree of accuracy between the calculated fusion zone boundary isotherms and the experimental fusion profiles.

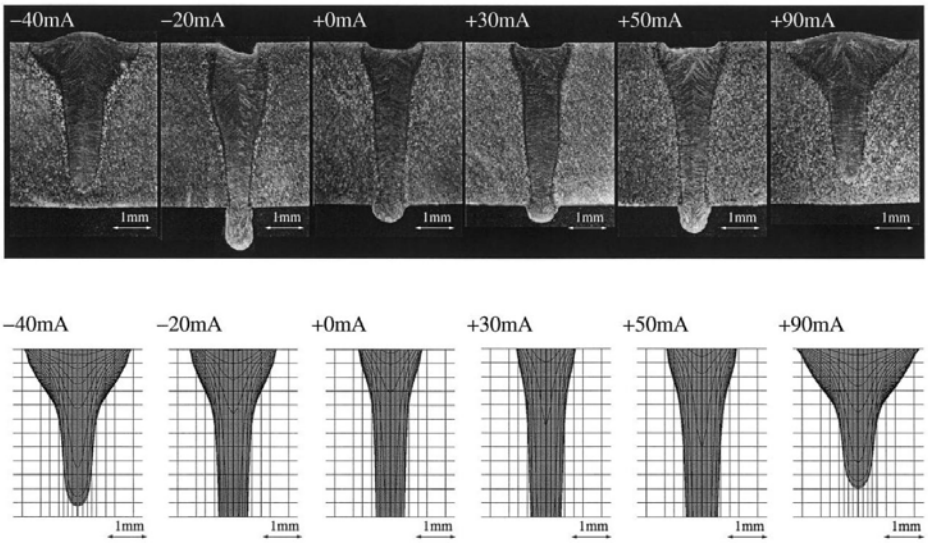

Figure 2.13: Photographs of the metallographic sections welded at different beam defocus current (upper) and relevant simulation results of fusion zone boundary isotherms [49].

Although very good agreement between the calculated fusion zone and experimental fusion zone profiles can be achieved by using a volumetric heat source model, the physics phenomena inside weld pool are still not actually represented by these models, *e.g.* the interaction between

electron beam and the material, fluid flow inside the weld pool. For residual stress and distortion prediction during the welding process, in which little attention has been paid to the material behaviour above the liquidus, these models may be practical. But in some cases, fluid flow inside the weld pool needs to be considered. For example Figure 2.14 shows that fluid patterns inside the weld pool may be critical for porosity formation [50]. It is also known that the surface of the weld bead is not flat, so that humps and undercut exist. These phenomena are all related to convection inside the weld pool [51]. It has been pointed out that convection inside the weld pool may be the dominant mechanism of heat transfer during the welding of metals of low heat conductivity, such as titanium (Ti-6Al-4V about 10 to 20 W/m-K) and steel (20 to 34 W/m-K) [25], compared to some metals with high conductivity, such as aluminium-based alloys with heat conductivity about 150 to 200 W/m-K. For the above reason, details inside the weld pool need to be better understood.

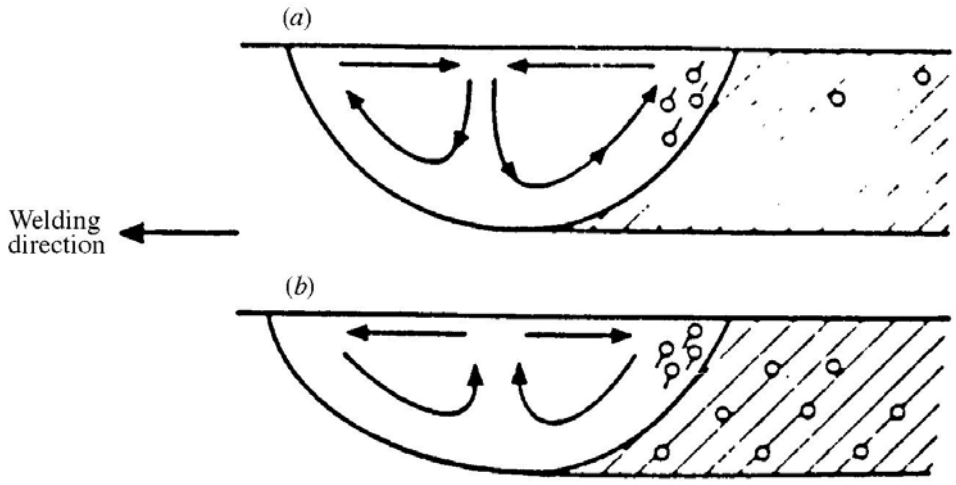

Figure 2.14: Influence of weld pool motion influence on porosity (a) inward surface flow; (b) outward surface flow [50].

In reality, the interaction between the welding heat source and work piece can be very complicated. The forces acting on the weld pool may be very complex depending on the welding process. The common forces which drive fluid flow inside weld pool were illustrated schematically in Figure 2.15 [50]. In electron beam welding, thermocapillary (Marangoni) force recoil force

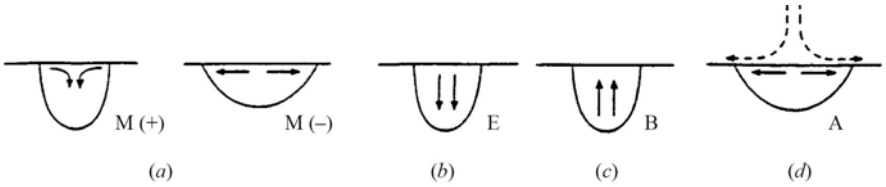

Figure 2.15: Common driving force inside weld pool (a) thermocapillary (Marangoni) forces M(+) or M(-); (b) electromagnetic (Lorentz) forces E, resulting from interaction of current; (c) buoyancy forces B, resulting from density differences caused by temperature gradients; (d) aerodynamic drag forces A, caused by passage of plasma over surface [50].

due to rapid evaporation may be considered as the main driving force in the weld pool. The Marangoni effect is the motion induced by tangential gradients of variable surface tension. When there is a gradient of surface tension along a surface, there is a fluid flow along the surface from the region of low surface tension to the region with high surface tension. For most substances, the surface tension decreases with increasing temperature (negative temperature coefficient), which induces an outward flow in the weld pool. However when a substance has a positive temperature coefficient (which means surface tension increases with increasing temperature) inward flow in the weld pool occurs. Figure 2.16 shows the Marangoni effect on fluid flow in the weld pool. Normally surface tension is the function of temperature, but for alloys, concentration of alloy elements also has significant effect on surface tension, as has been reported by Mills [53] and Lee [52]. The surface tension induced fluid flow has been reported in recent work by Rai [54], in which the keyhole is calculated based on Kaplan's model [55] prior to the fluid flow calculation and then keyhole was assumed to be stationary during the fluid flow calculation. Although the recoil pressure effect on the dynamics of fluid flow during laser welding has been reported in many studies [56, 57, 58], no work is available which considers the effect of recoil pressure on fluid flow dynamics during electron beam welding.

During the electron beam welding process, when the accelerated electrons are incident on the workpiece surface, the impact zone is heated rapidly, and evaporation starts when the temperature reaches the boiling point. If the beam intensity is high enough, explosive evaporation can occur with the generation of high vapour pressure, which drives the molten metal away. This

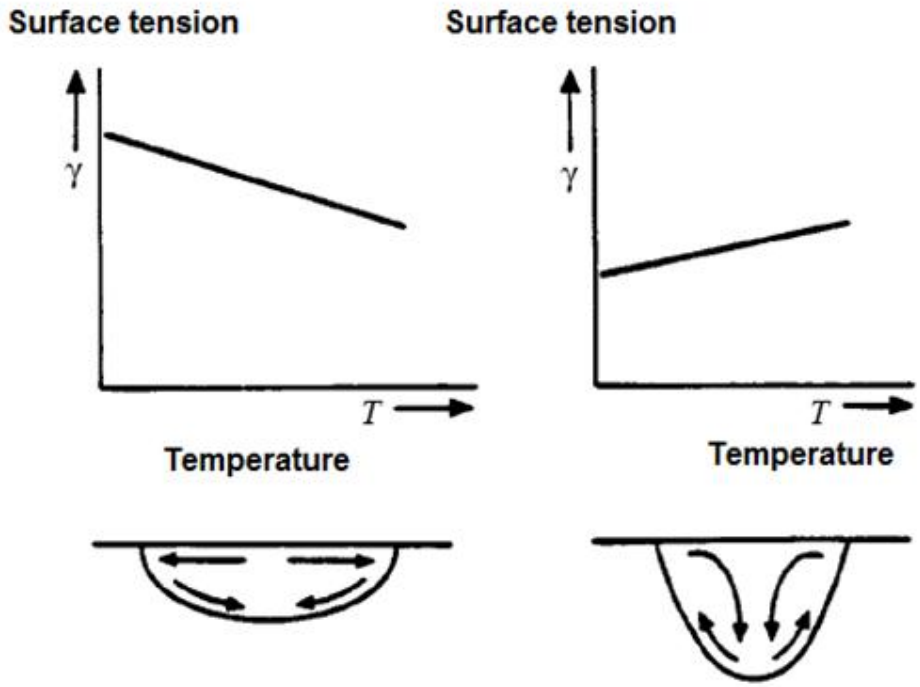

Figure 2.16: Marangoni effect on fluid flow in weld pool with negative temperature coefficient (left) and positive temperature coefficient (right) [52].

digging effect leads to the formation of the keyhole [36]. The dynamic behaviour during the electron beam welding process can thus be very complicated. With the beam moving forward, electron beam energy is transferred into the work piece through the keyhole wall accompanied by intensive evaporation. The whole welding process is characterised by a rapid solid-liquid-gas phase transformation with moving interfaces. To capture the above characteristics and to get a more accurate description of the physics inside the weld pool, the keyhole effect needs to be taken into account in the process model. Keyhole phenomena occurs for all high energy beam welding processes when the energy density exceeds a critical value, *e.g.* laser beam (LB) welding, plasma beam welding, and electron beam welding. Due to metal evaporation at the keyhole wall, this keyhole modelling remains a significant challenge.

Among the keyhole welding processes modelling, keyhole phenomenon research during laser beam welding is the most active. Even though slight differences in energy transfer mechanism

exist between the processes, the general principles of keyhole formation are very similar. Some notable studies on development of keyhole modelling in laser welding are now reviewed. Early studies of keyhole mode process modelling by Andrews & Atthey [59] and Klemens [35] used analytical or semi-analytical solutions to explain the keyhole phenomena and accounted for energy and pressure balance at the keyhole wall, vapour flow inside the keyhole, and penetration depth. Dowden [60] extended the previous work and constructed a general model to estimate the motion of liquid and vapour in the keyhole. For more complicated issues, such as variation of surface tension with temperature, vapour plume etc, it is necessary to resort to numerical approaches. Numerical models have been proposed by Kroos [61, 62] and Sudnik [63], aiming to study the keyhole geometry or dynamic behaviour, but these models are limited by assumptions of cylindrical keyhole shape, stationary state, or very slow welding speed. Direct experimental observation of the keyhole shape by using in-situ X-ray transmission [64] indicated that the keyhole was not symmetrical when welding at high speed welding. Kaplan [55] predicted the asymmetry of the keyhole profile using a point-by-point determination of the energy balance at the keyhole wall. Dowden & Kapadia [65] investigated the instability inherent in the variable absorption capability of the laser bean energy at the keyhole wall due to reflection. The keyhole instability and transient dynamic behaviour of the keyhole front wall was then further studied by Matsunawa & Semak [66, 67], accounting for the drilling effect due to recoil vapour pressure. 3D weld pool and keyhole geometry was determined by using the model constructed by Solana & Ocana [68], in which Fresnel and inverse Bremsstrahlung absorption were considered and the keyhole wall was treated as a free boundary. Fabbro & Chouf [69] calculated the inclined keyhole wall by considering the sideways melt displacement, multiple reflection and ray tracing procedure. Details of the implementation of multiple reflection and Fresnel absorption are described by Cho [70]. From the above studies, keyhole modelling is critical for the development of more complicated models to provide useful physical insight into welding with the keyhole model.

However, due to the very complex physical phenomena during the keyhole welding process, very few of models have yet considered all the relevant physical processes, despite enormous effects towards this target. Ki *et al* [56, 57, 71], Dasgupta *et al* [72], Cho *et al* [73], Geiger *et al* [58] and Otto & Schmidt [74] constructed models which are capable of doing 3D transient heat and mass transfer calculations by considering surface tension induced thermo-capillary, recoil vapour pressure and surface evaporation. The most difficult challenges in these models are surface evaporation, and implementation of boundary condition at the keyhole wall due to the very complicated phenomena there, such as the formation of a kinetic Knudsen layer and metal vapour flow. The required amount of computation in these models is tremendous. The reported calculation results are limited to the very early stage of the welding process (welding time shorter than 100 ms); this limits the application of these models in weld design and manufacturing. To make the keyhole modelling approach amenable to welding process optimisation, keyhole modelling needs to be simplified to balance the accuracy and computational time. One promising approach has been demonstrated by Rai & Debroy [51, 53, 54, 75], in which the keyhole is calculated based on a separate model, prior to the heat transfer and fluid flow calculation inside the weld pool. The calculated keyhole profile was then mapped into the coordinate system for the thermo-fluid calculation and then treated as a stationary wall. The results from these models show that appropriate balance of accuracy and computational time can be achieved.

2.3 General Reasons for Porosity Formation in Welds

Porosity caused by welding has been studied by many researchers. It has been pointed out that there are many reasons for porosity formation during welding, such as physical trapping of shielding gas [76], chemical reaction in the welding pool [77], keyhole phenomenon and evaporation of the low boiling point elements [78]. It also has been widely believed that porosity forms due to dissolved gas, especially hydrogen [79, 80]. Depending on the precise formation mechanism, pores inside welds have different morphologies. The empirical classification of observed

pores is often based upon their shapes, *i.e.* rounded pores are classified as gas pores and porosity with roughly elliptical shape are regarded as wormhole, whereas irregular pores are classified as shrinkage pores. Gas pores are most prevalent; these are spherical and form via insoluble gas evolution in the liquid metal and bubble entrapment when the liquid metal solidifies. The gas sources can be various, *i.e.* shielding gas, surface contamination, dissolved gases, gas phases generated by chemical reaction and metal vapour. Wormhole pores are usually found at the solid/liquid interface, due to the poor fluidity of molten metal around the trapped gas. In practice, shrinkage porosity occurs during solidification as a result of volumetric differences between liquid and solid states; shrinkage porosity is less likely to happen in welds, because during the welding process, only small amount of metal is melted locally.

In reality, porosity formation in welds depends on the specific welding process and the alloy being welded. Porosity may also form due to a combination of the above mentioned mechanisms.

2.4 Porosity Formation in Electron Beam Welded Titanium

Electron beam welding is a reliable high energy beam joining method which can provide a very narrow weld bead with minimal distortion and shrinkage. Because welding is performed in a high-vacuum atmosphere, low contamination of the weld occurs. Nevertheless, porosity formation in electron beam welds has been reported frequently [81, 82, 83, 84, 85]. In early work [81] it was found that the occurrence of porosity in electron beam (EB) welded Ti-6Al-4V not only greatly depends on the intrinsic hydrogen content of the material being welded, but also on the quality of the edge preparation. It has also been pointed out that the appearance of pores during the fusion welding of a titanium alloy is influenced by the presence of gas forming substances (oil, grease, moisture) on the surfaces being welded, and therefore inadequate cleanliness levels [82]. To quantify the effect of surface contamination on porosity formation, a number of methods have been used to characterise the joint surface before welding, including X-ray photoemission spectroscopy (XPS), detection analysis (ERDA) and secondary ion mass

spectroscopy (SIMS) analysis. The most active substances found on the surface of titanium alloys are hydrogen, oxygen, moisture and carbonated substances [83]. Figure 2.17 shows the hydrogen distribution profile at the surface of Ti-6Al-4V plates found using ERDA, in which a steep hydrogen distribution profile was found within 60 nm of the surface. Figure 2.18 shows the H, O and C distribution at the same surface found using SIMS. For both elements, a very steep distribution profile has been found within 100 nm close to the surface. In Gouret's work [83], it

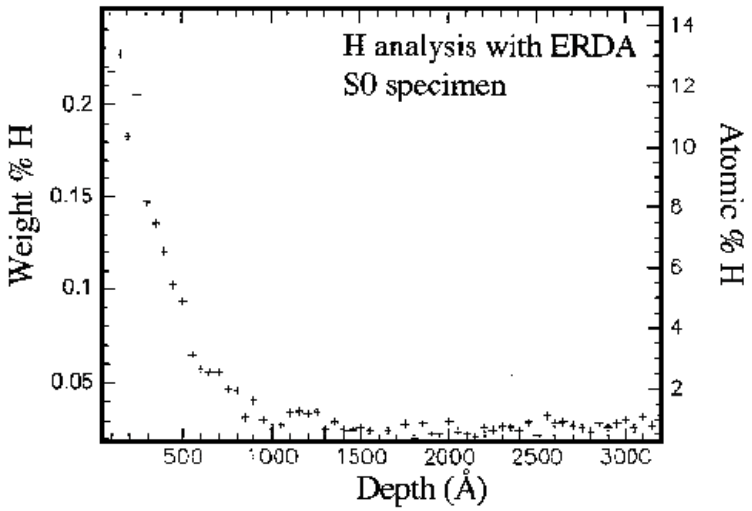

Figure 2.17: ERDA measurement result shows hydrogen concentration profile in the surface of Ti-6Al-4V plate [83].

is believed that porosity forms from entrapment of gases (H_2, CO_2, CO) produced by reaction of surface contaminants when the joint surface were melted. These gas bubbles oscillate inside the weld pool and were captured when the weld pool solidified. Different surface preparation methods were used, in which different level of contaminants were detected. The experiment results showed that C, O, and H are equally responsible for formation of gas from the surface. In some conditions, C and O have even more influence than H. Although contaminants at joint surfaces may favour the porosity formation during electron beam welding process, this cannot explain the porosity formation in a bead-on-plate electron beam welds, in which no joint surface exists [84]. In Mohandas's work [84], there is a different view of porosity formation; it is

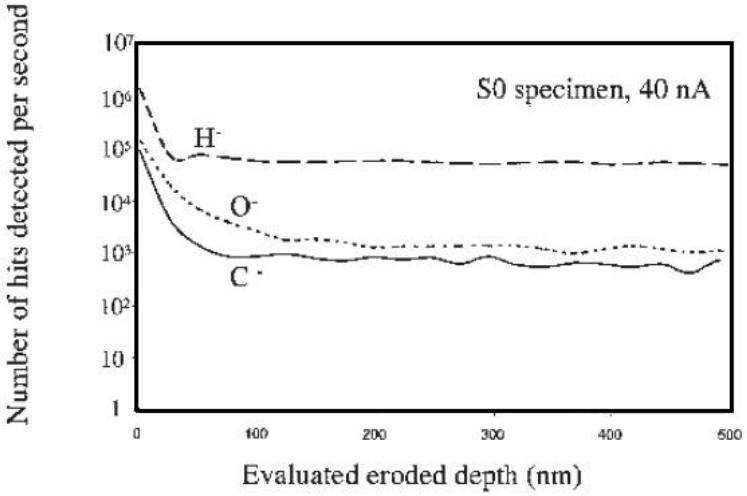

Figure 2.18: Evaluated concentration profile from SIMS measurement and calibrations [83].

believed that hydrogen is the root cause for porosity formation. Due to the decreasing hydrogen solubility with increasing temperature and low pressure in the working chamber during electron beam welding, hydrogen in weld pool becomes saturated, thus hydrogen bubbles form. The porosity formation mechanism is similar to porosity formation in aluminium casting, which has been reported by Atwood & Lee [86, 87, 88, 89]. It also has been found that the porosity formation is related to the welding speed. The highest porosity was observed at intermediate welding speeds. At low speeds, a majority of pores formed at the fusion boundary, while at high speeds, occurrence of porosity was found to be more frequently at the weld centre. This may be because the different welding speeds change the fluid flow dynamics inside the weld pool, so that the probability of bubble escape is altered.

Based upon the results reported in the literature, it would appear that it is very likely that hydrogen and hydrogen-rich contaminants are possible contributors to pore formation; moreover the welding parameters also have a strong effect on porosity formation. To improve the understanding of porosity formation in electron beam welding process, further investigation of the hydrogen in titanium-based alloys and its behaviour inside the weld pool during the electron beam welding process is required.

2.5 Hydrogen in Titanium Alloys

Hydrogen is a unique alloying element in titanium metallurgy, since unlike other elements it can easily be added and removed without melting. Titanium and conventional titanium-based alloys have a high affinity for hydrogen, being capable of absorbing up to 60 at. % hydrogen at 600°C; even higher contents can be alloyed with titanium at lower temperatures [90]. The enthalpy of solution of hydrogen in titanium is negative. Because of this characteristic, hydrogen solubility actually decreases with an increase in temperature. Figure 2.19 adapted from [84] shows the hydrogen solubility in commercially pure titanium at different temperatures. It can be seen that hydrogen solubility decreases both in solid and liquid titanium with increasing temperature, but an abrupt decrease of hydrogen solubility is found at the melting point when the liquid titanium solidifies. This means during the solidification process, liquid titanium rejects hydrogen. From this point of view, porosity is likely to form during the solidification process. But it also can be seen that hydrogen solubility in the solid with lower temperature (around 1200°C) is much higher compared to the hydrogen solubility in liquid titanium. When gas bubble forms in the weld pool, a hydrogen concentration gradient towards each gas bubble is set up. This leads to diffusion of hydrogen from hydrogen-enriched regions toward the gas bubble and favours bubble growth. If the generated bubble cannot escape from the weld pool, pores will exist in the solidified weld bead. However, at this stage, hydrogen behaviour and its effect on porosity formation during electron beam welding process is still not sufficiently understood. Hence many questions still remain answered, such as hydrogen transport during the welding process, hydrogen levels required to from bubble and the method of bubble escape and entrapment etc. To improve the understanding of hydrogen behaviour during the electron beam welding process of titanium alloys, measurement/assessment of thermodynamic and kinetic data of hydrogen in titanium alloys is critical. The following contains a review of previous work related to hydrogen in titanium alloys.

In early work, studies on hydrogen in titanium alloys focused on experimental hydrogen

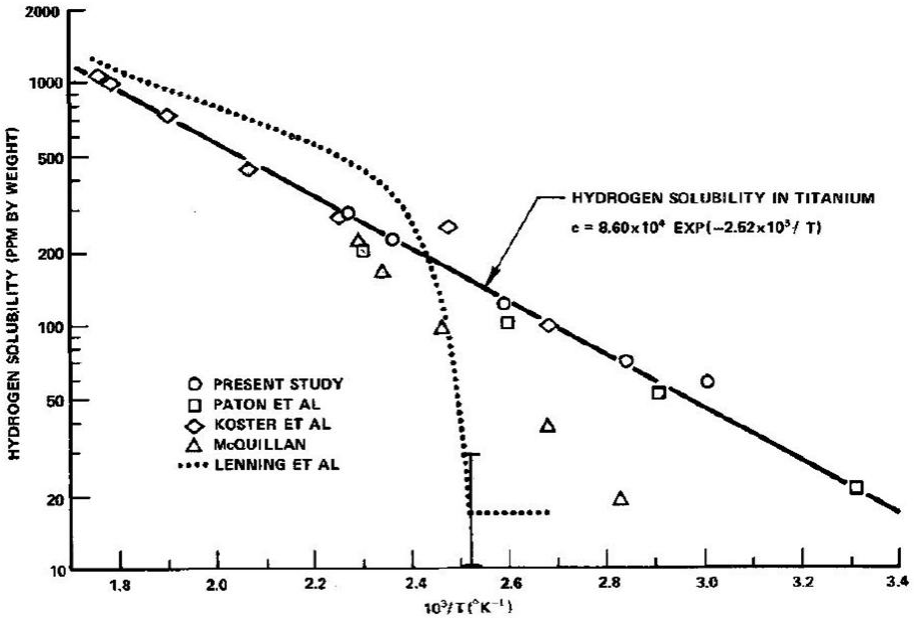

Figure 2.19: Solubility curve for hydrogen in titanium as a function of temperature, at 1 atmosphere external pressure [84].

solubility measurement [91, 92, 93, 94, 95]. Hydrogen solubility in α titanium has been studied by Ronald & Kanji [91]. Figure 2.20 shows the comparison result of hydrogen solubility in α titanium as a function of temperature from previous work. A least squares fit of the research data to the Arrhenius relation gives the maximum solubility of hydrogen in Ti in the temperature range of 60 to 170°C to be

$$C(\text{ppm}) = 4.55 \times 10^4 \exp(-2.25 \times 10^3/\text{T}) \tag{2.1}$$

At higher temperatures, Akito Takasai et.al investigated hydrogen solubility in two kinds of Ti-Al alloys [93]. In their research, a least squares fit of their data to the Arrhenius relations gave the maximum solubility of hydrogen in the temperatures range of 450°C to 570°Cto be for Ti-50Al alloy

$$C(\text{ppm}) = 1.12 \times 10^4 \exp(-4.83 \times 10^3/\text{T}) \tag{2.2}$$

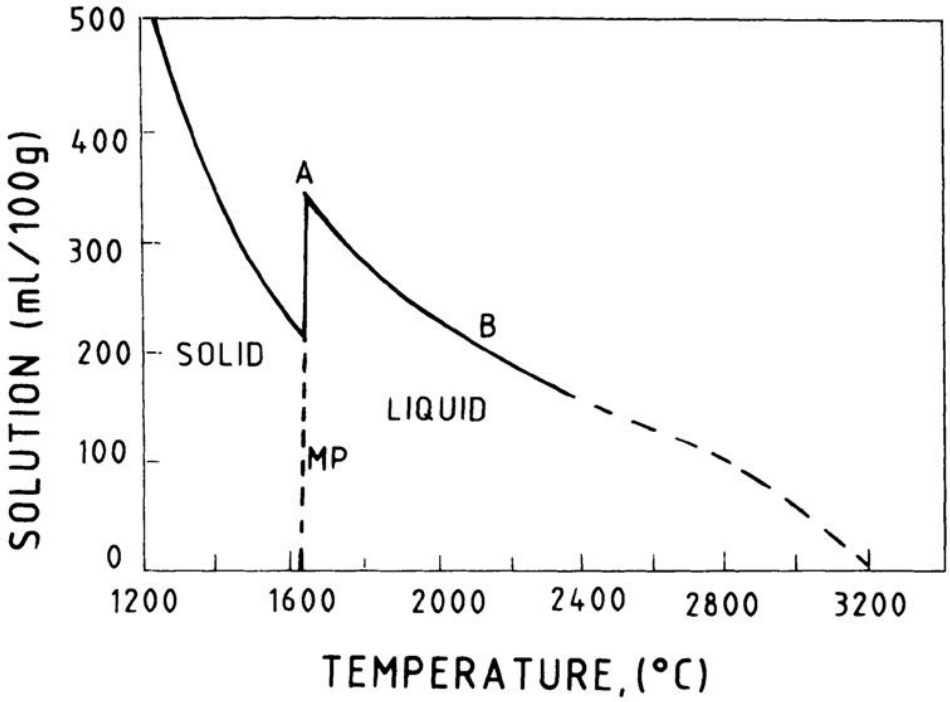

Figure 2.20: Hydrogen solubility in titanium [91].

and for the Ti-45Al alloy

$$C(\text{ppm}) = 1.53 \times 10^4 \exp(-7.01 \times 10^3/\text{T}) \tag{2.3}$$

Besides the temperature effect on hydrogen solubility, Chen et.al [94] also studied the hydrogen solubility in titanium at different hydrogen partial pressures. Figure 2.21 shows the hydrogen solubility as a function of temperature under different hydrogen partial pressures. It can be seen that these curves are almost parallel, obeying the Arrhenius relationship. Figure 2.22 shows hydrogen solubility in the Ti-60 alloy as a function of hydrogen partial pressure at different temperature. The results show that hydrogen solubility at different hydrogen partial pressure obeys Sievert's law in a temperature range of 800°C to 950°C. Hydrogen solubility above 950°C is rarely reported. This is because of the lack of refractory materials with which titanium will not react, and which will remain sufficiently imperious to hydrogen gas above 950 °C. In Takeuchi's work (1966), the temperature-pressure-concentration relationships of the

hydrogen-titanium system was studied at 900°C to 1500°C by a modified volumetric method [95]. A phase diagram of the hydrogen-titanium system was given above 950°C as shown in Figure 2.23. From the phase diagram, one would expect that hydrogen solubility in titanium at high temperatures to decrease rapidly with increasing temperature and hydrogen partial pressure.

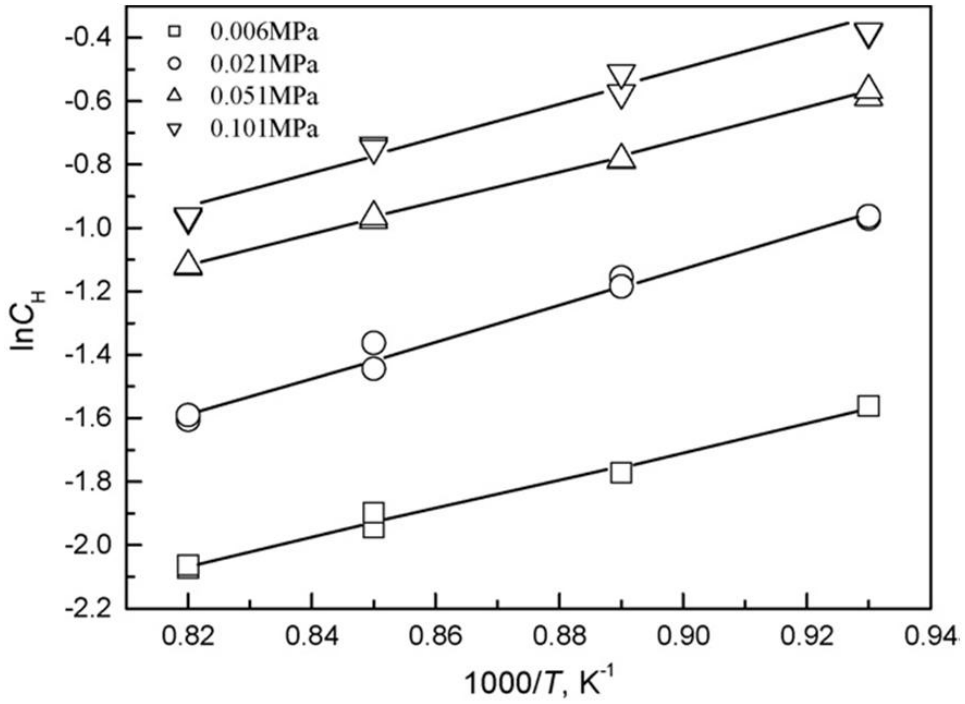

Figure 2.21: hydrogen solubility in Ti-60 alloys as a function of reciprocal absolute temperature [94].

In recent years, progress has been made in the measurement/assessment of thermodynamic and kinetic data relating to hydrogen in titanium-based alloy systems [96, 97, 98, 99]. For example, thermodynamic assessments of the Ti-H binary phase diagram have been made and are available for computer-based calculations [100, 101]. Similarly, good estimates now exist for the rates of diffusion of hydrogen in titanium and its alloys [102, 103, 104]. Influenced in this way, one would expect that an approach to investigate hydrogen behaviour during electron beam welding process by using numerical modelling is realistic. It is also expected that investigation of hydrogen transport during electron beam welding process might shed light on the factors influencing porosity formation in titanium alloys.

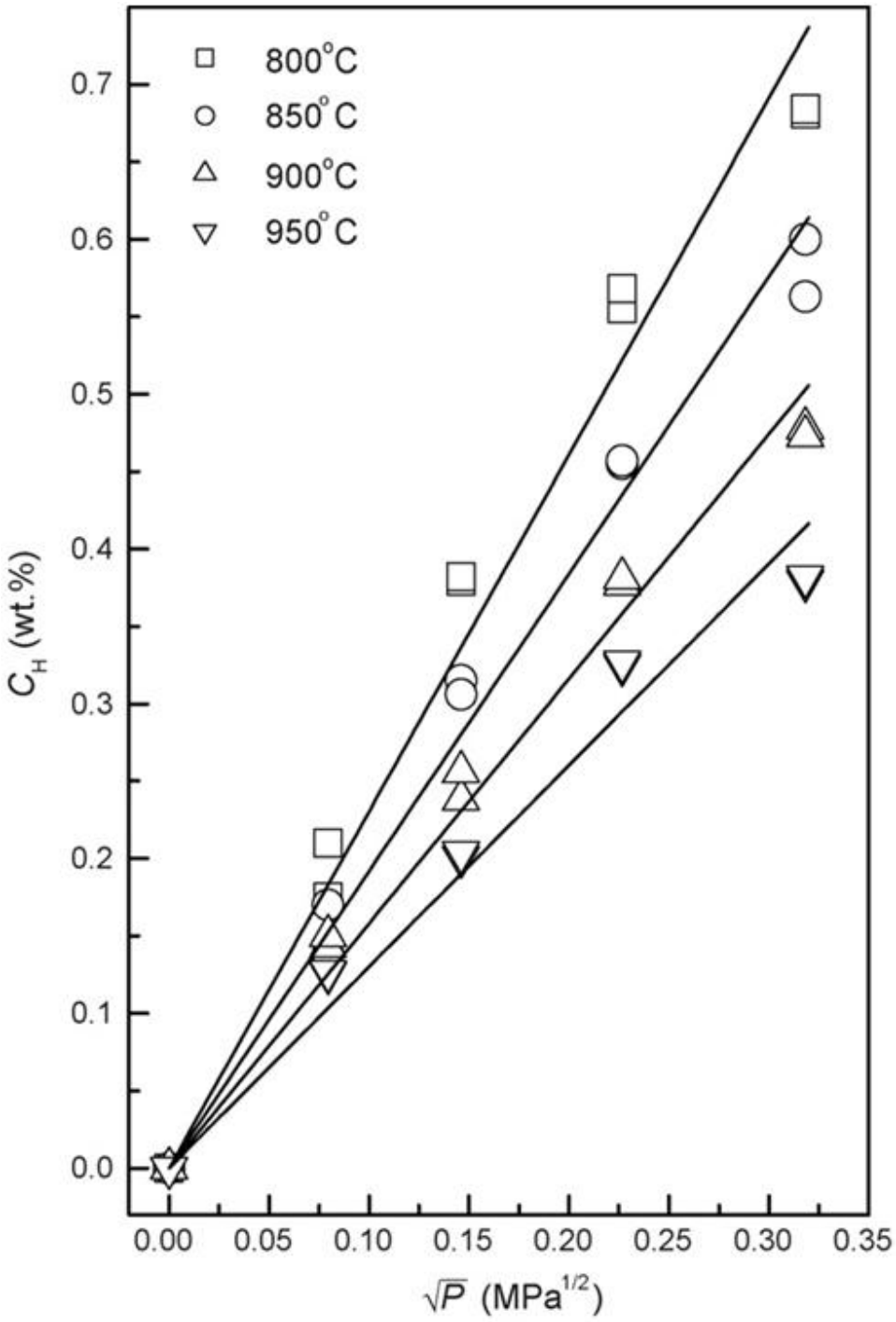

Figure 2.22: Hydrogen solubility as function of hydrogen partial pressure in temperature range of 800°C to 950°C [94].

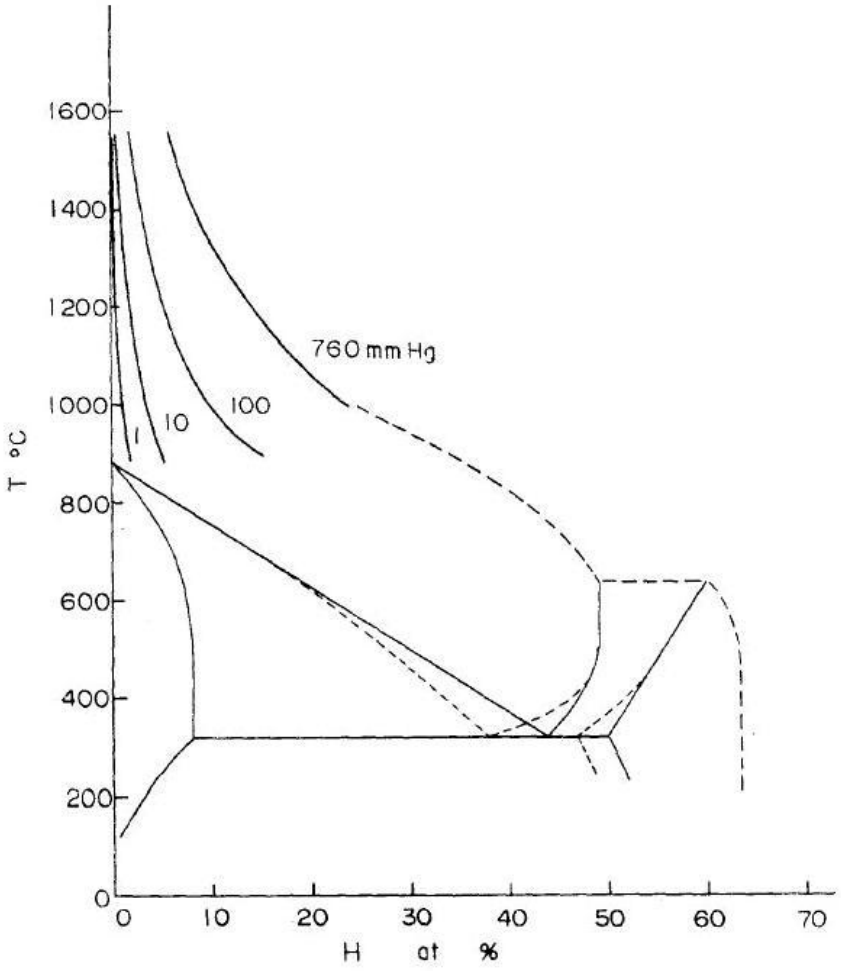

Figure 2.23: Solubility limits of hydrogen in β-titanium [95].

3

Characterisation of Electron Beam Welds of Titanium Alloys and Porosity Formation

Summary

Porosity formation during electron beam (EB) welding of titanium alloys needs to be better understood, particularly to minimise occurrence of porosity and to provide guidance for welding process optimisation. Porosity formation in EB welding of titanium alloys is investigated under keyhole and fully penetrating conditions. Characterisation is carried out using high resolution X-ray tomography, metallographic sectioning, energy and wavelength dispersive spectroscopy (EDS/WDS) analysis and residual gas analysis. The experimental characterisation results show that the porosity formation is associated with gas evolution, particularly hydrogen. Based on the characterisation results, the porosity formation mechanism is rationalised. To provide guidance for porosity formation reduction, more details, such heat and mass transfer, hydrogen behaviour, bubble growth and entrapment during electron beam welding process, needs to be investigated.

3.1 Background

Titanium alloys are widely used in the aerospace industry due to their excellent mechanical properties, especially the high specific strength. For example, in the modern aeroengine, a

number of critical components in the fan and compressor regions (particularly blades and discs) are fabricated from them, and the assembly process requires high integrity joints [3].Although many different welding methods are available, e.g. metal inert gas (MIG) welding, tungsten inert gas (TIG) welding, plasma arc welding (PAW), laser beam (LB) [105, 106, 107]. In recent years, friction welding methods have been increasingly used for titanium joining in aero-engines application , *e.g.* friction stir welding (FSW) [108, 109, 110] and linear friction welding [111, 112]. Since friction welding methods are solid-state process, the material does not reach the fusion temperature, thus no protective gas shielding is need during the welding. Defects which occur during fusion welding processes can be potentially eliminated. Despite the advantages of the friction welding methods, EBW welding remains the prevalent joining technique for a variety of components during manufacturing, for example compressor drum assemblies. During the process, electrons are accelerated at voltages up to 150 kV under a high vacuum, typically 10^{-4} mbar. The power density in the focussed electron beam is around 10^{13} Wm^{-2}, which enables joining with a single pass in keyhole mode and full penetration [6, 13]. Due to these characteristics, a high integrity joint can be made with a very narrow fusion zone, minimal distortion, and reduced levels of contamination from the environment.

Despite the above advantages, the possible formation of processing-induced defects needs to be considered; in practice this necessitates considerable emphasis on inspection after processing, and the possibility of the scrapping of non-conforming joints. Weld-induced porosity is one of the major practical problems. Even for the electron beam welding process which is performed under high vacuum conditions, pores are still occasionally found in the fusion zone. Titanium alloys are particularly prone to porosity formation, as has been reported in previous studies. In early work [81] it was found that the occurrence of porosity in electron beam (EB) welded Ti-6Al-4V depended both on the intrinsic hydrogen content of the material being welded and also the quality of the edge preparation. Silvinskii [79] believed that titanium hydride was responsible for porosity formation. It seems that hydrogen was considered to be the root cause,

but little was revealed about the critical hydrogen level needed to avoid porosity formation. Later, the appearance of pores during the fusion welding of a titanium alloy was attributed to the presence of gas forming substances (oil, grease, moisture) on the surfaces being welded and therefore inadequate cleanliness levels; presumably, decomposition of these might occur during processing [82, 84]. Welding speed has also been found to be correlated with porosity formation [84]. More recently, attempts have been made to understand the factors controlling bubble initiation [83, 113].

At this stage, it would appear that porosity formation during keyhole mode electron beam welding is still not sufficiently understood due to the very complex phenomena occurring. To provide guidance to minimise porosity formation, basic understanding of porosity needs to be improved. In this work, titanium EB welds are first characterised, and then pores formed in electron beam welded titanium alloys are investigated; we believe this work to contain the first reported gas chemical analysis results of gas pores formed in EB welds of these materials. From the porosity characterisation results, the porosity formation mechanism is rationalised.

3.2 Experiment Details

3.2.1 EB welds for Porosity Characterisation

To study the fundamental aspects of porosity formation mechanism during electron beam welding of titanium alloys, EB samples considered for porosity characterisation were commercially pure titanium (CP-Ti) and three titanium alloys, namely Ti-6Al-4V, Ti-6246 and IMI 834, which are widely used at low pressure (LP), intermediate pressure (IP) and high pressure (HP) sections respectively in aeroengine compressors. More details of the samples are now described:

Commercially pure titanium (CP-Ti) EB welds for porosity characterisation were 6.5 mm-thick butt joints, which were welded using the electron beam welding facility in TWI, UK with proprietary welding conditions. The welds were 300 mm in length and 50 mm in width. Joint surfaces were prepared by wet machining. Before welding, the sample surfaces were washed

using acetone and then swabbed with 5% hydrofluoric acid, 35% nitric acid, acid, and balance water, and finally washed in ethanol. The finished joint surfaces had a roughness of Ra 0.89 μm and Rz 4.46 μm.

EB welds of Ti-6Al-4V, Ti-6246 and IMI 834 were provided by Rolls-Royce plc. These samples were cut off from large forged compressor discs with 200 mm in length and 50 mm in width. The chemical compositions of the alloys are list in Table 3.1. Nominated hydrogen content in both alloys is less than 150 ppm (weight percentage). The thickness of the weld region varies from 4 mm to 6.5 mm. All the samples are butt joints, which were welded at Rolls-Royce plc, Derby, UK, with proprietry welding conditions.

Table 3.1: Chemical composition of the alloys in this study (weight percentage).

Alloys	Ti	Al	Sn	V	Zr	Mo	Si	Nb	C	O
Ti-6Al-4V	Bal	5.50	-	3.50	-	-	-	-	<= 0.1	0.17
		~6.75		~4.50						~0.23
Ti-6246	Bal	5.5	1.75	-	3.5	1.75	<= 0.1	-	<= 0.08	<= 0.12
		~6.5	~2.25		~4.5	~2.25				
IMI 834	Bal	6	4	-	3.5	0.5	0.35	0.7	0.06	-

To characterise the porosity in the EB welds, the following procedure was adopted. First, conventional X-ray film radiography with resolution of 50 μm was used to detect pores formed in the EB welds. After locating the pores, samples were sectioned and polished for metallurgical examination. Larger pores (of diameter greater than 1 mm) were located precisely by using X-ray tomography, and then prepared to perform the hidden residual gas analysis, with the aim of identifying the gas chemical composition inside them. It is emphasised that these larger pores were relatively rare; however they needed to be chosen due to the difficulty in applying the method to the smaller pores. More details of X-ray tomography and residual gas analysis can be found in the following sections.

3.2.2 X-Ray Detection of Porosity

X-ray non-destructive testing (NDT) methods were used for porosity detection. For a rapid investigation of large pore formation, conventional X-ray film radiography was performed in the electron beam welding unit, at Rolls-Royce plc, UK, Derby. The resolution of conventional X-ray radiography can approach around 2% of the thickness of the specimens. The advantage of X-ray radiography is the high efficiency for porosity detection in a large welded part, but there also some disadvantages, e.g. the overlap of pores and surface defects, and relatively low spatial resolution. For more details of the porosity detection, such as three-dimensional morphology, precise three-dimensional locating and high resolution etc, it is necessary to resort to X-ray computed tomography (CT).

Based on conventional X-ray radiography, a computed X-ray tomography uses projections obtained by conventional radiography many times in different orientations of the object, and then X-ray attenuation is calculated at all points within a volume to create a 3D image. In this study, if X-ray tomography needed to be carried out, two different X-ray tomography facilities were used: a desktop micro-CT SkyScan 1172 unit and X-Tek X-ray system (XT H 225L). The SkyScan 1172 desktop micro-CT contains a maximum X-ray source up to 100 kV, 100 mA, which enables 4mm-thick titanium sample analysis with good image quality. The maximum sample dimension is limited to 50 mm in the offset scanning mode enployed. For larger samples which needed a larger working chamber, a X-Tek X-ray system was used. In both CT facilities, either a 1 mm Al filter or a 0.5 mm Al+ Cu filter was used. Depending on the thickness of sample, exposure time for each projection varied from 0.2$\sim$0.5 s. A suitable projection procedure was chosen according to the image acquired. Normally, a step angle of 0.45° was used. Increasing the projection number has a tendency to increase the image quality, but it will dramatically increase the time for scanning and reconstructing. In this study X-ray CT with Skyscan 1172 was performed in School of Dentistry , the University of Birmingham with a resolution of 15 μm and X-ray CT with X-Tek X-Ray system was performed in the μ-VIS (Multidisciplinary, Multiscale,

and Microtomographic Volume Imaging at Southampton), The University of Southampton, UK with a resolution of 5 μm.

3.2.3 Metallographic Investigation

Metallographic investigation was performed to study the microstructures of the welds and associated porosity morphology. Cutting of the specimens was performed by using SiC cutting blades with water cooling. Mechanical polishing was used for preparation of microsections. In this study, for all titanium alloys, Struers MD-system discs were used for microsection preparation as follows: First, a MD-Piano 220 grinding disc was used for grinding. For the polishing stage, 9 μm grid diamond abrasive polishing with MD-Plan disc was used after grinding, and then followed with 1μm grid diamond abrasive polishing with MD-Nap disc. The final stage was OPS with MD-Chem disc. Between each stage, specimens were washed and rinsed using ethanol, and dried. After the final stage OPS polishing, specimens were finished by using ultrasonic cleaning in acetone. Specimens etching was performed with 2 ml HF (40% conc.) and 10ml HNO_3 (70% conc.) in 100 ml H_2O. The precise etching time was chosen through close microsection observation. Vickers microhardness across the weld has been measured, by using a load of 0.5 kg and 6-seconds holding time.

3.2.4 Energy and Wavelength Dispersive Spectroscopy Analysis (EDS/WDS)

EDS/WDS were applied to analyse the chemical composition distribution around the porosity, aiming to investigate whether there was any segregation or enrichment of elements, which may give some clues for the mechanism of porosity formation. Microsection was prepared by mechanical polishing as described in the above section, followed by EDS/WDS line measurement along the pore edges, which was performed using a JEOL 7000 analytical scanning electron microscope operating at 20 kV.

3.2.5 Residual Gas Analysis

To identify the gas composition inside the porosity, residual gas analysis (RGA) has been performed. A Hidden Analytical HAL 100-RC RGA (residual gas analysis) quadrupole gas analyser was employed with associated ultra high vacuum equipment, assembled by Leybold Ltd. A schematic diagram illustrating the residual gas analysis system is shown in Figure 3.1. The

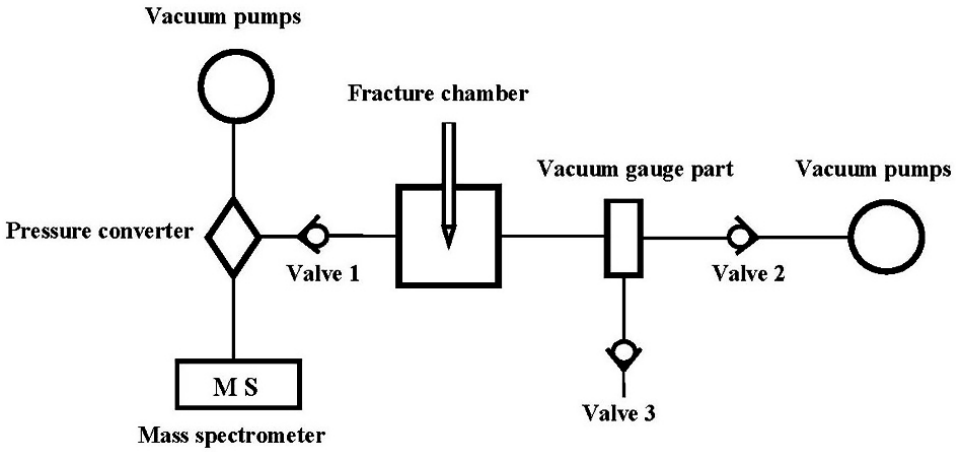

Figure 3.1: Schematic diagram of the residual gas analysis system.

sample is cracked to release the gas in the fracture chamber, which can be isolated from the system by 3 valves. To load the sample, valve 1 and 2 are closed, while valve 3 is open to vent the chamber. After loading the sample, valves 1 and 2 are opened and valve 3 closed to pump down the system. Due to the small volume of the system and the power of vacuum pumps, the system can be pumped down within a few hours and stabilised to a very high vacuum of 10^{-8} mbar, before the analysis proceeds. Before cracking the pore, valve 2 is closed to ensure the gas released from the sample will be directed to the mass spectrometer, which is run in multi-ion detection (MID) mode until the detected background signal becomes stable. The released gases are detected by mass spectrometer, and the data collected and analysed using MASsoft (version 5) software provided by Hidden Analytical Ltd. In practice, samples for residual gas analysis need to be prepared with caution. To make sure the samples can be cracked to release the gas quickly, sample surfaces need to be ground down very close to the pores (within μm), which

requires the pore to be located precisely in 3-dimensions. For this purpose, high resolution (10 μm) X-ray tomography was carried out using the desktop SkyScan 1172 unit, which in practice was found to provide the necessary resolution.

3.3 Results

3.3.1 Characteristics of Titanium EB Welds

CP-Ti exhibits a single phase; although it might contain small amount of impurities such as C, N, O, they do not change the HCP crystal structure. To distinguish fusion zone (FZ), heat-affected zone (HAZ) and base material (BM), the microstructure morphology and microhardness have been examined. Figure 3.2 shows the microstructure of the base material in the as-received CP-Ti, in which every fine grain is presented with average size around 30 μm. A typical cross section of the EB weld of CP-Ti is shown in Figure 3.3, in which the fusion zone (FZ) width is found around 2.8 mm with a large round pore with diameter of 0.5 mm located right in the centre of fusion zone. A high magnification micrograph of the phase transition between the HAZ and the base metal is shown in Figure 3.4, in which a noticeable grain growth has been found in the HAZ ($\sim$50 μm grain size) relative to the very fine equiaxed grains with size of 20 μm in the base material. Figure 3.5 shows the typical microstructure in the FZ, in which massive martensite is formed due to the large cooling rate experience. This massive martensite consists of large irregular regions, which has been found around 0.5mm for the weld centreline. The microhardness profile across the weld is plotted against distance from the weld centreline, see Figure 3.6. The results show the microhardness increases rapidly within the HAZ from HV 185 in the base material to average value of HV 215 in the FZ of the weld. The microhardness profile shows that the width of HAZ is found to be around 1.5 mm.

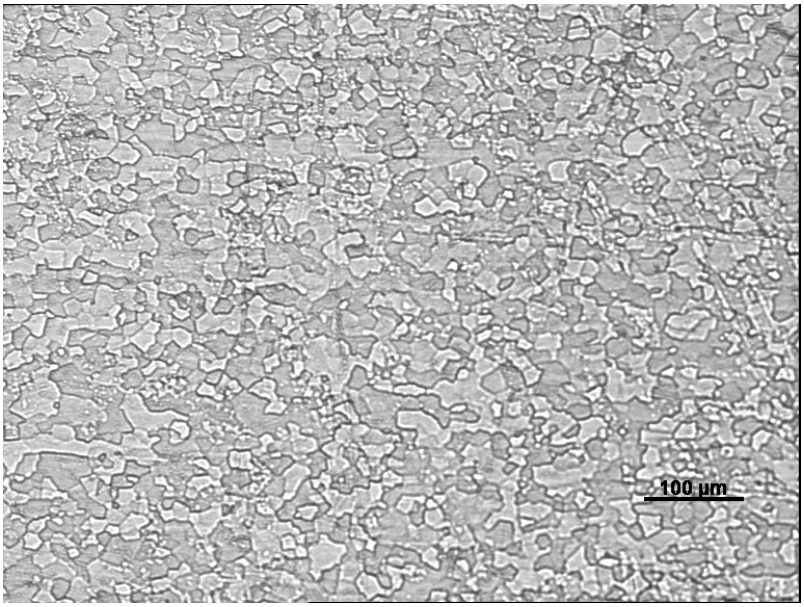

Figure 3.2: Optical micrograph illustrating the microstructure of as-received CP-Ti.

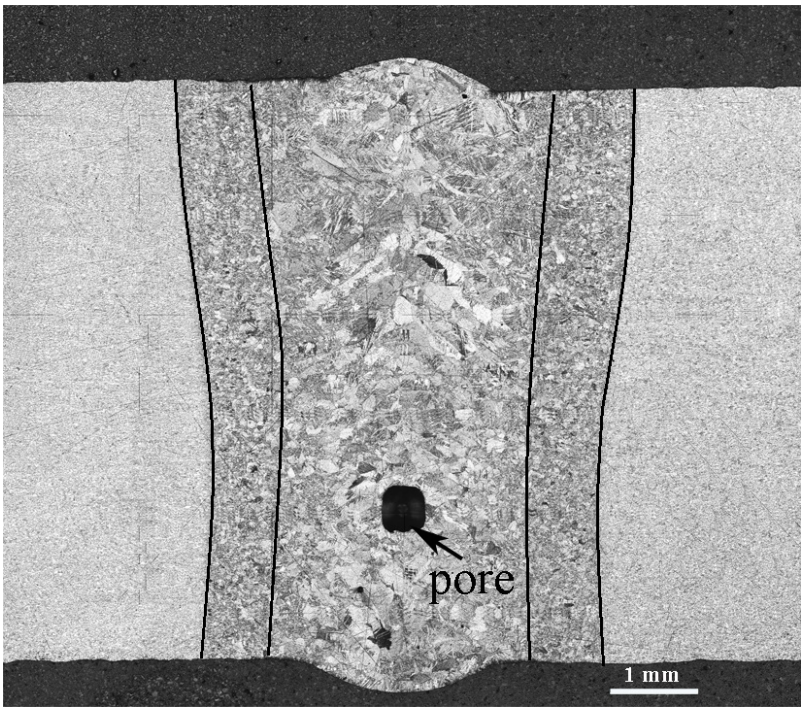

Figure 3.3: Typical cross section of EB welds of CP-Ti with a large pore located in the weld FZ centre.

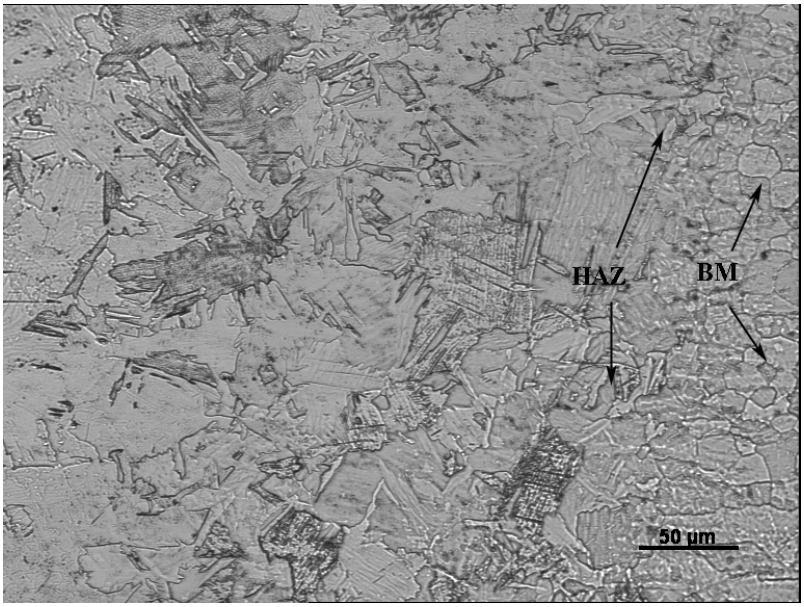

Figure 3.4: Optical micrograph illustrating microstructure transition from HAZ to BM in electron beam welded CP-Ti.

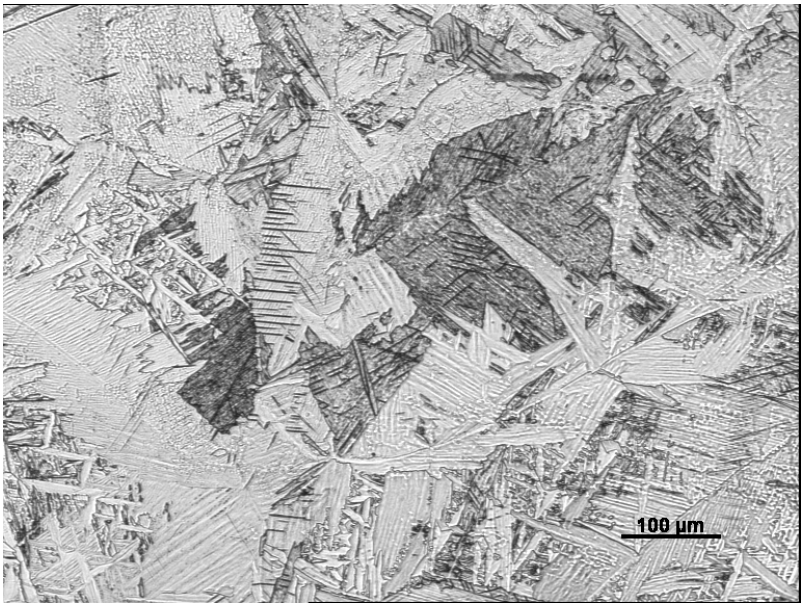

Figure 3.5: Optical micrograph illustrating the typical microstructure of the FZ, locating at the centre line of electron beam welded CP-Ti.

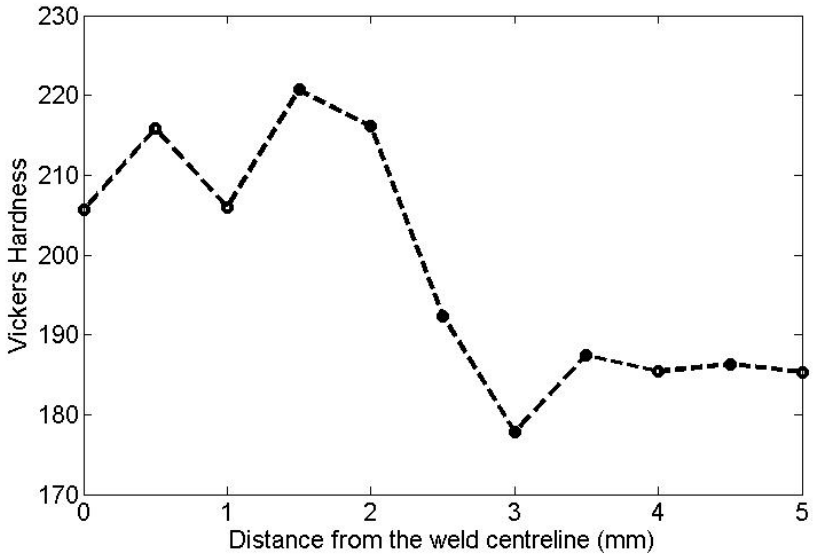

Figure 3.6: Microhardness across the weld in electron beam welded CP-Ti.

The microstructure in the as-received Ti-6Al-4V is shown in 3.7, in which a typical bimodal (duplex) microstructure containing equiaxed primary α (α_p) in a lamellar $\alpha + \beta$ matrix is observed. After welding, a typical weld zone is shown in Figure 3.8, in which the fusion zone slightly spreads at the top surface with width of about 3.1 mm, and then gradually decreases along the thickness direction down to 1.5 mm. Figure 3.9 and Figure 3.10 illustrate the microstructure in the BM-HAZ and HAZ-FZ regions respectively. It can be seen from Figure 3.9, that (unlike the CP-Ti, in which a noticeable grain growth has been found in the HAZ) the grain size in the heat-affected zone of Ti-6Al-4V weld remains the same across the base material and heat-affected zone. However the high magnification SEM images show the morphology changes inside the grains. Compared to the microstructure morphologies in the base material, the lamellar $\alpha + \beta$ matrix alters and more fine particles are found inside the previous primary α grains in the HAZ. Formation of very fine acicular martensite due to the rapid cooling of the weld pool is observed in the fusion zone as shown in Figure 3.11. Microhardness across the weld has been measured and the result is shown in Figure 3.12. The microhardness is found to

increase rapidly across the heat-affected zone, from the HV 350 in base material to HV 400 in the fusion zone. The microhardness profile shows that the HAZ width is around 1.5 mm.

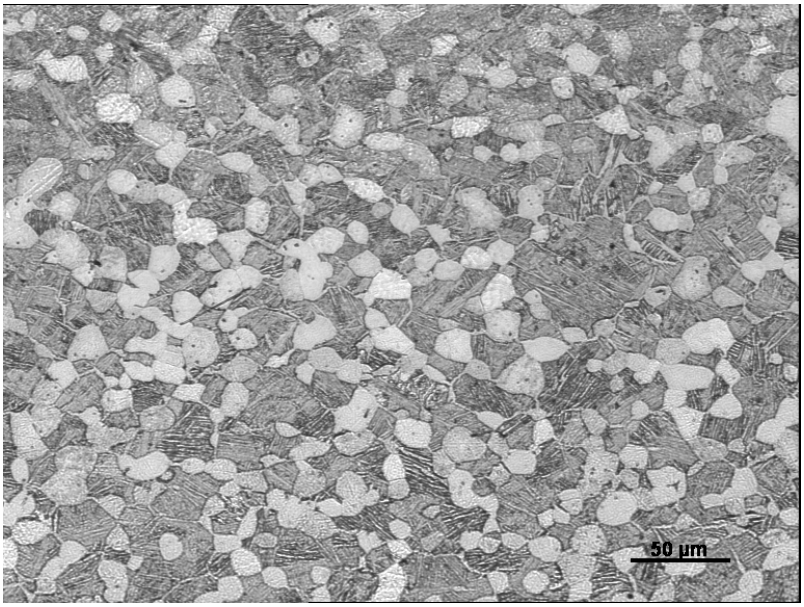

Figure 3.7: Optical micrograph illustrating the microstructure of BM in as-received Ti-6Al-4V sample.

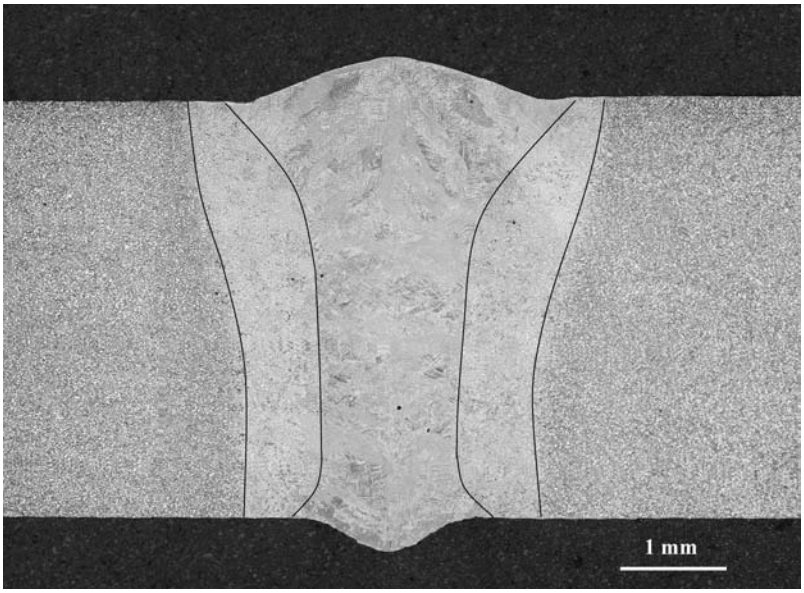

Figure 3.8: Typical cross section of electron beam welded Ti-6Al-4V alloy.

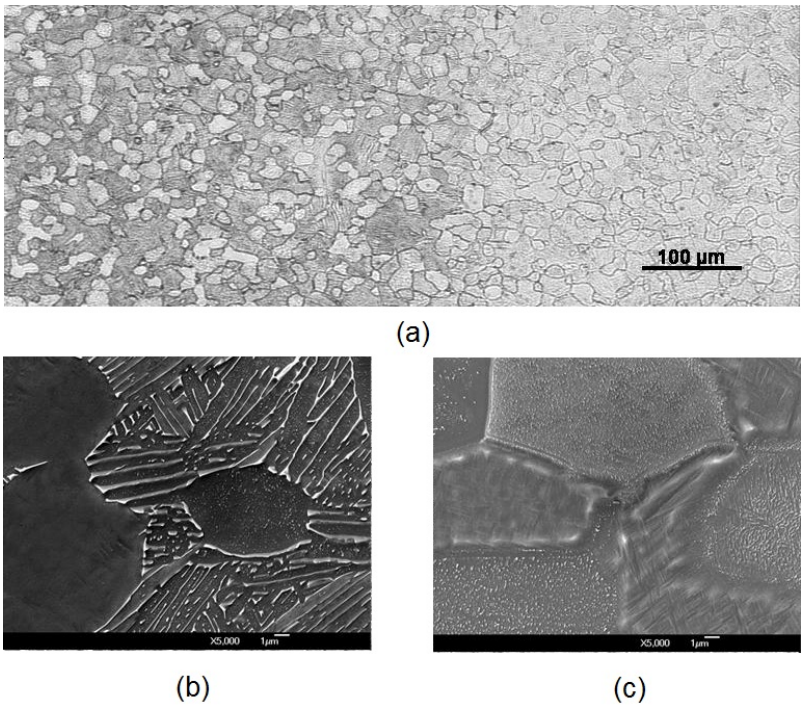

Figure 3.9: Optical micrograph illustrating transition of microstructures between BM and HAZ in electron beam welded Ti-6Al-4V.

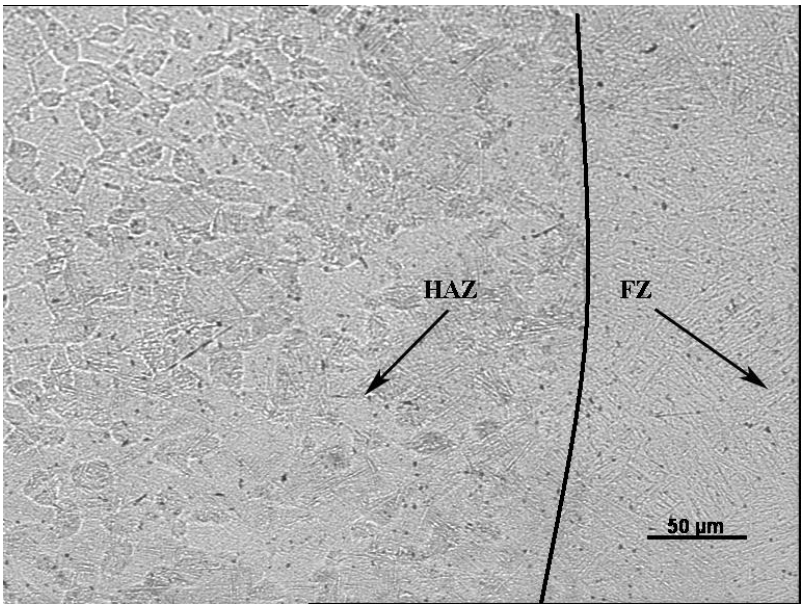

Figure 3.10: (a) optical micrograph illustrating transition of microstructures between BM and HAZ in electron beam welded Ti-6Al-4V; (b) SEM micrograph with higher magnification illustrating the microstructure in BM; (c) SEM micrograph with higher magnification illustrating the microstructure in HAZ.

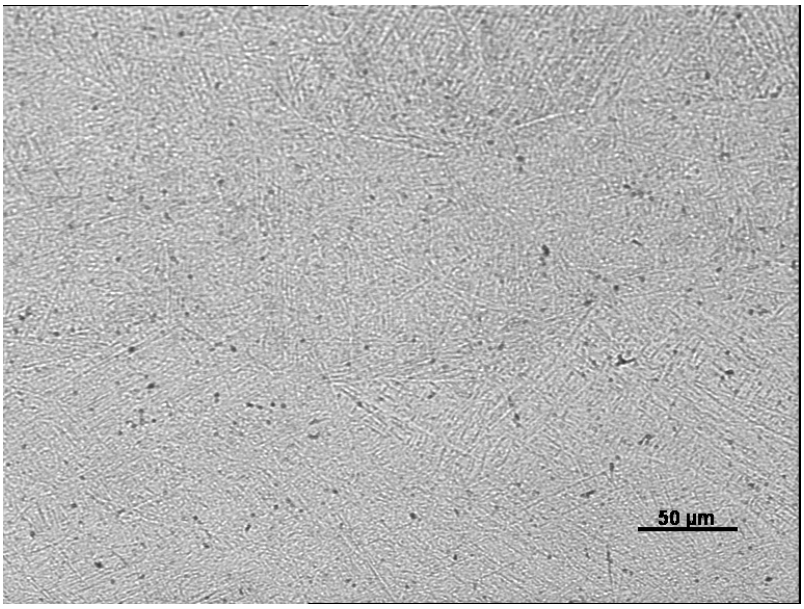

Figure 3.11: Acicular martensite in fusion zone of electron beam welded Ti-6Al-4V alloy.

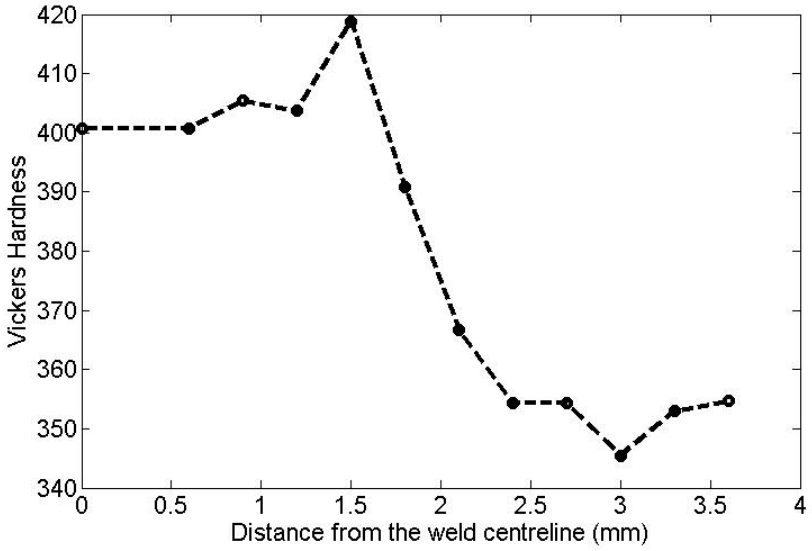

Figure 3.12: Microhardness across the weld in electron beam welded Ti-6Al-4V.

The microstructure in as-received Ti-6246 is shown in Figure 3.13; a high volume fraction of coarse α plates is seen. Figure 3.14 shows the cross section of electron beam welds, in which a curved fusion zone profile is found of a waist-type. The fusion width near the top and bottom surface is almost the same, which is around 2.8 mm, while the narrowest fusion zone width around the waist is around 1.8 mm. Figure 3.15 and Figure 3.16 show the transition of microstructure at BM-HAZ and HAZ-FZ respectively. In Figure 3.16, small pores are seen at the fusion boundary. Figure 3.17 illustrates the microstructure of the fusion zone, in which no martensite is observed. A metastable β phase rather than martensite is formed when β alloys are quenched to room temperature. A higher magnification SEM micrograph shows that α phase precipitates from the metastable β phase as very fine particles (platelets) with a high volume fraction. Similarly with the EB welded CP-Ti and Ti-6Al-4V alloy, microhardness increases rapidly across the HAZ, from HV 370 in the base material to HV 420 in the FZ as shown in Figure 3.18.

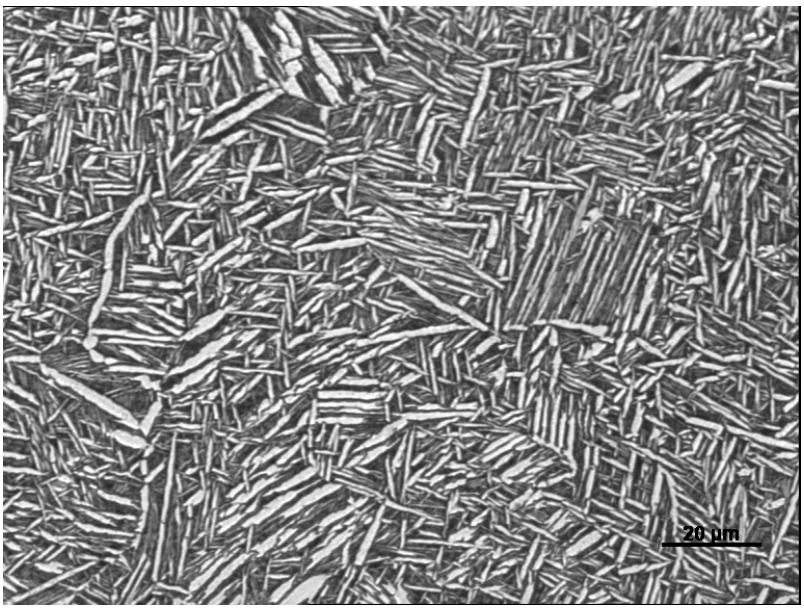

Figure 3.13: Optical micrograph illustrating the microstructure of BM in as-received Ti-6246 sample.

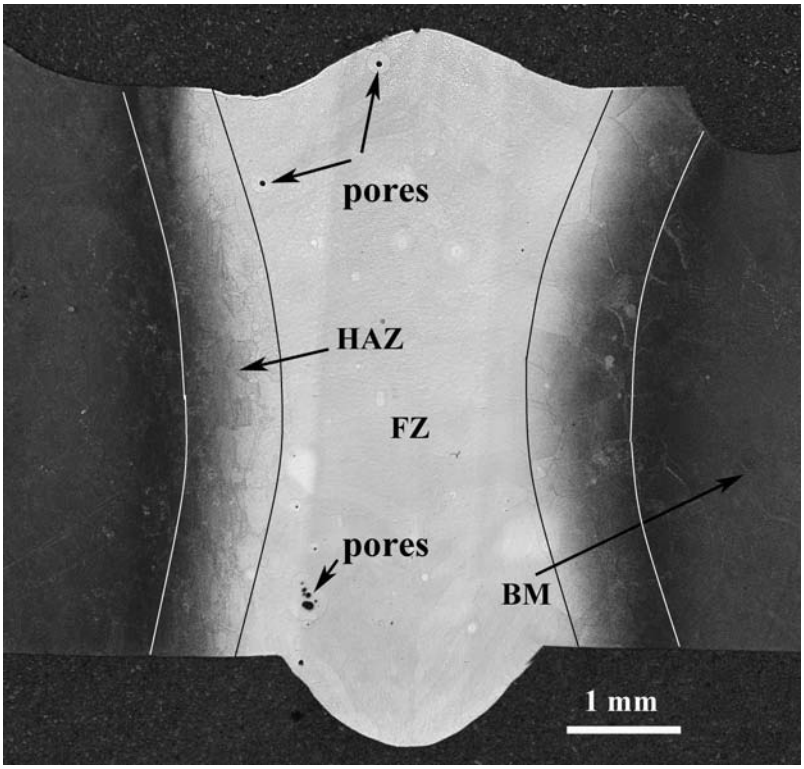

Figure 3.14: Typical cross section of electron beam welded of Ti-6246. Note the pores in the toe of the weld.

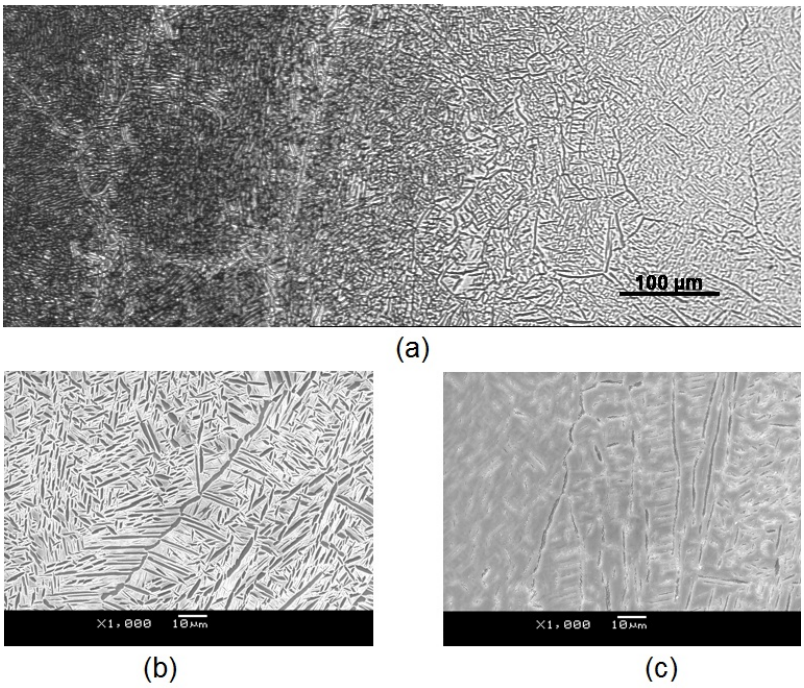

Figure 3.15: (a) optical micrograph illustrating transition of microstructures between BM and HAZ in electron beam welded Ti-6246; (b) SEM micrograph with higher magnification illustrating the microstructure in BM; (c) SEM micrograph with higher magnification illustrating the microstructure in HAZ.

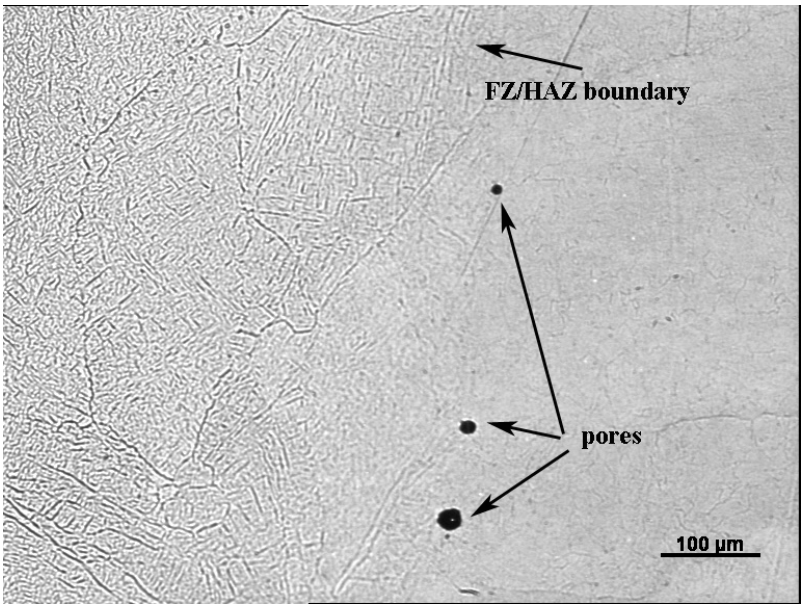

Figure 3.16: Optical micrograph illustrating transition of microstructures between HAZ and FZ in electron beam welded Ti-6246.

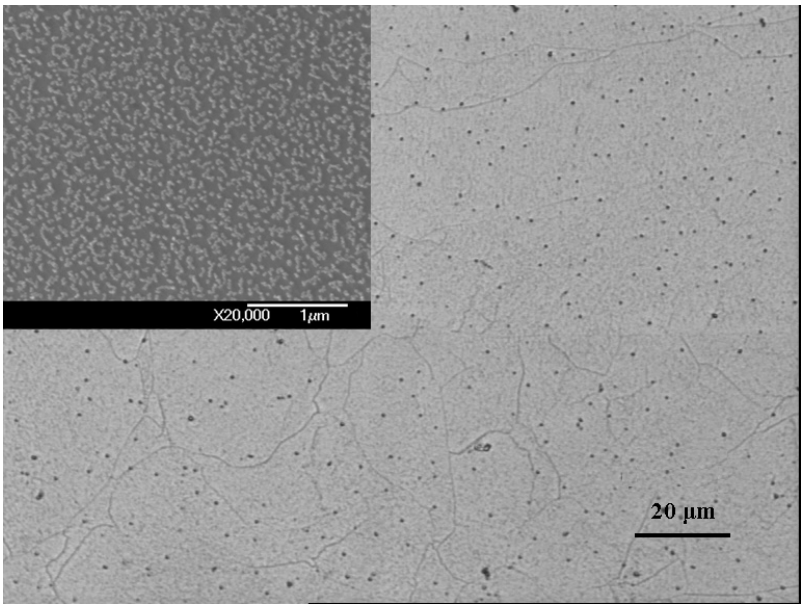

Figure 3.17: Microstructure in fusion zone of electron beam welded Ti-6246 alloy.

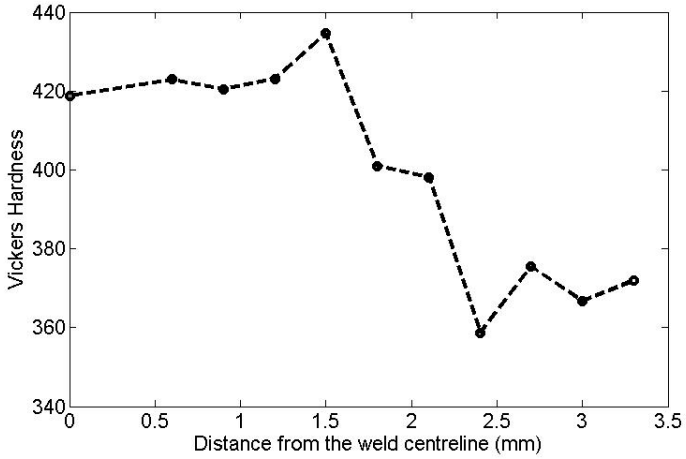

Figure 3.18: Microhardness profile across the weld cross section in electron beam welded Ti-6246.

The microstructure of the base material in as-received IMI-834 sample consists of about 15% of equiaxed primary α, in a fine-grained matrix of lamellar transformed β microstructure, forming the so-called bimodal microstructure as shown in Figure 3.19. Compared to the microstructure found in Ti-6Al-4V alloys as shown Figure 3.7, this alloy contains less primary equiaxed primary α grains. Most of the small primary α grains locate at"triple-point" at transformed β grain boundary. Fine continuous α layers are found at β grain boundaries. Figure 3.20 shows a typical cross section of EB welded IMI-834. Similar to the fusion profile found in Ti-6246 as shown in Figure 3.14, a waist-type fusion profile is found in EB welded IMI 834 alloy. The fusion zone is observed with width varying from 1.8 to 3.2 mm with the wider fusion zone close to the top and bottom surfaces and the narrowest part at mid-section. The high magnification optical images in Figure 3.21 and Figure 3.22 show the microstructure evolution at BM-HAZ and HAZ-FZ transition regions respectively. It can be seen that across the HAZ primary α grains are dissolved. Due to the fast cooling of weld pool, fine acicular martensite is found at the fusion zone of the weld as illustrated in Figure 3.23. The hardening of the weld region is confirmed by the microhardness profile across the weld, see in Figure 3.24. The microhardness profile shows that the HAZ width is around 1.0 mm.

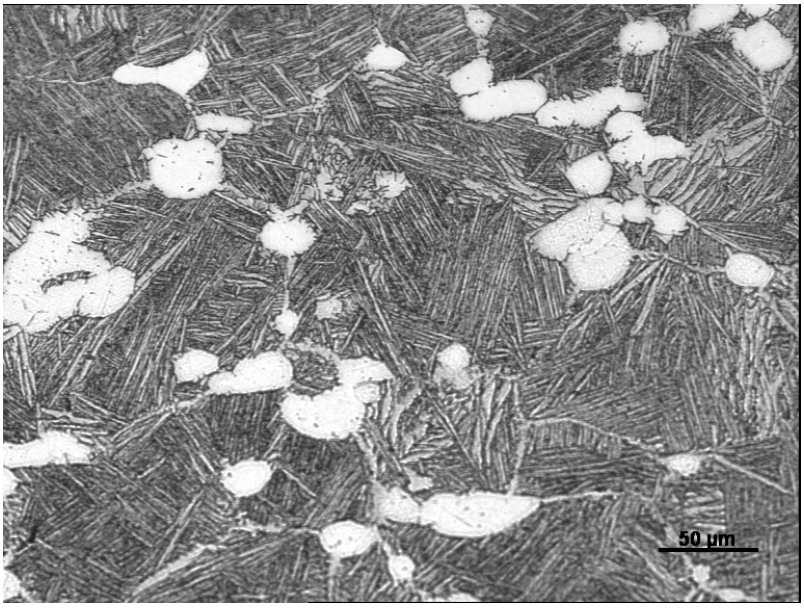

Figure 3.19: Optical micrograph illustrating the microstructure in base material of as-received IMI 834.

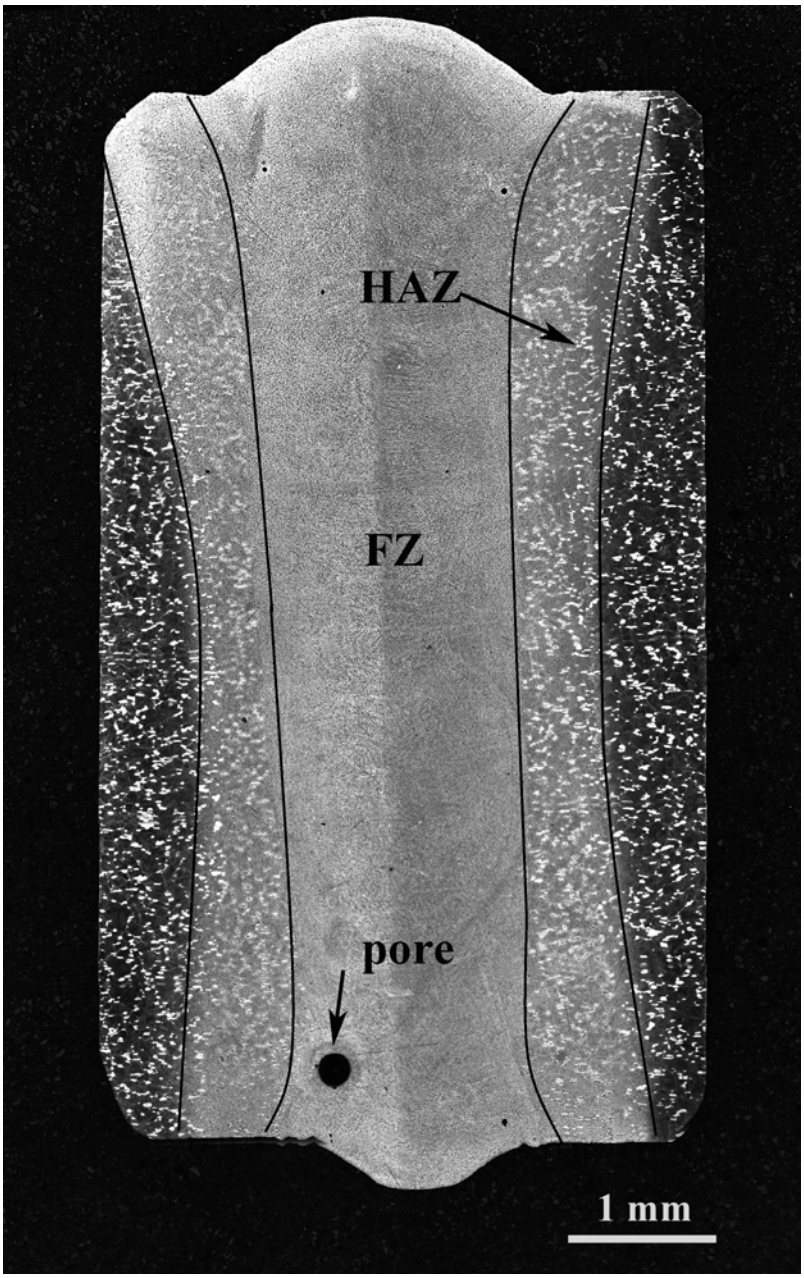

Figure 3.20: Typical cross section of EB weld of IMI-834.

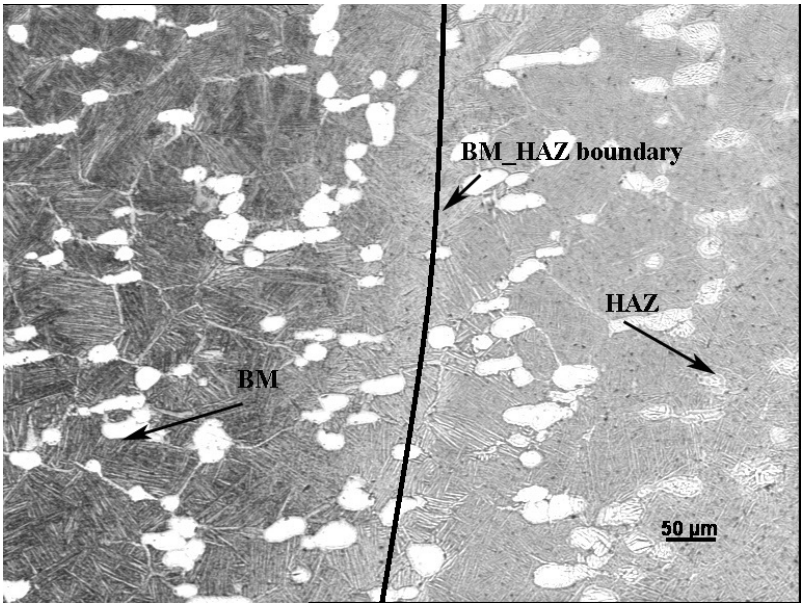

Figure 3.21: Optical micrograph illustrating transition of microstructures between BM and HAZ in electron beam welded IMI 834.

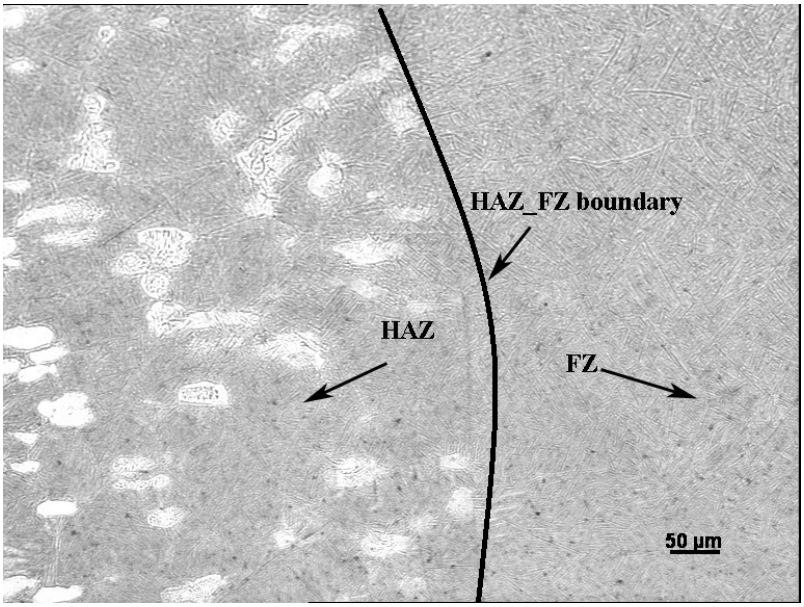

Figure 3.22: Optical micrograph illustrating transition of microstructures between HAZ and FZ in electron beam welded IMI 834.

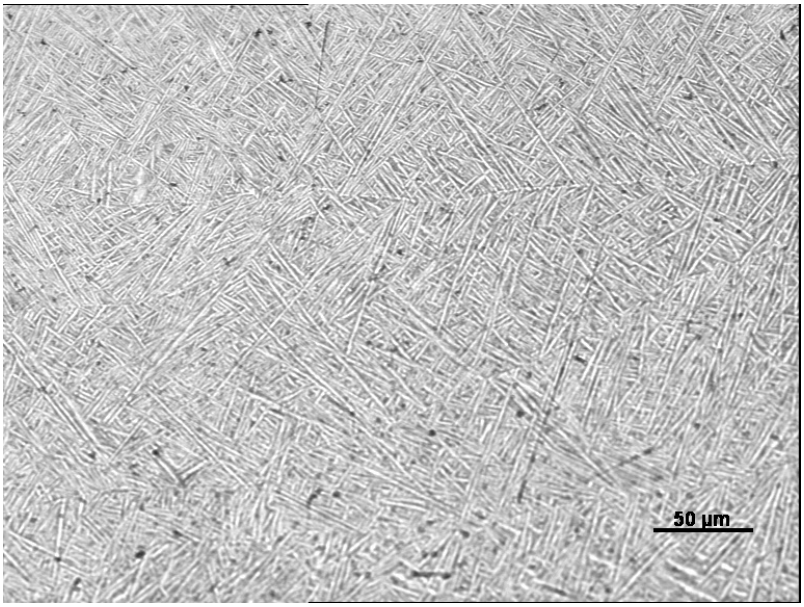

Figure 3.23: Acicular martensite in fusion zone of electron beam welded IMI 834 alloy.

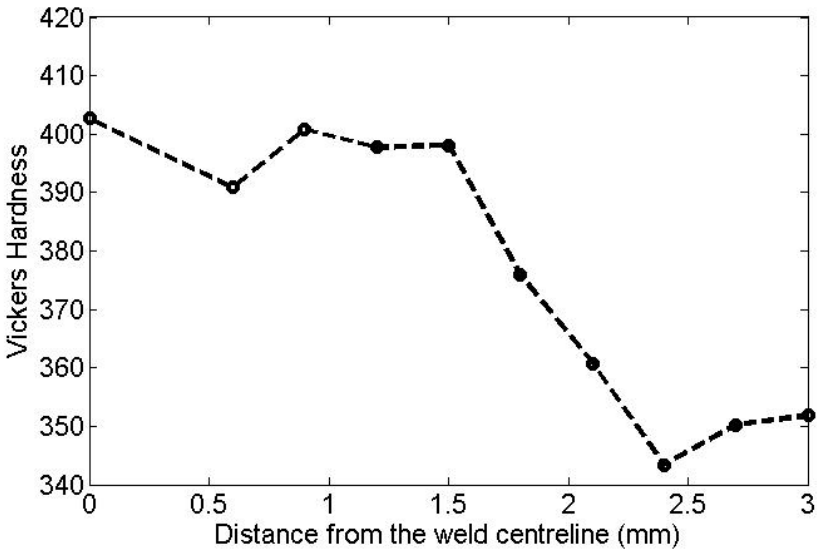

Figure 3.24: Hardness profile across the electron beam welded IMI 834 alloy.

3.3.2 Pore Morphology and Distribution

Pores formed in EB welds were detected by conventional X-ray radiography and X-ray CT. After locating these, welds were sectioned to reveal the morphologies. Figure 3.25 illustrates the porosity found at the cross section of CP-Ti. A large pore (diameter around 500 μm) can be seen in the weld centre line with nearly round shape, below which some circular pores were found. Pores were more frequently located at the lower part of the weld bead, and small pores were often found very close to the fusion boundaries. This may because the flow dynamics within the lower part of the weld pool decrease the possibility of a bubble escaping from the weld pool. The reason for more small pores found in the fusion boundaries is the very poor fluidity and small dragging forces, which cause bubbles to detach from the solid wall at the fusion boundary and escape. Due to this reason, small gas pores can be trapped at any almost

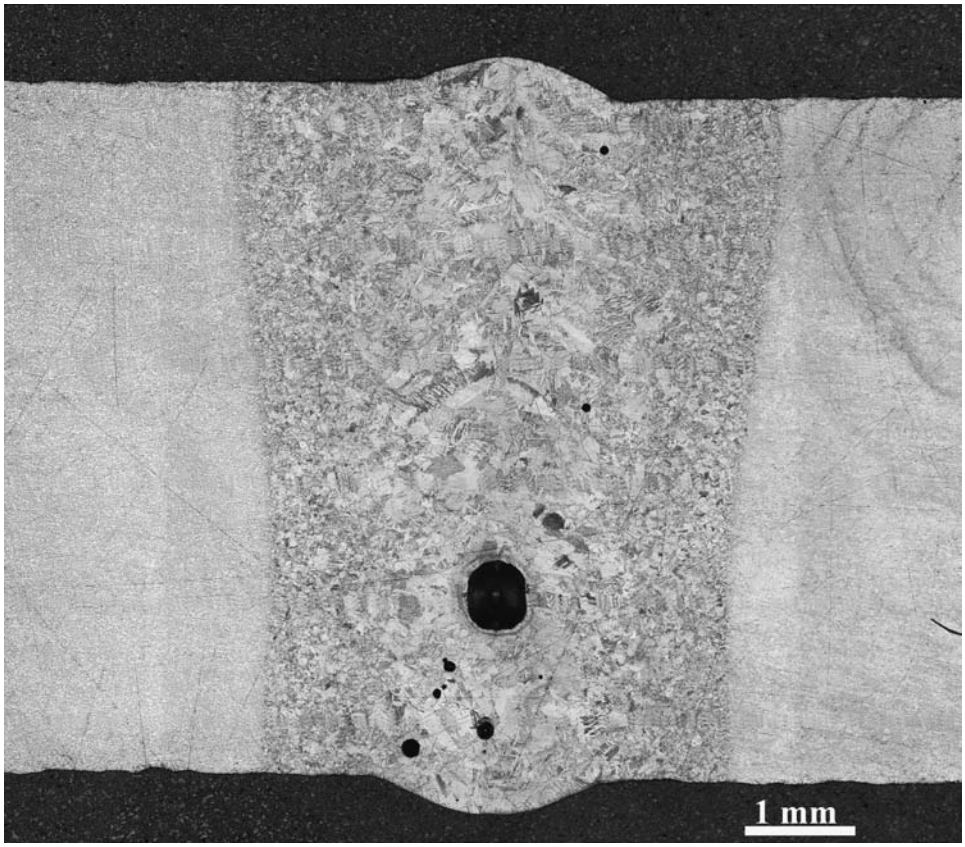

Figure 3.25: Porosities formed in electron beam welded of CP-Ti.

any depth along the thickness direction at the fusion boundaries, see Figure 3.25. Figure 3.26 is an image reconstructed from the X-ray tomography results, showing the pores formed in a CP-Ti EB weld. It can be seen in this alloy pores have a perfect sphere shape. It needs to be mentioned that most of the pores have a size ranging from 100 μm to 300 μm in diameter. Larger pores were rarely found, which may be due to the large buoyancy force favouring their escape from the weld pool. The higher magnification SEM micrograph in Figure 3.27 shows the inner surface of the small pores; it can be seen that the inner surfaces are very smooth and the acicular microstructure is clearly presented. Similar pores were also found in EB welded Ti-6Al-4V as shown in Figure 3.28 and in Ti-6246 as shown in Figure 3.6.

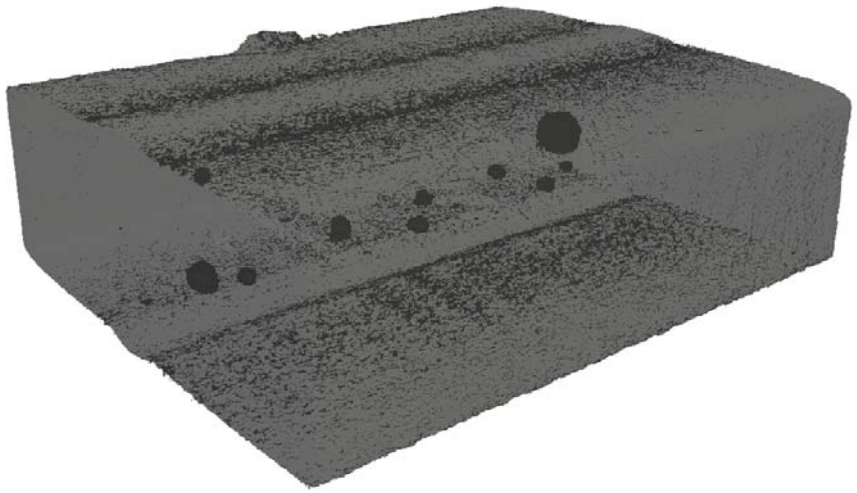

Figure 3.26: Reconstructed image from X-ray tomography (CT) results illustrating pore distribution inside electron beam welded CP-Ti.

Figure 3.29 shows a series of slices of the reconstructed CT images crossing a detected pore in an EB weld of IMI-834, which is also found to have a perfect round shape. The pores are located at the lower part of the weld bead, close to the FZ boundary. Scanning electron microscopy confirmed the smooth inner surfaces of the pores; see Figure 3.30 and Figure 3.31. In Figure 3.31 it seems likely two bubbles were captured when they were trying to merge together due to

the fast cooling of the weld pool. This may indicate that small bubbles can merge together to form large bubbles if weld pool life is long enough.

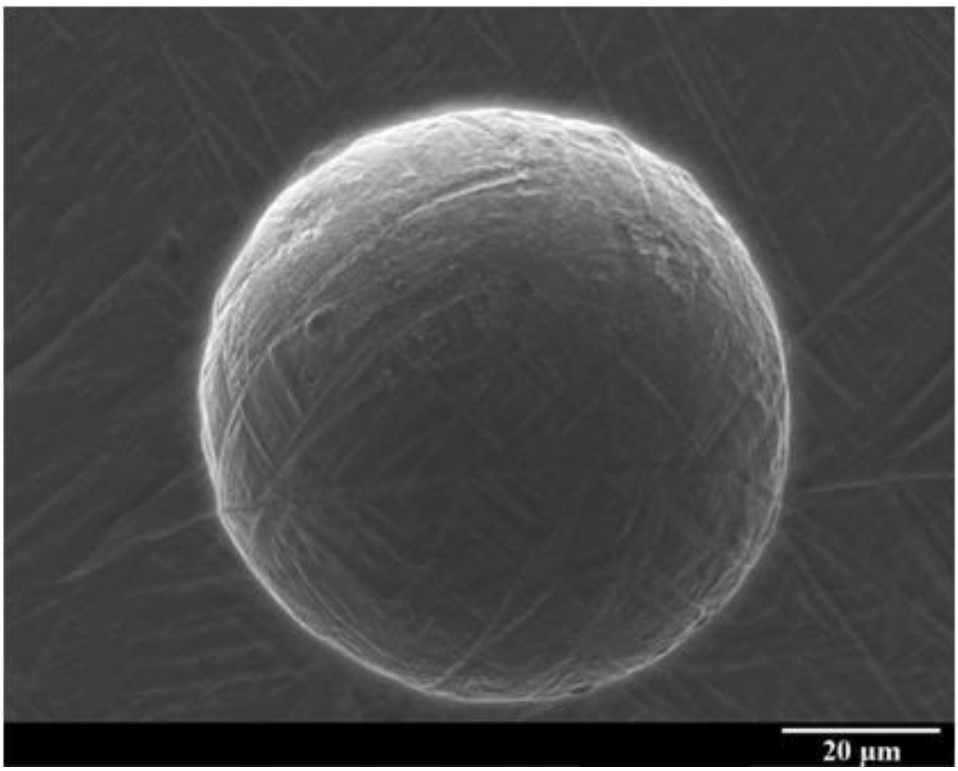

Figure 3.27: SEM micrograph illustrating the inner surface of a small pore formed in electron beam welded CP-Ti.

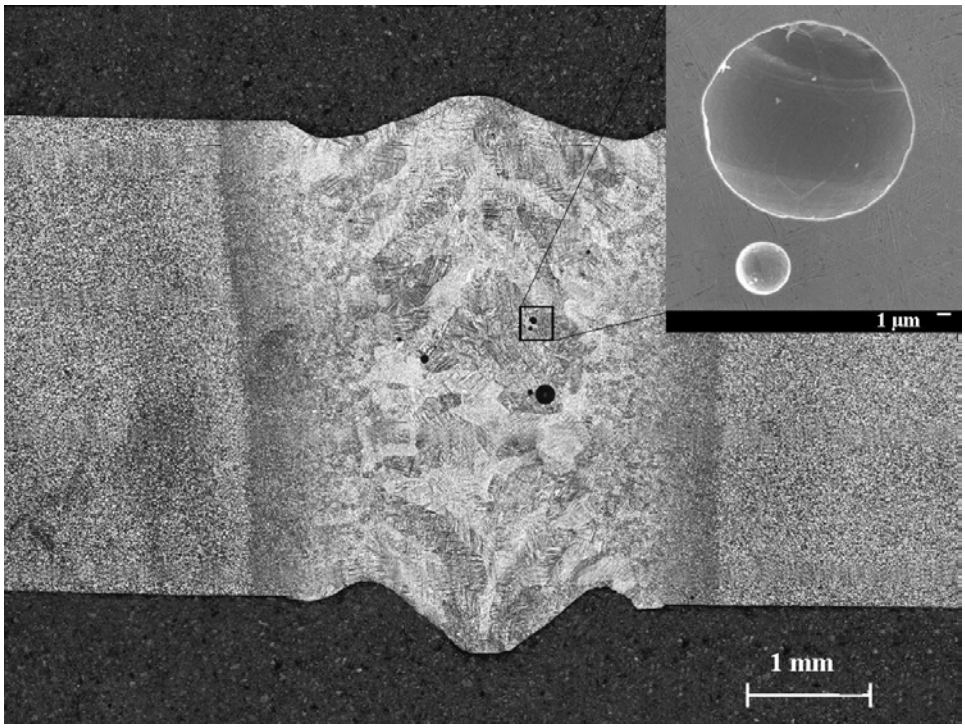

Figure 3.28: Pores formed in electron beam welded Ti-6Al-4V alloy.

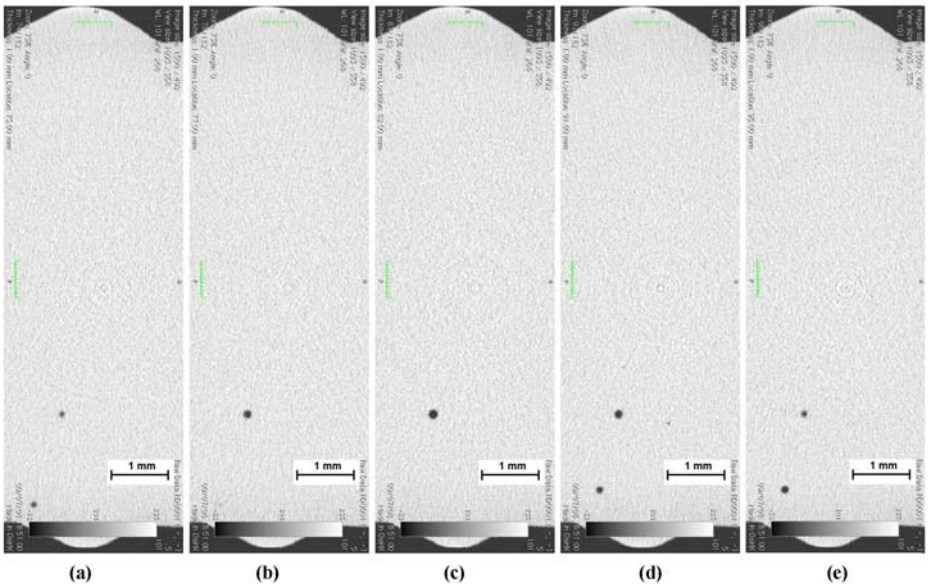

Figure 3.29: Series of tomography sections across a detected porosity in IMI-834 EB welds.

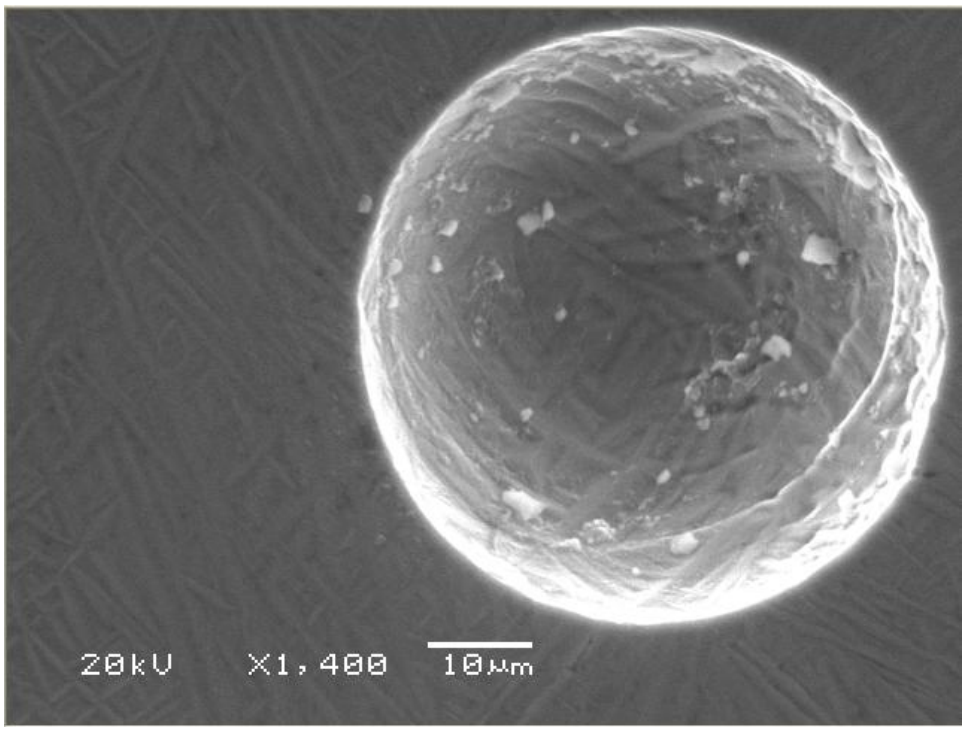

Figure 3.30: SEM micrograph illustrating the morphology of porosity formed in electron beam welded IMI-834 alloy.

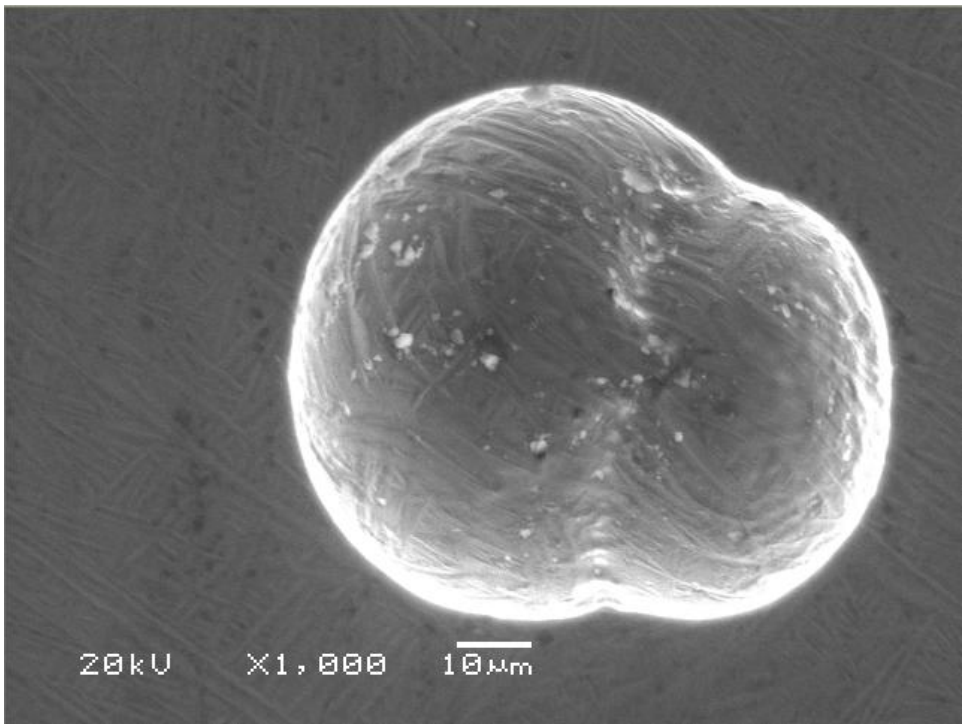

Figure 3.31: Merged pores found in electron beam welded IMI-834 alloy.

3.3.3 Chemical Composition Analysis around Porosity Edges

Porosity formation may be associated with metal vapour evolution during keyhole mode high energy beam welding process [78]. If this is the case, one would expect chemical partitioning at the edges of the pores. To identify the chemical element distribution around the pore edges, EDS/WDS line scanning was performed. The result is shown in Figure 3.32, in which the line scanning length along a large pore formed in EB welded Ti-6246 alloy is 6 μm. Wavelength dispersive (WD) analysis is activated for oxygen detection to improve the resolution and reliability. It can be seen that with the exception of oxygen, the detected signals of all other elements, such as titanium, aluminium, molybdenum and zirconium, decrease close to the pore edges, which is obviously due to the edges effect, but the line scanning profile shows that a significant signal has been detected from oxygen close to the pore edge, which means the pore edge is rich in oxygen content. When the distance from the pore edge is beyond 2 μm, the distribution profiles of all the elements are fairly uniform. The line scanning profile shows that oxygen content at pore edges is almost twice as high as that far from the pore edges, but at this stage the reason for this is not clear. One would expect two possibilities for the oxygen source, either from surface oxides of joint surfaces, or due to the oxidation during the metallographic sample preparation. Oxidation at the sample surface layer may occur during the mounting process or from the chemicals used in grinding and polishing. Considering the sample has been ground to more than 0.5 mm to reveal the porosity, the usage of grinding and polishing solutions and short delay after polishing for line scanning analysis, it would appear it is more likely that oxygen comes from the joint surfaces. The effect of oxygen contaminant at joint surfaces been reported in [83], with the oxygen favouring the porosity formation during welding in an indirect way by producing CO_2 or CO due to reaction with carbon. These gases play a critical role via stabilising the bubbles in the early stage of bubble formation.

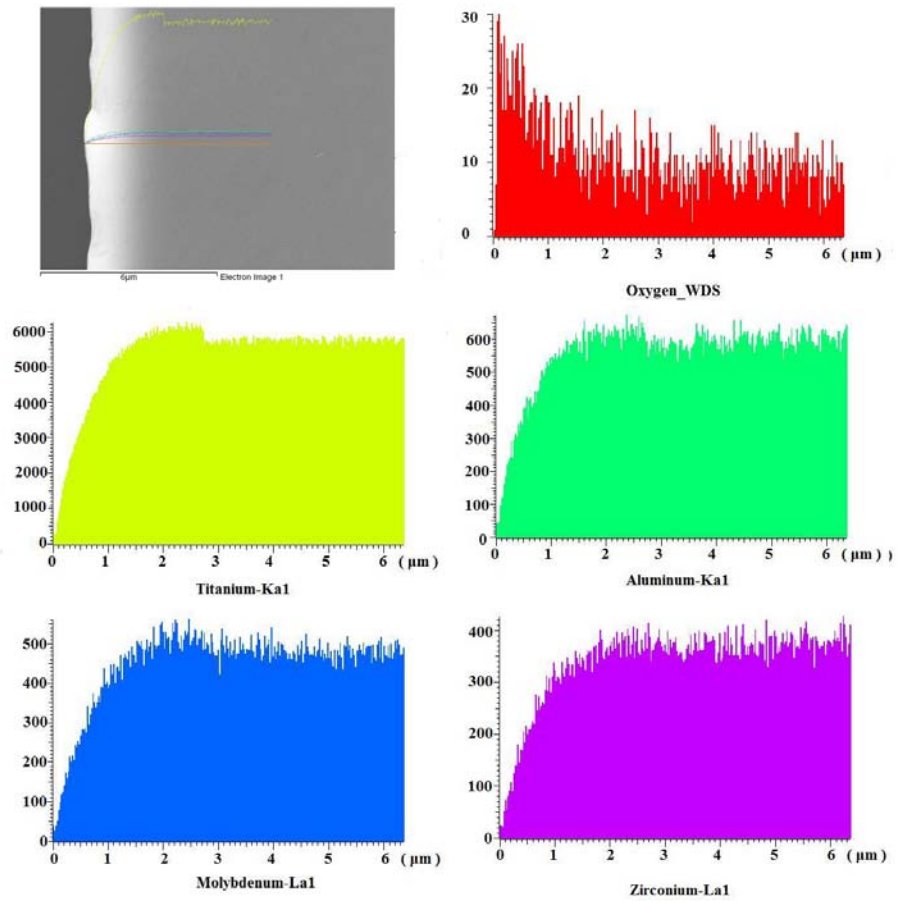

Figure 3.32: Line scanning along pore edge formed in electron beam welded Ti-6246 alloy to identify the chemical composition distribution.

3.3.4 Gas Composition inside Porosity

A large pore of diameter around 1.8 mm was identified for residual gas analysis, see Figure 3.33. The detected partial pressure confirms that most of the gas inside the pore is hydrogen. A small amount of CO2 was also detected. Beside H_2 and CO_2, gas with atomic mass unit (amu) of 28 was also found but with amount slightly less than for CO_2. Since both N_2 and CO have the same atomic mass unit of 28, it is not possible to distinguish these two gases from the mass spectrometry results. In principle, one would like to distinguish between these two gases, because they will be associated with completely different mechanisms of pore initiation. If N_2 exists inside the pores, it indicates that air is involved with the porosity formation. Even though

the EB welding process is performed at high vacuum condition, it is still possible that small air pockets can be entrapped between the two joint surfaces due to mechanical assembly before the welding chamber is pumped down. If the gas with amu of 28 is CO, it suggests that the porosity formation is related to the decomposition of hydrocarbon. In both cases, it suggests that hydrogen favours porosity formation.

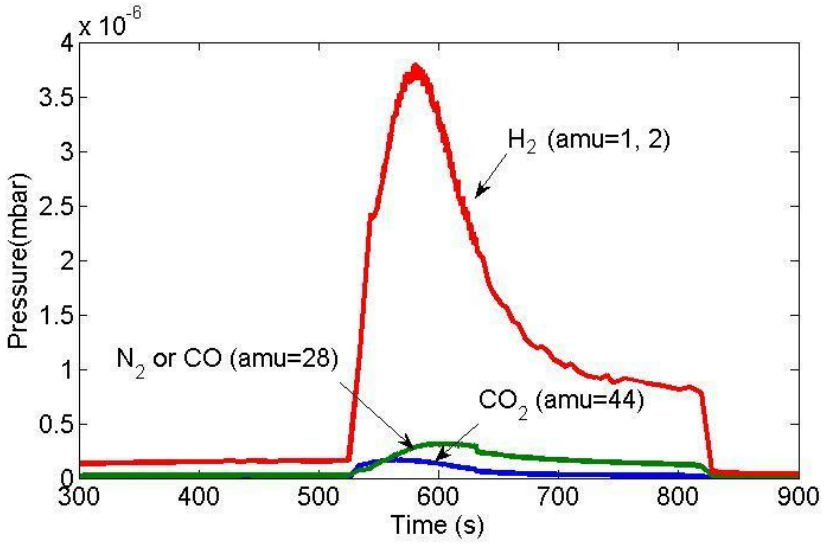

Figure 3.33: Gas analysis result by using MID (Multiple Ion Detection) mode.

3.4 Discussion

3.4.1 Hydrogen Effect on Porosity Formation

From above results, it is clear that pores formed in all titanium EB welds have circular shape and smooth inner surfaces, which indicate that the pores are formed due to gas evolution during the welding process. From the detected gas composition by residual gas analysis (RGA), it seems likely that hydrogen is responsible for porosity formation, but at this stage, it would be hasty to conclude that hydrogen is the root cause. This is because the high amount of hydrogen found in the gas pores may be due to the diffusion of hydrogen atoms into the already formed pores after welding. To investigate whether hydrogen is the root cause, understanding of hydrogen behaviour during electron beam welding process needs to be improved, such as the hydrogen

migration, the role of hydrogen in bubble growth etc. Further investigation of hydrogen effect on porosity is needed and this is done in the rest of the thesis.

3.4.2 Bubble Initiation and Growth

From the above results, it would seem that porosity formation in electron beam welded titanium is associated with hydrogen, but the details of the porosity formation mechanism need to be further investigated, particularly the mechanism of bubble initiation and bubble growth. Homogenous bubble formation is particularly impossible due to the hydrogen content in the base material being far below the required levels to nucleate a critical size of microbubble. Another popular theory about bubble nucleation in the weld pool is heterogeneous nucleation at the boundary between the solid and liquid metal when the dissolved gas exceeds its solubility. The heterogeneous nucleation theory reduces the required hydrogen level to form bubble in certain conditions, but it still needs very high hydrogen content. Previous work suggested that decomposition of titanium hydrides may meet the requirement of very high local hydrogen content needed. If this is the formation mechanism, pores should be expected to occur continuously along the welds. But in reality, the formation of porosity is more like a random process, which is correlated to the surface condition. It has been pointed out that nuclei of gas bubbles occurs in front of the molten pool as a result of irregularities of joint surface and formation of closed cavities formed due to the thermal deformation of the edges, whose surfaces contain absorbed gas-forming substances [83]. When the electron beam passes through these closed voids, these act as pre-existing nuclei for gas bubbles. When bubbles grow, the impurities at the pore edges may remain at the edges and move together within the bubble. It seems that the characterisation results in this work support this porosity formation mechanism, such as the higher amount of oxygen at the pore edge and the detected CO_2 trapped inside the pores. Once the bubbles nucleate inside the weld pool, highly mobile hydrogen atoms could diffuse into these bubbles, favouring the formation of large bubbles. If this is the case, porosity formation should be dependent not only on the hydrogen content in the base material, but also the surface condition, which

provides the nuclei in the early stage of bubble formation. The final size should be determined by the dynamics of bubble growth inside the weld pool, which needs further investigation.

3.4.3 Fusion Zone Shapes and Bubble Escape

The pores form if the gas bubble cannot escape before the weld pool solidifies. The driving force for the bubble escaping includes buoyancy forces and dragging forces due to the stirring effects inside the weld pool. If the buoyancy force dominates, it would be expected that weld pool life needs to be sufficient for enough bubble growth to occur, to provide the sufficient buoyancy force; this will cause the detachment of the bubble from the fusion boundary and its movement to the weld pool surface. In the electron beam welding process, the weld pool is normally very narrow; thus it solidifies very quickly with high cooling rate, which means that the time for the bubble to flow up to the weld pool surface is very short, so that it is less likely that bubbles can escape from the weld pool driven by buoyancy force. Another way to favour the bubble escaping from the weld pool is the dragging force by the fluid flow inside the weld pool. During electron beam welding, intensive evaporation occurs; this generates a large recoil pressure, which drives the molten material flow around the keyhole. The dragging force from the flow of molten metal increases the possibility of bubble to detachment from the fusion zone boundary. Due to the existence of the keyhole inside the weld pool, the bubble may escape by breaking through the keyhole wall rather than the weld pool surface. From the above cross sections of EB welds, fusion profiles vary from near parallel-type to a waist-type which indicates that the fluid dynamics inside the weld pools changes due to combination of electron beam parameters and material properties. From this point of view, the fusion zone profile may potentially correlate with porosity formation in electron beam welded titanium alloys.

3.5 Summary and Conclusions

Electron beam welded titanium alloys and porosity formation have been investigated experimentally to shed light on the mechanism of pore formation. The findings can be summarised as

follows:

1. Pores have been found both in CP-Ti and three other different titanium-based alloys namely Ti-6246, Ti-6Al-4V and IMI-834. No strong evidence has been found that porosity formation is related to specific alloy compositions.

2. Pores found in EB welds of titanium are round and have smooth inner surfaces, which suggests that porosity formation is associated with gas evolution during the welding process. Typical diameters are around$\sim$ 300 μm; large pores (diameter $>$ 0.5 mm) are rarely found.

3. Residual gas analysis has been performed on large pores found in electron beam welded CP-Ti. This confirms that hydrogen is the majority gas inside the pore; a small amount of CO_2 also exists.

4. EDS/WDS analysis shows that the pore edges are rich in oxygen, which may suggest that bubbles initiate from voids between the joint surfaces. Oxides at the void surfaces may contribute the higher amount of oxygen at pore edges.

5. Hydrogen may play a critical role in bubble growth due to its high mobility; this needs further investigation.

6. Dragging forces due to fluid dynamics may be the dominant effect causing bubble escape from the keyhole, by breaking through the keyhole wall. Different fusion zone profiles will display different force magnitudes, so that different porosity formation tendencies then arise.

4

Numerical Process Models for Electron Beam Welding

Summary

In this chapter, numerical process models are developed for electron beam welding, aiming to predict heat transport; this is a prerequisite for further investigation of other phenomena occurring during the process, such as hydrogen migration behaviour, and bubble formation. Numerical modelling is performed using two different approaches, involving (i) heat conduction modelling with a volumetric heat source model and (ii) a treatment of keyhole. The heat conduction modelling enables a transient three-dimensional thermal analysis on a large scale due to its high computational the efficiency, which is practical when the modelling of the complex phenomena inside the weld pool is not needed. The second approach, namely keyhole modelling, enables a more realistic representation of the process by taking account of the vapour keyhole inside the weld pool. Modelling results from this model shed light weld pool behaviour, which is crucial for the understanding of bubble formation and porosity formation.

4.1 Introduction

Since the welding parameters in the electron beam welding process can be easily controlled and monitored by computer, fundamental understanding of the influence of welding parameters,

effects on the electron welding process has an obvious reward: it provide guidance for the optimisation of the welding parameters. In past decades, numerical simulation and process modelling has advanced significantly [45, 46, 47, 56, 57, 58, 74, 114, 115]. Some complicated models have been developed which allow the implementation of mass and energy transport calculations [56, 57, 115]. More recent studies on laser welding modelling have greatly advanced the modelling capability for this very complex problem but it should be noted that keyhole dynamics modelling is still a challenge [58, 74].

When the fluid flow effect inside the weld pool can be neglected, volumetric heat source models are commonly used in welding process modelling [6, 48, 49]. Ideally, parameters used in the heat source models can be obtained directly from the welding parameters. However, in current volumetric heat source models input parameters are obtained from empirical studies. This is because the heat input varies in a complex manner dependent upon the materials and the electron beam welding parameters.

The keyhole phenomena have been considered to play a critical role in the energy transport during electron beam welding process. Due to the very complex physical phenomena involved, the keyhole effect was either neglected or oversimplified. In previous work, analytical or semi-analytical ways have been used, aiming to predict temperature field and penetration depth [35, 42, 116, 117]. Dowden [60] constructed a general model to estimate the motion of liquid and vapour in the keyhole. This has been furuther studied by Matsunawa & Semak [66, 67], accounting for the drilling effect due to recoil vapour pressure. 3D weld pool and keyhole geometry was determined by using the model constructed by Solana & Ocana [68], in which Fresnel and inverse Bremsstrahlung absorption were considered and the keyhole wall was treated as a free boundary. Fabbro & Chouf [69] calculated the inclined keyhole wall by considering the sideways melt displacement, multiple reflection and a ray tracing procedure. Models constructed by Ki *et al* [56, 57, 71], Dasgupta *et al* [72], Cho *et al* [73], Geiger *et al* [58] and Otto & Schmidt [74] are capable of doing 3D transient heat and mass transfer calculations by considering surface

tension induced thermo-capillary, recoil vapour pressure and surface evaporation. But at the same time, these models make the computation very expensive. More recently. a combined analytical and numerical approach has been demonstrated by Rai & Debroy [51, 53, 54, 75],which show that appropriate balance of accuracy and computational time has been achieved.

In this chapter, two different approaches have been developed for modelling of electron beam welding process. One is the heat conduction modelling using a volumetric heat source model, which is developed to achieve high computational efficiency for transient three-dimensional calculation when the convection inside weld pool can be neglected. The other approach is keyhole modelling, which is developed to investigate more details of the weld pool formation during the process.

4.2 Modelling the Heat Source

A description of the heat deposition to the work-piece from the electron beam is the key factor for models of the electron beam welding process. This section details the volumetric heat source models which have been used.

4.2.1 Three-Dimensional Conical (TDC) Heat Source Model

A three dimensional conical (TDC) model is widely used in heat transfer calculations for electron beam and laser beam welding. Figure 4.1 (a) illustrates the standard TDC model, in which the heat intensity is distributed in a Gaussian form as according to [48]

$$Q(r,z) = Q_0 \exp\left\{-\frac{3r^2}{r_0^2(z)}\right\} \tag{4.1}$$

$$r_0(z) = r_e + \frac{r_i - r_e}{z_i - z_e}(z - z_e) \tag{4.2}$$

where Q_0 is the maximum value of the heat intensity, $r_0(z)$ is the Gaussian distribution parameter and r_e, r_i are the radial coordinate at the top and bottom planes respectively, and z_e, z_i are the z coordinates at the top and bottom plane respectively.

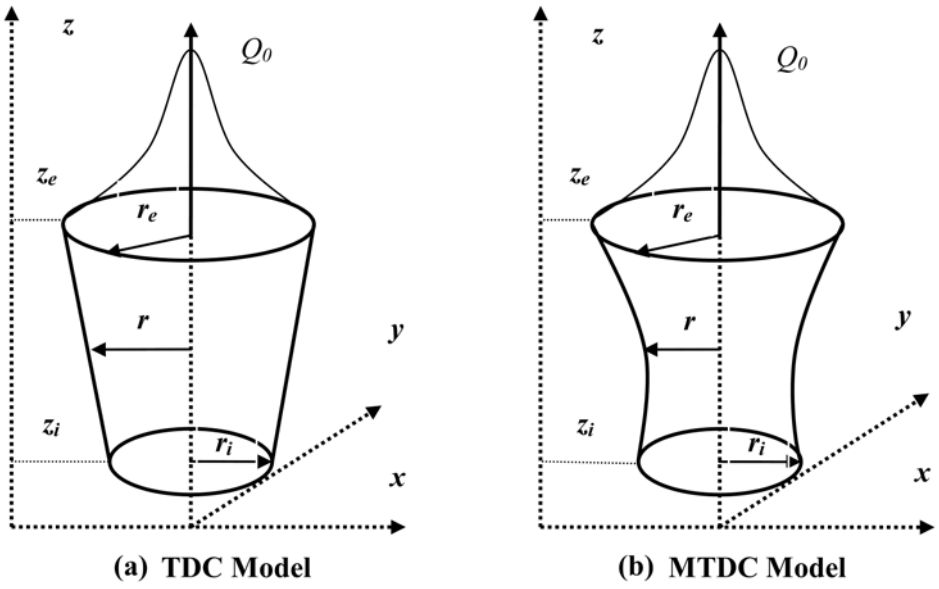

Figure 4.1: Schematic illustration of (a) standard three dimensional conical (TDC) heat source and (b) modified three dimensional conical (MTDC) heat source model.

In the standard TDC model, the maximum heat intensity Q_0 is constant at each plane perpendicular to the thickness direction (z-direction), and the Gaussian distribution radius $r_0(z)$ decreases linearly along the thickness direction. In each plane perpendicular to the z-direction the energy input is obtained by integrating equation (4.1) consistent with

$$Q(z) = \int_0^{2\pi} \int_0^{r_0(z)} Q_0 \exp\left\{-\frac{3r^2}{r_0^2(z)}\right\} r dr d\theta = \frac{\pi Q_0 \left(1 - e^{-3}\right)}{3} r_0^2(z) \tag{4.3}$$

For the total energy input in the workpiece, integration equation (4.3) along the thickness direction yields:

$$Q_v = \frac{\pi Q_0 \left(1 - e^{-3}\right)}{3} \int_{z_i}^{z_e} r_0^2(z) dz \tag{4.4}$$

The energy balance yields,

$$Q_v = \eta U I \tag{4.5}$$

where η is the power efficiency and U, I are the electron beam accelerating voltage and electron beam current, respectively. Combining equation (4.4) and equation (4.5), we can define the

maximum intensity Q_0 according to

$$Q_0 = \frac{9\eta UIe^3}{\pi(e^3-1)} \times \frac{1}{(z_e - z_i)(r_z^2 + r_z r_i + r_i^2)} \tag{4.6}$$

Hence the energy distribution function inside the heat source domain can be written as:

$$Q_0(r,z) = \frac{9\eta UIe^3}{\pi(e^3-1)} \times \frac{1}{(z_e - z_i)(r_z^2 + r_z r_i + r_i^2)} \times \exp\left\{-\frac{3r^2}{r_0^2(z)}\right\} \tag{4.7}$$

In the TDC model, the Gaussian distribution parameters are linear functions of the weld thickness as shown in equation (4.2), so that the predicted fusion boundaries at the cross section are linear. However, in practice this is not always the case, as it can be seen in Chapter 3, where curved fusion boundaries of waist-type are observed. To account for curved fusion, the linear decay rule of the Gaussian distribution parameters along the thickness direction needs to be altered in a modified TDC model. This is described in the following sections.

4.2.2 Modified Three Dimensional Conical (MTDC) Heat Source Model

One possible reason for the formation of curved fusion boundaries is the beam focussing condition, which leads to an effective change in beam radius along the thickness direction. Another possible reason is the strong convection within the weld pool, which causes the fusion zone to spread. To model the curved fusion zone profile well, a varying effective beam radius is used to describe the energy deposited; this is typically implemented by varying the Gaussian distribution radius in the heat source model. For example in the MTDC model, the linearly decayed Gaussian distribution radius of equation (4.2) is replaced by the following equation:

$$r_0(z) = f(z) \qquad (z_i \le z \le z_e) \tag{4.8}$$

where $f(z)$ is an arbitrary function correlating the Gaussian distribution radius to the coordinates in the thickness direction. The terms z_e, z_i are again the z coordinates at the top and bottom surfaces respectively. Similarly, in each plane perpendicular to the z-direction the energy input is modelled as,

$$Q(z) = \int_0^{2\pi}\int_0^{r_0(z)} Q_0 \exp\left\{-\frac{3r^2}{f^2(z)}\right\} r dr d\theta = \frac{\pi Q_0\left(1-e^{-3}\right)}{3} f^2(z) \tag{4.9}$$

For the total energy input in the workpiece, integration along the thickness direction, yields:

$$Q_v = \frac{\pi Q_0 \left(1 - e^{-3}\right)}{3} \int_{z_i}^{z_e} f^2(z) dz \tag{4.10}$$

The maximum intensity Q_0 is,

$$Q_0 = \frac{9\eta U I e^3}{\pi(e^3 - 1)} \times \frac{1}{\int_{z_i}^{z_e} f^2(z) dz} \tag{4.11}$$

Therefore, the energy distribution function can be written as:

$$Q_0(r, z) = \frac{9\eta U I e^3}{\pi(e^3 - 1)} \times \frac{1}{\int_{z_i}^{z_e} f^2(z) dz} \times \exp\left\{-\frac{3r^2}{f^2(z)}\right\} \tag{4.12}$$

In principle, the MTDC model can be used to fit arbitrary fusion boundaries precisely by choosing appropriate function $f(z)$. In practical $f(z)$ is chosen as a simple function for the sake of simplicity of integration. A polynomial function is typical.

4.2.3 Determination Parameters in Heat Source Model

Ideally, parameters used in the heat source model should be either electron beam welding parameters or material properties. However, due to the complexity of the interaction of electron beam welding and the workpiece, some empirical parameters are necessary. These are typically estimated from the fusion zone profile obtained by metallographic section of the welded samples. The parameters used in the heat source model are manually optimised by comparing the measured fusion zone profile to provide the optimum agreement. So in these models, it is not surprising that a good agreement is achieved between the model and the experimental results. To construct a constitutive electron beam process model, interaction between the electron beam and workpiece needs to be taken into consideration, *e.g.* the evaporation, fluid flow and keyhole etc.

The procedure for the heat source fitting in this work is briefly described below:

Step1: Get metallographic section and identify the FZ and fusion boundary by etching.

Step2: Measure the FZ width at different thickness position.

Step3: Plot the FZ width against z coordinates (thickness direction) in Matlab.

Step 4: Perform the polynomial fitting on the curve generated in Step 3, which gives function *g(z)*, describing the fusion width various z coordinates in the thickness direction.

Step 5: Using function *g(z)*, determine the Gaussian distribution radius *f(z)* in the MTDC model.

Step 6: Iterate power efficiency η from an initial value 0.8 to calculate the power density distribution from equation (4.12).

Step 7: Compare the calculated cross section with the metallographic section obtained in Step 1. Depending on the comparison results, either increase or decrease the power efficiency η, go to Step 6, do the next iteration calculation until a reasonable agreement between the calculated and measured weld regions has been reached.

4.3 Keyhole Profile Calculation

The keyhole effect is crucial to understand the deep penetration and weld pool formation. But due to the intensive evaporation and interface evolution which occurs, modelling of the keyhole dynamics is still a challenge. In this work, the keyhole modelling strategy is mainly based on Kaplan's model [55]. A brief description of the modelling procedure is presented next.

4.3.1 Assumptions for Keyhole Modelling

To simplify the interaction between the electron beam and workpiece and to avoid the modelling of phase transformations induced solid/liquid and liquid/vapour interfaces, the following assumptions are made:

1) Cross section of the electron beam perpendicular to the welding thickness direction is circular and the energy density obeys a Gaussian distribution.

2) The keyhole is in a quasi-steady state, and the energy is balanced at the keyhole wall.

3) Vapour flow and convection inside the weld pool is neglected.

4) The keyhole profile is calculated only at longitudinal cross section through the weld centre

line, which is a symmetry plane.

4.3.2 Electron Beam Focus Properties

Estimation of the optical properties of the electron beam are essential for the modelling of keyhole phenomena, as these determine the electron beam propagation along the beam axis direction. This requires the knowledge of the electric and magnetic fields influencing the electron beam. From previously reported electron beam diagnostic and characterisation results [118, 119], the electron beam radius and shape propagation vary in a very complicated manner, which is highly dependent on the specific design of the electron beam machines. One important parameter used to describe approximately the electron beam focus is the aperture angle, which is determined by the aperture size and focus distance [5]. Figure 4.2 illustrates the cross section of the focussed electron beam along the beam axis direction. The term d_A is the aperture size, F_d is the focus

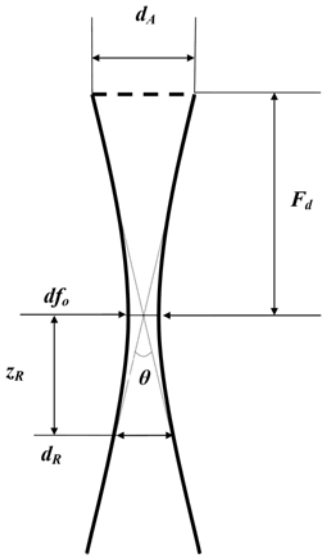

Figure 4.2: Waisting of the electron beam at focus showing the definition of aperture angle towards the workpiece.

distance and df_0 is the beam size at the waist (focus plane), θ is the aperture angle, and z_R is the

Rayleigh range, which is the distance along the propagation direction of beam from the waist to the place where the area of the cross section is doubled. When the beam focus plane is very close to the workpiece, the beam radius propagation needs to be carefully considered. In this study, the electron beam is simplified as a Gaussian beam, and the beam radius propagation along the axis direction is fitted by a parabolic equation. If z_0 is the coordinate of the focus plane in the axis direction, the beam radius $r(z)$ along the beam axis direction can be written as

$$r(z) = \frac{df_0}{2}\sqrt{1 + \left(\frac{z - z_0}{z_R}\right)^2} \tag{4.13}$$

Consistent with equation (4.13), beam waist size df_0 and Rayleigh range z_R need to be determined. In this study, these parameters are estimated by beam focus measurement, which as detailed in section 4.6. The waist beam size is assumed to be the narrowest fusion width. After finding the beam waist size, the Rayleigh range is obtained by solving equation (4.13), by substituting the aperture size and focus length into the equation.

After determining the beam profile, the Gaussian beam intensity can be expressed as [55]:

$$I(r, z) = I_0 \left(\frac{r f_0}{r(z)}\right)^2 \exp\left\{-\frac{2\mathrm{r}^2}{\mathrm{r(z)}^2}\right\} \tag{4.14}$$

where $I(r, z)$ is the beam intensity distribution, I_0 the peak intensity, $r f_0$ the focal radius, $r(z)$ depth dependent local beam radius, and r the distance to the beam axis. The peak intensity I_0 is defined as

$$I_0 = \frac{2P}{\pi(r f_0)^2} \tag{4.15}$$

where P is the electron beam power.

4.3.3 Energy Balance at Keyhole Wall

In this study, the energy at keyhole wall is balanced by the energy absorbed from the incident beam and the rate of energy flow into the surrounding material. Evaporation and convection inside the weld pool is neglected. To simplify the calculation, the keyhole profile is calculated only at the longitudinal section through the weld centre line, which is the symmetry plane of

three-dimensional temperature filed. A schematic illustration of the heat balance of the keyhole wall at this plane is shown in Figure 4.3.

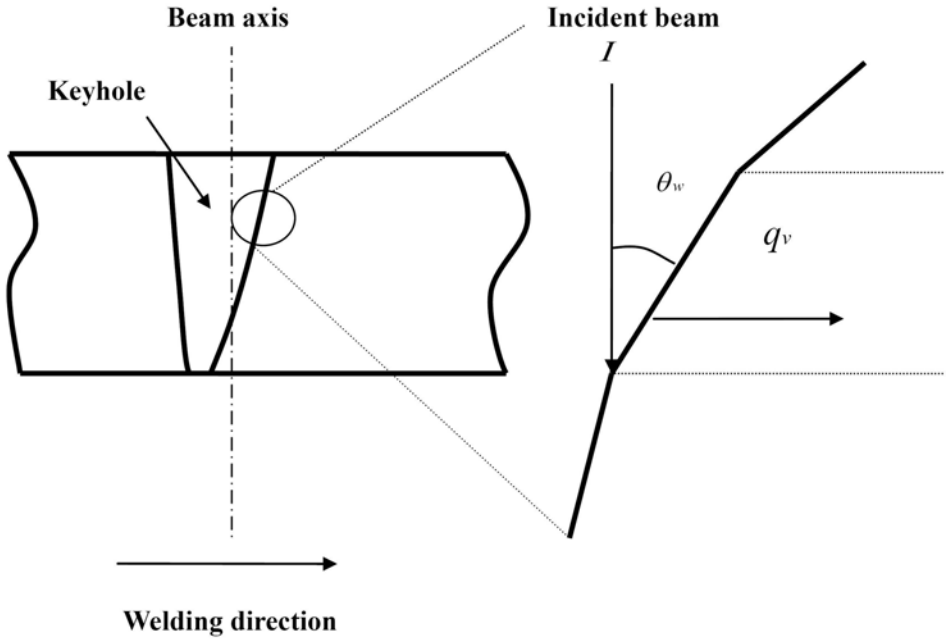

Figure 4.3: Schematic illustration of heat balance at keyhole wall in the longitudinal section through the weld centreline.

The energy balance at keyhole wall is

$$\tan(\theta_w) = \frac{q_v(r,v)}{I_\alpha(r,z)} \tag{4.16}$$

where θ_w is the local wall angle, $q_v(r,v)$ is energy flow into the surrounding material, $I_\alpha(r,z)$ is the absorbed energy from the incident electron beam, which is determined both by the beam intensity and absorptive coefficient η consistent with

$$I_\alpha(r,z) = \eta I(r,z) \tag{4.17}$$

In this study, the temperature field at the longitudinal section through the weld centreline is estimated by using Rosenthal's analytical solution [46] of the temperature field for a moving line source in cylindrical coordinates (r, φ, z) with r and φ being the equivalent polar coordinates

corresponding to x and y. The temperature in the workpiece $T(r, \varphi)$ is then

$$T(r, \varphi) = T_a + \frac{P}{2\pi\lambda_k} K_0\{P_e' r\} e^{-P_e' r \cos\varphi} \tag{4.18}$$

with modified Peclet number

$$P_e' = \frac{v}{2\kappa} \tag{4.19}$$

where T_a is the ambient temperature, P is power per unit depth of the line source, λ_h is the heat conductivity, and K_0 is the modified Bessel function of second kind and zero order, defined by:

$$K_0(x) = \sqrt{\frac{\pi}{2x}} \times \exp(-\mathrm{x}) \tag{4.20}$$

The heat flow $q_v(r, z)$ can be determined by Fourier's law of of heat conduction which can be simplified by considering the radial component:

$$q(r, z) = -\lambda_h \nabla T \approx -\lambda_h \frac{\partial T}{\partial r} \tag{4.21}$$

The spatial derivation of equation (4.18) with respect to leads to r

$$\frac{\partial T}{\partial r} = \frac{P}{2\pi\lambda_k} P_e' e^{-P_e' r \cos\varphi} \left[-K_0\{P_e' r\} \cos\varphi + K_0'\{P_e' r\} \right] \tag{4.22}$$

The calculation was performed layer by layer in the thickness direction. The keyhole wall angles were calculated from top surfaces downwards point-by-point in each layer. The keyhole wall positions (front wall and rear wall) in the next layers were determined from the previous keyhole positions and their local keyhole angles. To calculate the keyhole size on the top surface, line source power at the top surface needs to be determined. The line source power is different from the beam power, which is related to the penetration depth. To determine the line energy power at the top surface, the line energy power at the top surface is estimated by the beam power divided by penetration depth. The initial penetration depth is a guessed value. The calculation is an iterative process, which will stop when the penetration depth reach the stable value. The calculation procedure is illustrated in Figure 4.4. Gas phases and the plasma effect were neglected in this study.

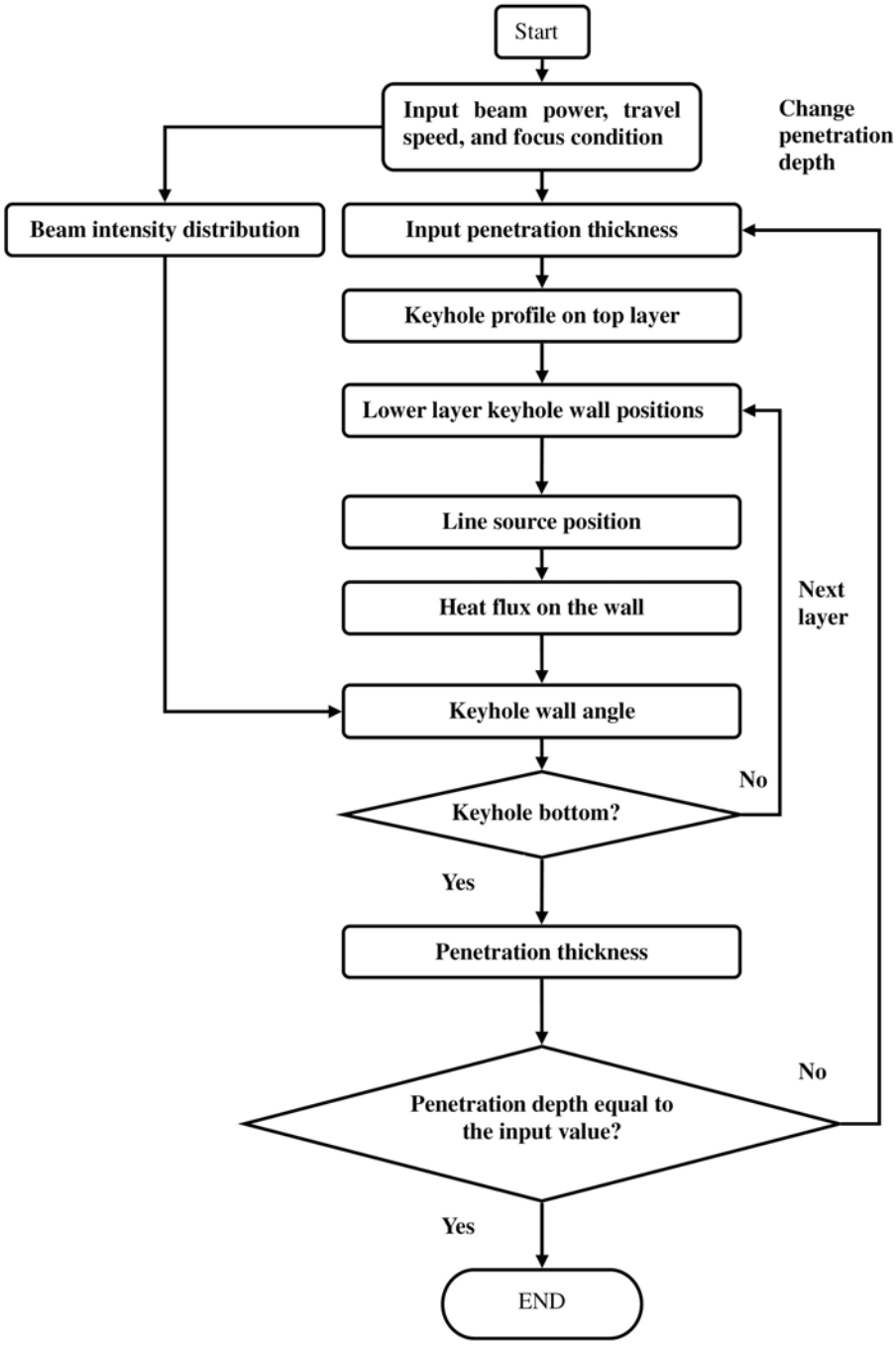

Figure 4.4: Flow diagram for the keyhole profile calculation.

4.4 Material Properties

Temperature dependent material properties used in the calculations are for the Ti-6Al-4V alloy and are taken from literature [25]. The temperature dependent data density, heat capacity and heat conductivity are illustrated in Figure 4.5. In the keyhole modelling, some temperature independent material properties are also used. The material data used in the keyhole modelling are taken from literature [54], and are listed in Table 4.1.

Table 4.1: Material properties of Ti-6Al-4V used in the keyhole calculations.

Boiling temperature,(K) [120]	3315
Density, (kg m^{-3}) [25]	4200
Specific heat of solid, (J $kg^{-1}K^{-1}$)[25, 121]	670
Heat conductivity, (W m^{-1} K^{-1}) [25]	21
Electron beam absorption coefficient η,[122]	0.25

4.5 Mesh Generation

The test piece used in this study is a simple plate, the dimensions chosen to ensure that the welding pool can reaches a steady state, with the calculation domain kept as small as possible to reduce the calculation time. The dimensions are 4 mm in thickness, 50 mm in width and 100 mm in length. The mesh was generated by using commercial software VisualMesh (Version 6.0). The mesh size is graded in the horizontal plane (x-y plane) and taken to be uniform along the thickness direction. A fine mesh is needed close to the joint edges to capture the characteristics of heat deposition from the electron beam. In the fine mesh region, the mesh size along the welding direction and transverse direction is limited by the size of the electron beam. Generally, at least three elements are required across the heat source region. In the thickness direction, a coarser mesh may be used to reduce the total number of elements. An example of a mesh used in this study is illustrated in Figure 4.6. The mesh were exported to the commercial software Sysweld to perform the finite element calculation.

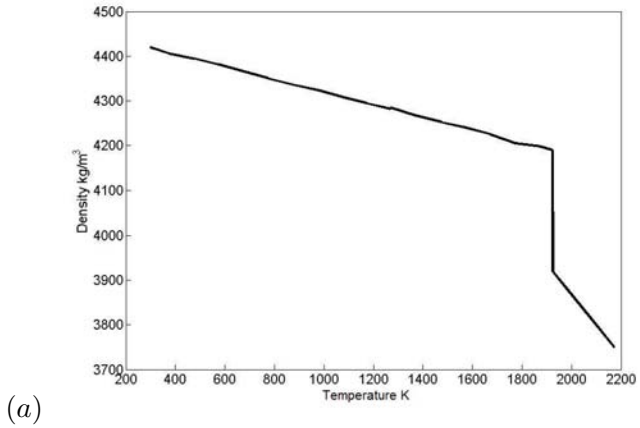

(a)

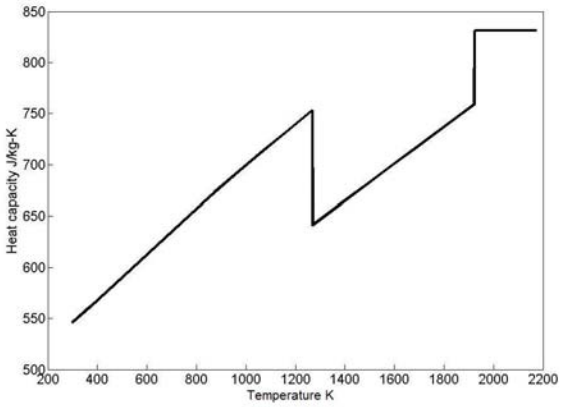

(b)

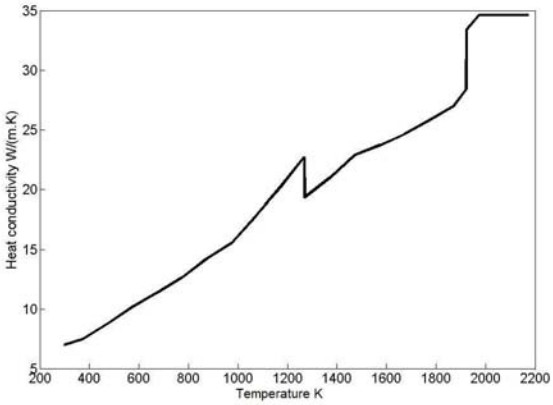

(c)

Figure 4.5: Temperature dependent material properties of Ti6Al4V: (a) density, (b) heat capacity and (c) heat conductivity [25].

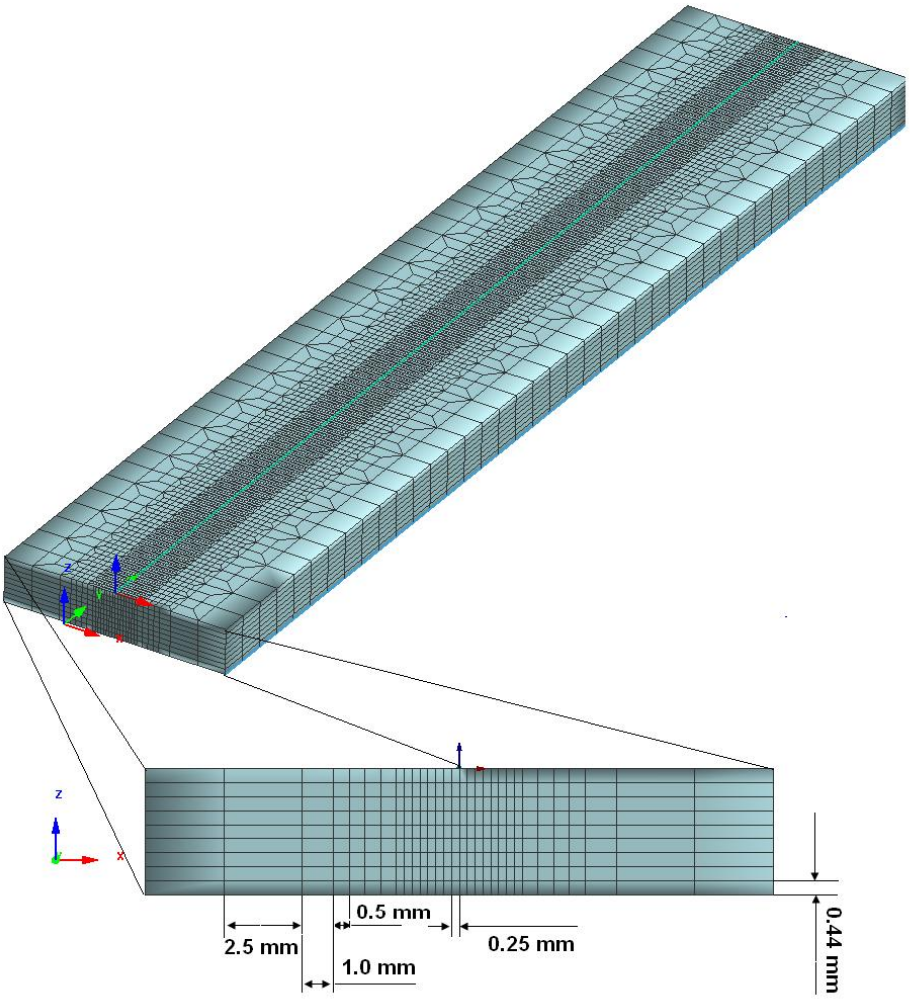

Figure 4.6: Graded mesh used in this study.

4.6 Beam Focus Point Measurement

The focus point is one of the most important parameters in the electron beam welding process, since it affects the shape of the melt zone and the penetration depth. The common way to change the focus point is to adjust the focus current, keeping the working distance constant. By changing the focus current the focus point can be above the workpiece surface (overfocusing), inside the workpiece (sharp focus) and below the workpiece (underfocusing). To investigate the correlation between focus position and weld fusion profile, the focus point has been measured in this study within a small range of variation of focus current. The measurement results are

expected to provide useful information for selection of parameters used in the heat source model. The setup of the experiment is illustrated in Figure 4.7. Two plates were welded at different working distances. In each welding trial, the focus current was decreased linearly from 2380 mA to 280 mA with the beam moving within a distance of 240 mm during the welding process. The working distance was chosen between the minimum and maximum focus distance due to the changing focus current. In each plate, the welds undergo an overfocusing, sharp focusing and underfocusing welding process, which leads to a variation in fusion zone width. The weld beads width is expected to decrease when the beam changes from the overfocusing condition to the sharp focus condition, and increase again during the welding process as the beam tends to the underfocusing condition. The narrowest weld bead region is associated with the focus point. As the working distance is different in the two testing plates, the focus point will occur at different distances from the weld start position. Since the focus distance is inversely proportional to the square of the focus current [5], the relation between focus current and focus distance can be obtained from the measured two focus points.

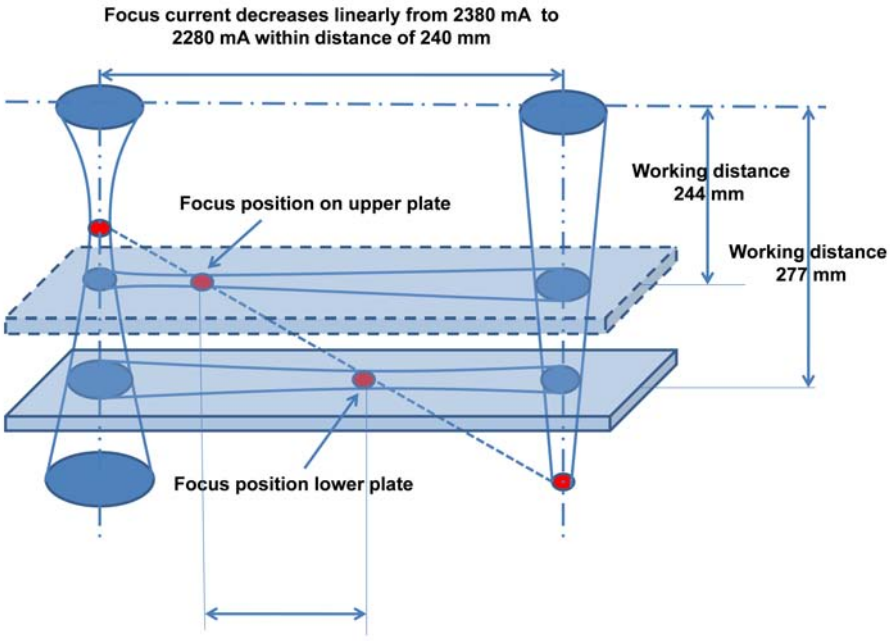

Figure 4.7: Measurement of focus position.

4.7 Beam Probing Measurement

Beam geometry is also very important during the electron beam welding process. In order to provide uniform and reproducible fusion zones and penetration depths during electron beam welding, beam geometry, energy distribution and the interaction between the beam and work-piece need to be investigated. In this work, beam probing measurements using slit sensors were performed. A schematic illustration is shown in Figure 4.8, in which the electron beam is rotating at high speed, crossing two slit sensors arranged at an angle of 90°. When the slit sensor is crossed, some of the electrons can flow through the narrow slit. These are picked up by a Faraday cup, then diverted over a precision resistor. The time progressing signal intercepted at

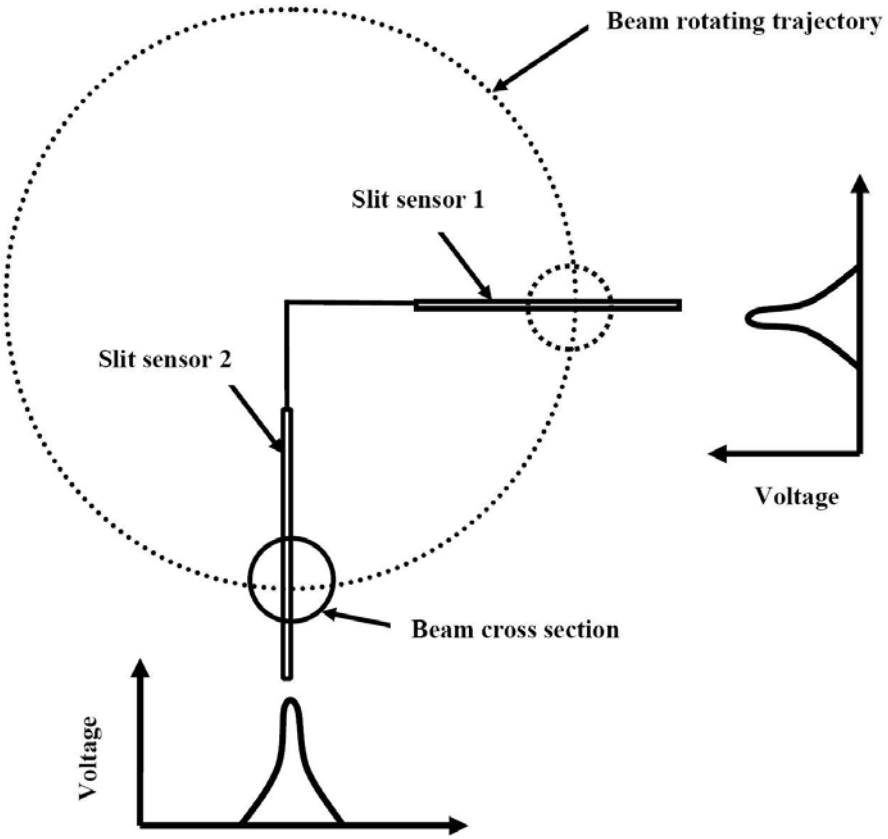

Figure 4.8: Electron beam probing by using slit sensor.

the resistor corresponds to the intensity distribution of the electron beam in the scanning path. Due to the specific arrangement of the two slit sensors, the intensity distribution at the electron beam cross section can be scanned in two directions. Ideally, the intensity distribution profiles in these two directions are identical when the electron beam has a circular cross section, in which case the intensity has a Gaussian distribution. If the electron beam rotating speed is known, the beam radius can also be estimated from the width of the detected intensity distribution profile.

4.8 Metallographic Sectioning

Metallographic examination of electron beam welds under different welding parameters was performed to determine the fusion zone and heat affected zone profiles. Details of the metallographic sample preparation can be found in Chapter 3. The polished surfaces were etched with Kroll's reagent (2 ml HF, 4 ml HNO_3 and 1000 ml H_2O), following the methods advised for titanium alloys [123]. The measured fusion zone profiles were used to determine the parameters for the volumetric heat source models in the following way. First, since the fusion width normally changes along the weld thickness direction, a function $g(z)$ was constructed to correlate the fusion width with z-coordinates along the weld thickness direction; the function $g(z)$ can be mapped to the function $f(z)$ defined in equation (1.8), which defines the variation of Gaussian distribution parameters along the weld thickness direction. The easiest way to obtain function $f(z)$ is to do a linear translation from the function $g(z)$. To get the best agreement between the calculated fusion zone profiles and the measurement results, mapping from function $g(z)$ to function $f(z)$ needs to be optimised; this is an iterative process. After choosing the appropriate parameters in the heat source model, the modelling results obtained from the chosen heat source model were further evaluated by comparing the heat affect zone profile and weld pool dimensions etc. The details are given in the following section. A longitudinal section through the weld bead centre is also examined to provide melt front information for validation purposes.

4.9 Results and Discussion

Using the above approaches, characterisation and modelling of electron beam welding of a 4-mm thick Ti-6Al-4V alloy plate butt joint was performed. The results are detailed in the following sections.

4.9.1 Focusing Position and Weld Zone Profiles

To investigate the effect of beam focus position on weld zone profiles, two test plates were welded at different working distance as shown in Figure 4.7. The welds were sectioned at different locations from the weld start. The results are shown in Figure 4.9.The upper plates were welded at a working distance of 244 mm, as it can be seen in Figure 4.9 (a), with the beam moving forwards and the focus current decreasing linearly. The fusion zone width was found to decrease initially, and then increase, which indicates the welding process undergoes a slight overfocusing, sharp focusing and then under focusing condition. The narrowest fusion zone is found around 60 mm from the start position, which can be assumed to be the focus position. By checking more metallographic sections, the focus position was located at 58 $\pm$ 5 mm from the weld start position. Similarly, the fusion zone changes in the lower plate, which was welded at working distance at 227 mm, are shown in Figure 4.9 (b). Once again, the welding process undergoes overfocusing, sharp focusing and slight underfocusing conditions. The narrowest fusion zone is found 180 mm away from the weld start. More metallographic sections around this region have been checked with the results confirming the focus position to be at 218$\pm$5 mm from the weld start. From the above testing results, the two focus distances have been found. To estimate the relationship between the focus current and focus distance, the estimate focusing position is taken as 60 mm away from the weld start, and the focusing distance is taken as 246 mm, which is in the middle of the plate. Similarly the focusing position is taken as 220 mm away from the weld start, and focusing distance assumed to be 279 mm. Due to the linear decrease of focusing current from 2380 mm to 2280 mm within a distance of 240 mm, the focus current at

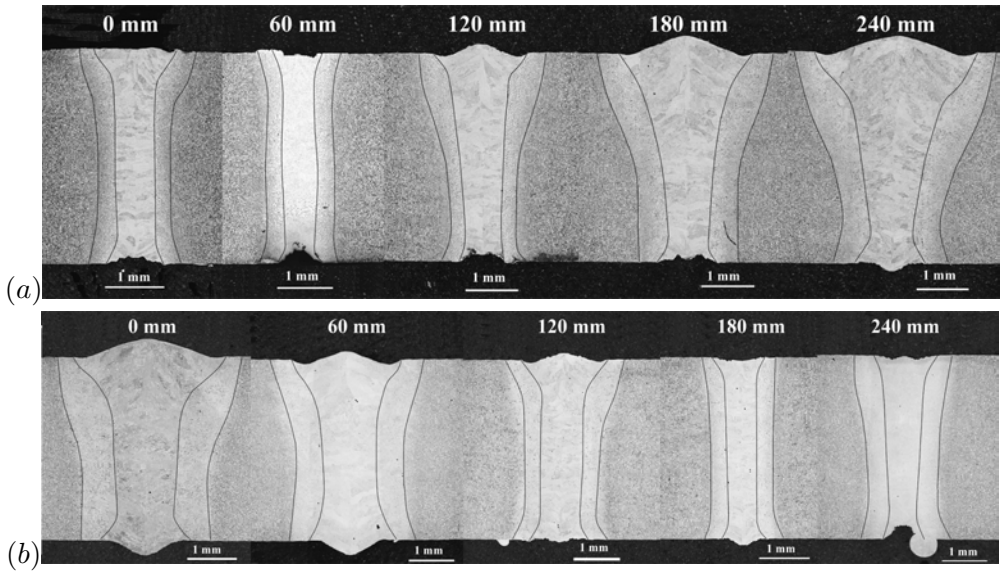

Figure 4.9: Cross sections located at different distance from the start of the welds designed for beam focus measurement: (a) upper plate, welded at working distance at 244 mm; (b) lower plate, welded at working distance of 277 mm.

the position of 60 mm away from the start of weld in the upper plate is around 2355 mA, while the focus current in the lower plate 220 mm away from the start of weld is 2288 mA. Since focus distance is inversely proportional to the focus current, this can be written as

$$f_d(I) = \frac{a}{I^2} + b \tag{4.23}$$

where $f_d(I)$ is the focus distance at give specific focus current I and, a and b are constants which depend on the construction of electron beam machine. Since we already know two focus distances at specific focus currents, the two constants can be determined by solving the following equation set

$$\begin{aligned} f_d(2355) &= \frac{a}{2355^2} + b = 246 \\ f_d(2288) &= \frac{a}{2288^2} + b = 279 \end{aligned} \tag{4.24}$$

By solving the above equations, the focusing distance under specific range of focus current can be estimated. The results are shown in Figure 4.10. It can be seen that the focus distance decreases linearly with increasing focus current within the specific range used in the testing. The

narrowest fusion zone is 0.4 mm, which is taken as the focus radius of the electron beam at the focus plane. The focus position measurement results will be used to estimate the electron beam profile for the keyhole shape calculation which follows. It needs to be pointed out again that the beam profile is simplified and can be represented by equation (4.13), but in reality the beam cross section may be irregular and the energy distribution may be rather more complicated.

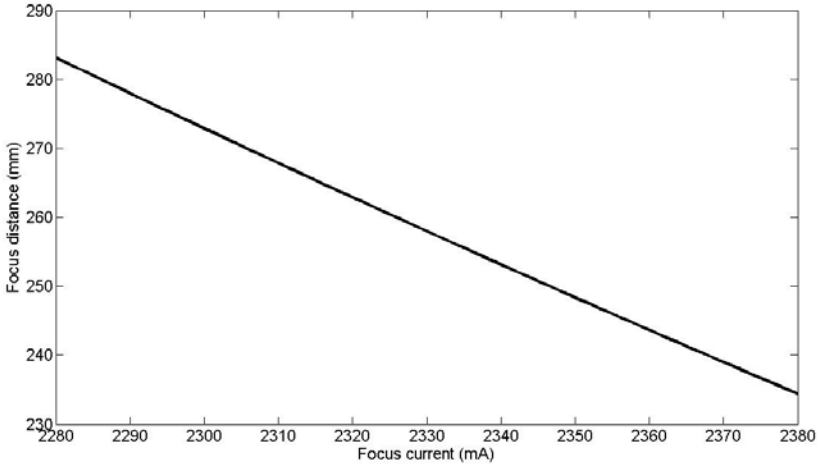

Figure 4.10: The relationship between the focus distance and the given specific range of focus current.

4.9.2 Beam Current Probing Results

The beam probing results are shown in Figure 4.11; two profiles obtained from the slit sensors are compared. Slight differences can be identified between the two profiles. Ideally, the areas under the two profiles should be the same because the scanning along the different direction should not affect the total electrons entering the slit sensors for a given electron beam. The differences may be caused by two reasons, the asymmetry of the electron beam shape or alternatively slight differences between the two slit sensors construction, such as the width of the slits. From the results it also can be seen that the width of the two profiles is almost the same, which indicates that the dimensions of the electron beam cross section along the two different directions are identical, and thus it is reasonable to treat beam cross section as circular. Since the exact beam

moving speed is not quantified, the beam radius size cannot be estimated from the current beam probing results, but this provides a method to estimate the electron beam profile by analysing different probing profiles at different working distances.

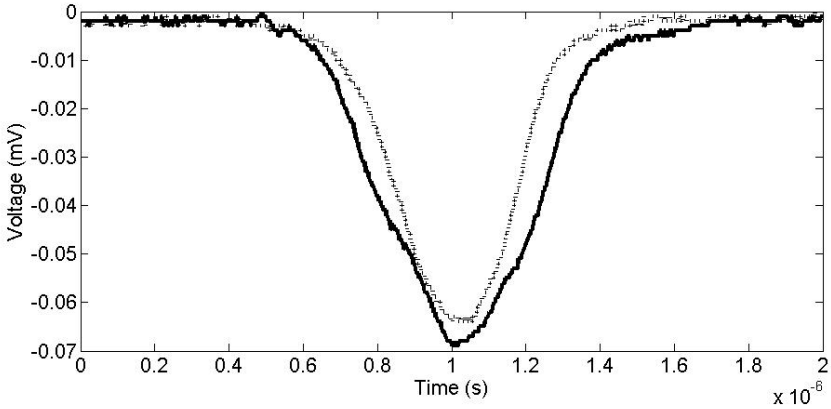

Figure 4.11: Beam probing profiles from two directions by using slit sensors.

4.9.3 Comparison of Calculated and Measured Weld Zone

Using the procedure described in section 4.2.3, the Gaussian distribution parameters *f(z)* were determined by fitting the fusion boundary, see Figure 4.12. The modelling results from the MTDC heat source model are presented and compared with the experimental results. The final fitted power efficiency is 0.85, which is a typical value as mentioned in refernce [5]. The experimental and predicted cross sections of the weld bead are shown in Figure 4.13. In Figure 4.13 (a) a curved fusion zone profile is predicted which shows reasonable agreement with the experimental results. Calculated temperature profile and measured microhardness across the weld region in the middle of thickness direction were plotted, see Figure 4.13 (b) and reasonable agreement were achieved in different weld regions. Figure 4.14 provides the weld pool dimensions predicted. The predicted weld pool length and width at top and bottom surfaces can be compared with the experimental measurement results in Figure 4.15. The weld pool was captured by deflecting the beam away from the joint line when the welding process reaches the steady state. The predicted weld pool at the top surface is 12 mm in length and of 3.2 mm

width, whilst at the bottom surface the figures are 7.5 mm and 1.68 mm respectively. These values are in reasonable consistent with measured results.

	X	Y
1	0.787643	0.0109098
2	0.792039	0.170336
3	0.795806	0.306988
4	0.801457	0.511965
5	0.796715	0.750866
6	0.803308	0.990006
7	0.809274	1.20637
8	0.826888	1.43436
9	0.844188	1.65097
10	0.871568	1.82226
11	0.899262	2.00494
12	0.938291	2.18786
13	0.977634	2.38216
14	1.01478	2.49675
15	1.05192	2.61135
16	1.08938	2.73733
17	1.13786	2.85216
18	1.18729	3.00115
19	1.23608	3.12737
20	1.2855	3.27637
21	1.34689	3.44838
22	1.44291	3.64388
23	1.49265	3.80426
24	1.55278	3.93072
25	1.58898	4.01115

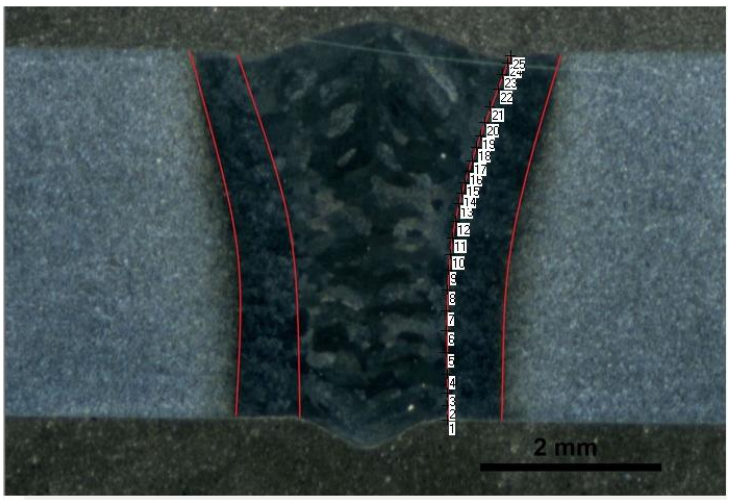

(a)

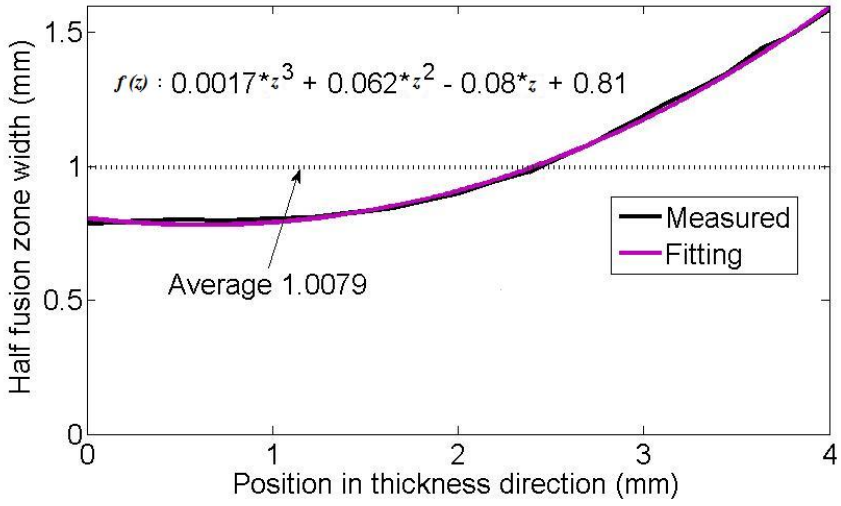

(b)

Figure 4.12: Heat source parameter fitting: (a) measure the fusion zone width at different thickness position; (b) fitting the curve to get Gaussian parameter distrubtion fuction f(z).

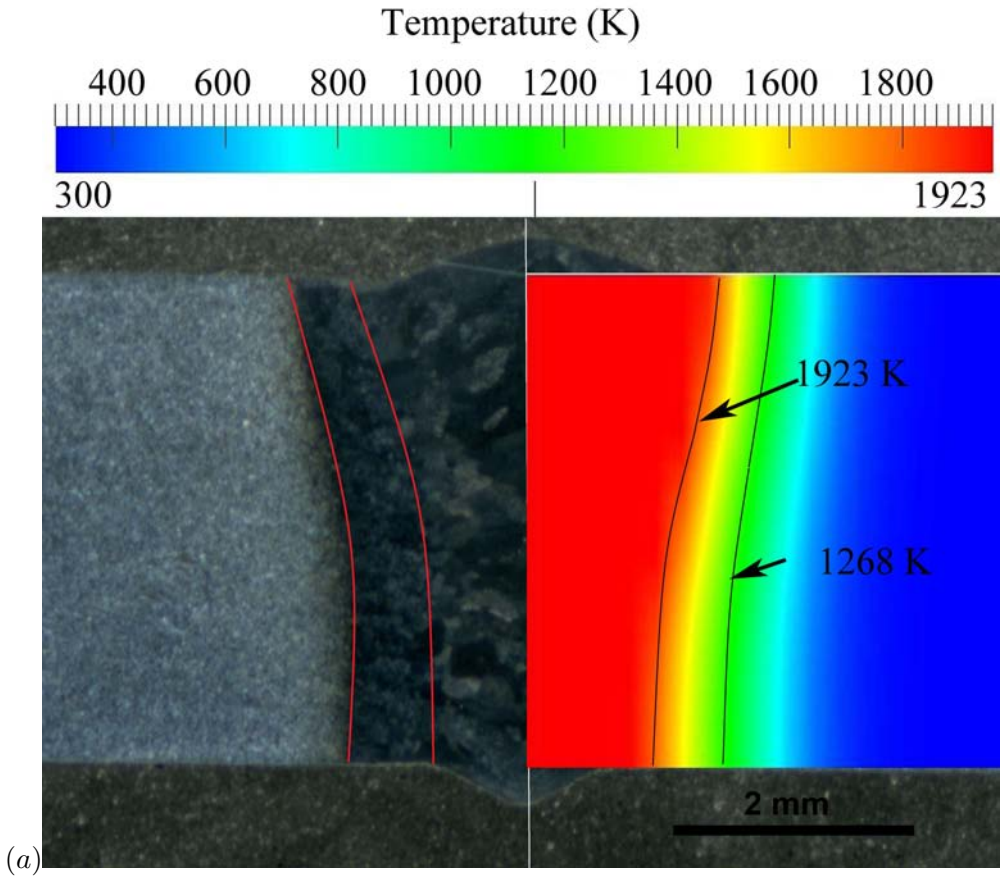

(a)

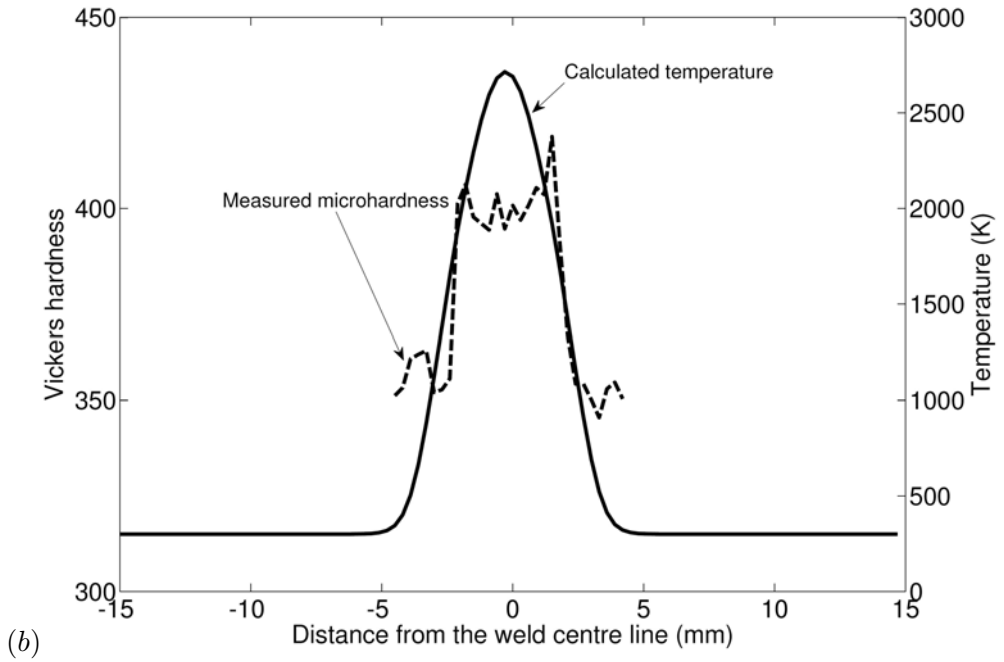

(b)

Figure 4.13: (a) measured and predicted cross section for plane near the electron beam centre; (b) measured microhardness profile and predicted temperature profile across the weld region in the middle of thickness direction.

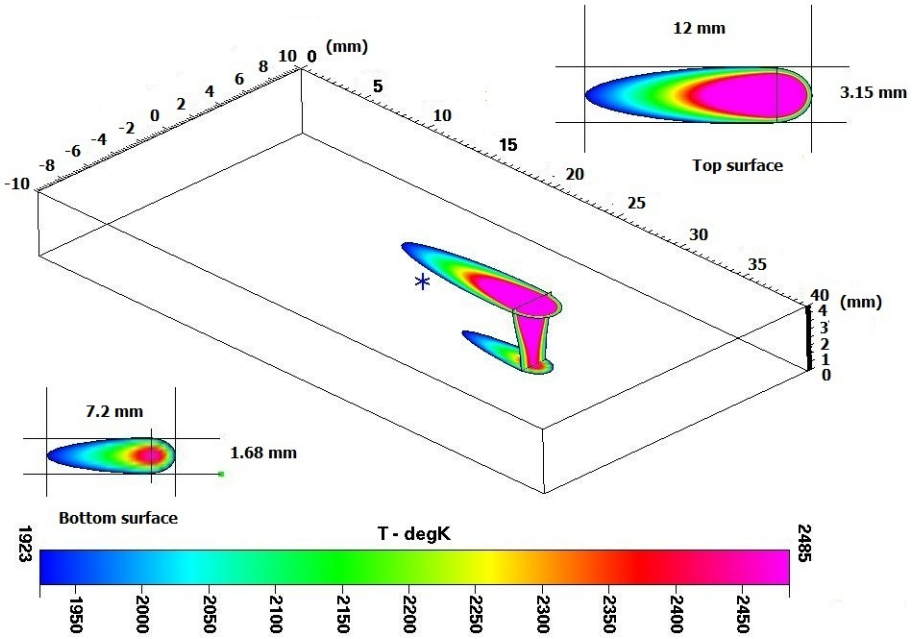

Figure 4.14: Predicted weld pool dimensions.

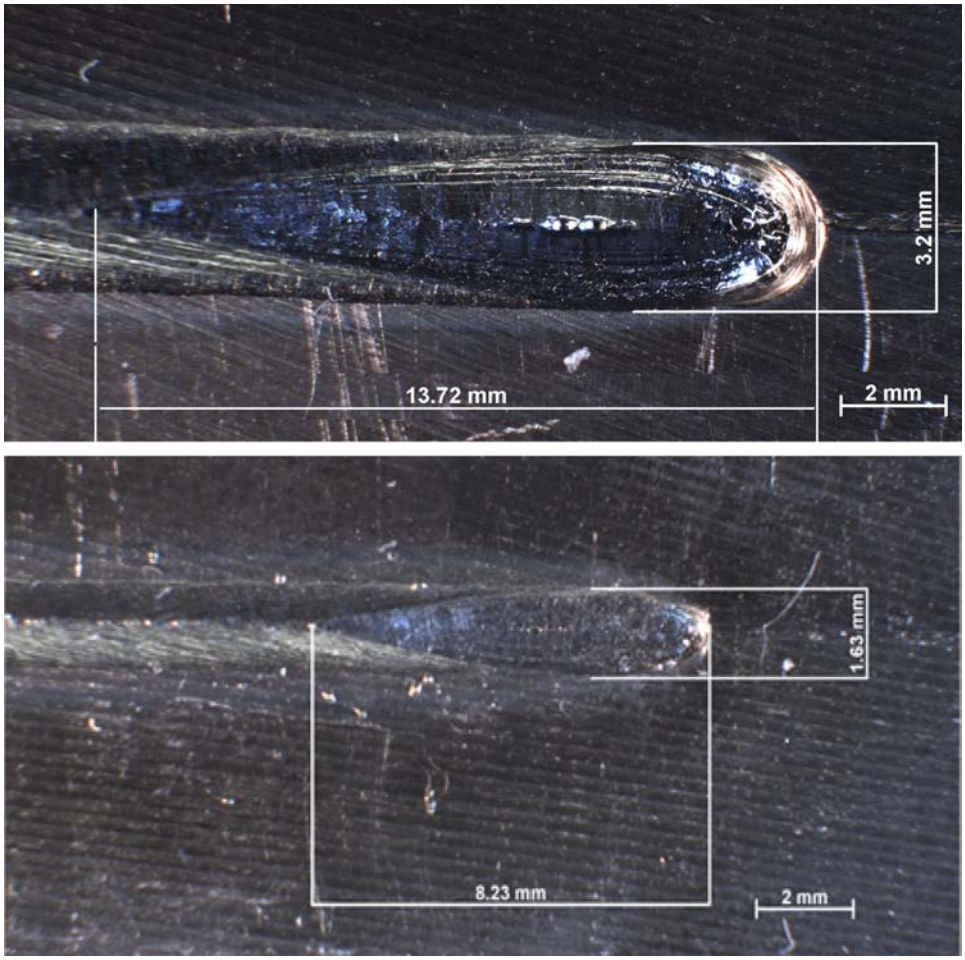

Figure 4.15: Measured weld pool dimensions at the top and bottom surfaces.

4.9.4 Keyhole Profile and Melting Front

The keyhole profile calculation was performed under identical welding conditions. The working distance is 277 mm and the focus current is 2380 mA. From previous beam focus and probing results, the focus radius of the electron beam at the focus plane is about 0.4 mm. The predicted keyhole profile is shown in Figure 4.16, in which it can be seen that the keyhole front wall is inclined as the beam moves forward; thus most of the beam impinges on the front wall. The energy flow at the front and rear wall and the beam intensity are shown in Figure 4.17. The results indicate that the heat flow at the keyhole front wall is much higher than that at the rear wall. The keyhole wall angles at the rear and front wall are shown in Figure 4.18. The result indicates that the front keyhole wall angle is slight larger at the rear wall, due to the effect of keyhole wall inclination as the beam moves forwards. In fact the front keyhole wall can be revealed by capturing the melting front profile. Figure 4.19 is the reconstructed X-Ray CT image, which shows the concave weld pool shape and a deep cavity formed as a result of an incompletely collapsed keyhole due to the fast cooling caused by deflecting the beam away at steady state. A longitudinal cross section through the weld centreline is shown in Figure 4.20. It can be seen that an inclined melting front is found, consistent with the calculation results. Higher optical magnification images in Figure 4.21, Figure 4.22, and Figure 4.23 show that at the melting front the liquid zone is very narrow, around 50 μm. It can be argued that the during the steady-state process, the liquid film at the melting front surrounding the keyhole may be wider, because during the experimental capture of the melting front, the cooling rate may not high enough to prevent liquid film from collapsing. If this is the case, one would expect that the liquid film thickness at the lower part of the weld beam would increase due to the accumulation of liquid metal falling down from the upper part, but this is not the case as it can be seen from the experimental results; the liquid region thickness at melting front is fairly uniform. Therefore it would seem that the liquid region at the melting front is very thin under the welding conditions employed.

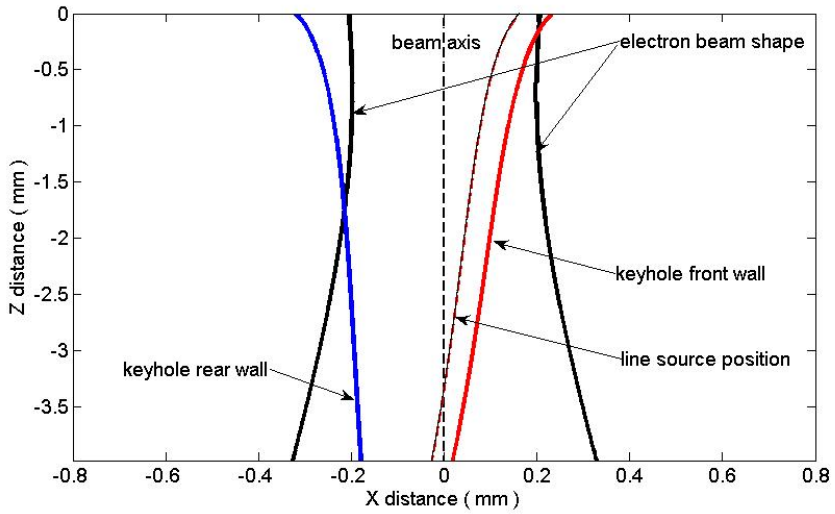

Figure 4.16: Calculated keyhole profile.

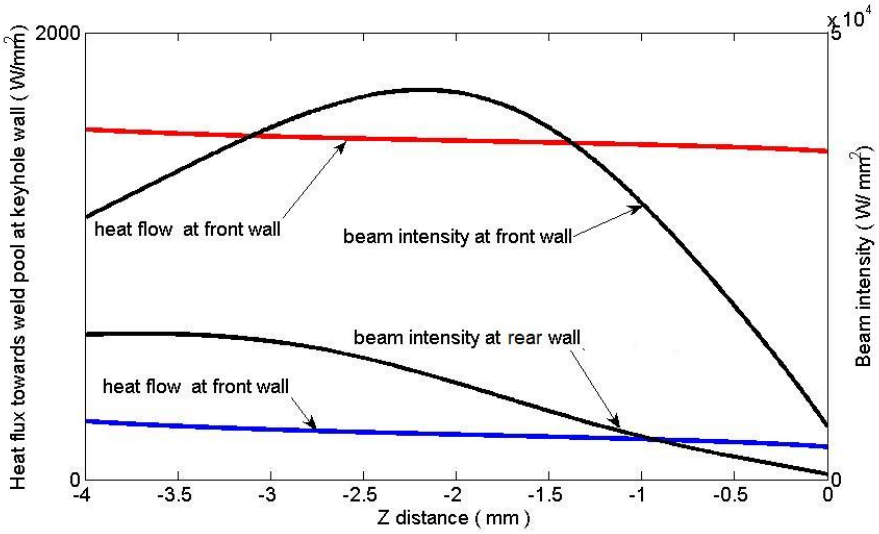

Figure 4.17: Calculated beam intensity and heat flow at keyhole wall.

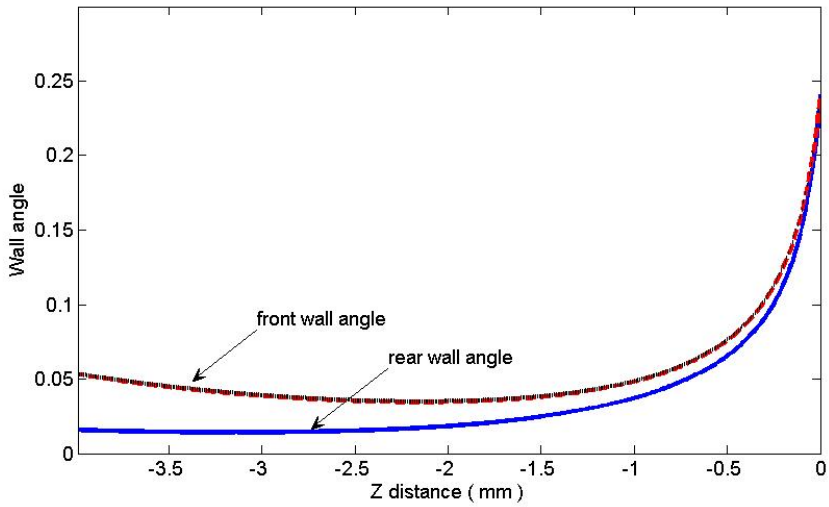

Figure 4.18: Calculated local keyhole angles.

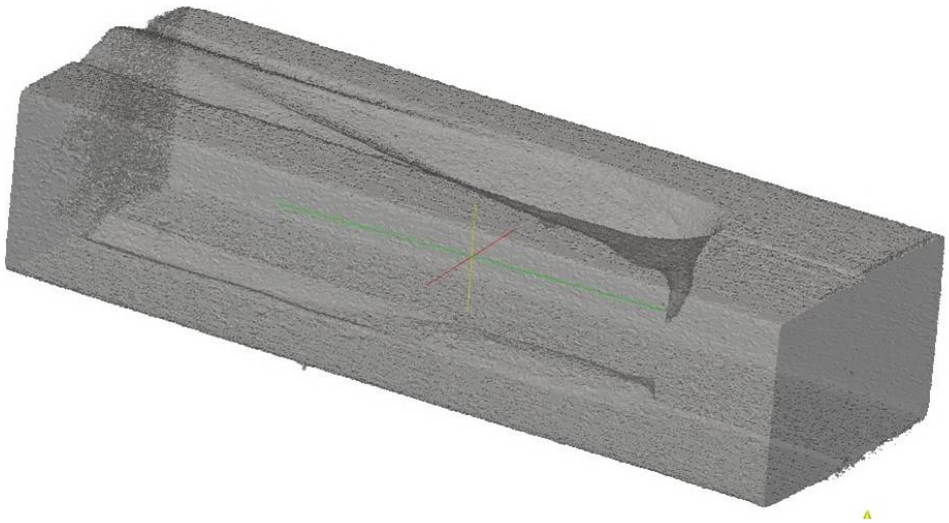

Figure 4.19: Reconstructed CT image illustrating the captured melt front.

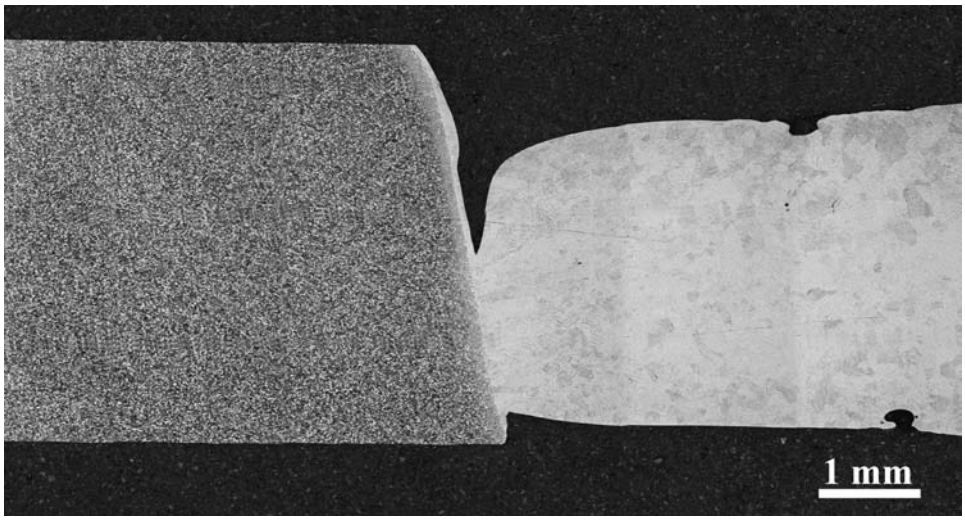

Figure 4.20: Optical micrograph showing the captured melting front at the longitudinal section through the weld bead centre.

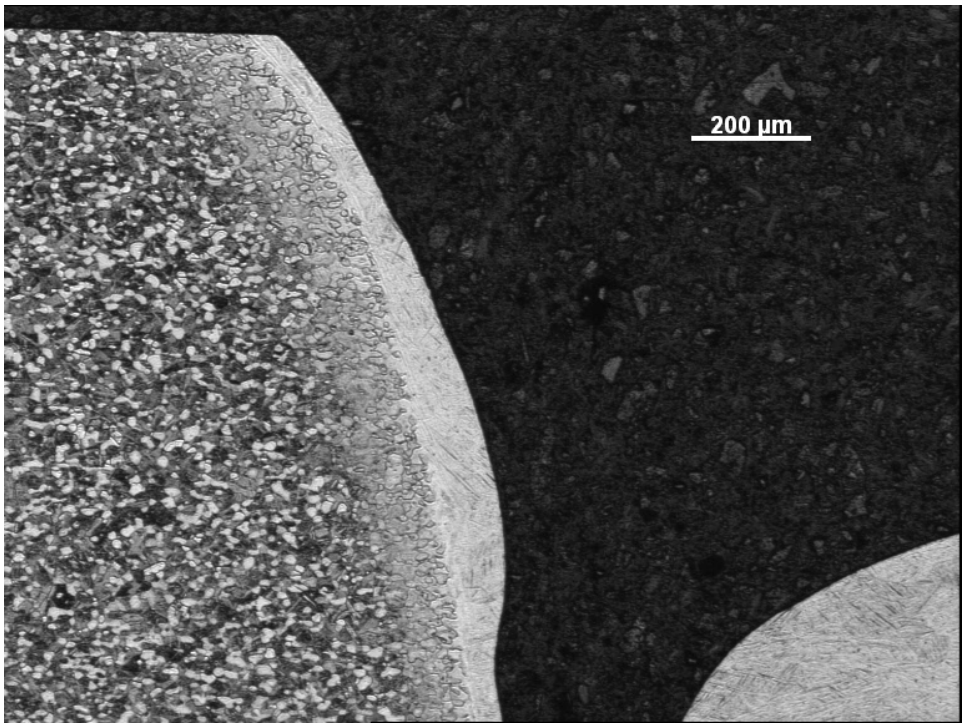

Figure 4.21: Optical micrograph illustrating the melting front at the upper part of the longitudinal section through the weld bead centre.

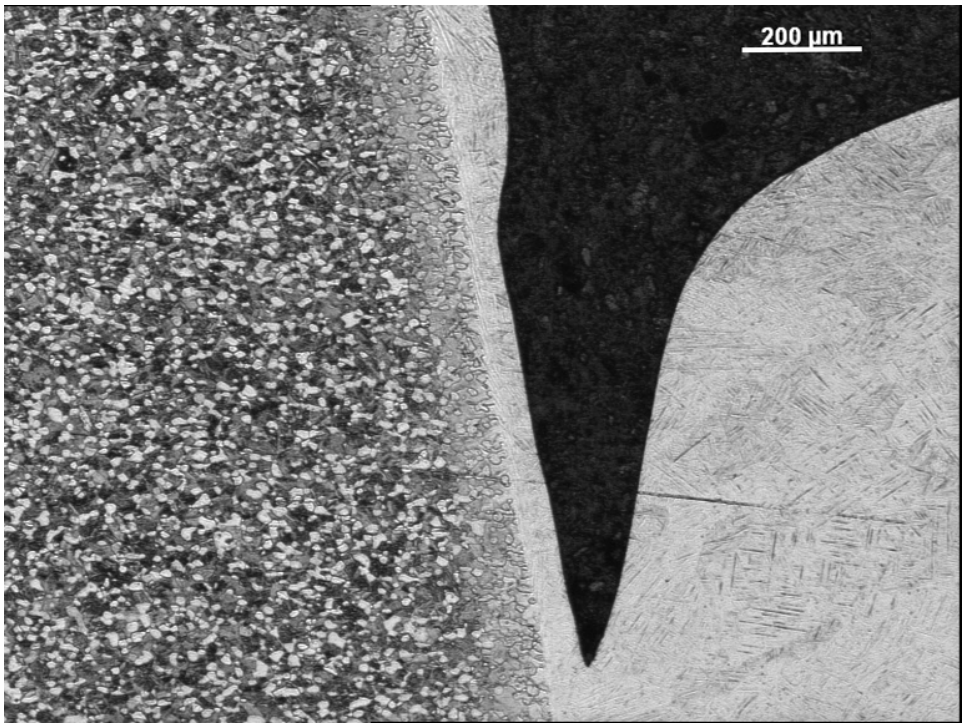

Figure 4.22: Optical micrograph illustrating the melting front at the middle part of the longitudinal section through the weld bead centre.

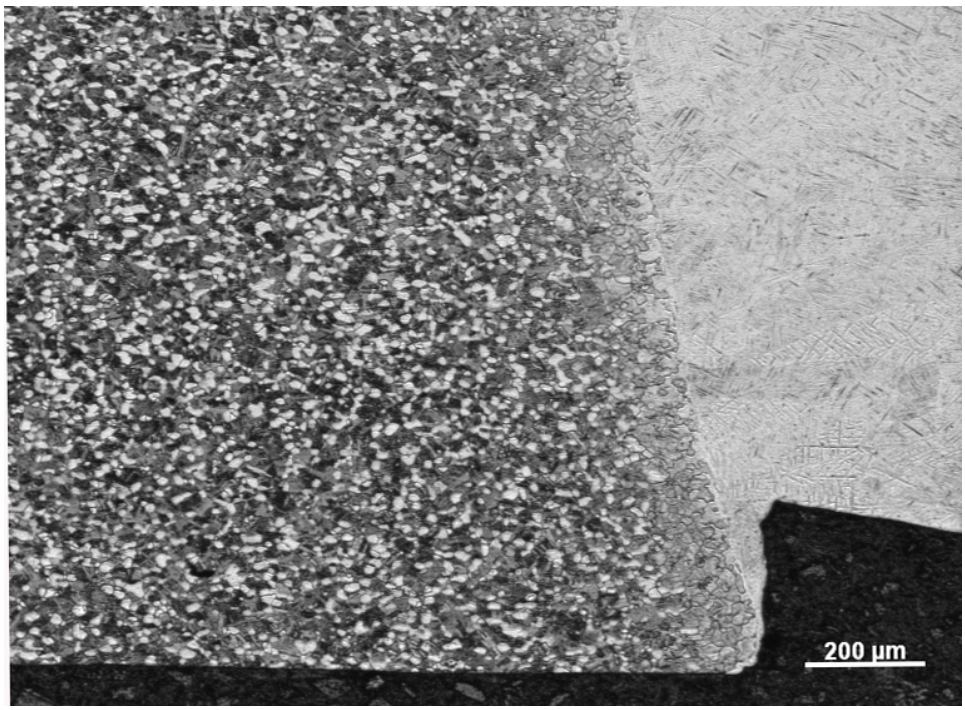

Figure 4.23: Optical micrograph illustrating the melting front at the lower part of the longitudinal section through the weld bead centre.

The thickness of the liquid region will change with different welding parameters. Therefore, to predict the exact details of the melting front around the keyhole is still a challenge; this is left for future research. One would expect that by modeling the dynamical change of the liquid region around the weld pool, our understanding of defect formation during electron beam welding would be enhanced.

4.10 Summary and Conclusions

Process models have been developed for electron beam welding process using two different approaches. A modified three-dimensional conical heat source model has been used for heat conduction prediction, which accounts for arbitrary fusion zone shapes arising from different welding parameters. Since the interaction between the electron beam and work piece is neglected, parameters used in the heat source model are determined from the weld zone profiles obtained from metallographic sectioning. Due to this limitation, the predicted results inside the weld pool may not be totally reliable; and the temperature evolution outside the weld pool is the main concern in this model.

The keyhole effect has also been investigated by using a simplified keyhole treatment, which enables the weld pool formation to be studied in more detail, such as the inclination of the melting front, and the size of the size of the liquid zone around the keyhole.

5

Modelling of Hydrogen Transport during Electron Beam Welding Process

Summary

Hydrogen transport during the electron beam welding of the titanium alloy Ti-6Al-4V alloy is analysed. A coupled thermodynamic/kinetic treatment is proposed in which the driving force for hydrogen migration is its chemical potential gradient which is in turn calculated using the Thermo-calc software package. The model is applied to the case of the electron beam welding of Ti-6Al-4V, for which a simple process model is presented for the temperature evolution expected. There is a thermodynamic driving force for accumulation of hydrogen in the weld pool. However, comparison with the limited amount of experimental data in the literature for the hydrogen field caused by welding indicates that account needs to be taken of the hydrogen degassing from the weld pool.

5.1 Introduction

Titanium alloys offer remarkable mechanical properties, which are especially impressive when judged on a density-corrected basis. Hence there is widespread usage of them for high performance applications, particularly in the aerospace sector [1, 3]. However, structural components

fabricated from these materials usually need to be welded – and hence the weldability of titanium alloys is an important issue. Although the popularity of solid-state joining (e.g. linear-friction and inertia welding) is growing, fusion processes are most commonly employed on account of their inherent flexibility, low cost and ease of application. Processes such as gas tungsten arc (GTA) and electron beam welding (EBW) are important examples [5, 117]. In practice, the design of welded structural components from titanium alloys for adequate static and fatigue strength is a significant challenge. For example, localised heating causes microstructure and properties to be altered in the vicinity of the joint. Thermal gradients cause residual stresses and distortion; in procedures for component lifetime estimation, these need to be accounted for. Moreover, unwanted defects can be introduced during processing which can be life-limiting.

One possible defect relevant to the fusion welding of titanium is porosity due to trapped gas. Such features – which should not be confused with microporosity arising on the scale of the dendritic structure – are formed in the weld, often close to the boundary with the heat-affected zone (HAZ). Their size can be large enough to impair structural integrity [80] and therefore their possible presence necessitates the use of non-destructive testing (NDT) methods. Previous experimental work [79, 81, 82, 83, 84, 85, 113] has demonstrated that hydrogen is the root cause of such porosity formation, but at this stage more basic knowledge is required about the behaviour of this element in and around the weld pool and the mechanism of porosity formation. Hydrogen transport during fusion welding processes has of course been much studied, but most research to date has focused on the effects of hydrogen absorption from shielding gas [124]. Unfortunately, this is not relevant to the electron beam welding considered here which is carried out in vacuum without the use of shielding gas; thus any gas porosity must be due to intrinsic hydrogen from the alloy being welded or from surface impurities caused by breakdown of hydrocarbons, e.g. contaminants such as grease or cleaning agents. Clearly, previous models are then unsuitable for application in this case. Some diffusion-based diffusion models are available [125, 126, 127] in which the driving force for hydrogen diffusion is taken to be the hydrogen concentration gradient.

A difficulty however is that some parameters used are difficult to measure, e.g. dislocation density, trapping parameters etc and this has limited the applicability of these treatments.

In this paper, a coupled thermodynamic/kinetic model is proposed for the prediction of hydrogen migration during the fusion welding process, in which the driven force for hydrogen diffusion is modelled consistent with its chemical potential gradient. In recent years, progress has been made in the measurement/assessment of thermodynamic and kinetic data relating to hydrogen in titanium-based alloy systems [96, 97, 98, 99]. For example, thermodynamic assessments of the Ti-H binary phase diagram have been made and are available for computer-based calculations [100, 101]. Similarly, good estimates exist for the rates of diffusion of hydrogen in titanium [92, 102, 103, 104]. These recent advances suggested to us that a detailed analysis of the behaviour of hydrogen in and around the weld pool might be possible. We test our predictions against the available experimental measurements [128, 129, 130] to shed light on the behaviour of hydrogen in and around the molten weld pool, and the mechanism of porosity formation in these systems.

5.2 Process Model

Figure 5.1 illustrates the situation which is modelled in this chapter. An electron beam is assumed to be moving with constant velocity U_s (welding speed) relative to the workpiece of the Ti-6Al-4V material; a Cartesian coordinate system (x, y, z) is taken to be fixed within the plate. Before the welding process is applied, hydrogen is assumed to be uniformly distributed within the plate so that its source is intrinsic to the alloy. During the welding process, the action of the electron beam is modelled as a three conical volumetric heat source Q_v. Thus a temperature field is set up by heat conduction. Note that no attempt is made here to model convection or aspects of key-hole formation, since the reaction of the initially-constant hydrogen field to the application of heat is primarily concerned. As the hydrogen chemical potential in the Ti-6Al-4V system is a function of both temperature and hydrogen concentration, a chemical

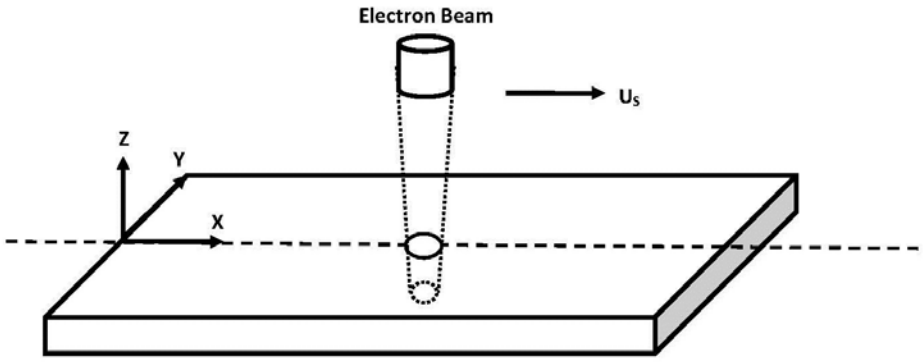

Figure 5.1: Schematic diagram of electron beam full penetration welding (Cartesian coordinate system and conical heat source).

potential gradient is set up and this causes migration of hydrogen.

The modelling methods employed are described in detail below but the basic strategy is now summarised. First, the temperature field is calculated and this – together with the initial hydrogen concentration field – is used to estimate the hydrogen chemical potential field. Thereafter, a generalized diffusion equation is used to calculate the extent of hydrogen diffusion. The modified hydrogen concentration field was then used in the next iterative step in the calculation, consistent with an integration over time using the finite volume method. The kinetic calculations were programmed in Fortran making use of the TQ-interface (Version 6.00) to the Thermo-calc software package. The Thermotech thermodynamic database TTTI3 for titanium alloys was used.

5.2.1 Governing equations

5.2.1.1 Thermal model for EBW process

The temperature field during electron beam welding process is assumed to be governed by heat transfer by conduction, with no contributions from other sources such as convection and

radiation:

$$\rho C_p \left(\frac{\partial T}{\partial t} \right) = \nabla \cdot (k \nabla T) + Q_v \tag{5.1}$$

where ρ is the density, C_p the heat capacity, k the heat conductivity and Q_v is the volumetric rate of heat production from the source. The heat source term Q_v is represented by a three-dimensional frustum heat source, which has been described in chapter 4. Note once again that the model used for the heat source is purely phenomenological and chosen to set up a temperature field which is representative of the electron beam welding process. With the defined TDC heat source, equation 5.1 is solved by the finite volume method (FVM). The commercial computational fluid dynamics software CFD - ACE+ has been used for this purpose. The calculated temperature field is coupled with hydrogen diffusion model described as below.

5.2.1.2 Hydrogen diffusion equation

The hydrogen chemical potential and thermodynamic activity at a given temperature and hydrogen concentration have been determined using the Thermo-Calc software. After calculating the chemical potential, the hydrogen diffusion flux driven by the chemical potential gradient can be expressed as [131]

$$J_{\mathrm{H}} = -L_{\mathrm{H}} \nabla \mu_{\mathrm{H}} \tag{5.2}$$

where J_{H} is the flux density of hydrogen atoms and L_{H} is the kinetic coefficient. Thus the hydrogen transport in the Cartesian coordinate system in this study can be described as

$$\frac{\partial C_{\mathrm{H}}}{\partial t} = \nabla \cdot (L_{\mathrm{H}} \nabla \mu_{\mathrm{H}}) \tag{5.3}$$

where C_{H} is the hydrogen concentration.

To solve equation (5.3), the kinetic coefficient L_H needs to be determined. Following [132], this can be related to the hydrogen diffusivity and hydrogen concentration via

$$L_{\mathrm{H}} = \frac{D_{\mathrm{H}} C_{\mathrm{H}}}{R_{\mathrm{g}} T} \left(1 + \frac{\partial \ln \gamma_{\mathrm{H}}}{\partial \ln N_{\mathrm{H}}} \right)^{-1} \tag{5.4}$$

where D_{H} denotes the hydrogen diffusivity, C_{H} is the hydrogen mole concentration, R_{g} is the universal gas constant, T is the absolute temperature, γ_{H} is the hydrogen activity coefficient and N_{H} is the mole fraction of hydrogen. One can define the hydrogen mobility B_{H} according to

$$B_{\mathrm{H}} = \frac{D_{\mathrm{H}}}{R_{\mathrm{g}}T}\left(1 + \frac{\partial \ln \gamma_{\mathrm{H}}}{\partial \ln N_{\mathrm{H}}}\right)^{-1} \tag{5.5}$$

By combining Equation (5.3), Equation (5.4) and Equation (5.5), the hydrogen flux driven by its chemical potential gradient is consistent with

$$\frac{\partial C_{\mathrm{H}}}{\partial t} = \nabla \cdot \left(-C_{\mathrm{H}}\frac{D_{\mathrm{H}}}{R_{\mathrm{g}}T}\left(1 + \frac{\partial \ln \gamma_{\mathrm{H}}}{\partial \ln N_{\mathrm{H}}}\right)^{-1}\nabla \mu_{\mathrm{H}}\right) \tag{5.6}$$

as expected.

In order to solve equation (5.6), estimates of the hydrogen diffusivity are needed. Hydrogen diffusion in titanium and its alloys has been studied by many researchers [104, 117, 133, 134]. Since Ti-6Al-4V is a two-phase (α+β) alloy, the hydrogen diffusivity in Ti-6Al-4V depends both on the temperature and different phases. In this study, the following hydrogen diffusivity expressions have been used in different phases [133]:

For the hexagonally close-packed (HCP) α-phase:

$$D_{\mathrm{H}}^{\alpha} = 1.8 \times 10^{-6}\exp\left\{-\frac{6230}{T}\right\} \tag{5.7}$$

For the body-centered cubic (BCC) β-phase:

$$D_{\mathrm{H}}^{\beta} = 1.95 \times 10^{-7}\exp\left\{-\frac{3342}{T}\right\} \tag{5.8}$$

where the units of the diffusivities are m^2/s, temperature T in K Arrhenius plots of hydrogen diffusivity represented by Equation (5.7) and (5.8) are given in Figure 5.2. For hydrogen diffusion in liquid titanium, it would appear that accurate diffusivity coefficient data are lacking. Consequently, in this work, the hydrogen diffusivity value in liquid is assumed to be $D = 2\times10^{-7}\mathrm{m}^2/\mathrm{s}$, as used in [128].

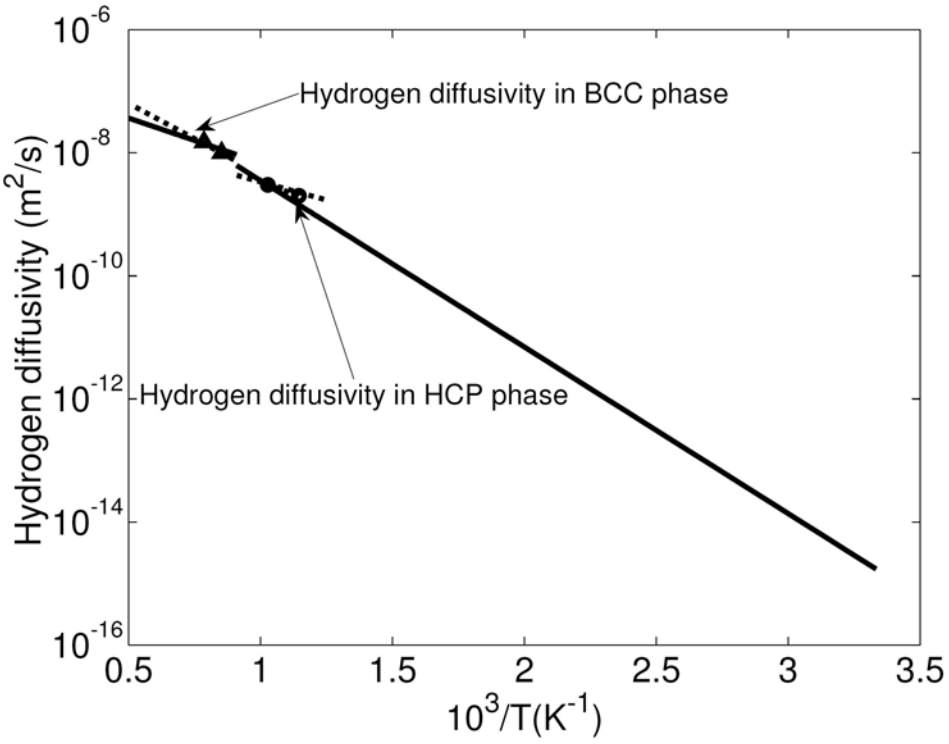

Figure 5.2: Arrhenius plots of the hydrogen diffusivity in HCP and BCC phases in Ti-6Al-4V, solid lines represent the data from reference [133],which were used in the this work, compared to the data represented by dash lines from reference [1]

5.2.1.3 Treatment of two phase region

In the alloy Ti-6Al-4V, a two-phase region exists between the HCP α phase and the body centred cubic β phase. Treatment of hydrogen diffusion here requires careful consideration. To do this, the phase fractions and corresponding hydrogen concentrations in each phase are calculated in order to obtain an effective hydrogen flux in the two-phase region, assuming that the two phases are in local equilibrium. Following [135], the effective hydrogen flux J_{H} in the $\alpha + \beta$ region is the calculated according to

$$J_H = J_{\mathrm{H}}^{\alpha} f^{\alpha} + J_{\mathrm{H}}^{\beta} f^{\beta} \tag{5.9}$$

where f^{α}, f^{β} are the phase fractions of the HCP and BCC phases respectively, and J_{H}^{α}, J_{H}^{β} are the corresponding hydrogen fluxes; these are calculated from Equation (5.6) using the hydrogen concentration and hydrogen mobility in each phase as follows:

$$J_{\mathrm{H}}^{i} = -C_{\mathrm{H}}^{i} B_{\mathrm{H}}^{i} \nabla \mu_{\mathrm{H}} \tag{5.10}$$

where C_{H}^{i}, D_{H}^{i} and B_{H}^{i} $(i = \alpha, \beta)$ are hydrogen concentration, diffusivity and mobility in each phase respectively.

5.2.1.4 Hydrogen escape during welding

Since electron beam welding is performed under vacuum conditions (typically 10^{-4} mbar or thereabouts) escape of hydrogen during the welding process is an effect which is considered in the later part of the paper. In principle, hydrogen can escape both from the weld pool and the solid material at elevated temperatures. Unfortunately, not much is currently known about the rate of hydrogen escape under vacuum welding conditions. In section 5.4, hydrogen escape from the weld pool surface is modelled in a rather simplistic way according to

$$-D_{\mathrm{L}} \frac{\partial C_{\mathrm{H}}}{\partial z} = K(C_{\mathrm{H}} - C_{\mathrm{inf}}) \tag{5.11}$$

where D_{L} is the hydrogen diffusivity in the liquid metal, C_{H} is the hydrogen concentration at the weld pool surface, K is a degassing rate coefficient with unit of m/s and C_{inf} is the limiting concentration of hydrogen in the far field, in practice taken to be zero.

5.3 The Numerical Implementation of the Model

Experimental information on hydrogen redistribution caused by welding of titanium alloys would appear to be extremely rare; we have been able to find only one study in which detailed measurements have been made [130]. In it, electron beam welds in Ti-6Al-4V material were made in plates of thickness 2.7 mm; the welding parameters are given in Table 5.1. Unfortunately, information concerning the beam focus is lacking so approximations have been made. The beam radius at the top surface r_t is assumed to be 1.5 mm and r_b at the bottom surface 1.0 mm; these values have been shown to provide a reasonable description of the fusion zone dimensions reported in [130]. The material properties used in the calculations are the same as those used in chapter 4.

Table 5.1: EB parameters used in the calculations [130].

Accelerating Voltage (kV)	Beam current (A)	Welding Speed (mm/s)
100	10.3	14

The finite volume method (FVM) was used to solve equation (5.1) and equation (5.3). At each time step, the temperature field predicted by equation (5.1) is coupled with the Thermo-Calc software to calculate the hydrogen chemical potential, which is needed to perform the transient hydrogen evolution calculation using equation (5.3). To calculate the hydrogen flux driven by the chemical potential gradient, thermodynamic data including phase fractions (f^i) and hydrogen concentrations (C_{H}^i) in each phase are needed. To reduce the time for the thermodynamic calculation and to make three-dimensional calculation of hydrogen diffusion possible, special treatment of the thermodynamic calculation was needed. Since the hydrogen thermodynamic data are a function of temperature and hydrogen content only, they can be calculated and stored prior to the main calculation. The remaining problem is to choose the appropriate range and step size of temperature and hydrogen content to calculate the thermodynamic data matrix

and the mapping method. In this study, thermodynamic data matrix is calculated with hydrogen content range from 1 ppm to 500 ppm and a step size of 1 ppm. The mapping procedure can be described, taking hydrogen chemical potential as an example. For given temperature T and hydrogen concentration C_{H} in each cell, find the nearest temperature value of T_i and hydrogen concentration $C_{\mathrm{H_i}}$ in the thermodynamic data matrix, denoting the hydrogen potential at this data point as $\mu_{\mathrm{H}}(T_i, C_{\mathrm{H_i}})$; then, the hydrogen chemical potential at this cell $\mu_{\mathrm{H}}(T, C_{\mathrm{H}})$ can be calculated according to

$$\begin{aligned}\mu_{\mathrm{H}}\{T, C_{\mathrm{H}}\} = \quad & \mu_{\mathrm{H}}\{T_i, C_{\mathrm{H_i}}) + (T - T_i)\frac{\partial \mu_{\mathrm{H}}(T, C_{\mathrm{H}})}{\partial T}\Big|_{(T_i, C_{\mathrm{H_i}})} \\ & + (C_{\mathrm{H}} - C_{\mathrm{H_i}})\frac{\partial \mu_{\mathrm{H}}(T, C_{\mathrm{H}})}{\partial C_{\mathrm{H}}}\Big|_{(T_i, C_{\mathrm{H_i}})}\end{aligned} \tag{5.12}$$

In equation (5.12), the necessary partial differentiation has been determined from the neighbouring data points in the thermodynamic matrix using the finite difference method.

The numerical routine described is illustrated in the flow chart of Figure 5.3.

5.4 Results and Discussion

We consider first the case of hydrogen evolution at a welding speed of 14 mm/s with initial (uniform) hydrogen concentration of 205 ppm, consistent with the experiments reported in [130]. The calculation domain is 40 mm × 20 mm × 2.7 mm. In Figure 5.4, the predictions are illustrated for two sections on the xy and yz sections respectively. Figure 5.5 illustrates the weld pool at 1.7s on the xy plane at mid-section.

The results confirm that during the welding process, hydrogen migrates from the colder to the hotter part, which leads to hydrogen accumulation in the weld pool and a hydrogen depleted area close to the weld bead. The maximum hydrogen content is found close to the fusion boundary. The predicted results are further examined by looking at the fusion zone profile and hydrogen distribution field on a transverse cross-section, *i.e.* a section whose normal is in the welding direction. The fusion zone and hydrogen distribution at 1.48 s are shown in Figure 5.6.

To rationalise in greater detail the predictions of the modelling, consider the temporal evolution of the hydrogen content along a line oriented in the y direction at mid-plane, as marked

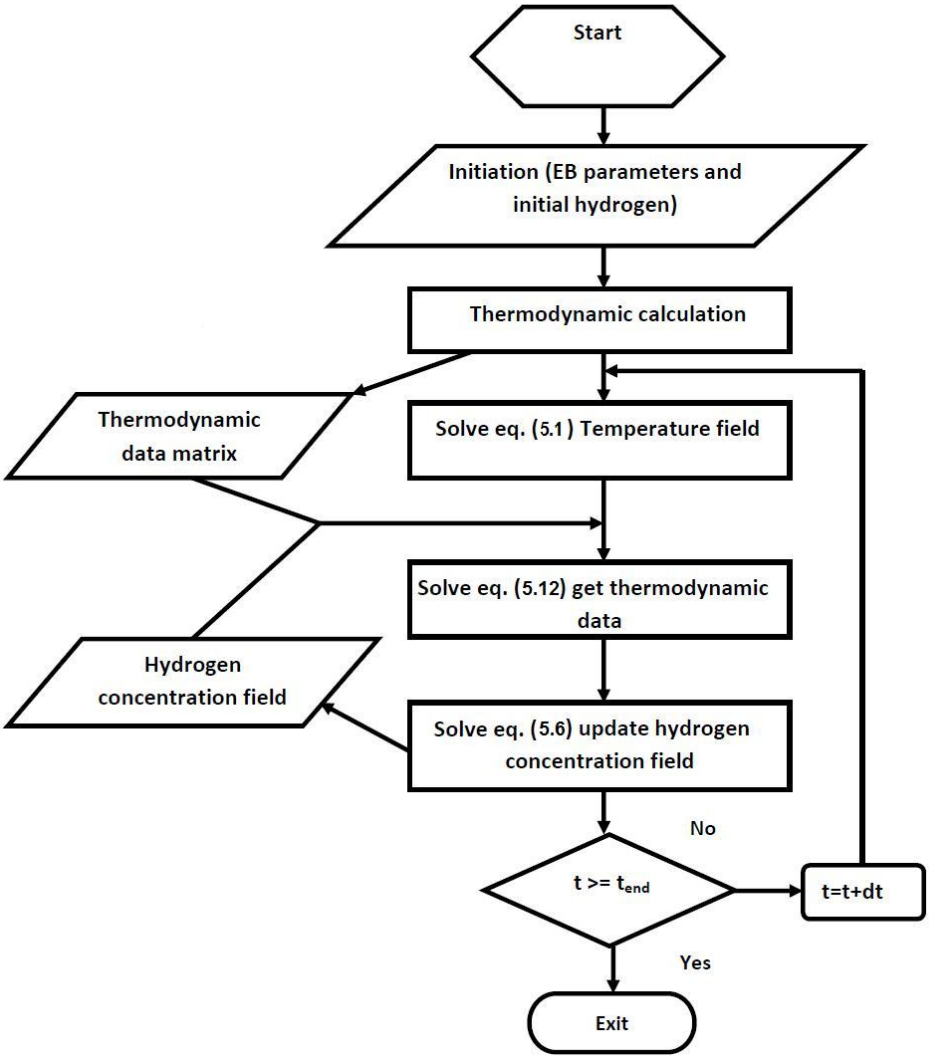

Figure 5.3: Flow chart illustrating the numerical implementation of the model.

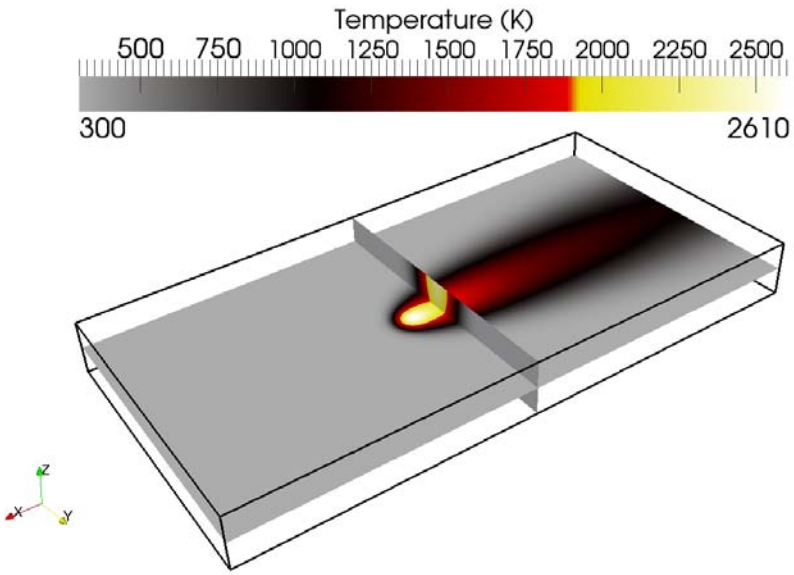

Figure 5.4: Locations of the two planes in the 3D calculation domain.

on Figure 5.6(b). In Figure 5.7 (a), at time equal to 1.42 s the heat source is approaching and material is being heated but no melting has occurred as yet. The discontinuity in the chemical potential gradient at x=0.75 mm is associated with the $\alpha \rightarrow \beta$ phase transition. In Figure 5.7 (b) for time 1.45 s melting has now occurred with the chemical potential showing a change in slope at the fusion boundary (x = 0.4 mm); once again the discontinuity due to the $\alpha \rightarrow \beta$ phase transition is evident at x = 1.9 mm. In Figure 5.7 (c), the electron beam has passed through the section, and solidification has occurred. Consistent with the laws of irreversible thermodynamics, the hydrogen flux is driven by the gradient of hydrogen chemical potential. Consequently, hydrogen is driven from the cooler parts towards the hotter regions during the heating part of the cycle, i.e. from right to left in Figures 5.7 (a) and (b); however, during cooling, see Figure 5.7 (c), the relatively flat temperature profile in the solidified metal coupled with the higher hydrogen content of the previously molten material means that hydrogen tends to diffuse back towards the base metal to minimise the chemical potential gradient. From the hydrogen distribution profile, Figure 5.7 (a), one can see that the hotter part has reached higher hydrogen content by depleting hydrogen from the colder part; thus the maximum hydrogen con-

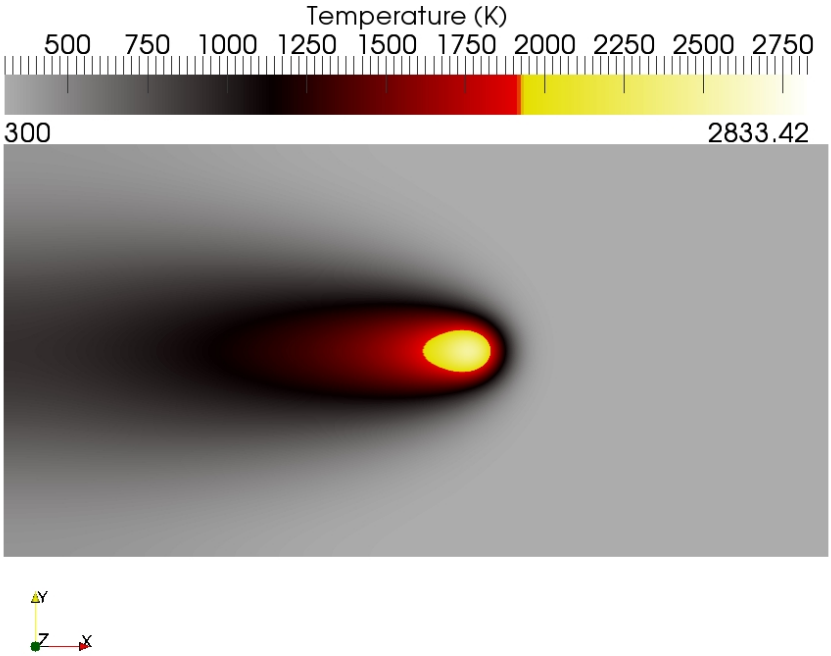

(*a*)

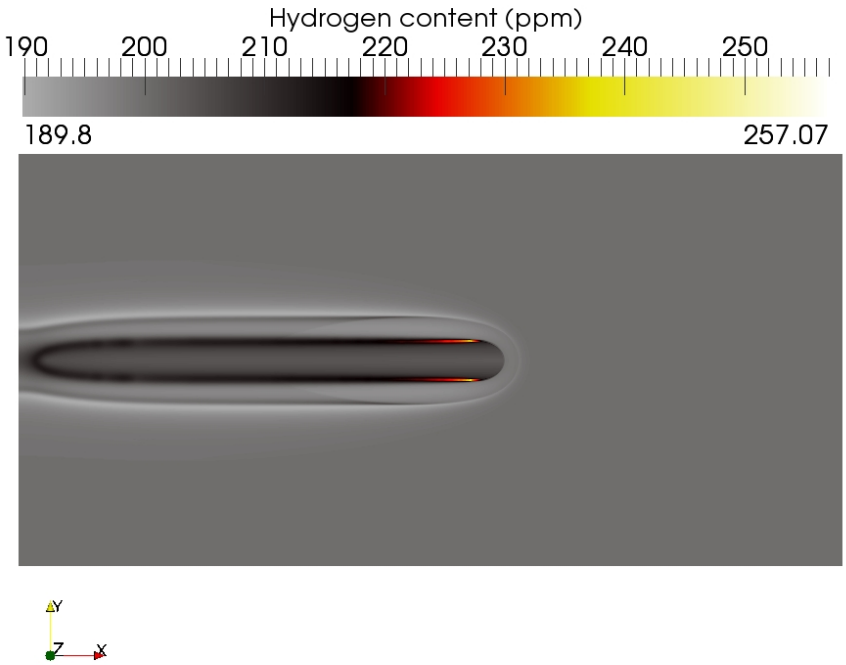

(*b*)

Figure 5.5: (a) Weld pool shape and (b) hydrogen distribution at middle plane of z direction with welding speed of 14 mm/s, t = 1.7s.

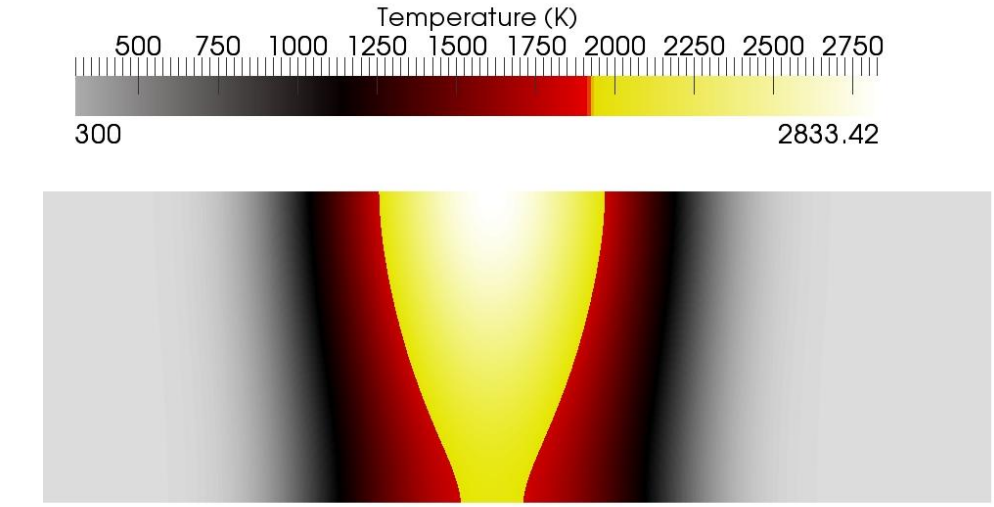

(a)

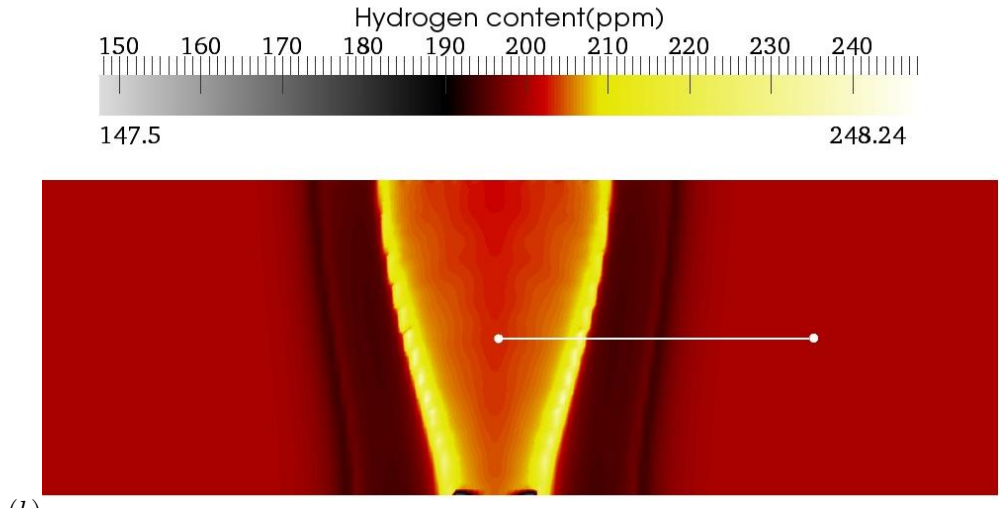

(b)

Figure 5.6: (a) Fusion zone and (b) hydrogen distribution and fusion zone profile at cross section at 1.48 s.

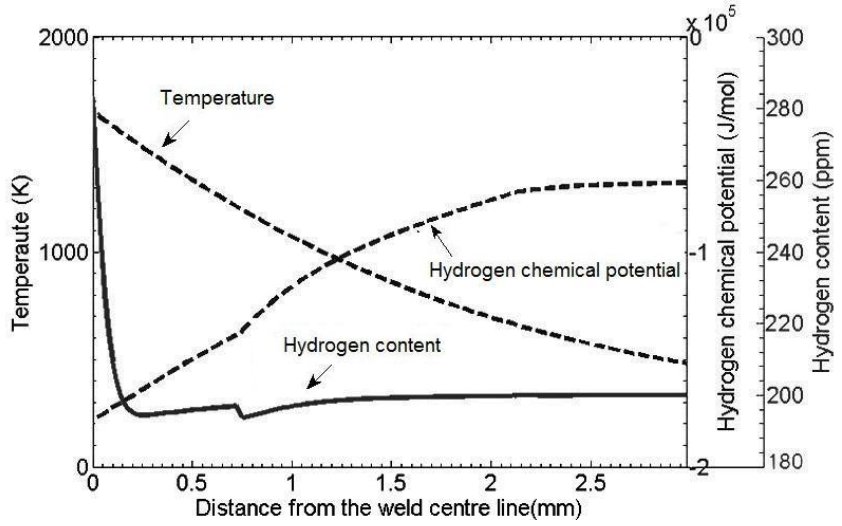

(*a*)

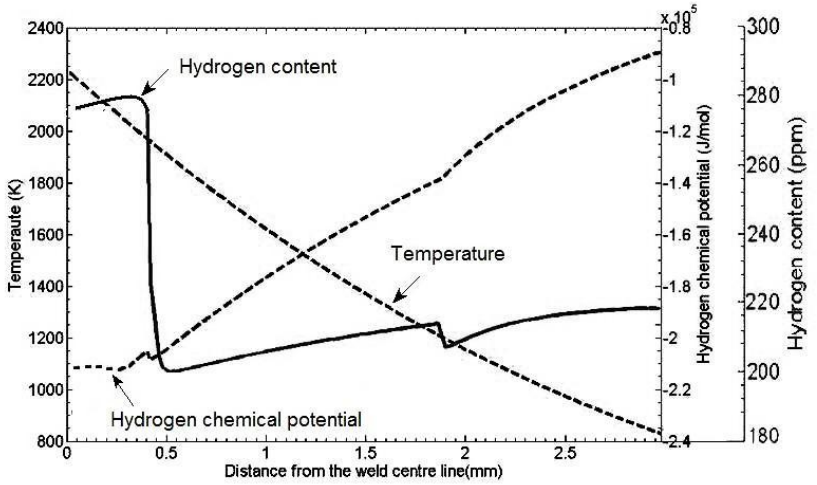

(*b*)

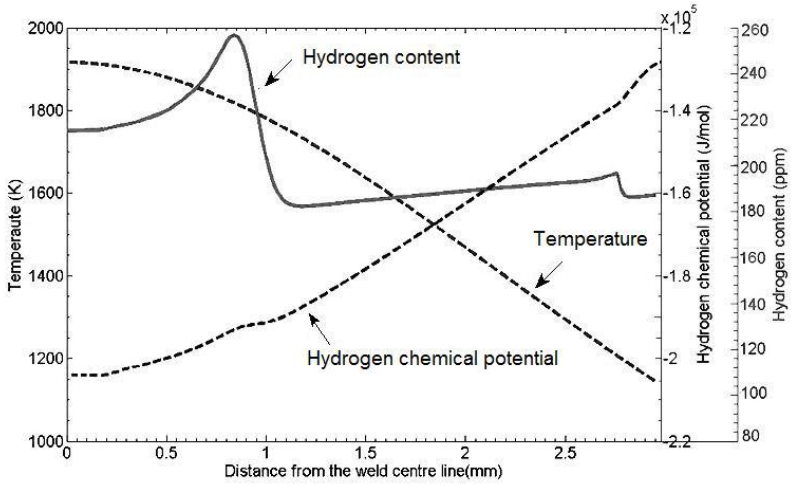

(*c*)

Figure 5.7: Predicted temperature, hydrogen chemical potential and hydrogen distribution profile of along the probing line at time, (a) $t = 1.42$ s, (b) $t = 1.45$ s and (c) = 2.0 s.

tent rises to 280 ppm from the initial hydrogen content of 205 ppm in the base material. One can see from Figure 5.7 (b) that due to the rapid melting process, the hydrogen concentration inside the weld pool becomes lower when compared to the hydrogen content in the hot part before melting. This is because the rapid hydrogen diffusion in the liquid leads to an averaging effect of hydrogen content at the hot part material after melting. Due to the steep hydrogen distribution profile in the hot solid part, the wider the molten region, the lower the mean hydrogen content in the weld pool. In Figure 5.7 (c) hydrogen is found to diffuse back towards the base material from the solidified metal. In principle, all hydrogen accumulated in the fusion zone during the heating process should diffuse back eventually to the base material; however due to the low thermal gradient and the very low hydrogen mobility at the later cooling stage, this redistribution is not fully accomplished and a signature of the passage of the welding source remains.

A discontinuity in the hydrogen concentration profile is observed at the location corresponding to the solid-state phase transition in Figure 5.7 (a),(b), *i.e.* around 1200 K. This has been further investigated by examining the phase fraction and hydrogen content in each phase, see Figure 5.8. The results are consistent with the hydrogen solubility being much lower in the HCP phase than the BCC phase. For example, at the temperature of 1180 K, hydrogen in the HCP phase is approximately 30 ppm while in the BCC phase it is 260 ppm, with the difference increasing rapidly with decreasing temperature. Due to the higher hydrogen dissolving capacity and associated higher hydrogen mobility in the BCC phase, hydrogen in the HCP phase is rapidly depleted, leading to the discontinuity observed. Our results also confirm that after welding, most hydrogen is dissolved in the BCC phase; this explains the redistribution of hydrogen into the region with higher content of β phase after welding, as reported in [128].

Finally, we now compare the results of our predictions with the experimental measurements reported in [130], in which the final hydrogen distribution profile for electron beam welded Ti-6Al-4V joints has been reported. Figure 5.9 is a comparison of the measured and predicted

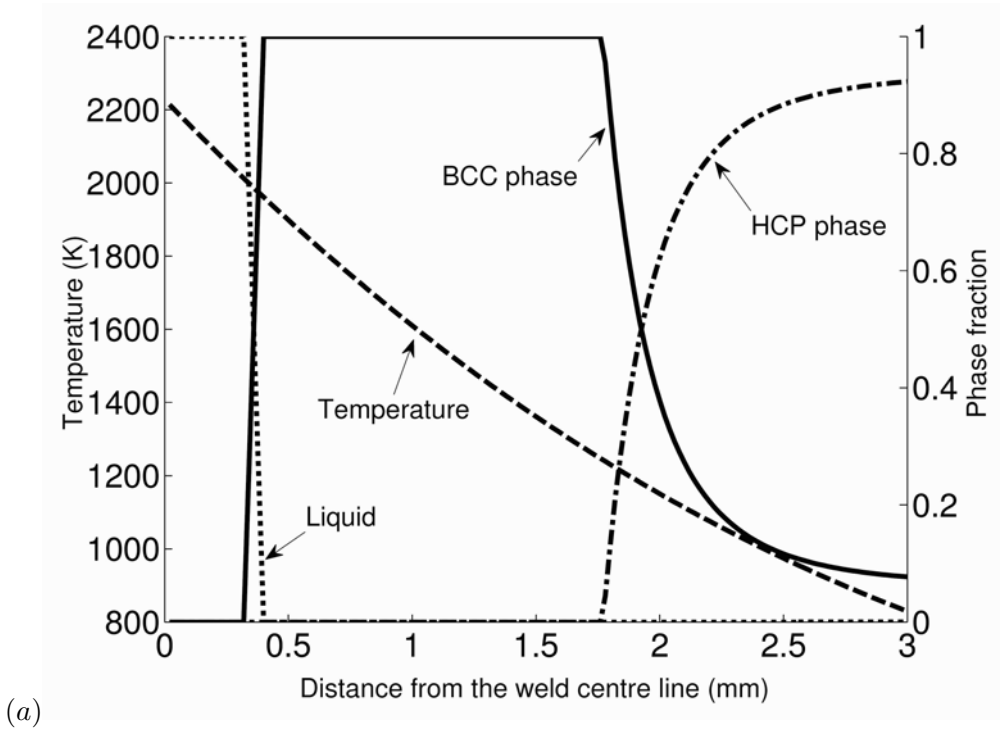

(*a*)

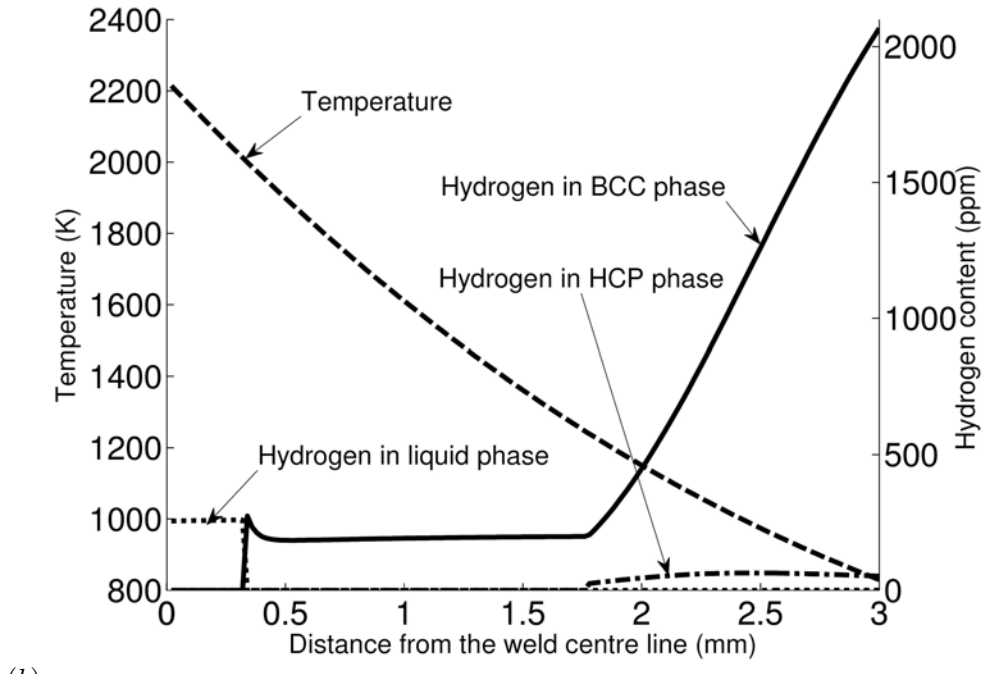

(*b*)

Figure 5.8: Associated (a) phase fraction and (b) hydrogen concentration in each phase along probing line at time $t = 1.45$ s.

results for the hydrogen profile. Figure 5.9(a) shows the hydrogen distribution field at the cross section of the weld bead after the end of the calculation. It can be seen that the predicted concentration field is fairly consistent with the experimental measurements. In [130], it should be mentioned that the hydrogen content measurement was carried out by wet chemical analysis by gradually removing slices of material orientated parallel to the fusion boundary at a step size of 0.1 mm, with the results plotted as hydrogen content in each slice against the distance of fusion centreline. Since the fusion boundary is somewhat curved and the fusion width varies along the thickness direction, some experimental error is inevitably introduced. In Figure 5.9 (a), since the fusion zone width changes along the thickness direction and hydrogen escapes only from the top surface in the current model, transverse hydrogen concentration fields at different thickness position vary. The hydrogen distribution field shows low hydrogen content is found close to the surface. In this simulation, because data for the degassing rate coefficient K in equation (5.11) is not well known, an estimated value of 0.18 was used in the calculation to fit the lowest hydrogen content in fusion zone has reported in [130]. The hydrogen concentration profiles at different depth are presented and shown in Figure 5.9 (b). The predicted hydrogen distribution profiles are sensitively varying with the depth, this is because in the current model, we only considered hydrogen degassing at weld pool surfaces, but in reality, hydrogen also can escape from the keyhole inside the weld pool, which has not been considered yet in the model. Furthermore, the fusion profile along thickness direction is inclined, which makes it more difficult for quantitative comparison. A hydrogen-depleted area is found both in the predicted and measured results at distance of 2 mm, and higher hydrogen level is found around the fusion boundary. The probing line result shows much lower hydrogen concentration compared to the measured results and a much steeper rise at the transition to the fusion boundary. In comparison, the measurement shows a smooth transition from the centre of the weld hydrogen concentration to the surrounding material. This behaviour can be attributed to the fact that the measurement averages the hydrogen concentration over a whole slice of the material. From the simulation

it is obvious that the hydrogen concentration field follows the shape of the weld pool, which is significantly curved, especially close to the centre of the weld. This averages out variations of hydrogen concentrations and leads to the observed smooth transition from weld pool to the boundary of the fusion zone. The fact that significantly lower hydrogen concentrations were measured in the centre of the weld, emphasizes the importance of hydrogen escape from the weld pool. This also indicates that the degassing rate coefficient used in the model is still rather low. In order to improve the predictive capability of the model,better understanding of the hydrogen escape mechanism is needed and the heat transfer modelling needs to be enhanced by considering convection. The dynamics of the keyhole is expected to play an important role in this.

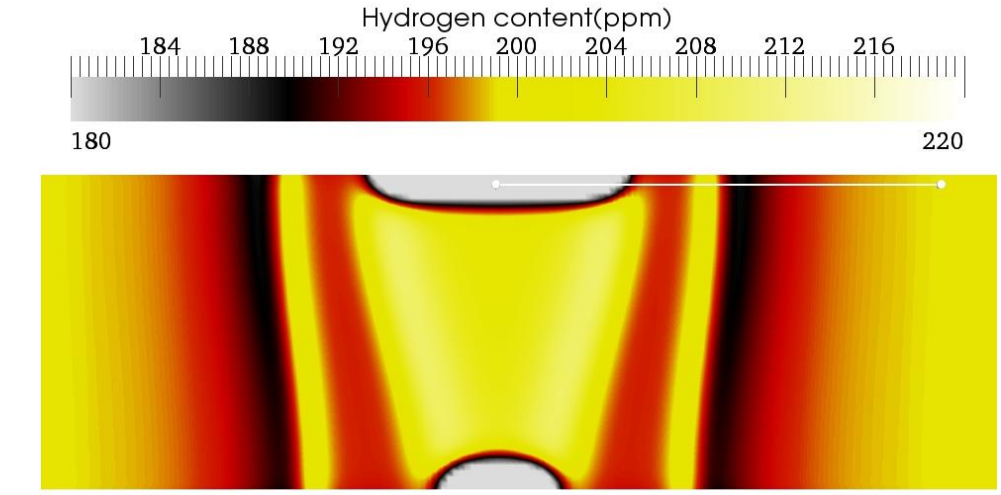

(*a*)

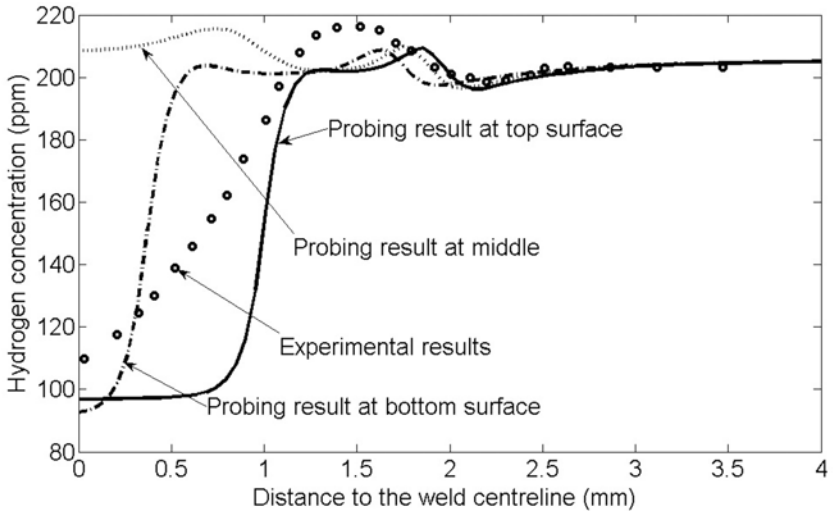

(*b*)

Figure 5.9: (a) Predicted hydrogen distribution at cross section and (b) Calculation results compared to the reported experimental measurement results [130].

5.5 Conclusions

A model for the transport of hydrogen in the welds of the titanium alloy Ti-6Al-4V has been proposed. It is based upon a coupled thermodynamic/kinetic treatment of the diffusion of hydrogen. The following conclusions can be drawn from this work:

(1) Hydrogen migrates to the hotter regions during the welding process and in particular the weld pool; this causes a depletion of hydrogen in the surrounding regions.

(2) Due to large differences in hydrogen dissolution in the BCC and HCP phases, a discontinuity in the hydrogen concentration field is predicted to occur at the location of the BCC/HCP transition interface. After welding, hydrogen diffuses preferentially into the region with higher fraction of the BCC phase.

(3) The measured hydrogen profiles cannot be rationalised without accounting for an anticipated degassing process caused by welding, which allows hydrogen to escape from the weld pool. The maximum hydrogen content is found at the fusion boundary after welding.

(4) The modelling indicates that the welding parameters are likely to exert a strong influence on the final hydrogen distribution in the joints, via the effects on hydrogen diffusion kinetics and rate of hydrogen escape from the weld pool.

6

Modelling and Rationalisation of Hydrogen Effect on Porosity Formation

Summary

A hydrogen diffusion-controlled bubble growth model is proposed to simulate the growth of a stationary bubble in molten titanium alloys at isothermal condition, which is a first approximation of early stage of porosity formation in the weld pool during electron beam welding of titanium alloys. Bubbles are assumed to be initiated due to the effect of the irregular profile of joint surfaces. This model is used to make predictions of the hydrogen concentration barrier needed for pore formation. The effects of surface tension of the liquid metal and the radius of pre-existing micro-bubble size on the barrier are discussed.

6.1 Background

Pores formed during electron beam welding of titanium-based alloy have been associated with gas evolution during welding process, especially hydrogen. Characterisation results in chapter 3 identified the majority gas trapped inside the gas pores are hydrogen. Hydrogen behaviour during electron beam welding of titanium based alloys has been investigated in chapter 5, in which hydrogen is found to have a tendency to migrate from the cold region to the hot region,

causing hydrogen accumulation in the weld pool. The developed hydrogen transport model enables estimation of hydrogen level in the weld pool during welding process, but the remaining question concerns the hydrogen level needed to form bubbles. To find out the critical hydrogen level to avoid porosity formation, the effect of hydrogen on bubble nucleation and growth inside the weld pool needs further investigation.

Porosity formation in electron beam welds has been studied for decades. It has been pointed out in early empirical studies that the porosity formation greatly depends on the edge preparation and hydrogen content in the base material [81, 82, 136]. More comprehensive study to clarify the qualitative dependence between weld porosity and surface condition has been carried out by Gouret etc [83], in which porosity formation is strongly related to the amount of surface contaminants due to different surface preparation methods. Mohandas *et al* [84] believed that porosity formation was due to the hydrogen solubility change during the welding process. It also has been shown that welding speed also has a strong effect on porosity formation. From the above studies, it seems hydrogen is responsible for porosity formation, but comprehensive study of hydrogen effect on bubble formation and growth is still lacking.

To understand the porosity formation mechanism and the effect of hydrogen on porosity formation, one can argue that three main aspects need to be considered: (i) the dynamics of bubble nucleation in the melt; (ii) the driving force for bubble growth; and (iii) bubble flow in the weld pool and its entrapment. It is agreed [84] that homogeneous bubble nucleation is not likely to occur due to the large internal pressure required within the bubble; thus bubbles are most likely to nucleate heterogeneously. During welding, pre-existing microbubbles are available at the melting front from asperities at the joint surfaces [83]. Once bubbles nucleate, a driving force is required for bubble growth. In aluminium alloys, hydrogen diffusion has been demonstrated to have a strong effect on bubble formation [86, 87, 88, 89] and it seems plausible that similar effects can occur in titanium systems. Vigorous convection and stirring in the weld pool might explain why porosity is observed only intermittently, since bubble escape is likely to be enhanced

by this effect.

In this chapter, a hydrogen diffusion-controlled bubble growth model is proposed, aiming to provide fundamental insights into the mechanism of porosity formation in these alloys, via quantitative modelling.

6.2 Model Description

The hydrogen diffusion-controlled bubble growth model is illustrated in Figure 6.1. A pre-existing bubble is assumed; it is surrounded by liquid metal, which contains a uniform hydrogen concentration C_0 at temperature T and pressure P_L. The surface tension between the liquid metal and gas bubble is σ. The bubble of initial radius r_0 is initially stabilised by insoluble gas inside it. The hydrogen dissolved in the melt diffuses towards the bubble, so that the pressure $P_g(t)$ inside the bubble and gas amount $n_g(t)$ evolves. As long as the pressure inside the bubble is higher than the pressure induced by the melt and surface tension, growth will occur. To investigate the hydrogen effect on bubble growth, the following assumptions are made:

- the temperature is isothermal;
- the gas inside the bubble is taken to be ideal;
- the melt is large compared to the bubble, so the bubble growth is unbounded and the hydrogen content far from the bubble is constant;
- thermodynamic equilibrium is maintained at the gas liquid interface, according to Henry's law;
- the liquid is incompressible.

6.2.1 Governing Equation

With the above assumptions, hydrogen diffusion in the liquid metal obeys [137]

$$\frac{\partial C_H}{\partial t} + \left(\frac{R}{r}\right)^2 \frac{dR}{dt}\frac{\partial C_H}{\partial r} = D\frac{\partial^2 C_H}{\partial r^2} + \frac{2}{r}D\frac{\partial C_H}{\partial r} \tag{6.1}$$

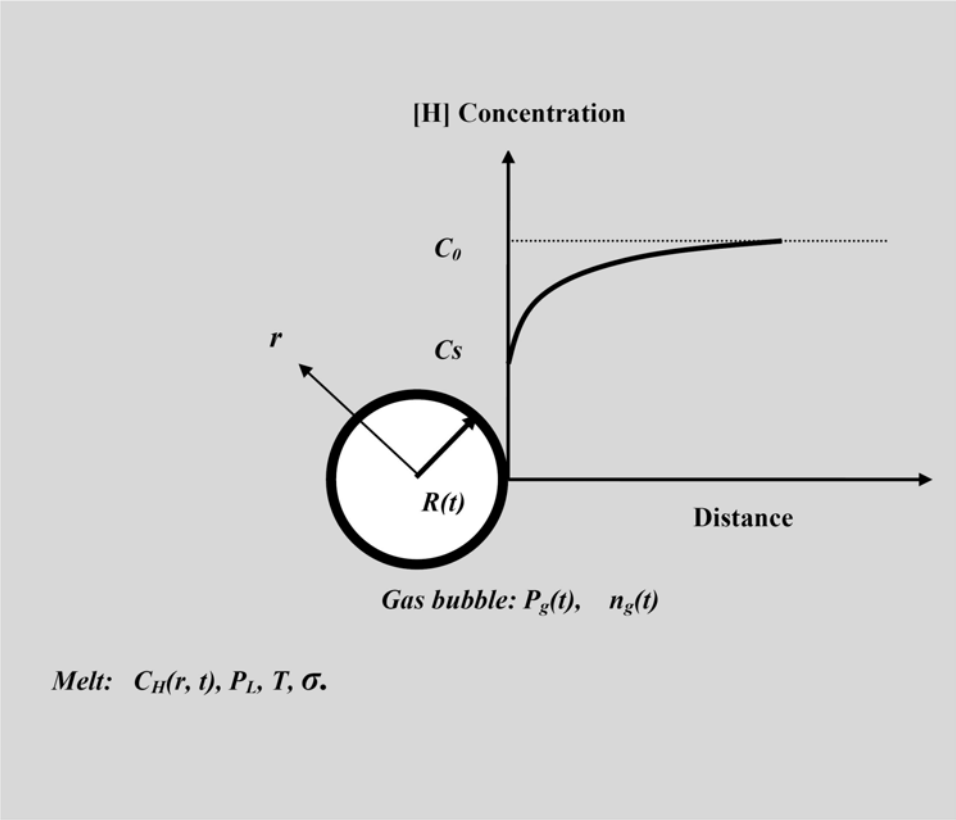

Figure 6.1: Schematic illustration of the hydrogen diffusion-controlled bubble growth model.

where t is time, r is the spherical radial coordinate, R is the bubble radius, C_H is hydrogen concentration and D is hydrogen diffusivity. The hydrogen diffusivity is taken to be 3×10^{-2} cm^2/s, following [128].

Inside the bubble, the gas obeys the ideal gas law

$$P_g V_g = n_g RT \tag{6.2}$$

where P_g , V_g and n_g are the total gas pressure, volume and number of moles respectively. The gases inside the bubble will in general be of two types: (i) insoluble gases of constant mass and (ii) hydrogen from the melt. From the ideal gas mixture law and pressure balance, one has

$$P_H + P' = \frac{3n_H R_g T}{4\pi R^3} + \frac{4\pi r_0^3 P_L + 8\sigma\pi r_0^2}{4\pi R^3} = P_L + \frac{2\sigma}{R} \tag{6.3}$$

where n_H is the hydrogen amount of hydrogen inside bubble, and P_H and P' are the partial pressures of hydrogen and insoluble gas in the bubble respectively.

6.2.2 Boundary and Initial Conditions

The initial and boundary conditions for Equation (6.1) are

$$\begin{aligned} &R(t) = r_0, \quad C_H(r,t) = C_0 \quad (t < 0, r > R(t)) \\ &C_H(r,t) = C_H^s \quad (t > 0, r = R(t)) \\ &C_H(r,t) = C_0 \quad (t > 0, r \to \infty) \end{aligned} \tag{6.4}$$

where C_H^L is the hydrogen concentration at the bubble/liquid metal interface; this is assumed to obey Henry's law

$$C_H^L = K_H (P_H)^n \tag{6.5}$$

where P_H is the hydrogen partial pressure inside the bubble. K_H is Henry's constant and n is set to 0.5 consistent with the published hydrogen solubility in the titanium system [94].

At the gas-liquid interface, due to the mass conservation of hydrogen diffusion, we have

$$\frac{dn_H}{dt} = 4\pi R^2 D \frac{\partial C_H}{\partial r}\Big|_{r=R} \tag{6.6}$$

The equation set (6.1)–(6.6) can be solved by using standard finite difference methods.

6.2.3 Implementation of the Model

The calculation procedure to solve the above equation set is as follows:

1. Input temperature T, initial hydrogen concentration C_0 and initial bubble radius r_0 and surface tension σ.
2. Set the initial and boundary conditions.
3. Calculate the insoluble gas content using equation (6.2).
4. Perform the hydrogen diffusion calculation within the melt by solving equation (6.1).
5. Calculate the hydrogen flux through the gas-liquid interface via equation (6.6).
6. Update the gas-liquid interface position by using the volume fraction method (VOF).
7. Check whether the hydrogen concentration at the gas-liquid interface reaches the hydrogen concentration at the surrounding liquid. If not, go to the next iteration, step 4.

The material properties and physical constants were taken from the literature, and are given in Table 6.1.

Table 6.1: Material properties and physical constants used in calculation.

Temperature of melt (K)	2000
Surface tension (N/m) [37]	1.18
Henry's constant for hydrogen in liquid titanium(Mol/L/atm)[84]	1.439

6.3 Results

6.3.1 Dynamic growth of bubble inside weld pool

Figure 6.2 shows the predicted pore radius as function of time for growth of a bubble in unbounded liquid metal, with the hydrogen level of the melt ranging from 100 ppm to 300 ppm.

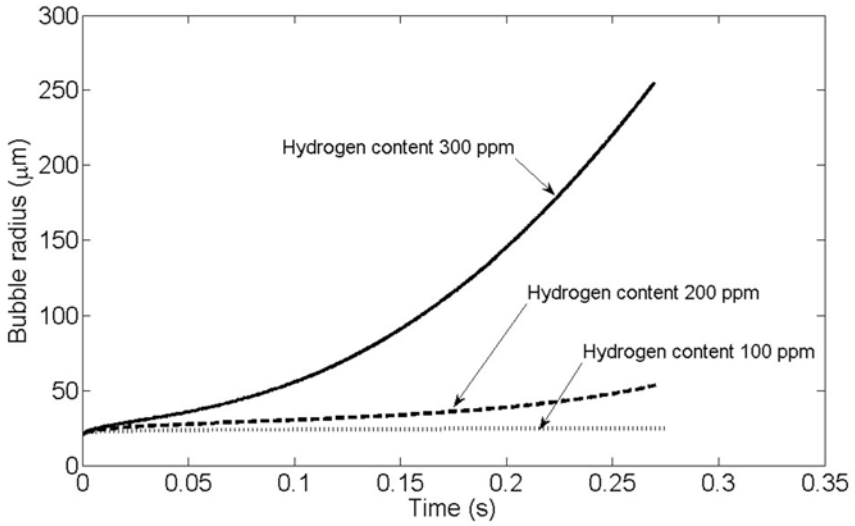

Figure 6.2: Calculated bubble radius evolution with differnt hydrogen content in the melt.

The pre-existing bubble size is assumed to be 20 μm, and ambient pressure to 10^{-4} mbar – typical of the vacuum conditions employed during the electron beam welding of titanium alloys. One can see that the hydrogen content of the melt has a strong influence both on the bubble growth rate and the final size of the bubble. During bubble growth, the associated pressure inside the bubble evolves as shown in Figure 6.3, in this case for hydrogen content of 300 ppm in the melt. The partial pressure of the pre-existing insoluble gas decreases, whilst the hydrogen partial pressure increases rapidly in the early stage of bubble growth due to the very small initial bubble volume. The rapidly increasing hydrogen partial pressure increases the hydrogen level at the interface, thus reducing the hydrogen concentration gradient in the liquid metal around the pores and thus slowing down bubble growth. After the hydrogen partial reaches a peak value of around 6×10^{-4} Pa, it decreases thereafter with a further increase of the bubble radius.

This is because the increasing bubble volume dominates the pressure change inside the bubble as its size gets large. The decreasing hydrogen level at the interface coupled with the increasing area surface of the bubble favours hydrogen diffusion into the bubble, and its rapid growth. Consistent with the local equilibrium assumption of the hydrogen concentration at the bubble/liquid metal interface, the hydrogen level at the interface evolves as shown in Figure 6.4.

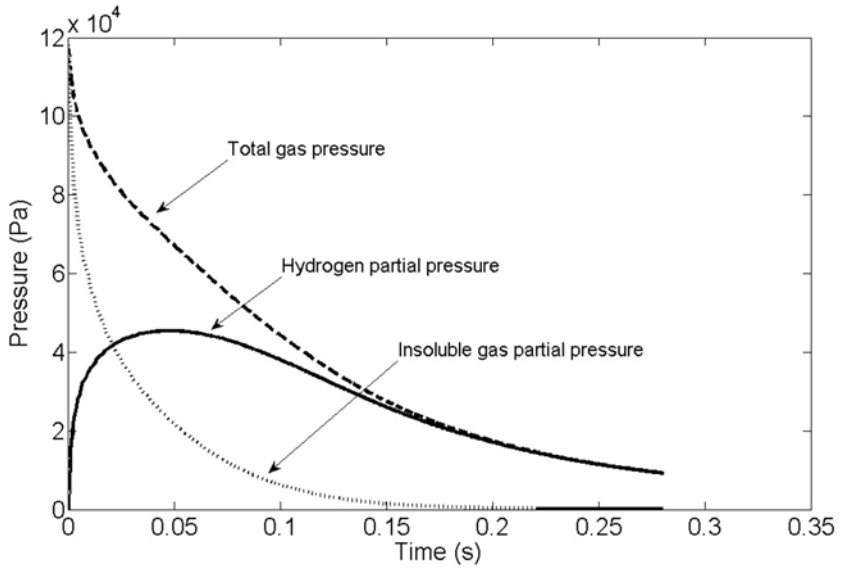

Figure 6.3: Pressure evolution during bubble growth with hydrogen content of 300 ppm in the melt.

The peak hydrogen level at the interface as indicated in Figure 6.4 is around 260 ppm, which is lower than the initial hydrogen level in the liquid metal (300 ppm). For as long as the hydrogen level in the liquid metal is higher than that at the interface, hydrogen diffuses from the liquid metal into the bubble, thus driving bubble growth. However, according to the evolution of the hydrogen level at the interface, there exists a hydrogen threshold in the liquid metal, which can limit bubble growth. The factors which affect this critical hydrogen level for bubble growth in the weld pool – pre-existing bubble size, surface tension and ambient pressure – are discussed in the next section.

6.3.2 Critical hydrogen level analysis

The above indicates that during bubble growth, a peak hydrogen level at the bubble/liquid metal exists. If the hydrogen level in the liquid metal is higher than this critical hydrogen level, the bubble keeps increasing in size until a balance between the hydrogen level at the interface and the residual hydrogen in the liquid metal is reached. It is of interest to determine the factors which influence this critical hydrogen level. Figure 6.5 illustrates how the pre-existing bubble

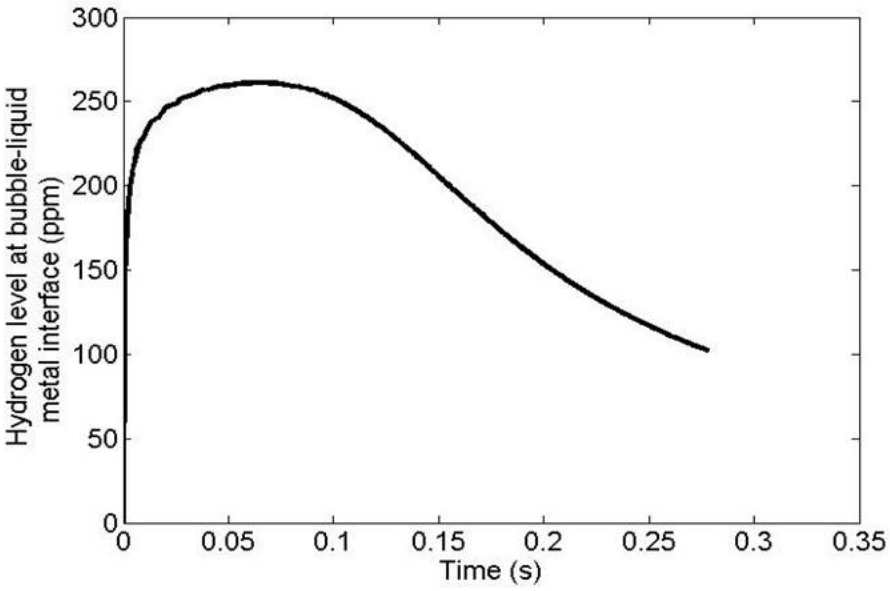

Figure 6.4: The evolution hydrogen concentration at gas-liquid interface during the bubble growth with hydrogen content of 300 ppm in the melt.

size, surface tension and ambient pressure affect the critical hydrogen concentration. When the pre-existing bubble radius decreases from 30 μm to 5 μm, the critical hydrogen level increases from 200 ppm to 450 ppm; hence the larger the pre-existing bubble, the lower the hydrogen level required in the liquid metal for pore formation. Our results indicate that surface tension will also play a crucial role in bubble formation; the critical hydrogen level drops with decreased surface tension. Since for titanium alloys the temperature coefficient of the surface tension has a gradient of -2.4$\times 10^{-4}$ N/m-K [37], higher temperatures in the weld pool (high beam powers and/or low welding speed) will favour bubble formation. Finally, one can see that the ambient pressure used for welding will also influence bubble formation: a better vacuum decreases the critical hydrogen level for bubble formation.

6.4 Discussion

The modelling results presented above provide insight into the factors leading to porosity formation in the welds of titanium alloys. In practice, these alloys are prone to the formation of

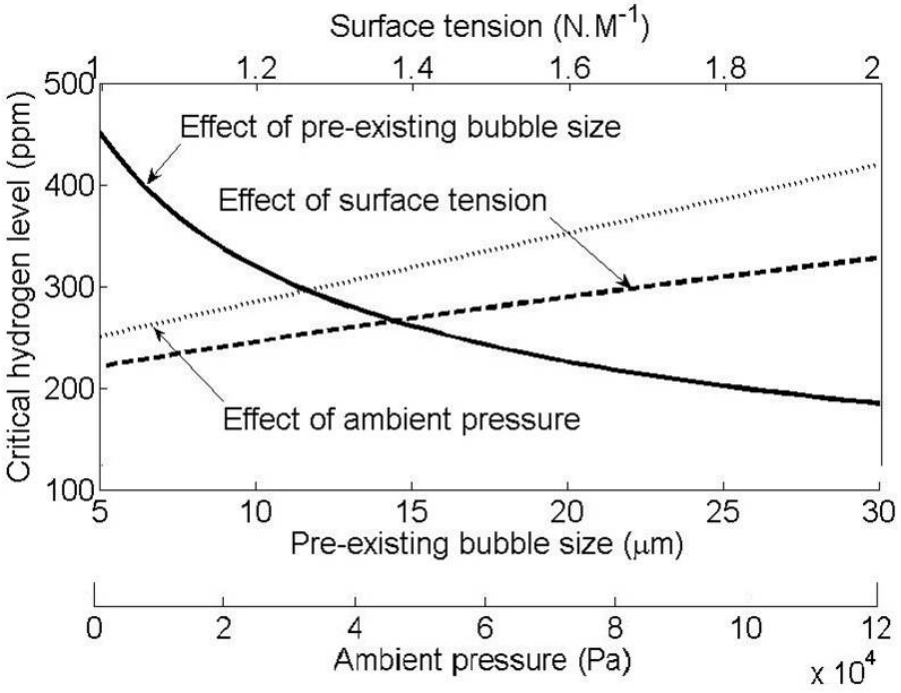

Figure 6.5: Effect of pre-existing bubble size, surface tension and ambient pressure on critical hydrogen level for bubble growth.

porosity [83, 84]. Pores are often of diameter 0.1 mm or greater, and can therefore be detected by non-destructive testing (NDT) methods such as x-ray tomography and the shape of the pores in these cases is spherical - which has been identified in chapter 3. Experimentation involving the piercing of such porosity followed by residual gas analysis using Residual Gas Analysis (RGA) hidden gas analyser in chapter 3 has confirmed that hydrogen is indeed present as the majority gas phases in the pores, confirming its involvement in this phenomenon.

The results indicate that hydrogen–whether present in intrinsic form in the metal being welded or alternatively produced by breakdown of hydrocarbons by the action of the welding arc–will prefer to migrate to the molten zone when fusion occurs. Then, as the molten zone cools prior to its solidification, the solubility of hydrogen will be reduced thus providing the opportunity for growth of hydrogen-filled bubbles by their diffusion-controlled growth from the hydrogen-enriched liquid. Unless such bubbles are able to escape from the molten pool, they will then become frozen into the weld region causing the porosity which is observed. This mechanism

of porosity formation explains a number of key observations concerning this phenomenon. First, that porosity is exacerbated when cleanliness is poor and/or when the hydrogen content of the metal is significant, because when no hydrogen is present this form of porosity will not occur. Second, that porosity is very much less likely in autogeneous (bead-on-plate) welds rather than butt joints, and exacerbated when the surfaces to be welded are rough. This is because–as indicated by the calculations– pre-existing bubbles are a prerequisite for their subsequent growth. We postulate that the pre-existing bubbles needed for large pore formation will become available when butt joints are used due to the presence of asperities at the mating surfaces; such sites will not be available when autogeneous (bead-on-plate) welds are produced. When the beam passes through these cavities, they can get filled with gas and form pre-existing bubbles in the weld pool which are needed for gross porosity to occur. Third, that porosity is more likely under improved vacuum conditions and at greater welding powers/slower speeds when the temperature of the melt pool is higher. It is our belief that these ideas are worthy of thorough testing using design-of-experimentation methods.

One final point relates to the frequency of hydrogen-based porosity in titanium welds. For such processing, the occurrence of such defects is relatively rare and usually irregular –so that one might think of its mechanism as being essentially stochastic. Why might this be the case? It is suggested that the necessary conditions needed for porosity to be present: (i) hydrogen of sufficient concentration, (ii) pre-existing sites for bubble growth, and (iii) trapping of the hydrogen-filled bubbles to form pores upon freezing, might combine to make porosity relatively rare even when conditions are favourable. One might argue for example that a majority of the gas bubbles are able to escape from the weld pool so that porosity is avoided. But more work is needed to expand on these ideas so that probabilistic modelling can be accomplished.

6.5 Summary and Conclusions

The following conclusions can be drawn from this work:

1. A hydrogen diffusion-controlled bubble growth model has been proposed, to quantify the effect of hydrogen on porosity in titanium welds.

2. A critical hydrogen level for pore formation in the molten zone is needed. Large pre-existing bubbles, low vacuum pressure and low surface tension – which is favoured by high temperatures and therefore high power intensity and/or low welding speeds – exacerbate hydrogen porosity.

3. The modelling provides insight into the role played by hydrogen during porosity formation caused by welding of titanium alloys. A potential way to suppress large porosity formation is to limit the bubble growth either by reducing hydrogen levels in alloys or improving the surface preparation to avoid large pre-existing bubbles formation, which significantly reduces the hydrogen barrier for large bubble formation.

7

Experimental Investigation of Proposed Porosity Formation Mechanism

Summary

The effect of hydrogen on porosity formation is further investigated in this chapter. Hydrogen charging is used to achieve different hydrogen levels prior to welding. The results confirm that porosity can be suppressed even at every high hydrogen levels, when welding is carried out with optimised welding parameters and perfect joint alignment; on the other hand, porosity is exacerbated when a small beam offset is employed. This is because any beam offset alters the size of the liquid zone at the melting front, where the joint edges first become melted. It is proposed the thickness of the liquid film at the melting front is crucial for bubble nucleation and their survival in the weld pool; bubbles can escape through the keyhole by breaking through this liquid film, when it is too thin. This challenges the common assumption of bubble escape by flotation to the weld pool surface. Thus the nucleation rate in the liquid zone at the melting front determines the likelihood of porosity occurrence. This suggests that the beam offset is likely to be one factor influencing porosity formation in these circumstances. This chapter provides fundamental insights into the mechanism of porosity formation during the welding of titanium alloys and guidance to aid in its elimination.

7.1 Background

Porosities are occasionally found in keyhole mode electron beam full-penetration welding of titanium-based alloys. Unfortunately, at the present time, an unequivocal explanation for porosity formation in titanium welds is unavailable. The literature does however provide some important clues concerning its probable cause. An early empirical study indicated that porosity formation depends greatly upon the geometry of the welded joint and its edge preparation [82]. More recent studies have identified a qualitative dependence of weld porosity on surface condition [83], so that surface contamination due to different surface preparation methods might be influential. The hydrogen content of the base material has also been implicated [79, 82]. Others have pointed out that the thermal cycles experienced during welding can be expected to cause hydrogen migration in and around the weld region [84].

In chapter 5, the weld-induced hydrogen migration in these systems is simulated, proving that a build up of hydrogen in the melted region is expected on the basis of a coupled thermodynamic/diffusion analysis of this problem [138]. The balance of evidence would seem to point to an effect due to hydrogen, although no categorical proof of this exists as yet; moreover a quantitative treatment of the effect of hydrogen on bubble formation and growth is carried out in chapter 6, experimental work on quantitative investingation of hydrogen effect on bubble formation is still lacking. In this chapter, a series of targetted experiments are designed to investigate the hydrogen effect on porosity formation quantitatively. Ti-6Al-4V samples are electrochemically charged to achieve different hydrogen content prior to welding. The welding of hydrogen charged samples is characterised, and hydrogen effect on porosity formation is discussed.

7.2 Experiment Details

7.2.1 Sample

Materials used in this study are Ti-6Al-4V plates, which are cut off from a large forged compressor disc. Samples are rectilinear plates with length of 300 mm, width around 30 mm and varying

thickness from 4.0. Figure 7.1 shows the microstructure of the as-received samples, which shows a bi-modal structure was developed with globular primary α with grain size of tens microns. Sample surfaces have been milled and the surface roughness measurement results shows that the joint surfaces of the as-received sample is very smooth, with Ra value around 0.5 μm as shown in Figure 7.2.

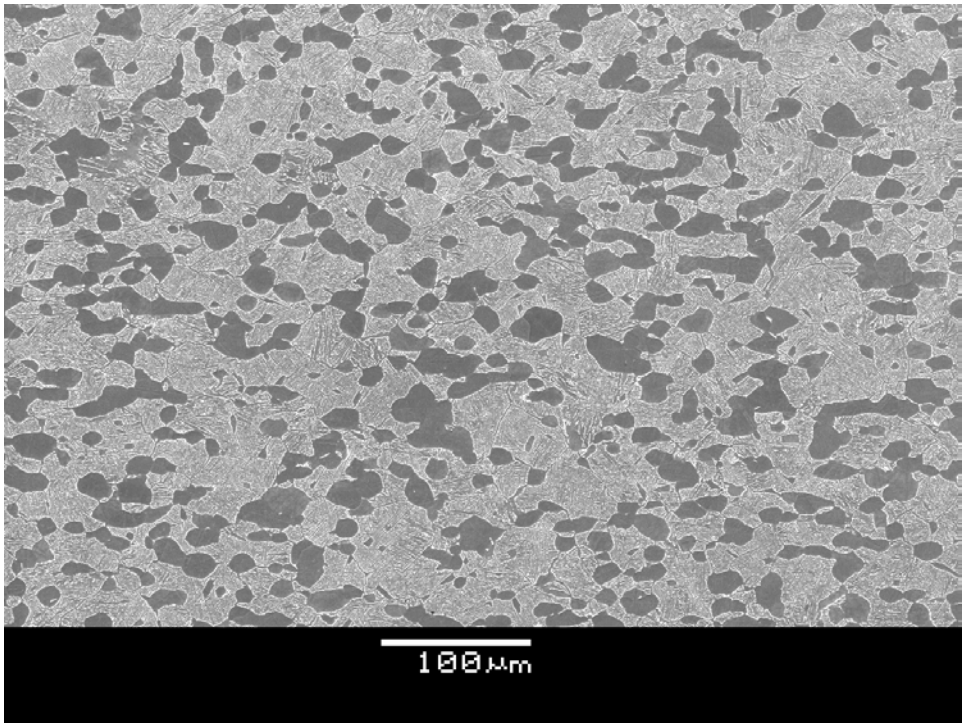

Figure 7.1: Scanning electron microscopy illustrating the microstructure of the as-received Ti-6Al-4V sample.

7.2.2 Welding Trials Design

To investigate hydrogen effect, surface preparation and electron beam parameters will affect porosity formation. Sets of welding trials have been carried out, as follow:

- Set 1: Samples are prepared with wide range of hydrogen content, aiming to determine the maximum bearable hydrogen content in electron welding process and the proper ranges of hydrogen content for further tests. Different surface preparation methods are also applied. Qualitative effects of hydrogen content and surface preparation on porosity formation

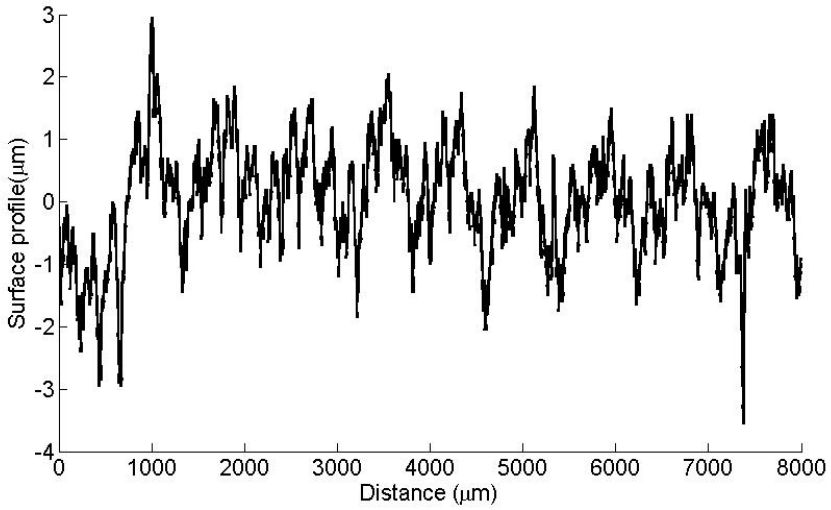

Figure 7.2: Measure surface roughness profile of as-received Ti-6Al-4V samples.

are expected from the results of this set of welding trials to determine which one is the dominant factor.

- Set 2: Samples with appropriate range hydrogen content and surface preparation determined in set 1 are prepared to repeat the welding process, aiming to quantify the effect of hydrogen content and surface preparation on porosity formation.

- Set 3. Sets of electron beam parameters are used to weld samples with fixed hydrogen content and surface preparation, aiming to investigate the effect of electron beam parameters on porosity formation. Guidance of minimisation of porosity formation by electron beam optimisation is expected from the results of this set of welding trials.

7.2.3 Electrochemical Hydrogen Charge

To increase the hydrogen content in the base material, electrochemical hydrogen charge (cathodic) was performed at room temperature, in a H_3PO_4: glycerine (1:2, v/v) electrolyte, with constant current density of 50 mA/cm^2 applied by using the DC power supply. More details of the hydrogen charge can be found in [139]. Due to the limit of the maximum power supply and the size of electrolyte basin, samples for hydrogen charging were cut to have dimensions of 100

mm in length, 30 mm in width and 4 mm thickness. For the 1st set of welding trials, the charging time applied to sets of samples ranged from 6 hours to 18 hours. Table 7.1 gives the details of the hydrogen charging time and samples surface preparation methods. To increase the possibility of bubble nucleation at the melting front, the joint surfaces were ground off by about 100 μm by using SiC paper (P60) to increase the surface roughness. Since the hydrogen charging was performed at strong acid conditions and the etching effect might decrease the surface roughness, surfaces were ground both before and after the hydrogen charging. To investigate whether the charged hydrogen can be held inside the sample during the storage time before they get welded, different delay time were applied prior to welding. For the quantitative hydrogen content in the charged sample, it has been reported that 18-hours charged samples have a hydrogen content more 2000 ppm in weight percentage as shown in for 18 hours charge as shown in Figure 7.3 [139]. However more reliable valves still need quantitative measurements, because the measured hydrogen content might depend on the size of the bulk material, which was not reported in previous research.

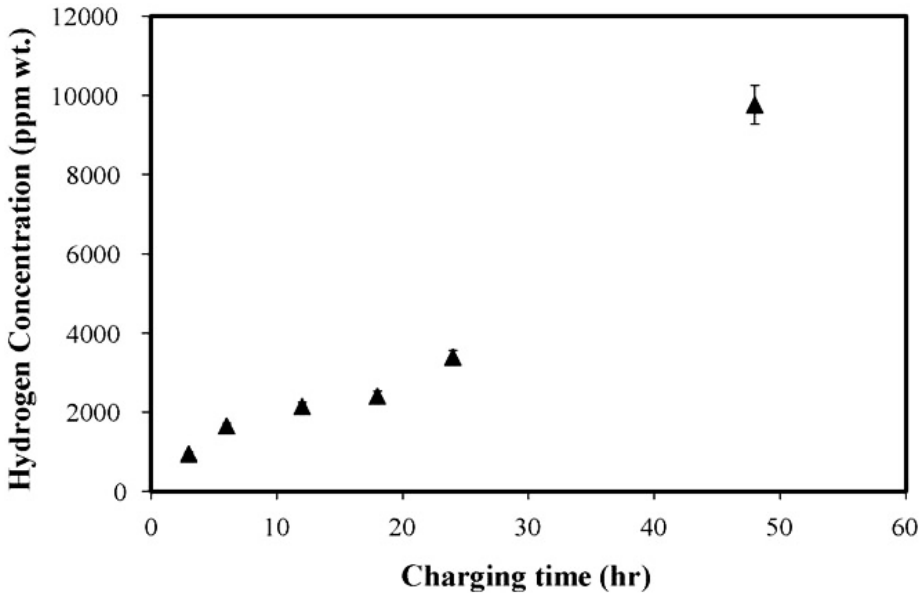

Figure 7.3: Reported hydrogen uptake in Ti6Al4V alloy after electrochemical hydrogen charge with different charging times [139].

Table 7.1: Sample preparation of the 1st set of welding trials.

Group NO.	Weld NO.	Charging time (hours)	Delay for welding after charging	Surface Preparation Method		
				1*	2**	3***
I	1	6	3 months	×		
	2	12	3 months	×		
	3	18	3 months	×		
II	4	6	2 weeks	×		
	5	12	2 weeks	×		
	6	18	2 weeks	×		
III	7	0	-	–		
	8	0	-	–		
IV	9	6	Within 1 week		×	
	10	12	Within 1 week		×	
	11	18	Within 1 week		×	
	12	12	Within 1 week	×		
	13	12	Within 1 week			×
	14	0	Within 1 week			×

Surface preparation method:

* Grinding by using SiC paper (P60) after hydrogen charge

** Grinding by using SiC paper (P60) before hydrogen charge

*** Polishing and making indentation before hydrogen charge

Table 7.2 summaries the sample preparation used in the 2nd set of welding trial, in which the charging time range is determined by the results of the 1st set of welding trials. Since at the specific electron beam welding condition, 6 hours charging samples contain the threshold value of hydrogen content to obtain a sound weld bead, the charging time applied ranged from 1 hour to 5 hours. To investigate the surface effect on porosity formation, joint surfaces with and without degrading are applied.

7.2.4 Electron Beam Welding

All welding trials were performed at Rolls-Royce plc, Derby, UK with proprietary welding conditions. For all the testing welds, the welding processes were monitored by measuring appropriate parameters, such as the beam current, vacuum inside the working chamber, etc...

Table 7.2: Sample preparation in the 2nd set of welding trials.

Group NO.	Weld NO.	Charging time (hours)	Delay for welding after charging	Surface Preparation Method	
				1*	2**
VI	15	5	3 months	×	
	16	4	3 months	×	
	17	3	3 months	×	
	18	2	3 months	×	
	19	1	3 months	×	
	20	5	3 months		×
	21	4	3 months		×
	22	3	3 months		×
	23	2	3 months		×
	24	1	3 months		×

7.2.5 Quantitative Hydrogen Measurement

Quantitative hydrogen measurement is a challenge due to the significant hydrogen range (namely hundreds of ppm to thousand ppm in weight percentage) used in this study. For low hydrogen levels, the inert gas fusion method can be used to do the hydrogen measurement. Here samples are melted under an inert gas stream in a graphite crucible and the gas evolved was measured by thermal conductivity or infra-red absorption. However, due to the difficulty of calibration, the maximum hydrogen which can be measured in this type of system is usually limited to around 200 ppm; for higher hydrogen content measurement, it is necessary to resort to thermogravimetric analysis (TGA). In both of the above two methods, samples are heated to release the volatile components from the samples; in the former method, the release of volatile components is monitored and quantified by mass spectrometry, and in the latter one, the amount of the volatile component is quantified by measurement of the weight loss during the operation. To identify the gas in the TGA measurements, mass spectrometry (MS) can also be used in a so-called TGA-MS system.

In this study, in order to determine the hydrogen content as a function of time, both the inert gas fusion method and the TGA-MS method have been used. The measurement strategy

was as follows: first, hydrogen in the uncharged samples was measured using the inert gas fusion method, using a LECO RH404 analyser at IncoTest, UK. After determination of the initial hydrogen content in the base material, hydrogen in charged samples were measured in the same way. Unfortunately, with sufficient charging, the hydrogen contents in the charged samples were beyond the calibration of the LECO system (>200 ppm). For higher hydrogen content from the longest changing times, the hydrogen was initially measured using the TGA-MS system, at Hidden Isochema Ltd, UK, and then, the analysed samples were sent to IncoTest for residual hydrogen measurement by using the LECO RH404 system. Concerning the accuracy and reliability of the measurement results, the LECO RH404 can provide an accuracy up to 2% of the reading. In the TGA-MS system, the resolution of weight measurement is 0.2 μg, and the maximum sample weight is limited to 4.5 g, so the accuracy depends upon the total weight of the sample tested.

Samples for hydrogen analysis were cut using SiC cutting blades with water cooling. This might have a tendency to induce more hydrogen into the cut surfaces of the samples due to high temperature at the front of the blade during the cutting process. To minimise any such effect, all cut surfaces of the samples were ground off by about 50 μm using a MD-Piano 220 grinding disc. After grinding, samples were washed using ultrasonic cleaning in ethanol and dried. The sample weight for the LECO RH404 system was around 0.1∼0.2 g, leading to Ti-6Al-4V sample volume of around 22∼44 mm^3. Considering a 4mm-thick plates, samples for hydrogen measurement were cut off parallel to the joint edges of the plates with 3 mm offset. So the samples for the hydrogen analysis in the LECO RH404 system had dimensions of 4 mm thickness, 3 mm in width, and a length of approximately 3 mm. The weight of samples for TGA-MS system was around 3.5 g, and typical dimensions 10 mm × 2 mm × 4 mm.

7.2.6 X-Ray examination of defects in welds

X-ray non-destructive testing (NDT) methods were used for porosity detection in this study. For a rapid investigation of large pore formation, conventional X-ray film radiography was

performed at Rolls-Royce plc, UK, Derby. The resolution of conventional X-ray radiography can approach around 2% of the thickness of the specimen. For higher resolution measurements, three dimensional X-ray computed tomography was used. Details of the X-ray tomography were given in chapter 3.

7.3 Results and Discussion

7.3.1 Characterisation of Hydrogen Charged Samples

Hydrogen charged samples were characterised. Figure 7.4 (a) shows the surface morphology of these samples prior to hydrogen charging. For short times (<6 hours), no change in surface morphology was found via scanning electron microscopy. For longer hydrogen charging, the sample surfaces were corroded, and small cavities were identified, see in Figure 7.4 (b). If the hydrogen charging time is longer enough (>18 hours), cracks occurred at the sample edges as shown in Figure 7.5. This might be due to the formation of the titanium hydride phase.

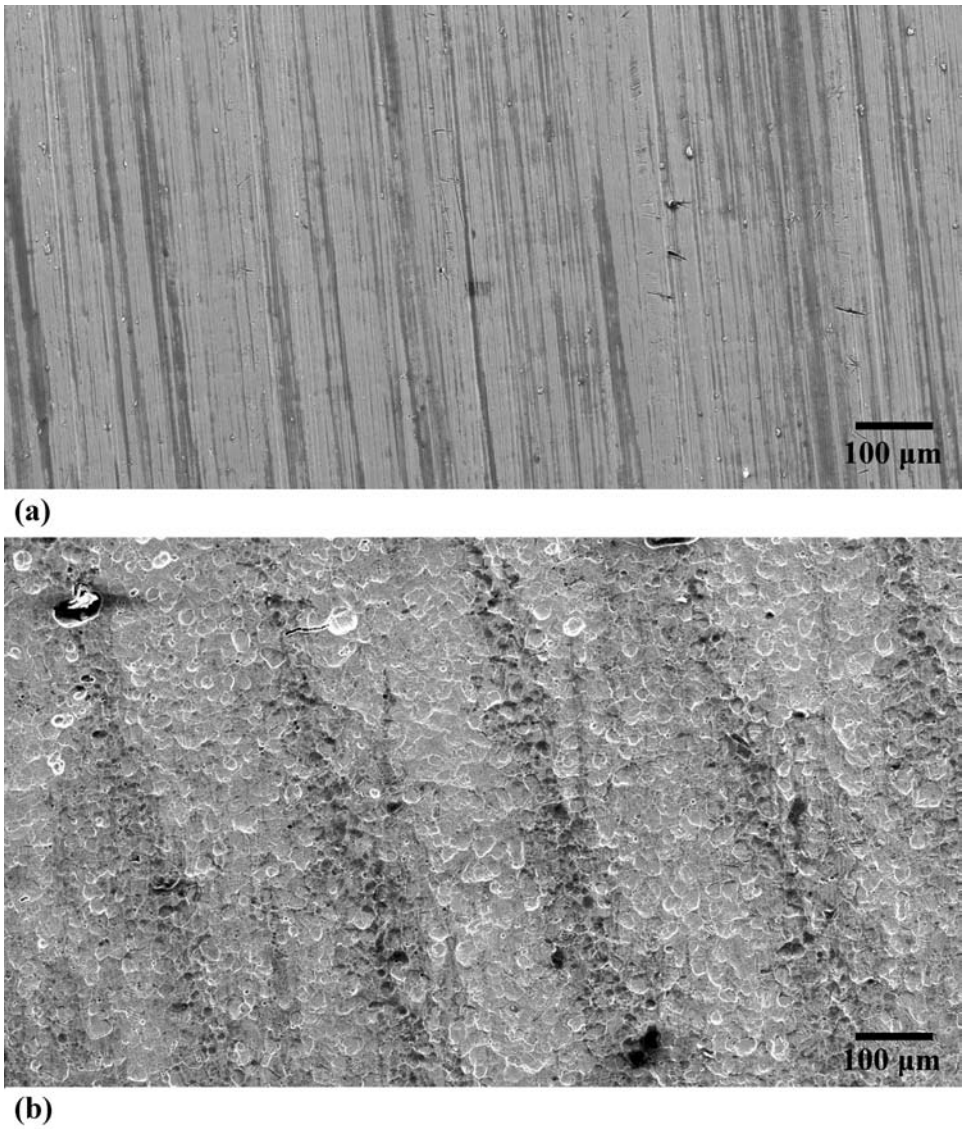

Figure 7.4: SEM micrograph of uncharged (a) and 12-hours charged (b) sample surfaces.

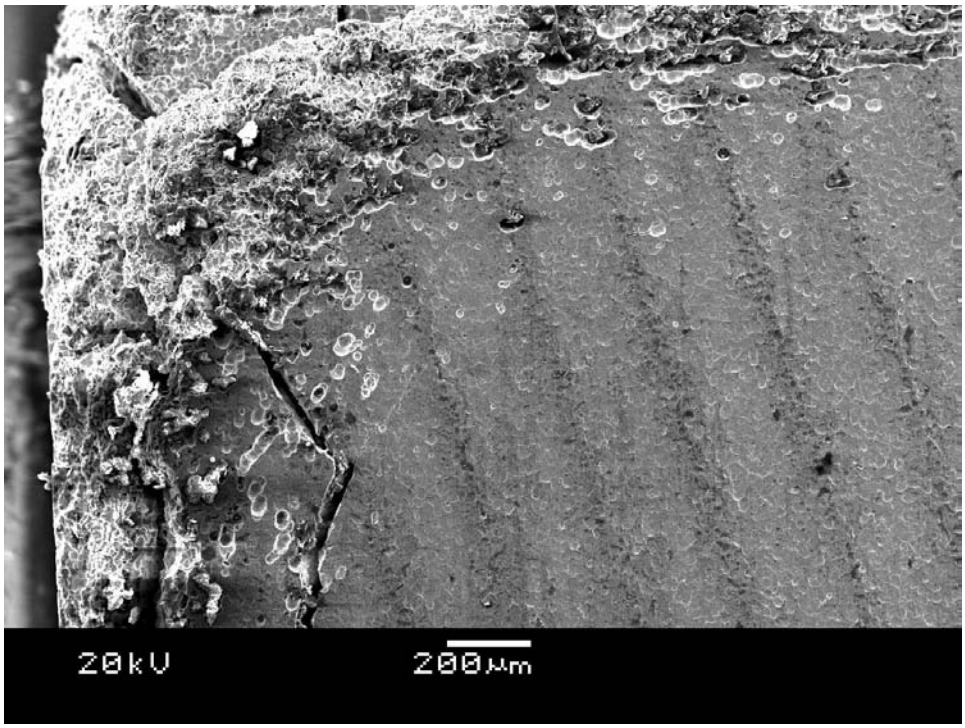

Figure 7.5: Crack at sample edge after 12 hours hydrogen charge.

The hydrogen measurement results obtained using the LECO RH404 system confirmed that the hydrogen uptake rate is approximately linear with time, at 50 ppm/hour. For measurements of higher hydrogen content, the TGA-MS system was used. The hydrogen content in the charged samples was found to be not high enough to provide sufficient signal due to the sensitivity limit of the TGA-MS system. It needs to be pointed out that the measurement result is different with the value reported in [139] as can be seen in Figure 7.3. This is probably due to the differing sample size.

7.3.2 Electron Beam Welding of the Hydrogen Charged Sample

Figure 7.6 shows the electron beam current and detected pressure rise in the working chamber when welding a sample charged for 6 hours. One can see that when the beam reaches its maximum power, a very significant pressure rise is detected, which confirms that strong hydrogen degassing occurs. With an increase in charging time, the detected pressure level also increases dramatically, see Figure 7.7. It can be concluded that the pressure rise in the working chamber

is directly related to the hydrogen gas released from the sample during the welding process. Unfortunately it is not totally clear whether hydrogen escaping from the weld pool induced bubbles and pores. If the bubbles were induced by hydrogen, one would expect that a few bubbles would be trapped during solidification or captured by the weld pool surface. None were identified.

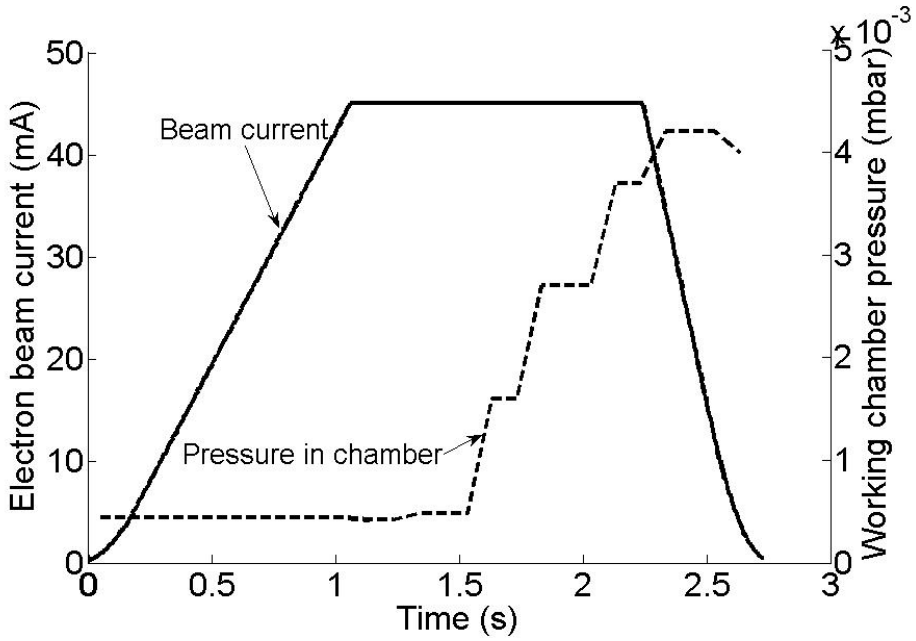

Figure 7.6: Measured pressure rise in the working chamber.

Figure 7.8 shows micrographs of the top surfaces of the weld beads after hydrogen charging to different times. As the hydrogen content increases, the quality of the weld joint was found to decrease. Charging for 12 hours caused extensive spattering. Nevertheless, no porosity was found either by conventional film X-ray radiography or high resolution X-ray tomography (5 μm). When looking at the cross-section of the 12-hours charged samples, significant undercut was observed, and very small pores (of diameter less than 1 μm) were located at the edge of the fusion zone, as shown in Figure 7.9. It seems that gas pores formed in the liquid metal when the hydrogen concentration was large, but due to the strong evaporation, hydrogen-rich liquid metal spattered away. This rationalises why there is no porosity found in samples with very high hydrogen content, but cannot explain why there is no porosity found in the 3-hours and

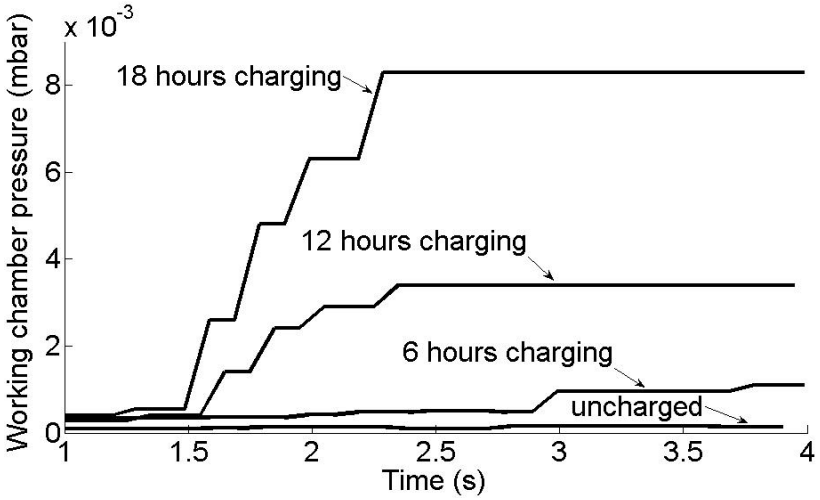

Figure 7.7: Detected pressure rise during welding of sample charged with different time.

6-hours charged samples. The quality of the weld beam seemed normal, and no undercut was found.

A further point relates to the very significant pressure rise observed in the pressure chamber during welding of the hydrogen-charged samples; this confirms that hydrogen does indeed outgas during processing. In an optimised electron beam welding process, the keyhole is stabilised by an optimised energy input. The liquid metal film around the keyhole at the melting front is very thin, which enables the bubbles nucleated at the joint edges to break through the keyhole wall and thus to escape. To increase the possibility of bubble survival inside the weld pool, we postulate that a wider liquid region at the melting front is required. One possible way to achieve this condition is beam offset welding, as illustrated in Figure 7.10. To confirm whether the beam offset contributes to the porosity formation, beam offset welding was performed by preparing butt joint welds using material charged for 6 hours. In Figure 7.10 (a), the beam offset value was increased linearly from 0.3 mm to 1.0 mm along a weld path of length of 100 mm. High resolution X-ray tomography was used for porosity detection. Pores were indeed found in the beam offset welds. Figure 7.10 (b) shows a gas pore from a beam offset value at 0.51 mm. Figure 7.10 (c) shows the cross section at a beam offset value of 0.65 mm, confirming lack of fusion and porosity formed at the joint edges. To elucidate the influence of the beam

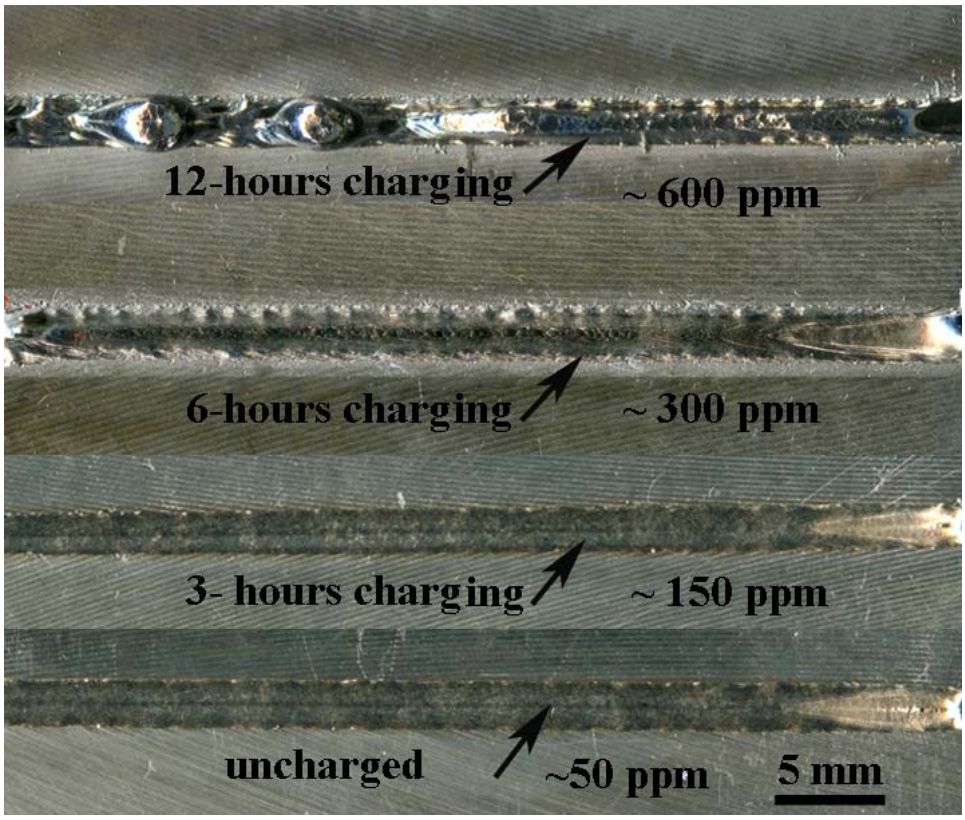

Figure 7.8: Top surfaces of weld beads for samples charged for different times.

offset effect on porosity formation more clearly, more work needs to be done. But from above the results we have presented here, it would appear the beam offset influences the probability of pore formation in a significant way.

One final point relates to the frequency of hydrogen-based porosity in titanium welds. The occurrence of such defects is relatively rare and usually irregular. It is suggested that the necessary conditions needed for porosity are: (i) hydrogen of sufficient concentration, (ii) pre-existing sites for bubble growth, and (iii) trapping of the hydrogen-filled bubbles to form pores upon freezing. These factors combine to make porosity relatively infrequent even when conditions are favourable. Undoubtedly, bubble escape from the keyhole is occurring, and this effect needs to be accounted for in future research efforts.

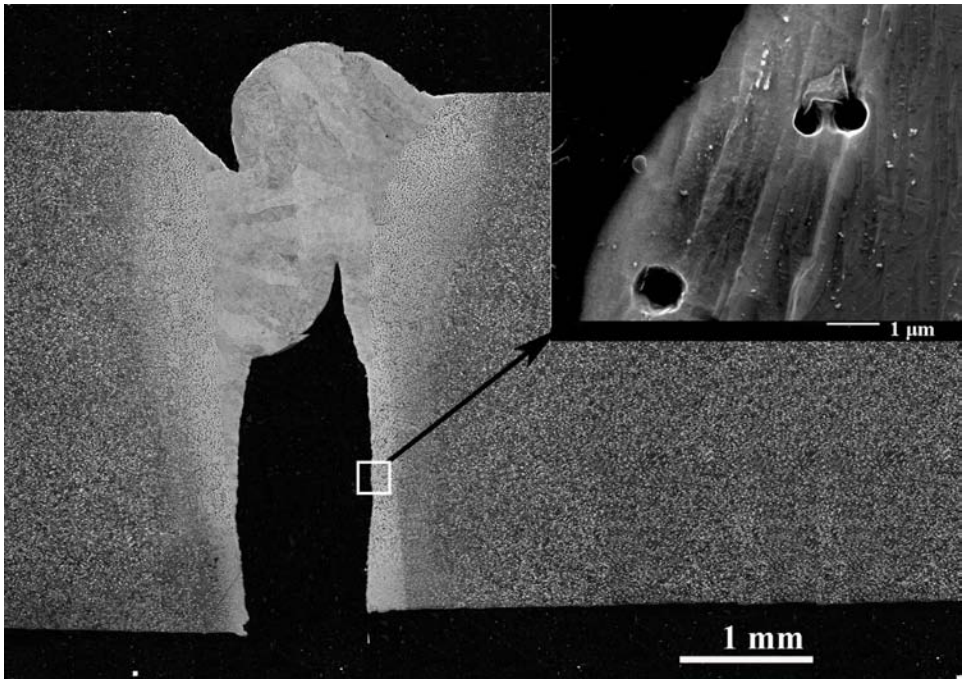

Figure 7.9: Undercut found in 6-hours charged sample with small pores at fusion boundary.

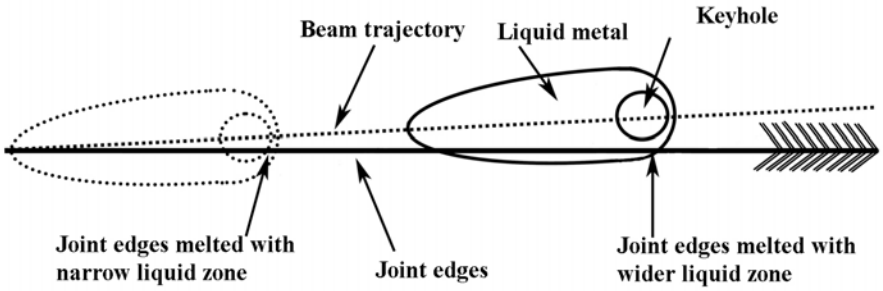

Figure 7.10: Liquid zone size around joint edges at melting front, and changes due to beam offset (BOF).

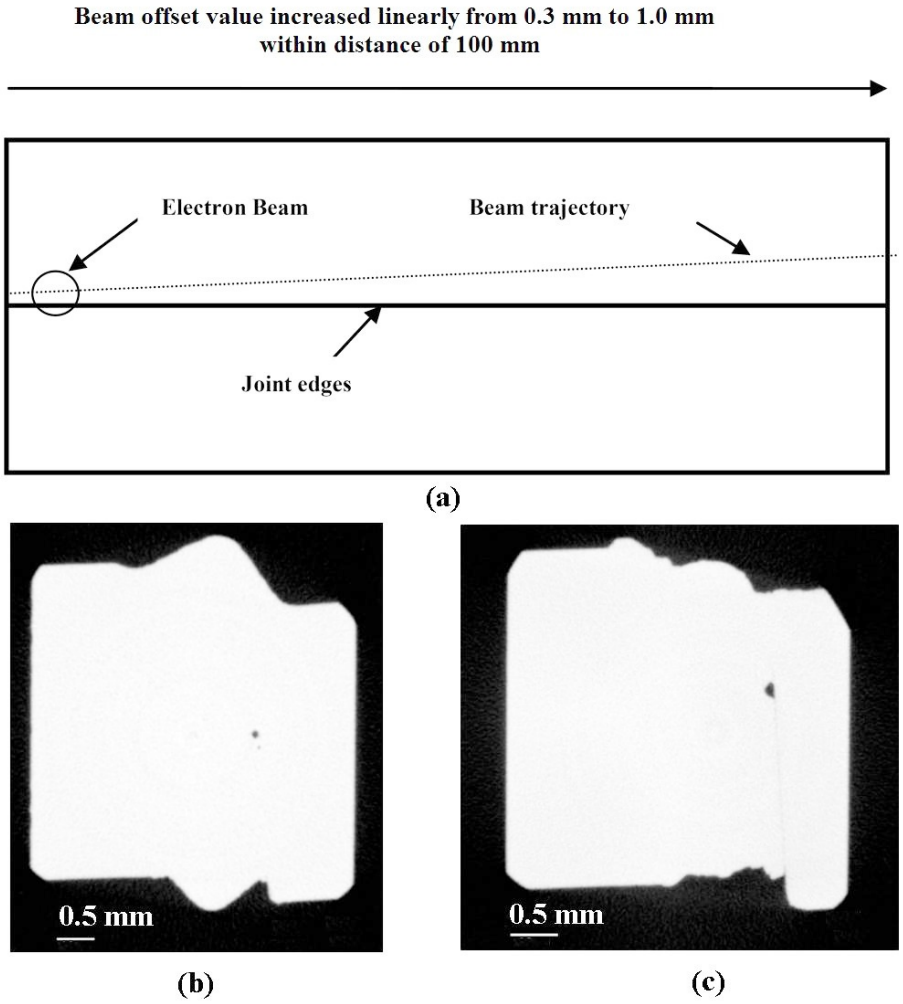

Figure 7.11: Porosity found in beam offset welding samples.

7.4 Summary and Conclusions

1. Electrochemical charging was used to achieve different hydrogen contents prior to welding; when optimised welding parameters were employed, it proved possible to suppress porosity formation by keyhole stabilisation.

2. Pores are found in hydrogen charged samples welded with a small beam offset. It is postulated that this is because a greater beam offset increases the size of the liquid region around the joint edges at the melting front. A wider liquid region at the melt front favours bubble growth and their survival after bubbles nucleate from the joint edges.

3. A stabilised keyhole, narrow melting front and perfect beam alignment are suggested to be effective ways to minimise porosity formation during keyhole mode electron beam welding of titanium alloys, where the possible presence of hydrogen cannot be avoided.

8

Conclusions and Future Work

This work has been concerned with the development of computational models for the electron beam welding process, and rationalising the porosity formation mechanism. The research conducted can be subdivided into three categories: (i) the characterisation of electron beam welded titanium-based alloys and the porosity formation in these welds, (ii) the modelling of electron beam welding process and hydrogen behaviour during welding and (iii) the modelling and rationalisation of the porosity formation mechanism.

By combining different X-ray non-destructive testing (NDT) methods, *e.g.* X-ray radiography and 3D computerised X-ray tomography (CT), the location and morphology of pores formed in the electron beam welds have been characterised precisely in three dimensions, this providing the basis for further experimental work on the pore formation mechanism. The detected spherical morphology and smooth inner surfaces of pores are strong evidence that porosity formation is involved with gas evolution during the electron beam welding process. It is believed that this work contains the first reported chemical analysis of the gas composition of such porosity. The results show that most of the gas inside the porosity is hydrogen (>90% volume percentage), with a small amount of CO_2 also being found. One gas has not been identified, whose atomic mass unit is 28 and with almost the same concentration as CO_2. Since both N_2 and CO have the same atomic mass unit of 28, they cannot be distinguished according to mass spectrometry analysis. If the unidentified gas is CO, this would indicate that the decomposition of hydrocar-

bons due to surface contamination is responsible for porosity formation; while if the unidentified gas is N_2, a totally different explanation for porosity formation is required. If N_2 exists, this indicates that air is involved with the mechanism of porosity formation. Pore formation can be triggered by small air pockets (asperities) entrapped between the two joint surfaces before the welding chamber is pumped down. Since the majority gas is hydrogen, for both of the above two cases, hydrogen is considered to be responsible for porosity formation.

There is a prerequisite for the investigation of hydrogen behaviour during electron beam welding process: modelling of the heat and mass transfer which occurs. To provide this, models have been built to simulate the electron beam welding process. Due to the very complex physical phenomena associated with the keyhole effect, modelling of the interaction between the electron beam and the weld material is still a big challenge. In this research, the deposition of electron beam energy into the workpiece is described using a modified three dimensional volumetric heat source model. Due to the flexibility of this approach, good agreement can be achieved between the predicted weld zone and the measured results. By combining heat transfer and thermodynamic/kinetic calculations, hydrogen distribution at the welded region has been estimated and found to be in good agreement with experiment, except within the fusion zone where the hydrogen level is very low. This is because in the current hydrogen transport model, hydrogen escape is assumed to occur at the surfaces of the weld pool only. In reality, hydrogen can also escape through the keyhole wall. To improve the model's accuracy for predicting hydrogen behaviour during the electron beam welding process, energy and mass transport modelling of the process needs to be improved, especially for the keyhole effect.

Due to the above mentioned limit of the models' capability to predict heat and mass transport inside the weld pool, the accuracy of the treatment of the hydrogen behaviour inside the weld pool is unlikely to be completely accurate. For this reason, models for prediction of hydrogen effect on dynamic bubble growth inside the weld pool need to be simple. First of all, a uniform hydrogen distribution inside the weld pool is assumed. To avoid a complicated coupled calculation of

liquid and gas fluid flow inside the weld pool, bubbles inside the weld pool are assumed to be quiescent. With the above assumptions, a pre-existing microbubble is assumed inside the weld pool, which triggers bubble growth; thus bubble nucleation process is unaccounted for. Bubble growth is driven by the diffusion of saturated hydrogen inside the weld pool towards the pre-existing microbubble, under the high vacuum condition. By taking account of the pre-existing bubble size, surface tension of the liquid metal, and the ambient pressure, dynamic bubble growth has been predicted, including the bubble radius dynamics, pressure change inside the bubble, and also the hydrogen profile in the liquid region surrounding it. The calculations show that a critical hydrogen level exists, which determines whether large bubbles can form. This sheds light on the answer to a challenging question: –what is the hydrogen level required in the weld pool required to form bubbles? It turns out that the required hydrogen level for bubble formation depends upon the temperature of the weld pool, the surface tension of the liquid metal, and also the nucleus size. Oxygen content inside the weld pool may be another factor which favours bubble growth. This is because the oxygen inside the weld pool changes the surface tension of the liquid metal; this is not considered in the current model. The reliability of the prediction for bubble growth model can be enhanced by coupling the diffusion of hydrogen, oxygen and liquid/gas two phases fluid flow calculation inside the weld pool. This is left for future research.

Quantitative experimental validation of the proposed models on porosity formation has proved a significant challenge. Based on the modelling results, the possibility of porosity formation depends strongly on the size of pre-existing microbubbles and the hydrogen content inside the weld pool. The size of pre-existing microbubbles should be related to the morphology of the joint surfaces, which can be quantified by surface roughness measurement. It is expected that by reducing hydrogen levels in the alloy to be welded and smoothing the jointed surfaces, porosity formation will be suppressed. To elucidate the surface roughness effect and threshold hydrogen level on porosity formation, attempts have been made to perform a series of designed

experiments. The surfaces of welding samples have been abraded to achieve different surface roughness and the hydrogen content in the welding samples controlled by applying different degrees of electrochemical hydrogen charge. The experimental results show that with very minimal roughness, porosity formation can be suppressed even if the hydrogen inside the base material is very high. A surprising result has been found: even when welding with high surface roughness and high hydrogen content, porosity can still be suppressed when optimised electron beam welding parameters are employed. This suggests that the weld pool dynamics play a critical role on reducing porosity formation, by favouring bubble escape. As mentioned above, at this stage, since modelling of weld pool dynamics during electron beam welding process is still a significant challenge, modelling of bubble escape from the weld pool has yet to be achieved. Since bubbles nucleate when the joint surfaces melt, the melting front ahead of the keyhole is critical for bubble survival. With optimised electron beam parameters and perfect alignment between the electron beam and joint edges, the liquid region of the joint edges at the melting front can be very thin, which favours bubble. This has been confirmed by welding samples with small beam offset, which changes the size of the liquid region around the joint edges at the melting front.

Although significant advances have been made in a number of areas in this study, due to the very complicated physical phenomena occurring particularly in the keyhole some gross assumptions have been necessary. To improve the capability of the model for porosity formation, fluid dynamics calculations need to be coupled with the current model, so that keyhole dynamics can be predicted more accurately. This is the major challenge for future research.

References

[1] Gerd Lutjering and James C. Williams. *Titanium*. Springer-Verlag, Berlin Heidelberg New York, 2nd edition, 2007.

[2] Vydehi Arun Joshi. *Titanium Alloys-An Atlas of Structures and Fracture Features*. Taylor and Francis, 2006.

[3] Leyens Christoph and Peters Manfred, editors. *Titanium and Titanium Alloys-Fundamentals and Application*. Wiley-VCH GmbH & Co. KGaA, Weinheim, Germany, 2003.

[4] Valentin N. Moiseyev. *Titanium Alloys-Russian Aircraft and Aerospace Applications*. Taylor and Francis, 2006.

[5] H Schultz. *Electron beam welding*. Abington publishing, Cambridge, 1993.

[6] R. C. Reed, H. J. Stone, S. M. Roberts, and J. M. Robinson. The development and validation of a model for the electron beam welding of aero-engine components. *Proceedings of the Institution of Mechanical Engineering, Part G: Journal of Aerospace Engineering*, 211:421–428, 1997.

[7] *The Jet Engine*. The Technical Publication Department, Rolls-Royce plc, Derby, England, 5th edition, 1996.

[8] R. C. Reed. *The Superalloys: Fundamentals and Applications*. Cambridge University Press, 2006.

[9] John Norrish. *Advanced welding process-Technology and process control.* Woodhead Publishing Limited, Abington, Cambridge, England, 2006.

[10] Nasir Ahmed, editor. *New developments in advanced welding.* Woodhead Publishing Limited, Abington publishing, Cambridge, 2005.

[11] *ASM Handbook, Volumn 6, Welding Brazing and Soldering.* ASM International, 1993.

[12] Mathew J. Donachie. *Titanium, A Technique Guide.* ASM International, 2nd edition, 2000.

[13] J. R. Cho, K. T. Conlon, and R. C. Reed. Residual stress in an electron beam weld of Ti-834: characterisation and numerical modelling. *Metallurgical and Materials Transaction A*, 34A:2935–2946, 2003.

[14] O. M. Ivasishin. Structure and mechanical properties of high-temperature titanium alloys after rapid heat treatment. *Materials Science and Engineering, A*, 168:23–28, 1993.

[15] S. L. Semiatin, V. Seetharaman, and A. K. Ghosh. Plastic flow, microstructure evolution, and defect formation during primary hot working of titanium and titanium aluminide alloys with lamellar colony microstructures. *Phil. Trans. R. Soc. Lond. A*, 357:1487–1512, 1999.

[16] P. Wanjara, M. Jahazi, Monajati, and S. Yue. Influence of thermomechanical processing on microstructural evolution in near- alloy IMI834. *Materials Science and Engineering A*, 416:300311, 2006.

[17] J.R. Wood, P.A. Russo, M.F. Welter, and E.M. Crist. Thermomechanical processing and heat treatment of Ti6Al2Sn2Zr2Cr2MoSi for structural applications. *Materials Science and Engineering A*, 243:109–118, 1998.

[18] Jong-Teak Yeom, Jeoung Han Kim, Jae keun Hong, and Nho-Kwang Park. Influence of initial microstructure on hot workability of Ti-6Al-4V. *International Journal of Modern Physics B*, 23:808–813, 2009.

[19] George Zheng Chen, Derek J. Fray, and Tom W. Farthing. Cathodic deoxygenation of the alpha case on titanium and alloys in molten calcium chloride. *Metallurgical and Materials Transaction B*, 32:1041–1052, 2001.

[20] L. N. Belyanchikov. Thermodynamics of titanium-based melts: Ii oxygen in liquid titanium. *Russian Metallurgy*, 2010:1156–1163, 2010.

[21] Si-Young Sung and Young-Jig Kim. Alpha-case formation mechanism on titanium investment castings. *Materials Science and Engineering A*, 405:173177, 2005.

[22] R.W. Evans, R.J. Hull, and B. Wilshire. The effects of alpha case formation on the creep fracture properties of the high-temperature titanium alloy IMI 834. *Journal of Materials Processing Technology*, 56:492–501, 1996.

[23] M. Gobel, V. A. C. Haanappel, and M. F. Stroosnijder. On the oxidation of diffusion coefficients of oxygen in one-phase ti (alpha-ti) and two-phase ti-4nb (alpha-and beta-ti) by micro-hardness measurements. *Oxidation of Metals*, 55:137–151, 2001.

[24] E. W. Collings. *The Physical Metallurgy of Titanium Alloys.* American Society for Metals, 1984.

[25] Kenneth C Mills. *Recommended values of Thermophysical properties for selected commercial alloys.* Woodhead Publishing Limited, Abington, Cambridge , England, 2002.

[26] M. Benedetti and V. Fontanari. The effect of bi-modal and lamellar microstructure of Ti-6Al-4V on the behavior of fatigue cracks emanating from edge-notches. *Fatigue and Fracture of Engineering Materials and Structure*, 27:1073–1089, 2004.

[27] R. R. Boyer. An overview on the use of titanium in the aerospace industry. *Materials Science and Engineering A*, 213:103–114, 1996.

[28] G. Welsch, R. Boyer, and E. W. Collings, editors. *Materials Properties Handbook: Titanium Allloys*. Ohio: ASM International, 1994.

[29] F. Bridier, P. Villechaise, and J. Mendez. Analysis of the different slip systems activated by tension in an $\alpha + \beta$ titanium alloy in relation with local crystallographic orientation. *Acta Materialia*, 53:555–567, 2005.

[30] S. Birosca, J.Y. Buffiere, M. Karadge, and M. Preuss. 3-d observations of short fatigue crack interaction with lamellar and duplex microstructures in a two-phase titanium alloy. *Acta Materialia*, 59:1510–1522, 2011.

[31] P. Pototzky, H.J. Maier, and H.-J. Christ. Thermomechanical fatigue behavior of the high-temperature titanium alloy IMI 834. *Metallurgical and Materials Transaction A*, 29:2995–3004, 1998.

[32] M. A. Daeubler, D. Helm, and D. F. Neal. Applications of IMI 834 in aeroengines. In *Titanium 1990: Products and applications*, volume 1, pages 78–87, Buena Vista, FL USA, Sept. 30-Oct 1990. Dayton, OH (US); Titanium Development Association.

[33] H. J. Stone. *The Characterisation and Modelling of Electron Beam Welding*. PhD thesis, The University of Cambridge, 1999.

[34] I. A. Krinberg and G. M. Mladenov. Formation and expansion of the plasma column under electron beam-metal interaction. *Vacuum*, 77:407–411, 2005.

[35] P. G. Klemens. Heat balance and flow conditions for electron beam and laser beam welding. *Journal of Applied Physics*, 47:2165–2174, 1976.

[36] Peter Petrov, Chavdar Georgiev, and Georgy Petrov. Experimental investigation of weld pool formation in electron beam welding. *Vacuum*, 51(3):339–343, 1998.

[37] K. W. Westerberg, T. C. Meier, M. A. McClelland, D. G. Braun, L. V. Berzins, T. M. Anklam, and J. Storer. Analysis of the e-beam evaporation of titanium and Ti-6Al-4V. In R. Bakish, editor, *Electron Beam Melting and Refining State of the Art 1997 Conference*. Englewood, NJ: Bakish Materials Corp., 1997.

[38] Roschen Sasikumar, Michael J Walker, S Savithri, and Suresh Sundarraj. Initiation of microporosity from pre-existing bubbles: a computational study. *Modelling Simul. Mater. Sci. Eng*, 16:0350049 (14pp), 2008.

[39] Hans-Jurgen Butt and Michael Kappl. *Surface and Interfacial Forces*. Wiley-VCH GmbH & Co. KGaA, Weinheim, Germany, 2010.

[40] Xi Chen and Hai-Xing Wang. A calculation model for the evaporation recoil pressure in laser material processing. *Journal of Physics D- Applied Physics*, 34:2637–2642, 2001.

[41] G Miadenov, K. Vutova, and S. Wojcicki. Experimental investigation of the weld depth and thermal efficiency during electron beam welding. *Vacuum*, 51(2):231–233, 1998.

[42] H. Hemmer and . Grong. Prediction of penetration depths during electron beam welding. *Science and Technology of Welding and Joining*, 4:219–225, 1999.

[43] R. L. O'Brien, editor. *Welding Handbook*, volume 2. American Welding Society, 8 edition, 1991.

[44] Katarzyna Olszewska and Kazimierz Friedela. Control of the electron beam active zone position in electron beam welding processes. *Vacuum*, 74:29–43, 2004.

[45] T. DebRoy and S. A. David. Physical processes in fusion welding. *Reviews of Modern Physics*, 65:85–111, 1995.

[46] Oystein Grong. *Metallurgical Medelling of Welding*. The Institute of Materials Press, London, 1997.

[47] M. Salcudan, M. ChoI, and R. Greif. A study of heat transfer during arc welding. *International Journal of Heat and Mass Transfer*, 29(2):215–225, 1986.

[48] C.S. Wu, H.G. Wang, and Y.M. Zhang. A new heat source model for keyhole plasma arc welding in FEM analysis of the temperature profile. *Welding Journal*, December:284–291, 2006.

[49] H.J. Stone, S.M. Roberts, and R.C. Reed. A process model for the distortion induced by the electron-beam welding of a nickel-based superalloy. *Metallurgical and Materials Transactions A*, 31A:2260–2272, 2000.

[50] K. C. Mills, B. J. Keene, R. F.Brooks, and A. Shirali. Marangoni effects in welding. *Phil. Trans. R. Soc. Lond. A*, 356:911–925, 1998.

[51] R. Rai, G. G. Roy, and T. DebRoy. A computationally efficient model of convective heat transfer and solidification characteristics during keyhole mode laser welding. *Journal of Applied Physics*, 101:054909, 2007.

[52] P. D. Lee, P. N. Quested, and M. Mclean. Modelling of Marangoni effects in electron beam melting. *Phil. Trans. R. Soc. Lond. A*, 356:1027–1043, 1998.

[53] R. Rai, S. M. Kelly, R. P. Martukanitz, and T. Debroy. A convective heat-transfer model for partial and full penetration keyhole mode laser welding of a structural steel. *Metallurgical and Materials Transactions A*, 39A:98–112, 2008.

[54] R. Rai, P. Brugard, J O Milewski, T J Lienert, and T DebRoy. Heat transfer and fluid flow during electron beam welding of 21-Cr-6Ni-9Mn steel and Ti-6Al-4V Alloy. *J. Phys. D: Appl Phys.*, 42:025503, 2009.

[55] A Kaplan. A model of deep penetration laser welding based on calculation of the keyhole profile. *J. Phys. D: Appl. Phys*, 27:1805–1814, 1994.

[56] Hyungson Ki, Pravansu S. Mohanty, and Jyoti Mazumder. Modelling of laser keyhole welding: Part I. mathematical modelling, numerical methodology, role of recoil pressure, multiple reflections, and free surface evolution. *Metallurgical and Materials Transaction A*, 33A:1817–1830, 2002.

[57] Hyungson Ki, Pravansu S. Mohanty, and Jyoti Mazumder. Modelling of laser keyhole welding: Part ii. simulation of keyhole evolution, velocity, temperature profile, and experimental verification. *Metallurgical and Materials Transaction A*, 33A:1831–1842, 2002.

[58] M. Geiger, K. H. Leitz, H. Koch, and A. Otto. A 3d transient model of keyhole and melt pool dynamics in laser beam welding applied to the joining of zinc coated sheets. *Prod. Eng. Res. Devel.*, 3:127–136, 2009.

[59] J. G. Andrews and D. R. Atthey. Hydrodynamic limit to penetration of a material by a high-power beam. *Journal of Physics D: Applied Physics*, 9:2181–2194, 1976.

[60] John Dowden, Nazmi Postacioglu, Michael Davis, and Phiroze Kapadia. A keyhole model in penetration welding with a laser. *Journal of Physics D: Applied Physics*, 20:36–44, 1987.

[61] J. Kroos, U. Gratzke, and G. Simon. Towards a self-consistent model of the keyhole in penetration laser beam welding. *Journal of Physics D: Applied Physics*, 26:474–480, 1993.

[62] J Kroos, U Gratzke, M Vicanek, and G Simon. Dynamic behavior of the keyhole in laser welding. *Journal of Physics D: Applied Physics*, 26:481–486, 1993.

[63] W. Sudnik, D. Radaj, and W. Erofeew. Computerised simulation of laser beam welding, modelling and verification. *Journal of Physics D: Applied Physics*, 29:2811–2817, 1996.

[64] Shigeki Fujinaga, Hiroo Takenaka, Toru Nrikiyo, Seiji Katayama, and Akira Matsunawa. Direct obervation of keyhole behaviour during pulse modulated high-power Nd-YAG laser irradiation. *Journal of Physics D: Applied Physics*, 33:492–497, 2000.

[65] John Dowden and Phiroze Kapadia. A mathematical investigation of the penetration depth in keyhole welding with continuous CO_2 lasers. *Journal of Physics D: Applied Physics*, 28:2252–2261, 1995.

[66] Akira Matsunawa and Vlad Semak. The simulation of front keyhole wall dynamics during laser welding. *Journal of Physics D: Applied Physics*, 30:798–809, 1997.

[67] Vladimir V Semak, Willian David Bragg, Brian Damkroger, and Steven Kempka. Transient model for the keyhole during laser welding. *Journal of Physics D: Applied Physics*, 32:L61–L64, 1999.

[68] P. Solana and J. L. Ocana. A mathematical model for penetration laser welding as a free-boundary problem. *Journal of Physics D: Applied Physics*, 30:1300–1313, 1997.

[69] R. Fabbro and K. Chouf. Keyhole modelling during laser welding. *Journal of Physics D: Applied Physics*, 87:4075–4083, 2000.

[70] Jung-Ho Cho and Suck-Joo Na. Implementation of real-time multiple reflection and fresnel absorption of laser beam in keyhole. *Journal of Physics D: Applied Physics*, 39:5372–5378, 2006.

[71] Hyungson Ki, Pravansu S. Mohanty, and Jyoti Mazunder. A numerical method for multiphase incompressible thermal flows with solid-liquid and liquid-vapor phase transformations. *Numerical Heat Transfer, Part B*, 48:125–145, 2005.

[72] A. K. Dasgupta and J. Mazumder. Physics of zinc vaporization and plasma absorption during CO_2 laser welding. *Journal of Applied Physics*, 102:053108–1–15, 2007.

[73] Jung-Ho Cho, Dave F Farson, John O Milewski, and Kendall J Hollis. Weld pool flows during initial stages of keyhole formation in laser welding. *Journal of Physics D: Applied Physics*, 42:175502(11p), 2009.

[74] Andreas Otto and Michael Schmidt. Towards a universal numerical simulation model for laser material processing. *Physics Procedia*, 5:35–46, 2010.

[75] R. Rai and T. DebRoy. Tailoring weld geometry during keyhole mode laser welding using a genetic algorithm and a heat transfer model. *Journal of Physics D: Applied Physics*, 39:1257–1266, 2006.

[76] Pierre Axlandre Legait. *Formation and Distribution of Porosity in Al-Si Welds.* PhD thesis, Worcester Polytechnic Institute, 2005.

[77] Hidetoshi Fujii, Hideaki Umakoshi, Yasuhiro Aoki, and Kiyoshi Nogi. Bubble formation in aluminum alloy during electron beam welding. *Journal of Materials Processing Technology*, 155-156:1252–1255, 2004.

[78] Alexander F. H. Kaplan, Masami Mizutani, Seiji Katayama, and Akira Matsunawa. Unbounded keyhole collapse and bubble formation during pulsed laser interaction with liquid zinc. *Journal of Physics D- Applied Physics*, 35(11):1218–1228, 2002.

[79] V. A. Silvinskii, V. N. Zamkov, G. S. Kirichenko, and P. V. Poritskii. Role of hydrides in pore formation in welding titanium. *Paton Welding Journal*, 6:265–269, 1994.

[80] F. Karimzadeh, M. Salehi, A.Saatchi, and M. Meratian. Effect of microplasma arc welding process parameters on grain growth and porosity distribution of thin sheet Ti-6Al-4V alloy weldment. *Materials and Manufacturing Processes*, 20:205–219, 2005.

[81] S. M. Gurevich, O. K. Nazarenko, V. N. Zamkov, V. E. Lokshin, and A. D. Shevelev. Ti-6Al-4V titanium alloy weldability in electron beam application. *Titanium 80 - Science and Technology*, 4:2347–2358, 1980.

[82] V. V. Redchits. Scientific fundamentals and measures used to prevent the formation of pores in fusion welded titanium and its alloys. *Welding International*, 11(9):722–728, 1997.

[83] N. Gouret, G. Dour, B. Miguet, E. Olliver, and R. Fortunier. Assessment of the origin of porosity in electron-beam-welded TA6V plates. *Metallurgical and Materials Transactions A*, 35A:879–889, 2004.

[84] T. Mohandas, D. Banerjee, and V. V. Rao. Fusion zone microstructure and porosity in electron bean welds of an alpha + beta titanium alloy. *Metallurgical and Materials Transactions A*, 30A:789, 1999.

[85] M. Strangwood. Porosity studies in high energy density welding processes. Technical report, Department of Metallurgy and Materials, University of Birmingham, 2007.

[86] P. D. Lee and J. D. Hunt. Hydrogen porosity in directional solidified aluminum-copper alloys: In situ observation. *Acta Mater.*, 45(10):4155–4169, 1997.

[87] R. C. Atwood, S. Sridhar, W.Zhang, and P. D. Lee. Diffusion-controlled growth of hydrogen pores in aluminium-silicon casting: In situ observation and modelling. *Acta Mater.*, 48(405-417):405–417, 2000.

[88] R. C. Atwood and P. D. Lee. A three-phase model of hydrogen pore formation during the equiaxed dendritic solidification of aluminum-silicon alloys. *Metallurgical and Materials Transactions B*, 33:209–221, 2002.

[89] R. C. Atwood and P. D. Lee. Simulation of the three-dimensional morphology of solidification porosity in an aluminum-silicon alloy. *Acta Materialia*, 51:5447–5466, 2003.

[90] O. N. Senkov and F. H. Fores. Thermohydrogen processing of titanium alloy. *International Journal of Hydrogen Energy*, 24:565–576, 1999.

[91] Ronald S. Vitt and Kanji Ono. Hydrogen solubility in alpha titanium. *Metallurgical Transactions*, 2:608–609, 1971.

[92] Y. Hirooka, M. Miyake, and T. Sano. A study of hydrogen absorption and desorption by titanium. *Journal of Nuclear Materials*, 96:227–232, 1981.

[93] Akito Takasaki, Yoshio Furuya, Koza Ojima, and You Taneda. Hydrogen solubility of two phase (Ti3Al+ TiAl) titanium aluminides. *Scripta Metallurgica et materialia*, 32(11):1759–1764, 1995.

[94] Yexin Chen, Xiaojing Wan, Fang Li, Qingjiang Wang, and Yuyin Liu. The behavior of hydrogen in high temperature titanium alloy ti-60. *Materials Science and Engineering A*, 466:156–159, 2007.

[95] Sakae Takeuchi, Toshio Honma, and Susumu Ikeda. Solubility of hydrogen in titanium at 900 °C to 1500 °C. Technical report, Tohoku University, 1966.

[96] H. Okamoto. H-Ti (hydrogen-titanium). *Journal of Phase Equilibria*, 13:443, 1992.

[97] Wei-E Wang. Thermodynamic evaluation of the titanium-hydrogen system. *Journal of Alloy and Compounds*, 238:6–12, 1996.

[98] Takeo Kasajima, Tokujiro Nishikiori, Toshiyuki Nohira, and Yasuhiko Ito. Thermodynamic evaluation of Ti-H system at medium-range temperature by molten salt electrochemical technique. *Journal of The Electrochemical Society*, 150:E355–E359, 2003.

[99] Tokujiro Nishikiori, Toshiyuki Nohira, and Yasuhiko Ito. Kinetics investigation of the Ti-H system by the molten salt electrochemical technique. *Journal of The Electrochemical Society*, 148:E127–E132, 2001.

[100] Daniel Laser. Kinetics of hydrogen dissolution by titanium, a digital simulation. *The Journal of Vacuum Science and Technology*, 20:37–44, 1982.

[101] E. Konigsberger, G. Eriksson, and W. A. Oates. Optimisation of the thermodynamic properties of the Ti-H and Zr-H system. *Journal of Alloy and Compounds*, 299:148–152, 2000.

[102] Omar Salman Abdul-Hamid. *Diffusion of hydrogen in titanium.* PhD thesis, Massachusetts Institute of Technology, 1993.

[103] H. J. Christ, M.Decker, and S. Zeitler. Kinetics and thermodynamics of the absorption of hydrogen in beta-titanium alloys. *Journal of Thermal Analysis and Calorimetry*, 55:609–617, 1999.

[104] H. J. Christ, M. Decker, and S. Zeitler. Hydrogen diffusion coefficients in the titanium alloys IMI834, Ti10-2-3, Ti21S, and Alloy C. *Metallurgical and Materials Transactions A*, 31A:1510–1517, 2000.

[105] N. Kishore Babu, S. Ganesh Sundara Raman, R. Mythili, and S. Saroja. Correlation of microstructure with mechanical properties of TIG weldments of Ti6Al4V made with and without current pulsing. *Materials Characterization*, 58:581–587, 2007.

[106] Aniruddha Kumar, Mark Sapp, Jay Vincelli, and Mool C. Gupta. A study on laser cleaning and pulsed gas tungsten arc welding of Ti3Al2.5V alloy tubes. *Journal of Materials Processing Technology*, 210:64–71, 2010.

[107] J. E. Blackburn, C. M. Allen, P. A. Hilton, L. Li, M. I. Hoque, and A. H. Khan. Modulated Nd:YAG laser welding of Ti6Al4V. *Science and Technology of Welding and Joining*, 15:433–439, 2010.

[108] Y. Zhang, Y. S. Sato, H. Kokawa, S. H. C. Park, and S. Hirano. Grain structure and microtexture in friction stir welded commercial purity titanium. *Science and Technology of Welding and Joining*, 15:500–505, 2010.

[109] R.W. Fonda and K.E. Knipling. Texture development in near-alpha Ti friction stir welds. *Acta Materialia*, 58:64526463, 2010.

[110] Suresh D. Meshram and T. Mohandas. A comparative evaluation of friction and electron beam welds of near-alpha titanium alloy. *Materials and Design*, 31:2245–2252, 2010.

[111] E. Dalgaard, P. Wanjara, J. Gholipour, X. Cao, and J. J. Jonas. Linear friction welding of a near-beta titnaium alloy. *Acta Materialia*, 60:770–780, 2012.

[112] R. Turner, J.-C. Gebelin, R. M. Ward, and R. C. Reed. Linear friction welding of ti-6al-4v: Modelling and validation. *Acta Materialia*, 59:3792–3803, 2011.

[113] V. I. Murav'ev. Problems of pore formation in welded joints of titanium allloys. *Metal Science and Heat Treatment*, 47:282–288, 2005.

[114] S. A. David and T. Debroy. Current issues and problems in welding science. *Science*, 257:497–502, 1992.

[115] W. H. Kim and S. J. Na. Heat and fluid flow in pulsed current gta weld pool. *International Journal of Heat and Mass Transfer*, 41:3213–3227, 1998.

[116] Toshiyuki Miyazaki and Warren H. Giedt. Heat transfer from and elliptical cylinder moving through an infinite plate applied to electron beam welding. *Journal of Heat and Mass Transfer*, 25:807–814, 1981.

[117] C. Y. Ho. Fusion zone during focused electron-beam welding. *Journal of Materials Processing Technology*, 167:265–272, 2005.

[118] T. A. Palmer, J. W. Elmer, K. D. Nicklas, and T. Mustaleski. Transferring electron beam welding parameters using the enhanced modified faraday cup. *Welding Research*, 86:388–398, 2007.

[119] T. A. Palmer and J. W. Elmer. Improving process control in electron beam welding using the enhanced modified faraday cup. *Journal of Manufacturing Science and Engineering*, 130:041008–1–15, 2008.

[120] E. A. Brandes and G. B. Brook, editors. *Smithells Metals Reference Book*. Butterworth-Heinemann, Linacre House, Jordan Hill, Oxford, 7th edition, 1992.

[121] S. Mishra and T. DebRoy. Measurements and Monte Carlo simulation of grain growth in the heat-affected zone of Ti-6Al-4V welds. *Acta Mater*, 52:1183–1192, 2004.

[122] Siegfried Schiller, Ullrich Heisig, and Siegfried Panzer. *Electron Beam Technology*. John Wiley & Sons Inc, 1982.

[123] *ASM Handbook, Volumn 9, Metallography And Microstructures*. ASM international, 1992.

[124] S. A. Gedeon and T. W. Eagar. Thermochemical analysis of hydrogen absorption in welding. *Welding Research Supplement*, July:264–s–271–s, 1990.

[125] J. B. Leblond and D. Dubois. A general mathematical description of hydrogen diffusion in steels-I derivation of diffusion equations from Boltzmann type transport equations. *Acta metall*, 31:1459–1469, 1983.

[126] J. B. Leblond and D. Dubois. A general mathematical description of hydrogen diffusion in steels-II numerical study of permeation and determination of trapping parameters. *Acta metall*, 31:1471–1478, 1983.

[127] Li Yajiang, Wang Juan, and Shen Xiaoqin. FEM calculation and effect of diffusion hydrogen distribution in the fusion zone of super-high strength steel. *Computational Materials Science*, 31:57–66, 2004.

[128] A. F. Fishgot, B. A. Kolacev, A. A. Mamaev, and Y. M. Shtemler. Diffusion of hydrogen during and after electron beam welding titanium alloys. *Welding International*, 7:230–233, 1993.

[129] V. V. Frolov. Distribution of hydrogen in the heat affected zone of a welded joint in alpha-alloy of titanium taking into account thermal diffusion. *Fiz Khim Obrab Mater*, 4:134–137, 1973.

[130] P. Wehr and J. Ruge. Hydrogen distribution in welded joints in TiAl6V4 alloys. *Schweissen und Schneiden*, 28:411–414, 1976.

[131] L. I. Smirnow. Diffusion of hydrogen in metals at arbitrary concentration gradients. *International Journal of Hydrogen Energy*, 24:813–817, 1999.

[132] Martin Eden Glicksman. *Diffusion In Solids-Field Theory, Solid-State Principles And Application*. John Wiley & Sons, Inc., New York, 2000.

[133] J. Gu and D. Hardie. Effect of hydrogen on structure and slow strain rate embrittlement of mill annealed ti6al4v. *Materials Science and Technology*, 12:802–807, 1996.

[134] Liangshun Luo, Yanqing Su, Jingjie Guo, and Hengzhi Fu. Formation of titanium hydride in Ti-6Al-4V alloy. *Journal of Alloy and Compounds*, 425:140–144, 2006.

[135] I. Katzarov, S. Malinov, and V. Yanakieva. Mathematical model and numerical simulation of the formation and growth of a two-phase layer during diffusion in ternary system. *Acta Mater*, 53:3091–3099, 2005.

[136] G. D. Nikiforov and V. V. Redchits. The mechanism of pore formation when thick titanium alloys are fusion welded. *Avt. Svarka*, 10:42–45, 1981.

[137] F. Jomni, A. Denat, and F. Aitken. The dynamics of microscopic bubbles in viscous insulating liquids. *Journal of Applied Physics*, 105:053301–9, 2009.

[138] Jianglin Huang, Nils Warnken, Jean-Christophe Gebelin, Martin Strangwood, and Roger C. Reed. Hydrogen transport and rationalisation of porosity formation during welding of titanium alloys. *Metallurgical and Materials Transaction A*, (Accepted), 2011.

[139] D. Eliezer, E. Tal-Gutelmacher, C.E. Cross, and Th. Boellinghaus. Hydrogen absorption and desorption in a duplex-annealed Ti-6Al-4V alloy during exposure to different hydrogen-containing environments. *Materials Science and Engineering A*, 433:298–304, 2006.